

Three-Dimensional Fluid Flow and Solute Transport in Rough-Walled Fractures

by

David J. Brush

A thesis
presented to the University of Waterloo
in fulfilment of the
thesis requirement for the degree of
Doctor of Philosophy
in
Civil Engineering

Waterloo, Ontario, Canada, 2001

© David J. Brush 2001



National Library
of Canada

Acquisitions and
Bibliographic Services

395 Wellington Street
Ottawa ON K1A 0N4
Canada

Bibliothèque nationale
du Canada

Acquisitions et
services bibliographiques

395, rue Wellington
Ottawa ON K1A 0N4
Canada

Your file Votre référence

Our file Notre référence

The author has granted a non-exclusive licence allowing the National Library of Canada to reproduce, loan, distribute or sell copies of this thesis in microform, paper or electronic formats.

L'auteur a accordé une licence non exclusive permettant à la Bibliothèque nationale du Canada de reproduire, prêter, distribuer ou vendre des copies de cette thèse sous la forme de microfiche/film, de reproduction sur papier ou sur format électronique.

The author retains ownership of the copyright in this thesis. Neither the thesis nor substantial extracts from it may be printed or otherwise reproduced without the author's permission.

L'auteur conserve la propriété du droit d'auteur qui protège cette thèse. Ni la thèse ni des extraits substantiels de celle-ci ne doivent être imprimés ou autrement reproduits sans son autorisation.

0-612-60525-6

Canada

The University of Waterloo requires the signatures of all persons using or photocopying this thesis.
Please sign below, and give address and date.

ABSTRACT

Predicting fluid flow and solute transport through fractured rock is an important component of engineering analysis and design in many disciplines including groundwater contamination, drinking water supply, nuclear waste disposal, petroleum and gas production, mine and excavation stability, and geothermal production. Fractures largely influence the flow of fluids in a fractured rock environment by forming conduits that are typically orders of magnitude more conductive to fluid flow than the surrounding rock.

This thesis examines flow and transport through a single laboratory scale rock fracture, which is the necessary starting point for predicting flow and transport through large scale fractured rock systems. In the past, single fractures were idealized as a set of parallel plates in order to obtain a tractable mathematical description of fluid flow, namely the cubic law. However, it is now well established in the literature that single fractures are rough-walled conduits with variable aperture and points of contact. In fact, modern laboratory methods have directly mapped the void space of fracture samples, and provide the unique opportunity of simulating flow and transport at the scale of these measurements.

The primary objective of this investigation was to develop a numerical model to simulate three-dimensional small-scale fluid flow within a single fracture using the Navier-Stokes (NS) equations. The NS equations are the fundamental equations for fluid flow and form a complex non-linear system of equations that require numerical solution. In this work, the NS equations were solved using the finite volume method with a structured non-orthogonal grid mapped onto the three-dimensional void space. The fracture flow model was verified by comparing simulations to analytical and published results of fluid flow through parallel and sinusoidal plates. The flow model was applied to numerous synthetic or randomly generated rough-walled fractures, and the results clearly demonstrate for Reynolds numbers (Re) above unity, that the inertial forces may significantly influence the internal flow field within a fracture and the bulk flow rate across a fracture. Conversely, these simulations demonstrated that inertial forces may be neglected when Re was below unity. Two additional constraints involving the product of Re and statistical roughness parameters were also used to delineate the influence of inertial forces. For simulations with Re below unity, the bulk flow rates were shown to be within 10% of a two-dimensional approximation commonly referred as the local cubic law.

The secondary objective of this investigation was to develop a numerical model to simulate three-dimensional small-scale solute transport within a single fracture using the flow field determined by the NS flow model. To accomplish this task, the random walk particle method (RWPM) which uses particle tracking methods to simulate advective transport of massless marker particles through the fracture flow field, and random displacements to simulate diffusive transport was employed. The fracture transport model was verified by comparing the simulation results to analytical solutions of solute transport through a set of parallel plates. Furthermore, the model

ABSTRACT

simulations were compared to observations of solute breakthrough during tracer experiments on an actual rough-walled fracture, and a rough-walled transparent fracture replica. The model was successful in predicting the breakthrough curve for the actual fracture, and moderately successful for the transparent fracture replica.

By comparing the developed models to analytical solutions, simplified numerical simulations, and laboratory experiments, it was concluded that the models adequately describe fluid flow and contaminant transport through a single rough-walled fracture. Some examples of future applications of these models include: the comparison of the three-dimensional RWPM to the two-dimensional advection-dispersion equation for various synthetic fractures, high Reynolds number fluid flow and contaminant transport, and the dissolution of immiscible fluids trapped within a rough-walled fracture.

ACKNOWLEDGEMENTS

I am grateful to Dr. Neil Thomson for allowing me to be a part of his fracture research program. He has been a thoughtful supervisor, a mentor, and an understanding friend.

The fellowship and support of many graduates students, staff, and faculty in the Water Resources Group at the University of Waterloo was greatly appreciated. I enjoyed working with Sarah Anderson and Bruce Tunncliffe in the fracture research program, and I am thankful for the use of their data to validate the models developed in this thesis. I am also thankful for the longtime comradery of Eric Hood and Stephen Fassnacht.

I am very thankful to my parents and family for their support, encouragement, and prayers throughout my academic career.

I am continually overwhelmed by my beautiful wife, Maggie. She has been a wise counsellor, a gifted manager, a strong leader, a giving and loving supporter, and my best friend. I could not have completed this work without her. I am thankful to my amazing daughters, Maurana and Ilia, for being so patient, understanding, and full of joy throughout this research project.

I am also grateful to Drs. Jon Sykes, Ed McBean, and Grahame Farquhar for providing me with graduate and undergraduate research positions that served as a foundation to this thesis work.

Funding for this research was provided by an NSERC PGS-B scholarship (D. J. Brush), an NSERC Research Grant (N. R. Thomson), and an NSERC Strategic Grant (N. R. Thomson and B. H. Kueper).

Finally, I would like to thank my Ph.D. thesis examination committee (Dr. C. F. Tsang from the Ernest Orlando Lawrence Berkeley National Laboratory, and Drs. J. F. Sykes, W. C. Lennox, and G. Stubbley from the University of Waterloo) for their careful review, constructive input, and overall support of this thesis.

I give thanks to my Lord and Saviour Jesus Christ for the grace to complete this thesis. I have learned that “I can do everything through him who gives me strength.” [Phil. 4:13]

TABLE OF CONTENTS

ABSTRACT	iv
ACKNOWLEDGEMENTS	vi
LIST OF TABLES	xi
LIST OF FIGURES	xii
 CHAPTER 1. Introduction	 1
1.1 Research Objectives	3
1.2 Scope of Thesis	4
 CHAPTER 2. Characterization of Single Fractures	 6
2.1 Introduction	6
2.2 Bulk Aperture Measurements	7
2.3 Aperture Distribution Measurements	9
2.4 Wall Topography Measurements	11
2.5 Two Laboratory Fractures Characterized using Wall Topography Measurements	12
2.6 Random Fracture Generation	13
2.6.1 Methodology	13
2.6.2 Parameter Selection and Examples of Generated Fractures	15
 CHAPTER 3. Fluid Flow and Solute Transport in Single Fractures	 35
3.1 Introduction	35
3.2 Governing Equations	36
3.2.1 Fluid Flow	36
3.2.2 Solute Transport	40
3.3 Review of Previous Work	42
3.3.1 Empirical Studies of Fluid Flow and Solute Transport	43
3.3.2 Theoretical Studies of Fluid Flow	46
Local Cubic Law	46
Navier-Stokes Equations	49
3.3.3 Theoretical Studies of Solute Transport	50
Parallel Plates	50
Rough-Walled Fractures	53

CHAPTER 4. Development of Fluid Flow and Solute Transport Models

4.1	Introduction	61
4.2	Discretization of Fracture Void Space	62
4.3	Three-Dimensional Flow Model Based on the Navier-Stokes Equations	63
4.3.1	Description of the Three-Dimensional Control Volume	63
	Interface Interpolation	65
	Nodal Gradients	66
	Normal Interfacial Gradients	67
4.3.2	Approximation of the Mass Conservation Equation	67
4.3.3	Approximation of the Momentum Conservation Equation	68
	Advection Term	69
	Diffusion Term	69
	Pressure Term	70
	General Algebraic Equation	70
4.3.4	Coupling the Momentum and Mass Conservation Equations	71
	PWI Method	71
	SIMPLE Algorithm	73
	General Algebraic Equation	74
4.3.5	Boundary Conditions	75
	Boundary Interface Extrapolation	75
	Inlet and Outlet Boundaries	76
	Wall Boundaries	78
	Side Boundaries	79
4.3.6	Segregated Solution Algorithm	80
4.3.7	Solution of the General Algebraic Equations	81
4.4	Two-Dimensional Flow Model Based on the Local Cubic Law	83
4.4.1	Description of the Two-Dimensional Control Volume	83
4.4.2	Approximation of the Local Cubic Law	84
4.5	Three-dimensional Solute Transport Model Based on the	
	Random Walk Particle Method	86
4.5.1	Description of the Three-Dimensional Control Volume	86
4.5.2	Approximation of the Advection-Dispersion Equation	87

TABLE OF CONTENTS

CHAPTER 5 Simulation Results and Discussion

5.1	Introduction	99
5.2	Fluid Flow through Parallel Plates	100
5.3	Fluid Flow through Sinusoidal Fractures	101
5.4	Fluid Flow through Synthetic Rough-Walled Fractures	103
5.4.1	LCL Simulations versus Cubic Law Calculations	103
5.4.2	Stokes versus LCL Simulations	105
5.4.3	Navier-Stokes versus Stokes Simulations	108
5.4.4	Navier-Stokes Simulations versus Cubic Law Calculations	112
5.4.5	Accuracy, Errors, and Variability of Synthetic Fracture Simulations	112
5.5	Solute Transport through Parallel Plates	114
5.6	Fluid Flow and Solute Transport through Laboratory Fractures	116

CHAPTER 6. Conclusion and Recommendations

6.1	Research Contributions	174
6.2	Future Work	175

APPENDIX

REFERENCES

LIST OF TABLES

2.1	Summary of various studies measuring bulk aperture values of a single fracture.	16
2.2(a)	Description of studies measuring the aperture distribution in a single fracture.	17
2.2(b)	Statistical summary of studies measuring the aperture distribution in single fractures.	18
2.3	Parameters used to generate random fractures.	18
3.1	Summary of constraints for the LCL	54
3.2	Summary of various studies that measured and predicted fluid flow through single rough-walled fractures.	55
4.1	Summary of the segregated solution algorithm.	88
4.2	Summary of SIP-multigrid solver algorithm.	89
5.1	Parameters used in parallel plate flow simulations	120
5.2	Parameters used in sinusoidal fracture flow simulations	121
5.3	Parameters used in synthetic fracture flow simulations	122
5.4	Parameters used in parallel plate transport simulations	123
5.5	Parameters used in laboratory fracture flow and transport simulations	124

LIST OF FIGURES

1.1	Conceptual models of a single fracture: (a) a set of parallel plates with length L , width W , and constant aperture b , and (b) a set of rough-walled surfaces with the same length and width, but variable aperture $b(x, y)$	5
2.1	Fracture I surface plots of (a) upper, and (b) lower wall topography [data from <i>Tunnicliffe</i> , 1999].	20
2.2	Fracture II surface plots of (a) upper, and (b) lower wall topography [data from <i>Anderson</i> , 2001].	21
2.3	Fracture I surface plots of (a) raw aperture, and (b) mid-surface.	22
2.4	Fracture II surface plots of (a) raw aperture, and (b) mid-surface.	23
2.5	Histograms of raw aperture fields from (a) Fracture I and (b) Fracture II, and (c) autocorrelation plots from Fracture I and Fracture II.	24
2.6	(a) Surface plot of inferred aperture field for Fracture I calculated using (2.11) with $b_m = 0.2$ mm, and (b) distribution of contact points within aperture field.	25
2.7	(a) Surface plot of inferred aperture field for Fracture II calculated using (2.11) with $b_m = 0.74$ mm, and (b) distribution of contact points within aperture field.	26
2.8	Plot of three dimensionless ratios ($b_m/\langle b \rangle$, $\sigma_b/\langle b \rangle$ and c) versus b_m for the inferred aperture field of (a) Fracture I, and (b) Fracture II.	27
2.9	Histograms of (a) standardized e_b field, (b) aperture fields with $b_m = 1$ and $\sigma_b = 0.25$, and (c) aperture fields with $b_m = 0.25$ and $\sigma_b = 0.25$	28
2.10	Surface plots of normally and lognormally distributed aperture fields shown in parts (b) and (c) of Figure 2.9.	29
2.11	Histograms of (a) a normally distributed aperture field, (b) a normally distributed mid-surface field, and (c) the resulting upper and lower walls.	30
2.12	Surface plots of (a) a normally distributed aperture field, (b) a normally distributed mid-surface field, and (c) the resulting upper and lower walls.	31
2.13	Examples of random fractures with $\sigma_z = 0$ and various values of σ_m/b_m	32
2.14	Examples of random fractures with $\sigma_m/b_m = 0.0625$ and various values of σ_z	33
2.15	Plot of the relationship between the final relative roughness $\sigma_b/\langle b \rangle$ and fraction of contact c versus the initial relative roughness σ_m/b_m of the normally distributed random aperture fields used in this work.	34
3.1	Breakthrough curve of a conservative tracer through a single rough-walled fracture. Laboratory data extracted from <i>Moreno et al.</i> [1985].	56
3.2	The total flow rate from LCL simulations Q_{LCL} compared to the cubic law Q_{CL} using $\langle b \rangle$ for various values of (a) relative smoothness b_m/σ_b , (b) and relative roughness σ_b/b_m	57
3.3	The total flow rate from Stokes simulations Q_S compared to LCL simulations Q_{LCL} for various values of relative roughness σ_w/b_m from <i>Mourzenko et al.</i> [1995].	58

3.4	Results of various simulations through sinusoidal fracture profiles from <i>Brown et al.</i> [1995].	59
3.5	Dimensionless breakthrough curves of solute transport through a set of parallel plates for various values of Péclet numbers: Pe , Pe_M , and Pe^*	60
4.1	Examples of fracture domains: (a) 3D void space generated over an x - y grid with uniform spacing Δ_x and Δ_y , and variable aperture $b(x, y)$, (b) 3D CV domain formed by subdividing void space into uniform x - y increments δ_x and δ_y , and variable z increments $\delta_z(x, y)$, (c) 2D CV domain formed by subdividing void space into uniform x - y increments δ_x and δ_y	90
4.2	Example of a 3D CV from the interior of the 3D domain shown in Figure 4.1(a).	91
4.3	Details of the east face from the 3D CV shown in Figure 4.2. (a) Definition of tangential vectors ζ_e and χ_e , unit normal vector \hat{n}_e , and the local vector ξ_e which connects nodes P and E . (b) Definition of normal vector η_e passing through integration point e connecting auxiliary nodes P' and E' , and the outline of the CV associated with the face.	92
4.4	General boundary conditions used for the 3D simulations. The 2D simulations used the inlet, outlet, and side boundary conditions.	93
4.5	Details of a general 3D CV boundary face bf . (a) Definition of unit normal vector \hat{n}_{bf} and the local vector ξ_{bf} which connects node P to integration point bf . (b) Definition of normal vector η_{bf} connecting auxiliary node P' to integration point bf , and the boundary interface CV.	94
4.5	(a) An example of a 2D CV from the interior of the 2D domain shown in Figure 4.1(c). (b) Detail of a general 2D face and the outline (dotted line) of the CV associated with the face.	95
4.6	Profiles through nodes P and F shown in Figure 4.6(b) with: (a) planar mid-surface (dashed line), and (b) undulating mid-surface. (c) Detail of profile shown in Part (b). . . .	96
4.7	(a) Layout of nodes (circles) used to interpolate velocity at CV corner (square). (b) Layout of CV corners used to interpolate velocity at a general point p within the CV. . . .	97
4.8	Illustration of RWPM wall boundary conditions for various situations: (a) particle reflection off a planar wall, (b) particle reflection off an undulating wall, and (c) particle adjustment for the minimum wall separation distance.	98
5.1	Navier-Stokes simulations through parallel plates : (a) cross-sectional velocity vector plot, (b) normalized velocity and pressure profiles, and (c) relative error e_Q versus vertical grid spacing δ_z	125
5.2	Stokes and Navier-Stokes simulations through sinusoidal surfaces: (a) schematic profile of sinusoidal surfaces, (b) velocity field from Stokes simulations through the middle oscillation, and (c) velocity field from NS simulations through middle the oscillation.	126

LIST OF FIGURES

5.3	Stokes and Navier-Stokes simulations through sinusoidal surfaces: vertical profiles of (a) velocity components, and (b) pressure, at vertical locations P1, P2, and P3 in (b) and (c) of Figure 5.2.	127
5.4	Stokes and LCL sinusoidal surface simulations: total flow ratio Q_S/Q_{LCL} versus the sinusoidal relative roughness A/b_{min} for (a) mildly sloped $A/\lambda = 0.1$, and (b) steeply sloped $A/\lambda = 0.4$ surfaces.	128
5.5	Navier-Stokes and Stokes simulations through steeply sloped ($A/\lambda = 0.4$) sinusoidal surfaces: (a) Total flow ratio Q_{NS}/Q_S versus the Reynolds number Re of the flow field. (b) Relative error e_Q in the simulations versus the inverse number of subdivisions n_{sub}^{-1} applied to the base grid of $60 \times 1 \times 20$ CVs.	129
5.6	Example fracture geometry: three-dimensional surfaces plots of (a) smooth fracture with $\sigma_m/b_m = 0.125$, and (b) rough fracture with $\sigma_m/b_m = 1.0$	130
5.7	Example fracture geometry: aperture contour plots of (a) smooth fracture with $\sigma_m/b_m = 0.125$, and (b) rough fracture with $\sigma_m/b_m = 1.0$	131
5.8	LCL example fracture simulations: fluid flow fields using (4.109) without corrections ($\beta_{fp} = 1$) for (a) the smooth fracture, and (b) the rough fracture.	132
5.9	LCL simulations and cubic law calculations for synthetic fractures: total flow ratio Q_{LCL}/Q_{CL} versus the relative roughness σ_m/b_m for three values of mid-surface variability: (a) $\sigma_z = 0$, (b) $\sigma_z = 0.5$, and (c) $\sigma_z = 1$ mm.	133
5.10	Stokes example fracture simulations: vertically integrated fluid flow fields for (a) the smooth fracture, and (b) the rough fracture.	134
5.11	Stokes and LCL example fracture simulations: LCL fluid flow fields minus Stokes flow fields for (a) the smooth fracture, and (b) the rough fracture.	135
5.12	Stokes example fracture simulations: cross-sectional velocity vector plot for (a) the smooth fracture, and (b) the rough fracture.	136
5.13	Stokes example fracture simulations: vertical profiles of the x - and z -components of velocity at the locations P1, P2, and P3 defined in Figure 5.12.	137
5.14	Stokes and LCL synthetic fracture simulations: total flow ratio Q_S/Q_{LCL} versus σ_m/b_m for fractures with (a) $\sigma_z = 0$, (b) $\sigma_z = 0.5$, and (c) $\sigma_z = 1$ mm	138
5.15	Stokes and corrected LCL synthetic fracture simulations: total flow ratio Q_S/Q_{LCL} versus σ_m/b_m for fractures with (a) $\sigma_z = 0$, (b) $\sigma_z = 0.5$, and (c) $\sigma_z = 1$	139
5.16	Stokes and corrected LCL synthetic fracture simulations: total flow ratio Q_S/Q_{LCL} versus σ_m/b_m for fractures with (a) $\sigma_z = 0$, (b) $\sigma_z = 0.5$, and (c) $\sigma_z = 1$	140
5.17	Stokes and corrected LCL synthetic fracture simulations: total flow ratio Q_S/Q_{LCL} versus (a) the actual relative roughness $\sigma_b/\langle b \rangle$, (b) the actual roughness slope σ_b/λ_b , and (c) the mean aperture aspect ratio $\langle b \rangle/\lambda_b$	141
5.18	Stokes and LCL synthetic fracture simulations: total flow ratio Q_S/Q_{LCL} versus the wall relative roughness σ_w/b_m	142

LIST OF FIGURES

5.19	Stokes and LCL synthetic fracture simulations: total flow ratio Q_S/Q_{LCL} versus (a) the mechanical roughness slope σ_m/λ_b , and (b) the mechanical aspect ratio b_m/λ_b	143
5.20	Navier-Stokes example fracture simulations: vertically integrated fluid flow fields for (a) the smooth fracture, and (b) the rough fracture.	144
5.21	Navier-Stokes and Stokes example fracture simulations: Stokes flow fields minus NS flow fields for (a) the smooth fracture, and (b) the rough fracture.	145
5.22	Navier-Stokes example fracture simulations: cross-section velocity vectors for (a) the smooth fracture, and (b) the rough fracture.	146
5.23	Navier-Stokes and Stokes example fracture simulations: vertical profiles of the x - and z - components of velocity at the locations P1, P2, and P3 defined in Figure 5.22.	147
5.24	Navier-Stokes and Stokes synthetic fracture simulations: total flow ratio Q_{NS}/Q_S versus the relative roughness σ_m/b_m for fractures with (a) $\sigma_z = 0$, (b) $\sigma_z = 0.5$, and (c) $\sigma_z = 1$. The synthetic fractures used normally distributed aperture with $\lambda_b = 2$ mm.	148
5.25	Navier-Stokes and Stokes synthetic fracture simulations: total flow ratio Q_{NS}/Q_S versus the relative roughness σ_m/b_m for fractures with (a) $\sigma_z = 0$, (b) $\sigma_z = 0.5$, and (c) $\sigma_z = 1$. The synthetic fractures used normally distributed aperture with $\lambda_b = 5$ mm.	149
5.26	Navier-Stokes and Stokes synthetic fracture simulations: total flow ratio Q_{NS}/Q_S versus the relative roughness σ_m/b_m for fractures with (a) $\sigma_z = 0$, (b) $\sigma_z = 0.5$, and (c) $\sigma_z = 1$. The synthetic fractures used lognormally distributed aperture with $\lambda_b = 2$	150
5.27	Navier-Stokes and Stokes synthetic fracture simulations: total flow ratio Q_{NS}/Q_S versus Re for fractures with (a) $\sigma_z = 0$, (b) $\sigma_z = 0.5$, and (c) $\sigma_z = 1$ mm.	151
5.28	Navier-Stokes and Stokes synthetic fracture simulations: Q_{NS}/Q_S versus the kinematic parameter $Re \langle b \rangle / \lambda_b$ for fractures with (a) $\sigma_z = 0$, (b) $\sigma_z = 0.5$, and (c) $\sigma_z = 1$ mm.	152
5.29	Navier-Stokes and Stokes synthetic fracture simulations: Q_{NS}/Q_S versus the kinematic parameter $Re \sigma_b / \langle b \rangle$ for fractures with (a) $\sigma_z = 0$, (b) $\sigma_z = 0.5$, and (c) $\sigma_z = 1$ mm.	153
5.30	Navier-Stokes simulations and cubic law calculations for synthetic fractures: Q_{NS}/Q_{CL} versus σ_m/b_m for fractures with (a) $\sigma_z = 0$, (b) $\sigma_z = 0.5$, and (c) $\sigma_z = 1$ mm.	154
5.31	Navier-Stokes simulations and cubic law calculations for synthetic fractures: ratio of hydraulic aperture to the arithmetic mean aperture $b_H / \langle b \rangle$ versus the relative roughness σ_m/b_m for fractures with (a) $\sigma_z = 0$, (b) $\sigma_z = 0.5$, and (c) $\sigma_z = 1$ mm.	155
5.32	LCL, Stokes, and Navier-Stokes synthetic fracture simulations: relative error e_Q versus the inverse number of subdivisions n_{sub}^{-1} applied to the base grids of 25×25 or $25 \times 25 \times 10$ CVs.	156
5.33	Stokes and Navier-Stokes synthetic fracture simulations: raw total flow ratio data Q_S/Q_{LCL} and Q_N/Q_S versus the relative roughness σ_m/b_m for fractures with normally distributed aperture, $\lambda_b = 2$ mm, and $\sigma_z = 1$ mm.	157
5.34	Schematic diagram of two-dimensional parallel plate domain and boundary conditions: (a) one-way inlet boundary, and (b) two-way inlet boundary.	158

LIST OF FIGURES

5.35	Simulated particle position at three values of normalized time (t/t_R) for parallel plate simulation T1 (see Table 5.4) with (a) the one-way inlet boundary, and (b) the two-way inlet boundary.	159
5.36	Simulated particle position at three values of normalized time (t/t_R) for parallel plate simulations (a) T4, and (b) T7. Both of these simulations use the one-way inlet boundary.	160
5.37	Normalized particle breakthrough curves using the one-way inlet boundary condition for parallel plate simulations: (a) T1 to T4, and (b) T4 to T7.	161
5.38	Normalized particle breakthrough curves using the two-way inlet boundary condition for parallel plate simulations: (a) T1 to T4, and (b) T4 to T7.	162
5.39	Normalized particle breakthrough curves using the one-way inlet boundary condition for parallel plate simulations T1, T2, and T4. (a) Results using the base time step Δt , $1/2\Delta t$, and $2\Delta t$. (b) Results using the base number of particles n_p , $1/2 n_p$, and $2 n_p$	163
5.40	Schematic diagram of (a) laboratory apparatus used to perform hydraulic and tracer tests on fracture samples [Anderson, 2001], and (b) cross-section of fracture sample and inlet and outlet cells.	164
5.41	Observed laboratory tracer (bromide ion) concentrations at inlet cell C_i , outlet cell C_o , and fracture exit C_f over time for (a) Fracture I, and (b) Fracture II.	165
5.42	Fracture I flow simulation: (a) aperture field, and (b) simulated integrated flow field for b_m equal 0.130 mm.	166
5.43	Fracture II flow simulation: (a) aperture field, and (b) simulated integrated flow field for b_m equal 0.585 mm.	167
5.44	Fracture I transport simulation: x-y position of 10,000 particles at three values of normalized time t/t_R	168
5.45	Fracture II transport simulation: x-y position of 10,000 particles at three values of normalized time t/t_R	169
5.46	Normalized solute and particle breakthrough over time: (a) Fracture I, and (b) Fracture II.	170
5.47	Normalized solute and particle breakthrough over normalized time: (a) Fracture I, and (b) Fracture II.	171
5.48	Normalized solute and particle breakthrough over time for Fracture I with two values of the minimum wall distance fraction ($F_w = 0.1$, and 0.0).	172

CHAPTER 1. Introduction

Predicting fluid flow and solute transport through fractured rock is an important component of engineering analysis and design in many disciplines including groundwater contamination, drinking water supply, nuclear waste disposal, petroleum and gas production, mine and excavation stability, and geothermal production. Fractures largely influence the flow of fluids and hence solute transport in a fractured rock environment by forming conduits that are typically orders of magnitude more conductive to fluid flow than the surrounding rock. The starting point or building block in these environments is fluid flow and solute transport through a single fracture.

The traditional and most basic conceptual model of a single fracture is a set of smooth parallel plates. Figure 1.1(a) shows an example of a single fracture formed by two parallel plates separated by a distance defined as the plate aperture b . This conceptual model has been widely used [e.g., *Snow*, 1965; *Louis*, 1969] since the steady flow rate between the parallel plates may be easily predicted by the so-called cubic law. Under a steady and uniform hydraulic gradient, the cubic law predicts that the one-dimensional flow rate Q will be

$$Q = W b U = - b^3 \frac{W \gamma}{12 \mu} \frac{\Delta H}{L} \quad (1.1)$$

where U is the average velocity between the upper and lower plates, ΔH is the average total head difference applied between the flow boundaries, W and L are the width and length of the plates, μ is the fluid viscosity, and γ is the specific gravity of the fluid. The cubic law is a simple closed form solution of the Navier-Stokes equations assuming that the velocity field is uniform, steady, one-dimensional and sufficiently slow to ensure laminar flow, and the plates are smooth, parallel and sufficiently wide so that edge effects are negligible. Under these assumptions the cubic law predicts that the velocity profile between the plates is parabolic, and that the flow rate is proportional to the cube of the plate aperture. This behaviour has been experimentally verified using smooth parallel plates with apertures ranging from 1 cm to below 1 μm provided that the flow regime was laminar [*Lomize*, 1951; *Romm*, 1968; *Louis*, 1969].

The parallel plate model and the cubic law are attractive for predicting fluid flow in fractures due to their simplicity. However, many laboratory and field studies have observed that single

fractures are not smooth parallel plates, but rather are rough surfaces that are locally non-planar, non-parallel and potentially in contact [e.g., *Hakami and Barton*, 1990; *Novakowski and Lapcevic*, 1994; *Brown*, 1995]. As a result, theoretical studies have revised the conceptual model of single fractures to include these characteristics by subdividing the fracture into piece-wise continuous voids with variable geometry [e.g., *Tsang*, 1984; *Brown*, 1987]. Figure 1.1(b) shows an example of a rough-walled fracture that has been formed using this conceptual model. The one-dimensional cubic law is not valid for predicting fluid flow in this fracture. It is clear that a hydraulic gradient imposed across the fracture will result in a three-dimensional, non-uniform and tortuous flow field. Moreover, it is possible that this complex flow behaviour will produce non-negligible inertial forces even though the flow field is laminar. In fact, this condition has been experimentally observed [*Sharp and Maini*, 1972; *Schrauf and Evans*, 1986] and it causes the flow field to be non-linearly dependent on the applied hydraulic gradient. Therefore, a complete description of fluid flow in this rough-walled fracture requires the use of the three-dimensional Navier-Stokes (NS) equations.

The NS equations form a nonlinear system of partial differential equations that are difficult to solve in complex geometries such as a rough-walled fracture. Due to this fact, there are apparently no published studies using the NS equations to simulate three-dimensional flow in a rough-walled fracture (as depicted in Figure 1.1(b)). At this time, the NS equations have only been used to simulate flow in fractures with ideal geometry. *Coakley et al.* [1987] simulated three-dimensional flow in a very simple fracture plane with four saw-tooth constrictions, and *Brown et al.* [1995] simulated two-dimensional flow in fracture profiles with sinusoidal surfaces. The only apparent work to simulate three-dimensional fluid flow in rough-walled fractures used the Stokes equations [*Mourzenko et al.*, 1995]. The Stokes equations are an important subset of the NS equations where the inertial force terms have been neglected and are often referred to as the creeping flow equations. The Stokes equations are a linear system of partial differential equations that are more easily solved than the NS equations. In practice however, the computational burden of solving either the three-dimensional NS or Stokes equations is significant. Consequently, it is widely assumed that the three-dimensional flow field in a rough-walled fracture may be approximated as two-dimensional and governed by a form of the Reynolds equation [e.g., *Iwai*, 1976; *Neuzil and Tracy*, 1981; *Tsang*, 1984; *Brown*, 1987]. The Reynolds equation comes from the field of hydrodynamic lubrication [see *Mitchell*, 1950] and it is a two-dimensional approximation of the Stokes equations for fluid flow through a set of plates with slightly non-parallel walls. The form used for flow in fractures is commonly referred to as the local cubic law (LCL) since the magnitude of fluid flow through the subdivided or local fracture voids is proportional to the cube of the local aperture. In other words, the cubic law is assumed to hold locally [*Walsh*, 1981].

The LCL currently represents the state-of-the-art for simulating fluid flow in rough-walled fractures. Numerical simulations have demonstrated complex two-dimensional flow fields and that

the total flow rate is a function of the mean and standard deviation of the local aperture distribution and the amount of surface contact [e.g., *Brown, 1987; Zimmerman and Bodvarsson, 1996*]. Qualitatively, these results agree with what has been observed in laboratory and field studies [e.g., *Novakowski and Lapevic, 1994; Brown et al., 1998*]. Quantitatively however, the LCL has predicted total flow rates that are over 1.5 to 2 times higher than those observed in laboratory flow experiments where the geometry of the fracture has been mapped [e.g., *Hakami and Larsson, 1996; Yeo et al., 1998*]. This magnitude of discrepancy has also been observed in flow simulations performed on randomly generated rough-walled fractures using the three-dimensional Stokes equations and LCL [*Mourzenko et al., 1995*]. An important and unresolved issue is whether these differences are due to experimental, numerical, or conceptual errors.

The tortuous nature of fluid flow through a rough-walled fracture will also impact the transport of solutes through the fracture. Several laboratory experiments have observed non-traditional breakthrough curves that exhibit a steep initial rise, long tail, and intermediate jumps or stair-step features [*Neretnieks et al. 1982; Moreno et al. 1985*]. These properties have been attributed to advection dominated transport along distinct channels contained within the overall flow field [*Tsang and Tsang, 1987*] and have been qualitatively reproduced using particle tracking models based on the LCL [*Moreno et al., 1988; Tsang et al., 1988*]. Other laboratory experiments and theoretical studies have observed traditional Gaussian s-shaped breakthrough curves that are easily fit to the one-dimensional advection-dispersion equation [*Thompson and Brown, 1991; Piggott and Elsworth, 1993*]. Thus, it is of interest to observe and assess the behaviour of a robust solute transport model applicable to rough-walled fractures that employs the flow field derived from the solution of the three-dimensional NS equations.

1.1 Research Objectives

The research objectives of this thesis are:

- ▶ To develop numerical models to simulate three-dimensional fluid flow and solute transport through a rough-walled fracture using the Navier-Stokes equations.
- ▶ To develop a numerical model to simulate two-dimensional fracture fluid flow based on the local cubic law approach.
- ▶ To demonstrate differences between various fluid flow models and to determine criteria for the validity of the two-dimensional local cubic law approximation using random rough-walled fractures generated from literature-based statistical parameters.
- ▶ To compare the results from fluid flow and solute transport simulations to experimental data.

1.2 Scope of Thesis

This thesis consists of five additional chapters. Chapter 2 examines the characterization of single fractures and presents the fracture characterization methodology used in this thesis. Chapter 3 presents the governing equations used to simulate flow and transport in single fractures, and also provides the relevant background that shaped this investigation. Chapter 4 presents the formulation of the numerical flow and transport models, and Chapter 5 presents and discusses the results of validation, random fracture, and laboratory fracture simulations. Finally, Chapter 6 outlines the paramount conclusions and important contributions of this thesis.

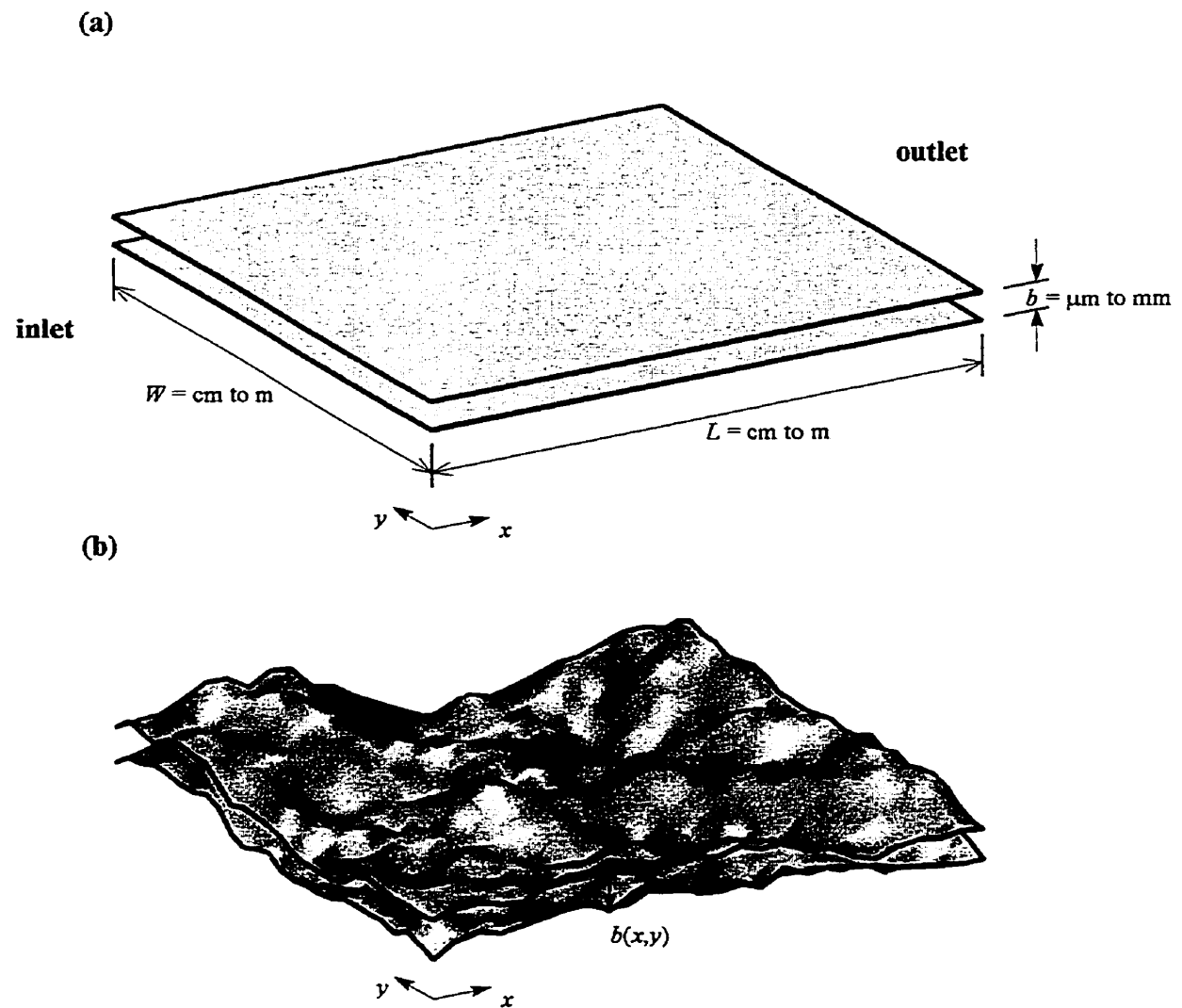


Figure 1.1. Conceptual models of a single fracture: (a) a set of parallel plates with length L , width W , and constant aperture b , and (b) a set of rough-walled surfaces with the same length and width, but variable aperture $b(x, y)$.

CHAPTER 2. Characterization of Single Fractures

2.1 Introduction

The void space in a single fracture is a complex three-dimensional volume formed between two rough surfaces. In the work presented in this thesis, this three-dimensional volume is mapped onto a reference plane, which is defined as the x - y plane. Given that the overall dimensions or x - y limits of this reference plane are known, the fracture void space may be fully characterized by measuring the distribution of aperture and mean wall topography relative to the plane. The distribution of aperture represents the variation in the separation of the fracture walls and includes potential points of contact. The distribution of the mean wall topography represents the alignment of the void space or the degree of fracture undulation that generally occurs at a larger scale than the aperture variation.

Many experimental, theoretical, and numerical studies have demonstrated that aperture variation has a very significant influence on the fluid flow and mass transport properties within a single fracture [e.g., *Neretnieks et al.*, 1982; *Tsang*, 1984; *Brown*, 1987; *Raven et al.*, 1988; *Tsang and Tsang*, 1989; *Thompson and Brown*, 1991; *Brown et al.*, 1998]. In fact, the majority of these studies conceptualize the fractures as two-dimensional planar fields of variable aperture and ignore undulation in the void space altogether. More recently, numerical studies using two-dimensional fracture flow models have incorporated corrections to reflect the influence of undulation on the void space geometry [e.g., *Ge*, 1997; *Nicholl et al.*, 1999]. In this thesis, two- and three-dimensional flow simulations are performed on variable aperture fractures with and without considering the effects of surface undulation.

The next section (Section 2.2) of this chapter examines the characterization of single fractures using bulk aperture measurements. Sections 2.3 and 2.4 examine the characterization of fractures by directly measuring the distribution of aperture and wall topography in laboratory samples. Section 2.5 presents wall topography data for two laboratory fractures used to validate the numerical flow and transport models. Finally, Section 2.6 presents the methodology and parameter selection used to generate random fractures in this thesis.

2.2. Bulk Aperture Measurements

Single fractures are most often characterized using bulk measurements of the fracture aperture. These are effective aperture values that are inferred from laboratory or field measurements of flow and/or transport parameters, and are analogous to effective permeability values defined in heterogeneous porous media. In practice, the most common definitions are the hydraulic, tracer, and mass balance apertures. These are defined for linear and radial flow fields which are typical of laboratory experiments and in situ field tests, respectively [see review by Tsang, 1992].

The hydraulic aperture b_H of a rough-walled fracture is defined as the effective parallel plate aperture required to satisfy the cubic law given the known flow rate, hydraulic head difference and fracture plane dimensions. Considering a linear flow field (as shown in Figure 1.1), b_H is given by rearranging (1.1) as

$$b_H = \left[\frac{12 \mu Q L}{W \gamma (H_i - H_o)} \right]^{\frac{1}{3}}, \quad (2.1a)$$

where H_i and H_o are the values of hydraulic head at the inlet and outlet boundaries of the fracture. The hydraulic aperture is a measure of the effective transmissivity (where $T = W b_H^3 / 12$) of the rough-walled fracture. Considering a radial flow field, b_H may be given as

$$b_H = \left[\frac{6 \mu Q \ln(r_o/r_i)}{\pi \gamma (H_i - H_o)} \right]^{\frac{1}{3}}, \quad (2.1b)$$

where r_i is the radius of the injection borehole and r_o is the radial distance from the injection borehole to the observation borehole or outflow boundary.

The tracer aperture b_T is defined by the velocity form of the cubic law where the average velocity of the flow field is estimated from the residence time t_R of a tracer as inferred from tracer breakthrough data. The tracer aperture for a linear flow field may be given as

$$b_T = L \left[\frac{12 \mu}{\gamma (H_i - H_o) t_R} \right]^{\frac{1}{2}}, \quad (2.2a)$$

and for a radial flow field as

$$b_T = \left[\frac{6 \mu \ln(r_o/r_i) (r_o^2 - r_i^2)}{\gamma (H_i - H_o) t_R} \right]^{\frac{1}{2}}. \quad (2.2b)$$

This bulk aperture is a measure of the effective permeability (where $k = b_T^2 / 12$) of the rough-walled fracture.

The mass balance aperture b_B is a measure of the average aperture required to balance a known volume of fluid ($Q t_R$) over the areal extent of a tracer assumed to migrate under plug flow conditions. The mass balance aperture for a linear flow field may be given as

$$b_B = \frac{Q t_R}{WL}, \quad (2.3a)$$

and for a radial flow field as

$$b_B = \frac{Q t_R}{\pi(r_o^2 - r_i^2)}. \quad (2.3b)$$

Tsang [1992] reviewed these three bulk aperture definitions in order to clear up discrepancies reported in the literature. Essentially the bulk apertures using tracer information (b_B and b_T as defined here) were used inter-changeably and yielded significantly different results. *Tsang* [1992] suggested the following order for two-dimensional heterogeneous aperture fields:

$$b_B \geq b_H \geq b_T. \quad (2.4)$$

This ordering of bulk apertures has been widely observed in field and laboratory observations (see Table 2.1). The hydraulic and tracer apertures are largely dependent on the hydraulic head difference across the flow field and are therefore sensitive to the regions of high head loss within the flow field. These high head loss regions typically correspond to regions of small aperture and/or high velocity. Consequently, b_H and b_T are weighted toward the small aperture values encountered along the flow pathways and/or the aperture values of high velocity regions such as the radially converging flow field at an extraction well. On the other hand, the mass balance aperture is not dependent on the pressure head difference and is sensitive to the storage of tracer mass in the void space. In other words, it is more sensitive to the large aperture regions. For this reason *Tsang* [1992] states that b_B is the best estimate of the arithmetic mean of the aperture distribution ($\langle b \rangle$) given that there is certainty in determining the areal geometry of the tracer flow pathways.

Silliman [1989] theoretically examined the ordering of bulk aperture measurements in fractures with two-dimensional aperture variation and presented the following bulk aperture:

$$b_A = b_H^3 / b_T^2, \quad (2.5)$$

which is defined here as the effective flow area aperture determined by dividing the fracture transmissivity by the permeability. For the special condition where the aperture variation is one-dimensional and parallel to the direction of flow, *Silliman* [1989] showed that b_A is equal to $\langle b \rangle$ (or b_B) and is smaller than b_H and b_T . This result suggests that there may be situations where the ordering of bulk apertures is different from (2.4) (e.g., see data from *Cady et al.*, [1993] presented in Table 2.1). Practically however, the definition of b_A may be subject to a large uncertainty since the uncertainties in b_H and b_T are magnified by (2.5) (e.g., see Figure 3 in *Rasmussen* [1995]).

There are several additional bulk aperture measurements that are specific to laboratory studies. In normal stress experiments the mechanical aperture is defined as

$$b_m = \delta_o - \delta, \quad (2.6)$$

where δ is the normal displacement in the void space at a specified normal stress, and δ_o is the total void space displacement at the maximum normal stress [e.g., *Raven and Gale*, 1985; *Durham and Bonner*, 1994]. At the highest applied normal stress, the fracture surfaces contact forming asperities, and by definition, b_m equals zero. However, except for well-mated surfaces under very high normal stresses [e.g., *Durham and Bonner*, 1994], the fracture void space will still conduct fluid flow. To reflect this property, many studies [e.g., *Iwai*, 1976; *Witherspoon et al.* 1980; *Raven and Gale*, 1985] have modified the mechanical aperture as

$$b_M = b_m + b_{Ho} , \quad (2.7)$$

where b_{Ho} is the hydraulic aperture at the maximum normal stress or the so-called residual aperture.

Finally, the volume aperture for a linear flow field may be defined as

$$b_V = \frac{V}{WL} , \quad (2.8a)$$

and for a radial flow field as

$$b_V = \frac{V}{\pi(r_o^2 - r_i^2)} , \quad (2.8b)$$

where V is the total volume of the void space. This void space volume has been measured using an ideal gas and a pycnometer [*Schrauf and Evans*, 1986; *Rasmussen*, 1995] or by weighing a removable cast of the void space [*Yeo et al.*, 1998]. *Rasmussen* [1995] found that b_V was equivalent to b_B , and *Yeo et al.* [1998] found that b_V was very close to $\langle b \rangle$.

Table 2.1 summarizes the results of various laboratory and field studies that attempted to measure the bulk aperture values of single fractures. In general, the bulk apertures followed the ranking given by (2.4), with b_B ranging from 0.05 to 1.54 mm, b_H ranging from 0.06 to 1.18 mm, and b_T ranging from 0.05 to 1.03 mm.

2.3 Aperture Distribution Measurements

The distribution of aperture in single fractures has been widely assumed to be lognormal [e.g., *Neuzil and Tracy*, 1981; *Moreno et al.*, 1988; *Tsang and Tsang*, 1989; *Pruess and Tsang*, 1990; *Murphy and Thomson*, 1993]. This follows the early field work of *Snow* [1970] who performed many hydraulic field tests on in situ fractures isolated with borehole packers and concluded that b_H was lognormally distributed. However, it is important to note that b_H is a bulk aperture measurement which characterizes the bulk flow behaviour of a region near the borehole using the cubic law. More recently, laboratory methods have been developed to sample the actual distribution of aperture or information used to infer the distribution of aperture in single rough-

walled fractures using the following techniques: (i) void space injection, (ii) void space casting, (iii) wall topography measurements, (iv) X-ray transmission, and (v) light transmission through transparent replicas.

The first group involves permanently injecting a dyed resin or epoxy into the fracture void space, sectioning the entire sample to expose the fracture profile at a desired interval, and mapping the aperture profile with image analysis or profilometry [e.g., *Gale et al.*, 1990; *Hakami and Larsson*, 1996]. The second group involves injecting the void space with a casting material, removing the cast by separating the fracture surfaces, and mapping the aperture field with image analysis or profilometry [*Gentier et al.*, 1989; *Yeo et al.*, 1998]. The third group measures the topography of each separated fracture wall using laser or stylus profilometry, and then combines the topographic surfaces to infer the fracture aperture field [e.g., *Reimus et al.*, 1993; *Brown*, 1995; *Tunnicliffe*, 1999]. The fourth group uses a computer aided tomography (CAT) X-ray scanner to image the three-dimensional fracture void space contained in core samples [e.g., *Keller et al.* 1995; *Keller*, 1998]. The final group measures the transmission of visible light through transparent fracture replicas containing dyed liquid within the void space using image analysis techniques to infer the aperture field [e.g., *Cox and Wang*, 1993; *Nicholl et al.*, 1999]. An interesting and simple variation of this method was developed by *Hakami and Barton* [1990] who placed liquid droplets of a known volume on one surface of a transparent replica, mated the adjacent surface, mapped the areal extent of each droplet, and calculated the average aperture encapsulated by each droplet.

Table 2.2 summarizes the results of various studies characterizing the aperture distribution of rough-walled fractures. The distributions are statistically described by the arithmetic mean $\langle b \rangle$, standard deviation σ_b , correlation length λ_b , and fraction of contact points c in the aperture field. Also included is the coefficient of variation $\sigma_b/\langle b \rangle$ which has been defined as the relative roughness of the aperture field [*Zimmerman and Bodvarsson*, 1996]. The information in Table 2.2 indicates that both normally and lognormally distributed aperture fields have been observed, that $\langle b \rangle$ ranged from 0.056 to 1.024 mm, σ_b ranged from 0.017 to 0.683 mm, $\sigma_b/\langle b \rangle$ ranged from 0.3 to 1.2, λ_b ranged from 0.65 to 24 mm, and finally, that c ranged from 0 to 35% but was typically below 5%. It is important to note that these ranges are subject to the scale of the measurements and the sample size.

2.4 Wall Topography Measurements

The topography of individual fracture walls has been studied to determine their fractal or self-affine characteristics [e.g., *Brown and Scholtz*, 1985; *Power and Tullis*, 1991; *Poon et al.*, 1992; *Brown* 1995], and to infer aperture distributions of the assembled fracture [*Brown*, 1995; *Tunnicliffe*, 1999; *Anderson*, 2001]. In this thesis, traditional statistical parameters (standard deviation and exponential correlation length) are used to describe the wall topography. *Brown et al.* [1986] examined 25 mm profiles along the walls of two natural granodiorite fractures and observed standard deviations in the topography of 0.18 and 0.23 mm. *Brown* [1995] examined 13 to 52 mm profiles in 23 rock samples and found that the wall topography was normally distributed with standard deviations ranging from 0.1 to 1 mm. *Tunnicliffe* [1999] measured the wall topography of an induced limestone fracture and found that the mean topography (formed by averaging the two fields of wall topography) was normally distributed with a standard deviation of 1.4 mm and a correlation length of 13 mm. *Anderson* [2001] also measured the wall topography of an induced limestone fracture and found that the mean topography was normally distributed with a standard deviation of 5.2 mm and a correlation length of 42 mm. The data of *Tunnicliffe* [1999] and *Anderson* [2001] are discussed in more detail in Section 2.5.

In this research effort, the mean wall topography is defined as the fracture mid-surface. For well-mated fractures the topography of the mid-surface will be very similar to the topography of each individual wall. For poorly-mated fractures the mid-surface will be smoother than the walls since the mismatched walls will tend to cancel the other in the calculation of the mean wall topography. For example, if a fracture wall is mated with its mirror image, the mean of these surfaces will form a plane. This suggests that the standard deviation of the mid-surface topography in natural fractures will be within the range of standard deviations observed on individual fracture walls. In the observations presented above this range is 0.1 to 5 mm; however, most observations fall within the range of 0.1 to 1.0 mm.

There are few measurements fitting the traditional exponential correlation model to the correlation structure of natural rock fracture walls. The work of *Tunnicliffe* [1999] and *Anderson* [2001] suggests that the correlation length of the mid-surface will be on the order of 10 to 40 mm. However, it is important to note, that other observations using fractal correlation models suggest that the traditional correlation lengths of natural fracture walls are a function of the sample size [e.g., *Brown and Scholtz*, 1985; *Power and Tullis*, 1991; *Poon et al.*, 1992; *Brown* 1995].

2.5 Two Laboratory Fractures Characterized using Wall Topography Measurements

This section presents the wall topography of two induced limestone fractures measured using stylus profilometry. These fractures were examined separately in the work of *Tunnicliffe* [1999] and *Anderson* [2001], and are referred to hereafter as Fracture I and Fracture II, respectively. The original rock samples were cut out of a limestone outcrop located near Kingstons, Ontario, and trimmed in the laboratory to overall dimensions (depth \times width \times length) of $130 \times 155 \times 255$ mm, and $130 \times 160 \times 245$ mm. Each sample was fractured along a horizontal bedding plane by forcing wedges into 3 mm deep grooves cut on opposite sides of the sample. Each part of the fractured sample was mounted on a steel baseplate which served as reference planes for the topographic measurements. The topography of each separated wall was measured over a 2×2 mm grid using a co-ordinate measurement machine with a pointed stylus. Further details of the sample collection, fracture induction and topography measurements are given in each source.

Figures 2.1 and 2.2 show the topography of the limestone fracture walls measured on a 2×2 mm x - y grid. A vertical distance of 10 mm is shown on each surface to indicate the relative scale of each field and the standard deviation and correlation length of each wall are also shown. Part (a) of each figure shows the topography of the upper walls which is defined as a two-dimension elevation field, $Z_U(x, y)$. Likewise, part (b) of the each figure shows the elevation field of the lower walls, $Z_L(x, y)$. It is important to note that any planar trends in the surfaces have been removed and that the mean elevation value of each wall has been set to zero ($\langle Z_U \rangle = \langle Z_L \rangle = 0$). In other words, the fields have been adjusted so that on average they lie along the x - y plane. These elevation fields may be used to define a raw aperture field as

$$b_r = Z_U - Z_L, \quad (2.9)$$

and a mid-surface field as

$$Z = \frac{1}{2} (Z_L + Z_U), \quad (2.10)$$

where $b_r(x, y)$ and $Z(x, y)$ are shown for each fracture in Figures 2.3 and 2.4. A vertical distance of 5 mm is shown on each surface to indicate the relative scale of each field. Figure 2.5 shows the histogram and correlation for each raw aperture field. These figures illustrate that the raw aperture is a function of the small scale differences between the wall elevation fields. These differences seem to be normally distributed and are correlated over shorter distances than the wall topography. It is also noteworthy that there is negligible cross-correlation between the b_r and Z fields.

The actual aperture field $b(x, y)$ of each fracture may be inferred from (2.9) using

$$b = \max(b_r + b_m, b_c), \quad (2.11)$$

where b_m is a constant separation distance or mechanical aperture that is added to the raw aperture field, and b_c is defined as the contact aperture, used to defined points of contact in the aperture

field. Equation (2.11) positively shifts the raw aperture field by b_m and truncates the aperture values below b_c . Figures 2.6 and 2.7 show the aperture fields inferred for each fracture using mechanical apertures that were estimated from exterior measurements on the assembled fracture samples. Also shown in the figures are the inferred distribution of contact points, and a summary of aperture and closure statistics. Figure 2.8 displays how $b_m/\langle b \rangle$, $\sigma_b/\langle b \rangle$ and c change with b_m for each inferred aperture field.

2.6 Random Fracture Generation

In this thesis, the random generation of fractures is largely based on the wall topography method of characterizing of the fracture void space (see Sections 2.4 and 2.5). The three-dimensional void space of a fracture is characterized with random two-dimensional fields of aperture and mid-surface. All aperture and elevation fields are defined perpendicular to the x - y plane and parallel to the z -axis or vertical-axis. This method is a simple extension to earlier theoretical work which used only two-dimensional aperture distributions to represent rough-walled fractures [e.g., *Tsang and Tsang*, 1989; *Pruess and Tsang*, 1990; *Murphy and Thomson*, 1993]. This new method is flexible in that it allows the two-dimensional fields to be described by any distribution function and correlation structure. In this work, the random aperture fields are normally and lognormally distributed, and the mid-surface fields are normally distributed. Both of these fields are generated independently using the exponential autocorrelation function with different correlation lengths. This method assumes that there is negligible cross-correlation between the aperture and mid-surface fields, and that the aperture fields do not contain planar trends.

2.6.1 Methodology

The method of fracture generation is presented in the following steps. The first step is to randomly generate two independent spatially correlated standardized normal distributions (i.e., having a mean of zero and standard deviation of unity) over a uniform x - y grid. One of the standardized distributions is associated with the aperture $e_b(x, y)$ and the other with the mid-surface $e_z(x, y)$. The traditional exponential auto-correlation function is used to model spatial correlation within each field and may be given as

$$r = \exp(-l/\lambda) , \quad (2.12)$$

where r is the auto-correlation between grid point values separated by a distance l , and λ is the correlation length. The correlation lengths of the e_b and e_z fields are λ_b and λ_z , respectively.

The second step is to transform the standardized e_b field into an initial aperture field with a specified mean and standard deviation (b_m and σ_m), and truncate this initial aperture field at a

specified contact aperture b_c . The initial mean, b_m , conceptually represents the mechanical aperture of the final aperture field. For normally distributed aperture fields, the second step may be given as

$$b = \max(b_m + \sigma_m e_b, b_c), \quad (2.13)$$

and for log-normally distributed aperture fields as [Aitchison and Brown, 1957]

$$b = \max(b_m^* \exp(\sigma_m^* e_b), b_c), \quad (2.14a)$$

with

$$b_m^* = b_m \exp\left[-\frac{1}{2} \sigma_m^{*2}\right], \quad (2.14b)$$

and

$$\sigma_m^{*2} = \ln\left[(\sigma_m / b_m)^2 + 1\right], \quad (2.14c)$$

where b_m^* and σ_m^* are the initial mean and standard deviation of the log-aperture field.

Equations (2.13) and (2.14) define the aperture fields by scaling and shifting the e_b or log- e_b fields, and potentially truncating aperture values below b_c . This truncation mimics fracture closure and conceptually assumes that the points of contact (or asperities) dissolve as the degree of closure increases [Brown, 1987]. If the aperture field is not truncated then the fracture is considered open and the final mean aperture $\langle b \rangle$ will equal b_m and the final standard deviation σ_h will equal σ_m . If the aperture field is truncated the fracture is considered closed and $\langle b \rangle$ will be greater than b_m and σ_h will be less than σ_m . In addition, the fraction of contact points c in the normally distributed aperture field may be approximated as

$$c \approx F((b_c - b_m) / \sigma_m), \quad (2.15)$$

and in a log-normally distributed aperture field as

$$c \approx F(\ln(b_c / b_m^*) / \sigma_m^*), \quad (2.16)$$

where F is the cumulative probability function of the standardized normal distribution. These equations are approximate since the aperture distributions are discrete and finite whereas the probability function is continuous and infinite.

The third step transforms the standardized e_z field into the desired mid-surface elevation field according to

$$Z = \sigma_z e_z, \quad (2.17)$$

where σ_z is the standard deviation of the mid-surface. Equation (2.17) defines a Z field with a mean of zero and a standard deviation of σ_z , and is not affected by truncation of the aperture field.

The final step defines the fracture walls by combining the aperture and mid-surface elevation fields according to

$$Z_U = Z + \frac{1}{2} b ; \quad Z_L = Z - \frac{1}{2} b , \quad (2.18)$$

where $Z_U(x, y)$ and $Z_L(x, y)$ are the elevation fields of the upper and lower surfaces of the fracture. Since b and Z are independent, it follows from (2.18) that

$$\langle b \rangle = \langle Z_U \rangle - \langle Z_L \rangle , \quad (2.19)$$

and

$$\sigma_U = \sigma_L = \left[\sigma_Z^2 + \frac{1}{4} \sigma_b^2 \right]^{\frac{1}{2}} = \sigma_w , \quad (2.20)$$

where σ_w is defined as the standard deviation of the wall roughness.

2.5.2. Parameter Selection and Examples of Generated Fractures

Table 2.3 summarizes the parameters used to generate the random fractures used in this study. All fractures were generated over 26×26 grid points with a uniform spacing of 2×2 mm yielding total dimensions along the x - y plane of 50×50 mm. The aperture field parameters were chosen to represent moderate to large aperture fractures (0.25, 0.5 and 1.0 mm) which are correlated on the scale of millimetres (2 or 5 mm). The range of aperture relative roughness values corresponds to the range previously examined in other fracture flow studies [e.g., Brown, 1987; Mourzenko *et al.*, 1995]. These aperture parameters were used to generate both normally and lognormally distributed aperture fields. Finally, the mid-surface field parameters were chosen to examine the influence of fracture undulation.

Figure 2.9 shows the histograms of various aperture fields generated over the standard x - y grid. Part (a) of this figure is a histogram of a normally distributed e_b field with a correlation length of 2 mm. Parts (b) and (c) are histograms of normally and lognormally distributed aperture fields defined by transforming e_b with (2.13) and (2.14) using different values of b_m and σ_m . Surface plots of these aperture fields are shown in Figure 2.10. The histograms in Figure 2.9(b) and the aperture fields in Figures 2.10(a) and 2.10(b) have an initial relative roughness (σ_m/b_m) equal to 0.25. These figures have no points of contact, and consequently, the values of $\langle b \rangle$ and σ_b are equal to the initial b_m and σ_m values. These figures demonstrate that the difference between the normal and lognormal aperture fields are minimal for small σ_m/b_m values. The histograms in Figure 2.9(c) and the aperture fields in Figures 2.10(c) and 2.10(d) have an σ_m/b_m value equal to 1.0. The normally distributed aperture field has a significant number of contact points, as indicated by the large spike ($\approx 15\%$) in the histogram at the value of b_c . Therefore, the values of $\langle b \rangle$ and σ_b for this truncated distribution are moderately different than the initial b_m and σ_m values. Conversely, the lognormal aperture field has no points of contact, and the values of $\langle b \rangle$ and σ_b are

approximately equal to the initial values. The truncated normal distribution is bimodal due to the spike at b_c , but for apertures greater than b_c , the typical Gaussian shape is maintained. On the other hand, the lognormal distribution is unimodal and has a significant positive skew (i.e., a large mode significantly less than the median with a long tail in the positive direction). Figure 2.10(d) clearly shows the effect of the positive skew where a large portion of the field has a low to moderate aperture values and a small portion of the field has large aperture spikes. These figures demonstrate that the normally and lognormally distributed aperture fields become significantly different for large σ_m/b_m values.

Figures 2.11(a) and 2.11(b) show histograms of the normally distributed b field from Figure 2.9(b) and a normally distributed mid-surface field defined by (2.17). Figure 2.11(c) shows histograms of the upper and lower fracture surfaces formed by substituting the Z and b fields into (2.18). Surface plots of the aperture field, mid-surface field, and resulting upper and lower walls are shown in Figure 2.12.

Figure 2.13 shows examples of fractures generated without undulation (i.e., $\sigma_z = 0$) and various values of σ_m/b_m . Figure 2.14 shows examples of fractures with low σ_m/b_m values and various values of σ_z . Both figures demonstrate that the geometry of the fracture void space becomes more variable and complex as σ_m/b_m and/or σ_z increase.

Finally, Figure 2.15 shows how the relative roughness of the truncated aperture field ($\sigma_b/\langle b \rangle$) and the contact ratio (c) relate to the initial or mechanical relative roughness (σ_m/b_m) for all the normally distributed aperture fields used in this work. As shown, for σ_m/b_m values greater than 0.25, the aperture fields become truncated, resulting in $\sigma_b/\langle b \rangle$ values are less than σ_m/b_m and non-zero c values that match (2.15).

Table 2.1. Summary of various studies measuring bulk aperture values of a single fracture.

source and description	mass balance aperture, b_B [mm]	hydraulic aperture, b_H [mm]	tracer aperture, b_T [mm]
<i>Raven et al.</i> [1988]; natural fracture, Chalk River Nuclear Laboratories, AECL, Canada; borehole test with $r_o - r_i = 13$ -30 m	0.045-0.115	0.110-0.190	0.045-0.115
<i>Novakowski</i> [1992]; natural fracture in shale with dolomitic interbed, Ontario, Canada; borehole test with $r_o - r_i = 15$ m	0.254, 0.745	0.213, 0.228	0.140, 0.240
<i>Cady et al.</i> [1993]; natural fracture in dolomite, Illinois, US; borehole test with $r_o - r_i = 20$ -22 m	1.540 0.39	0.580-1.180, 0.570	0.360-1.030 [†] , 0.690
<i>Piggot and Elsworth</i> [1993]; natural fracture in core sample from URL of AECL, Canada; laboratory test with $W = 190$, $L = 320$ mm	0.406, 0.304	0.325, 0.111	— —
<i>Novakowski and Lapcevic</i> [1994]; natural fracture in shale with dolomitic interbed, Ontario, Canada; borehole test with $r_o - r_i = 5$ -27 m	0.138-0.425	0.057-0.248	0.200-0.350
<i>Rasmussen</i> [1995]; natural fracture in core sample of Apache Leap Tuff, Arizona, US; laboratory test with $W = 202$, $L = 925$ mm	0.765	0.255	0.181
<i>Tunnicliffe</i> [1999]; induced fracture in outcrop sample of limestone, Ontario, Canada; laboratory test with $W = 150$, $L = 250$ mm	0.113 [‡]	0.055	0.041 [‡]
<i>Anderson</i> [2001]; transparent replica of induced fracture in outcrop sample of limestone, Ontario, Canada; laboratory test with $W = 160$, $L = 245$ mm	0.865	0.420	0.260

[†] b_T was back-calculated from (2.5) using b_H by assuming $b_B = b_A$ [‡] b_B and b_T were altered from original values after reinterpretation of tracer data

Table 2.2(a). Description of studies measuring the aperture distribution in a single fracture.

study source and description of fracture(s)	description of method
(a) <i>Hakami and Barton</i> [1990]; 5 transparent replicas	areal measurement of emplaced droplets
(b) <i>Gale et al.</i> [1990]; 2 natural fractures	resin injection, section imaging
(c) <i>Cox and Wang</i> [1993]; 2 natural rock replicas	light transmission through dyed fluid
(d) <i>Reimus et al.</i> [1993]; 1 natural rock	wall topography by laser profilometry
(e) <i>Brown</i> [1995]; 20 natural and 3 induced rock fractures; from outcrops in central New Mexico	wall topography by laser profilometry; 3-10 profiles of 13-52 mm; 0.025 mm resolution
(f) <i>Hakami and Larsson</i> [1996]; natural 190 × 410 mm granite fracture; core from south-eastern Sweden	epoxy injection, sectioning and image analysis; 65 profiles of ~100 mm; 0.2 mm resolution
(g) <i>Keller</i> [1998]; natural 53-82 × 165-240 mm granite fractures; induced ~50 × 225 mm sandstone fracture; cores from northern California, US	3-D imaging of cores by CAT X-ray scanner; 1-3 mm slices with resolution of 0.27 × 0.27 mm per pixel; minimum aperture of 0.038 mm
(h) <i>Yeo et al.</i> [1998]; 200 × 200 mm transparent fracture analog; replica of a natural sandstone fracture wall mated with its own negative cast	silicone casting, stylus profilometry of profiles exposed by subdividing cast into 5 mm slices; resolution of 5 × 5 mm
(i) <i>Tunnicliffe</i> [1999]; induced 150 × 250 mm limestone fracture; from outcrop in eastern Ontario	wall topography by stylus profilometry; resolution of 2 × 2 mm
(j) <i>Nicholl et al.</i> [1999]; 148 × 302 mm transparent fracture analog; mated roughened glass plates	light transmission through dyed fluid in voids; resolution of 0.15 × 0.15 mm per pixel
(k) <i>Anderson</i> [2001]; induced 160 × 245 mm limestone fracture; from outcrop in eastern Ontario, Canada	wall topography by stylus profilometry; resolution of 2 × 2 mm

Table 2.2(b). Statistical summary of studies measuring the aperture distribution in single fractures.

study	aperture distribution	arithmetic mean, $\langle b \rangle$ [mm]	standard deviation, σ_b [mm]	relative roughness, $\sigma_b/\langle b \rangle$ [-]	correlation length, λ_b [mm]	surface contact, c [%]
(a)	lognormal	0.083-0.494	0.295-0.340	0.37-0.63	—	~0
(b)	lognormal	0.180, 0.220	0.110, 0.162	0.61, 0.74	—	15, 35
(c)	lognormal	0.047, 0.053	0.039, 0.051	0.83, 0.96	0.03, 0.02	~0
(d)	normal/ lognormal	0.056	0.069	0.81	0.23	—
(e)	normal	—	0.017-0.180	—	0.65-15	—
(f)	normal	0.360	0.150	0.42	10	<5
(g)	lognormal	0.204-0.825	0.282-0.683	0.83-1.51	1.5-7	—
(h)	normal	0.607-1.024	0.160-0.332	0.26-0.32	12-24	<0.1
(i)	normal	0.201	0.230	1.14	4.1	1.6
(j)	normal neg. skew	0.226	0.062	0.27	0.8	~0
(k)	normal	0.750	0.550	0.73	6.3	3.6

Table 2.3. Parameters used to generate random fractures.

parameter	value(s)	units
<i>x-y</i> grid:		
total number of points, N_x, N_y	26, 26	—
uniform spacing, Δ_x, Δ_y	2, 2	mm
total dimensions, L, W	50, 50	mm
aperture field:		
correlation length, λ_b	2, 5	mm
initial mean, b_m	0.25, 0.5, 1.0	mm
initial standard deviation, σ_m	0.0625, 0.125, 0.25, 0.5	mm
initial relative roughness, σ_m/b_m	0.0625 - 2.0	—
mid-surface field:		
correlation length, λ_z	10	mm
standard deviation, σ_z	0.0, 0.5, 1.0	mm

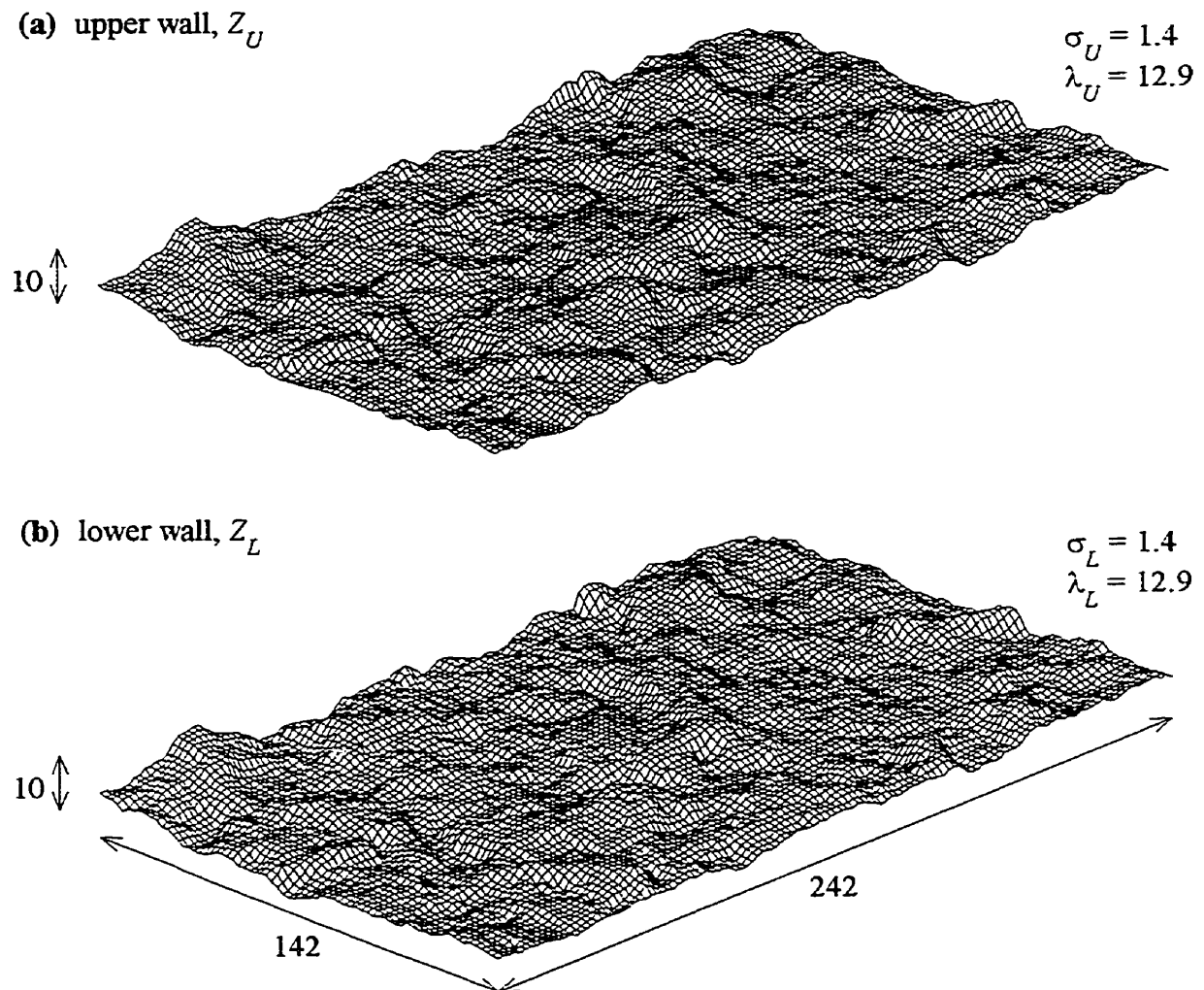


Figure 2.1. Fracture I surface plots of (a) upper, and (b) lower wall topography [data from *Tunnicliffe*, 1999]. These elevation fields were measured using stylus profilometry over a 2×2 mm grid. A vertical scale of 10 mm is displayed. All length dimensions are given in mm.

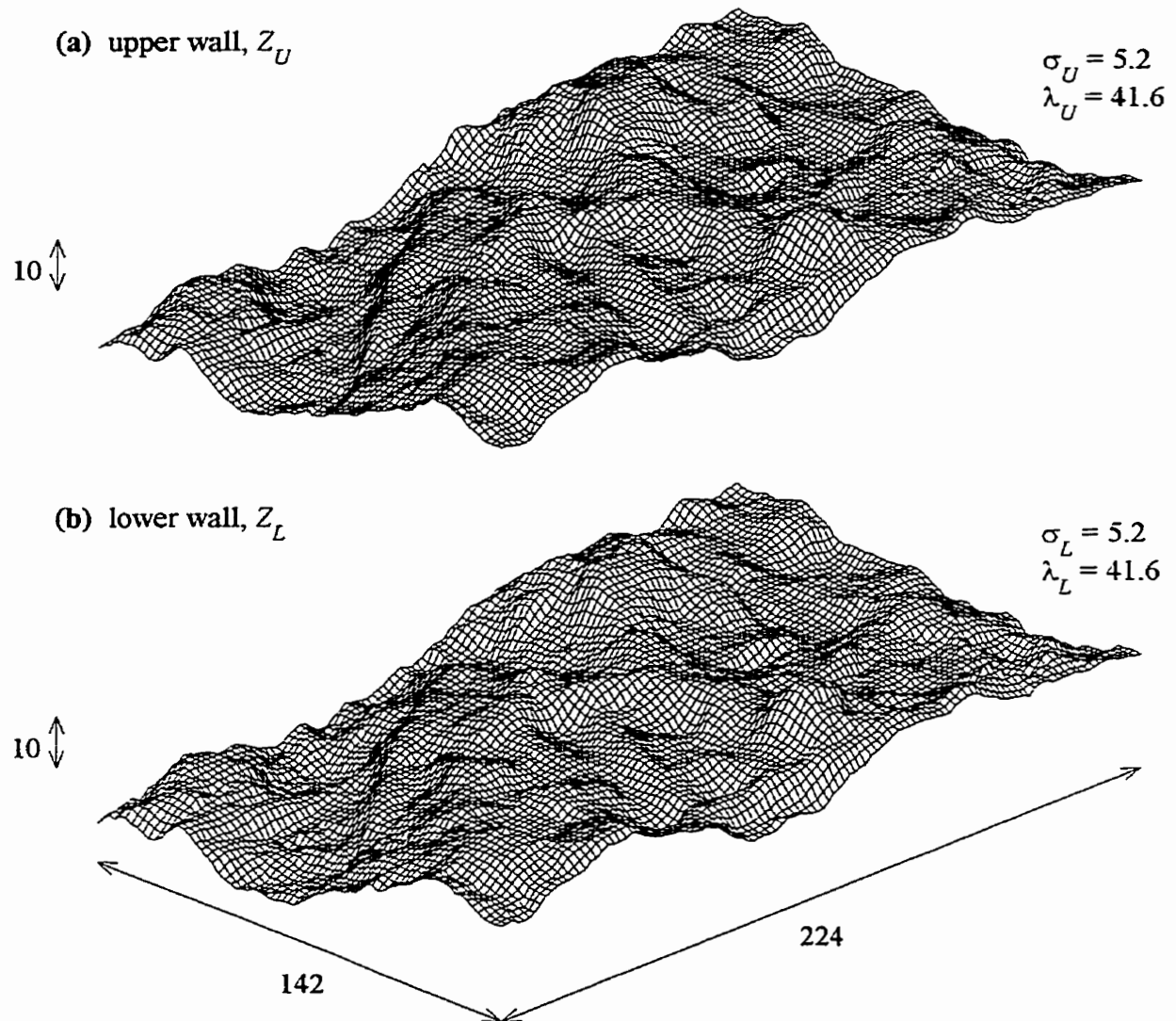


Figure 2.2. Fracture II surface plots of (a) upper, and (b) lower wall topography [data from Anderson, 2001]. These elevation fields were measured using stylus profilometry over a 2×2 mm grid. A vertical scale of 10 mm is displayed. All length dimensions are given in mm.

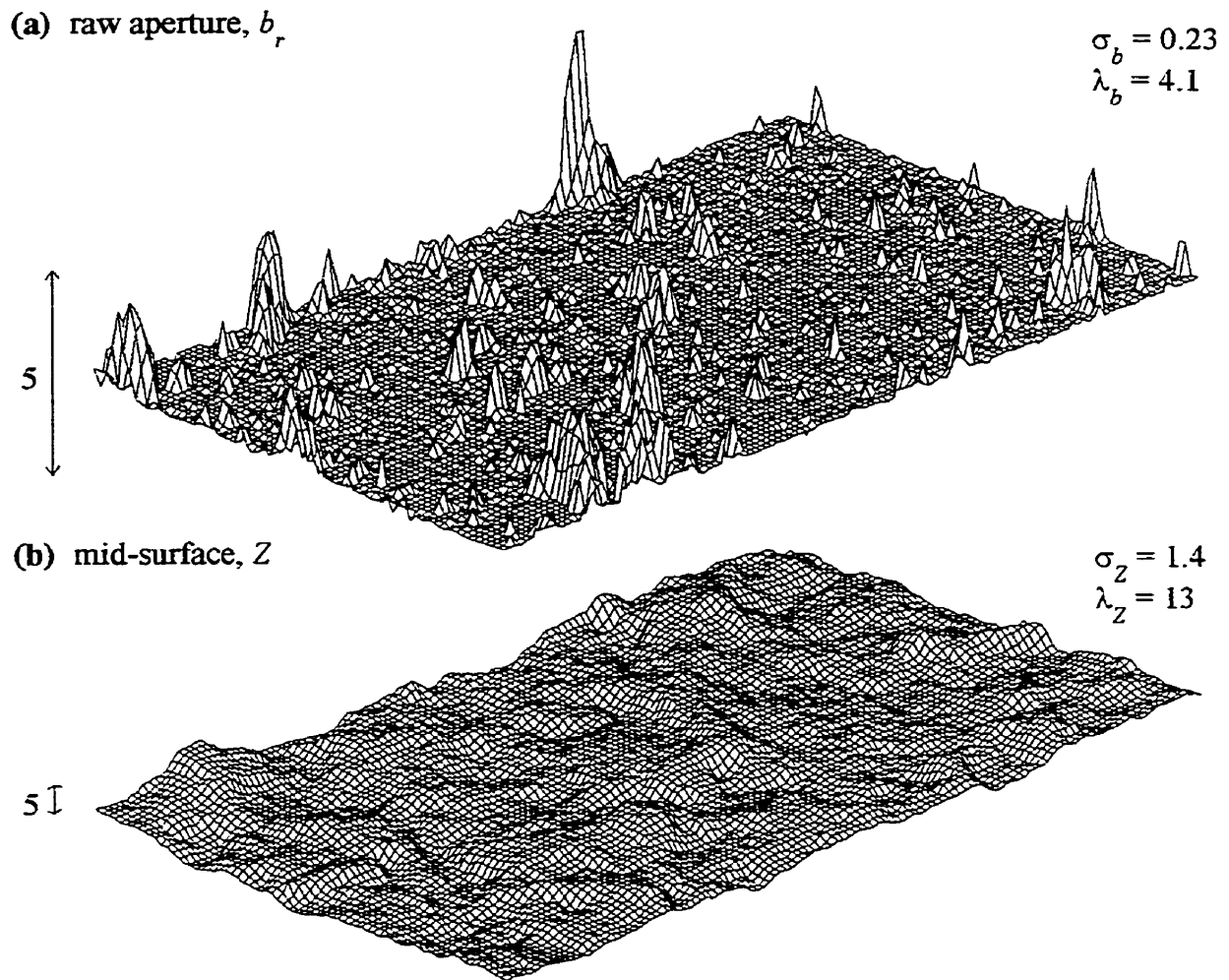


Figure 2.3. Fracture I surface plots of (a) raw aperture, and (b) mid-surface. These fields were calculated using (2.9) and (2.10), respectively. A vertical scale of 5 mm is displayed. All length dimensions are given in mm.

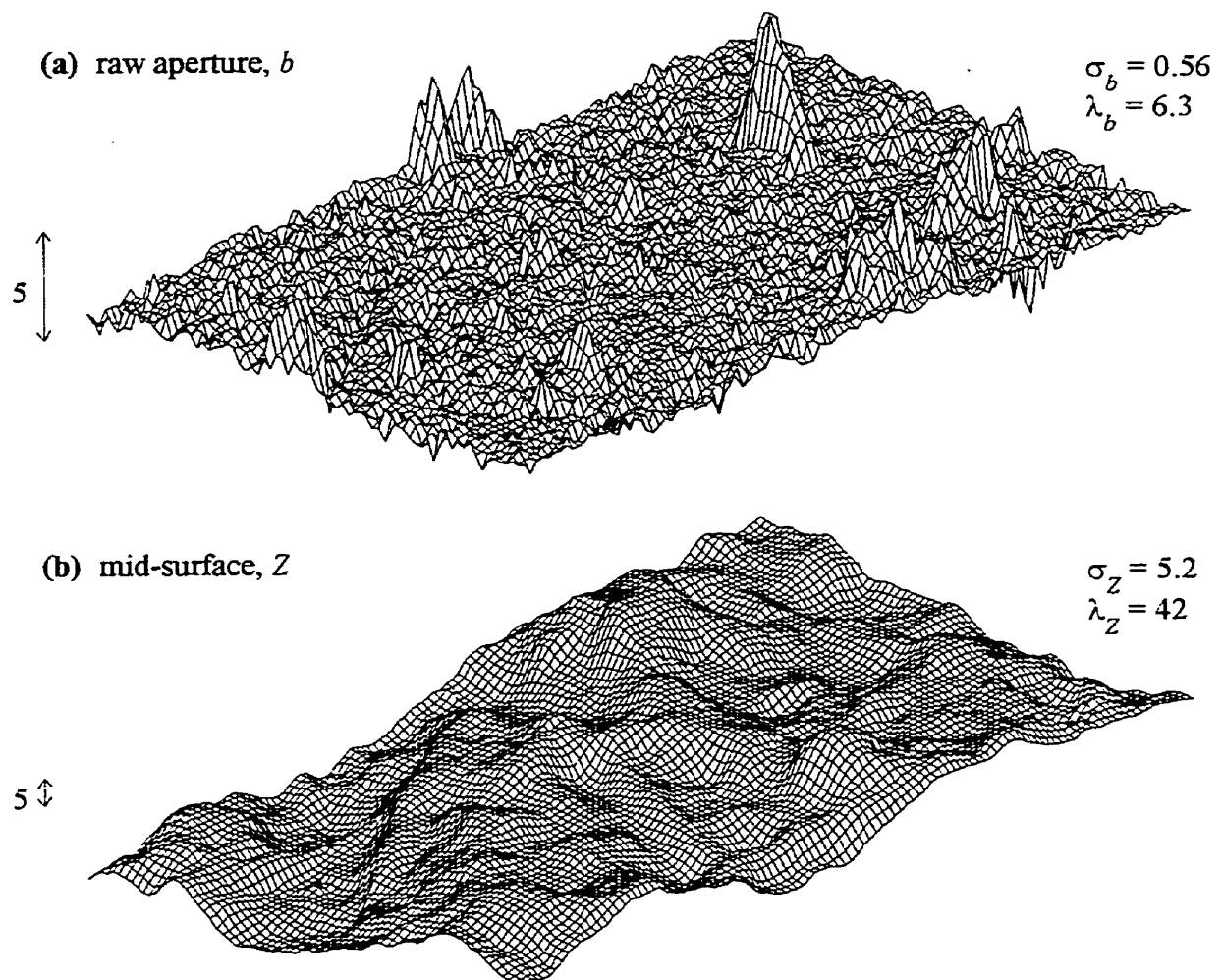


Figure 2.4. Fracture II surface plots of (a) raw aperture, and (b) mid-surface. These fields were calculated using (2.9) and (2.10), respectively. A vertical scale of 5 mm is displayed. All length dimensions are given in mm.

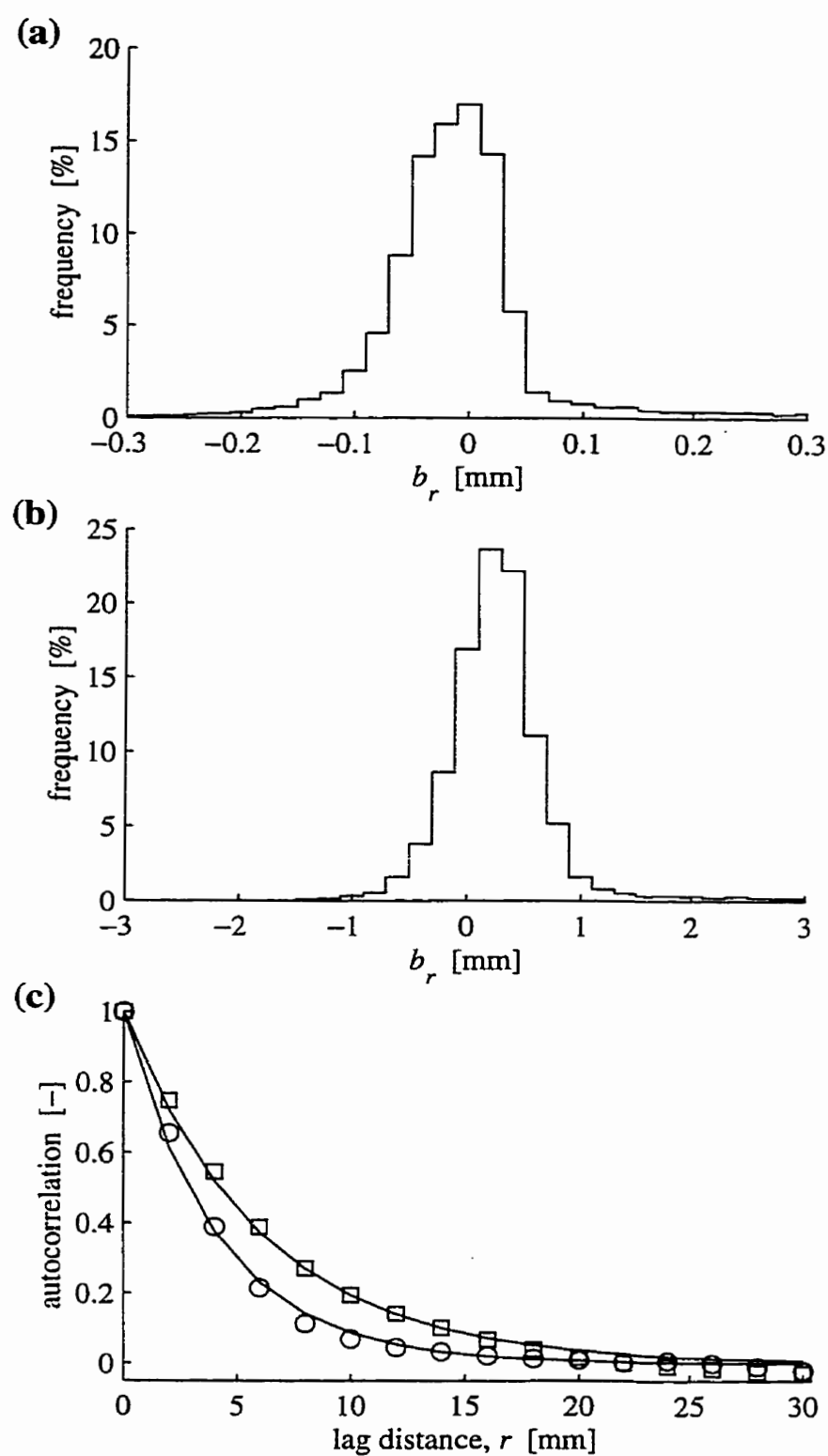


Figure 2.5. Histograms of raw aperture fields from (a) Fracture I and (b) Fracture II, and (c) autocorrelation plots from Fracture I (circles) and Fracture II (squares).

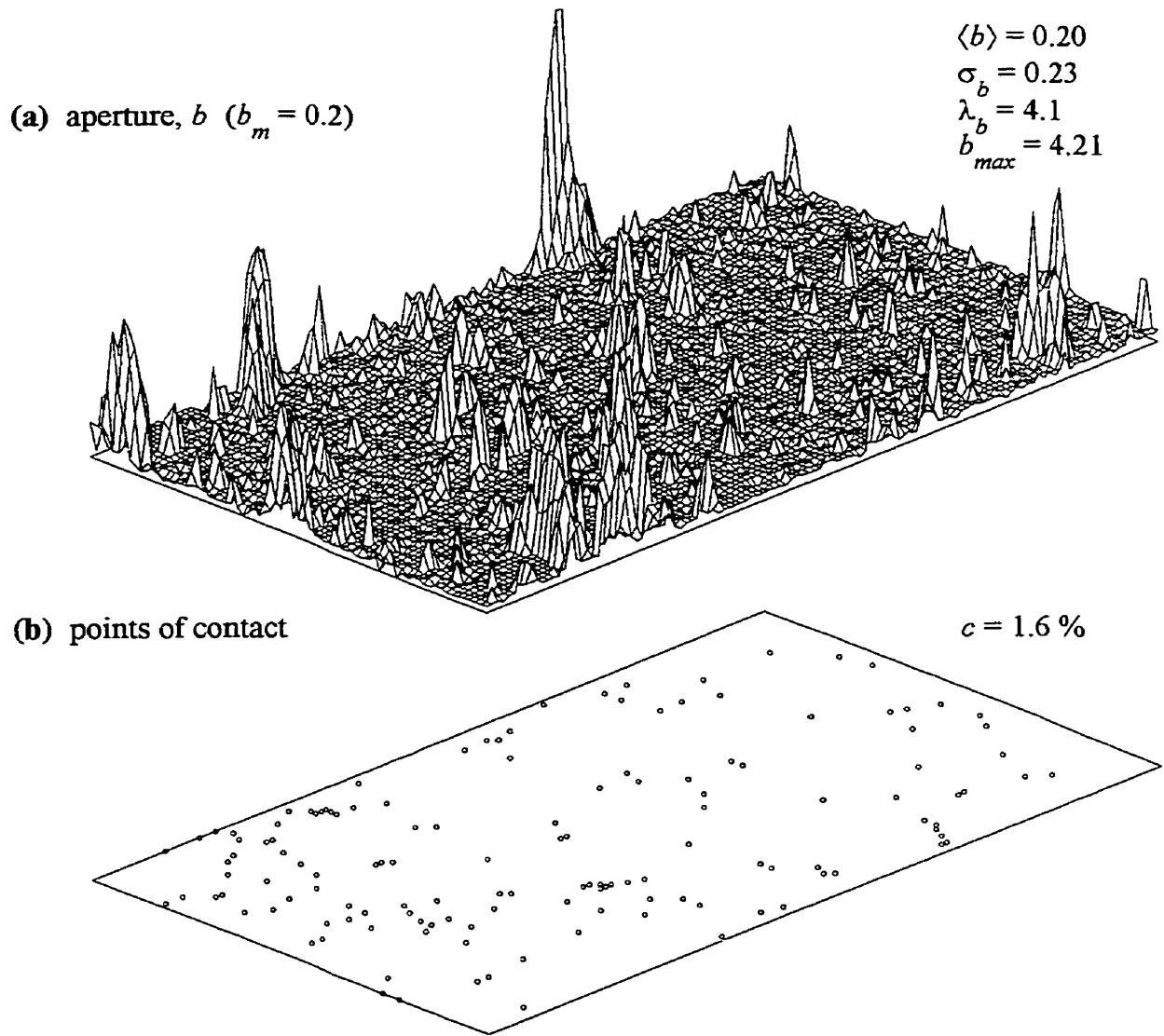


Figure 2.6. (a) Surface plot of inferred aperture field for Fracture I calculated using (2.11) with $b_m = 0.2$ mm, and (b) distribution of contact points within aperture field. All length dimensions are given in mm.

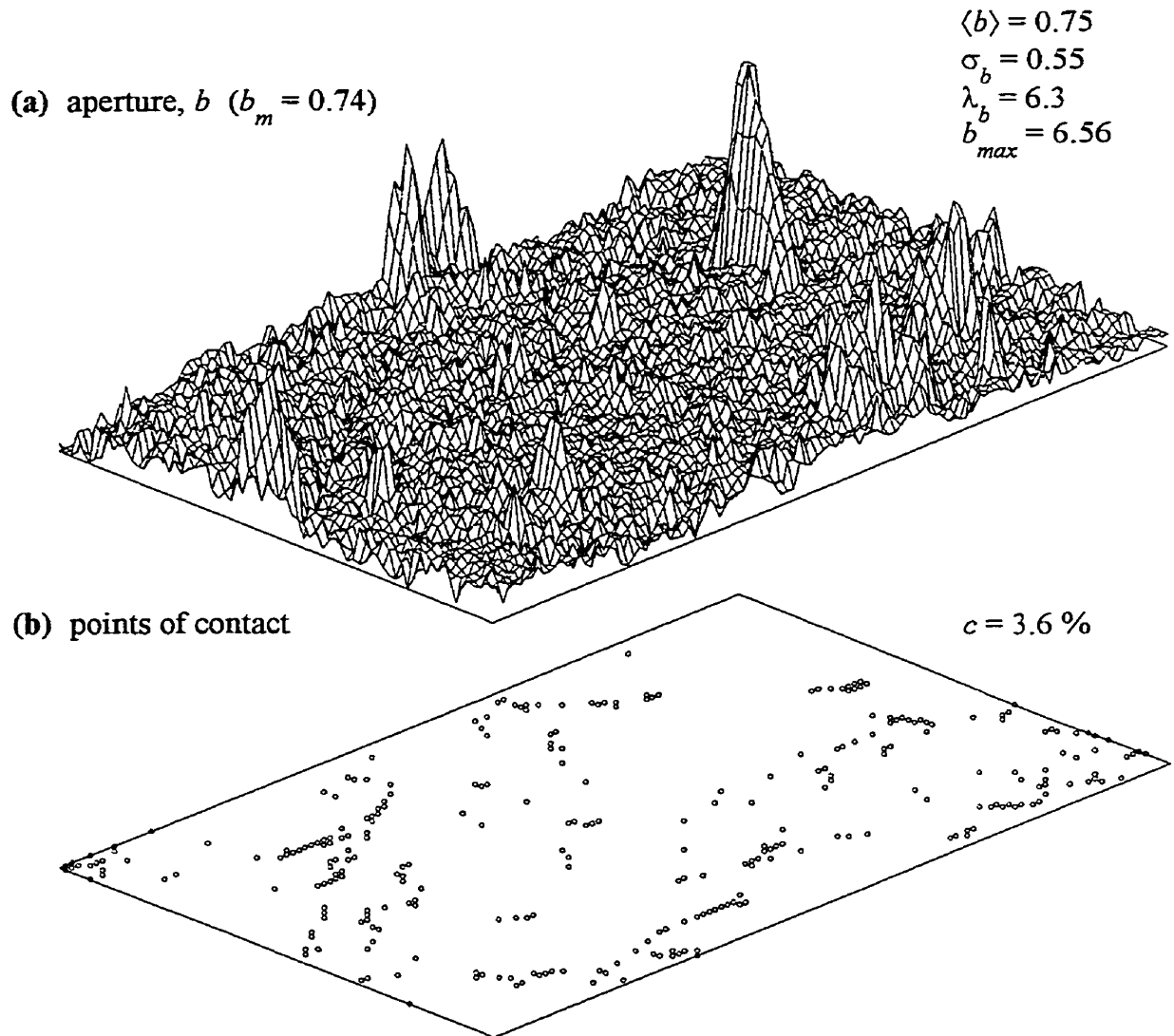


Figure 2.7. (a) Surface plot of inferred aperture field for Fracture II calculated using (2.11) with $b_m = 0.74$ mm, and (b) distribution of contact points within aperture field. All length dimensions are given in mm.

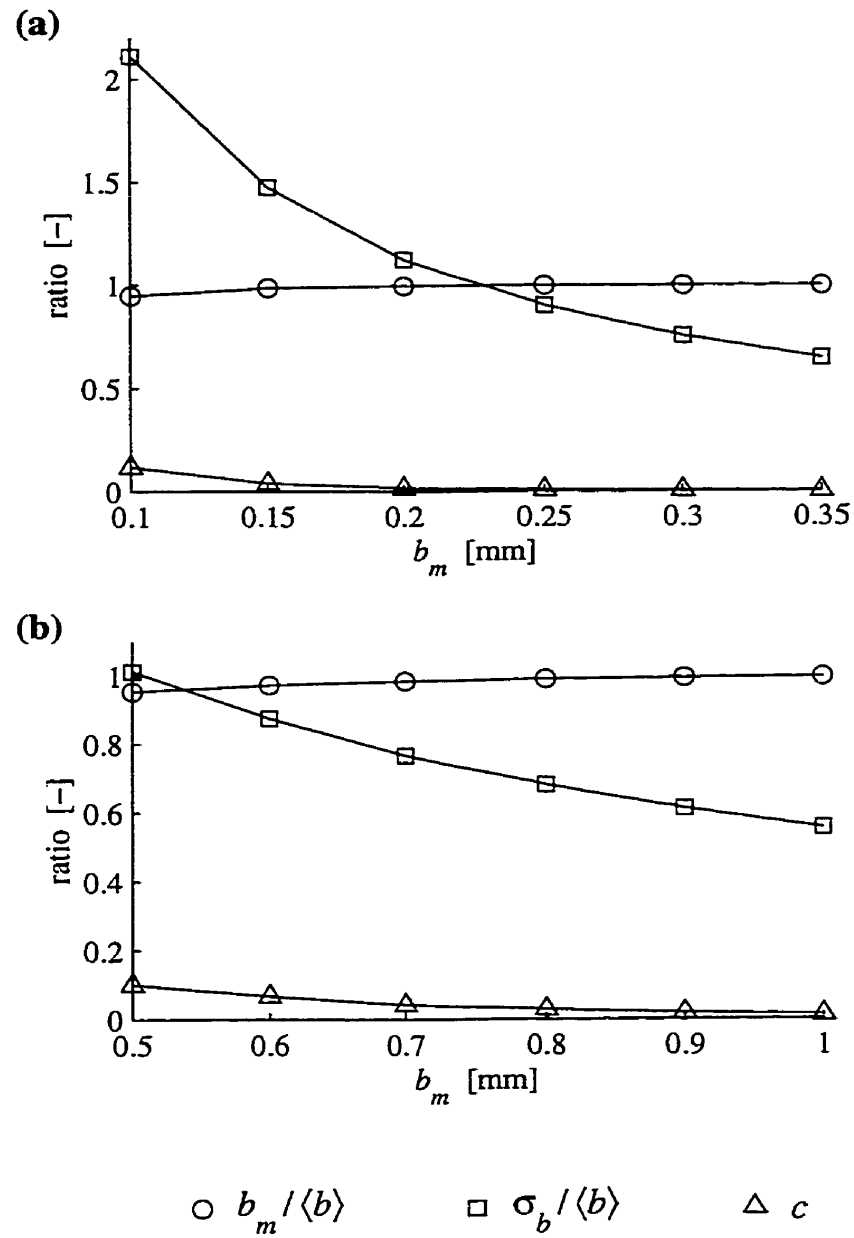


Figure 2.8. Plot of three dimensionless ratios ($b_m / \langle b \rangle$, $\sigma_b / \langle b \rangle$ and c) versus b_m for the inferred aperture field of (a) Fracture I, and (b) Fracture II.

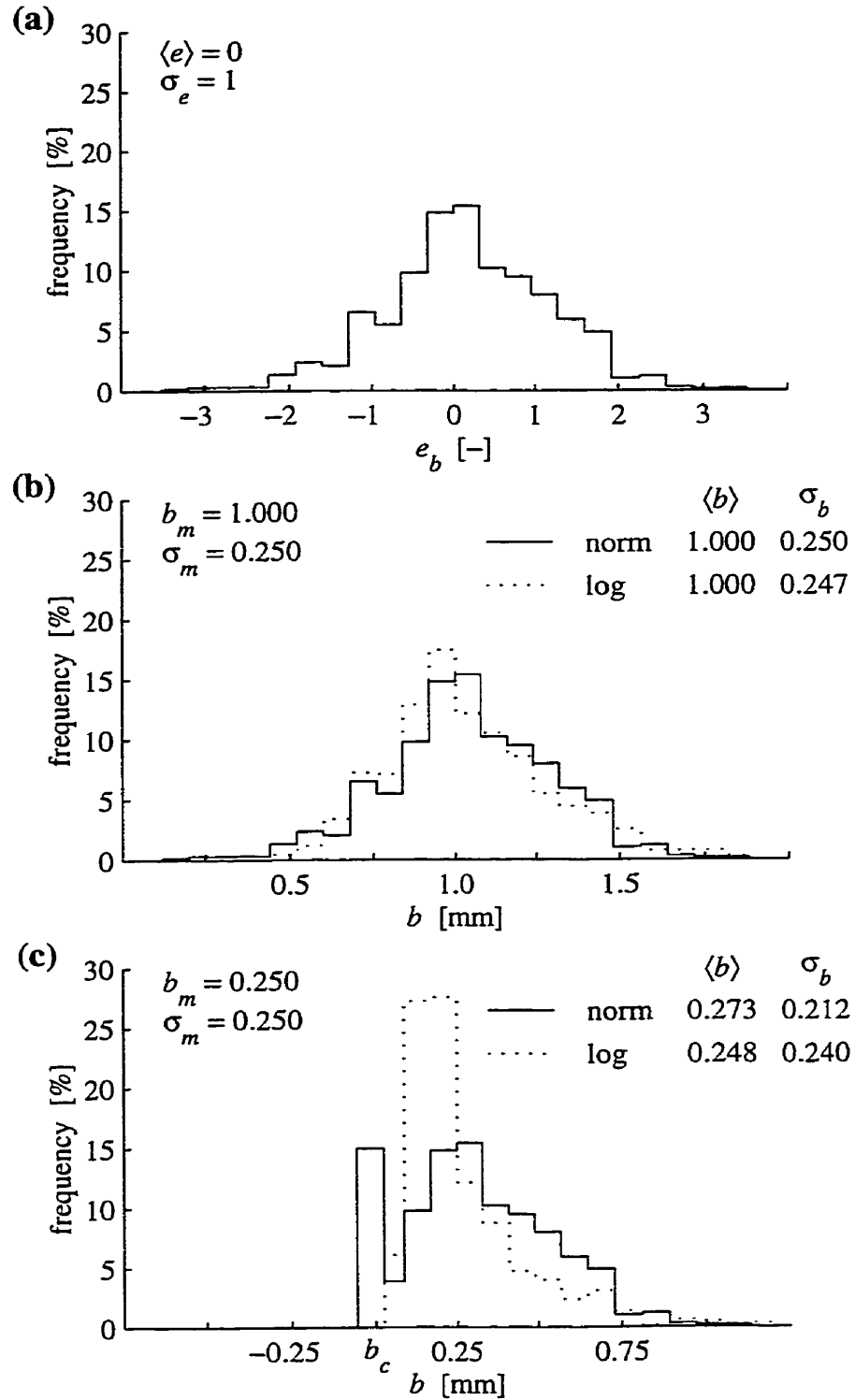


Figure 2.9. Histograms of (a) standardized e_b field, (b) aperture fields with $b_m = 1$ and $\sigma_b = 0.25$, and (c) aperture fields with $b_m = 0.25$ and $\sigma_b = 0.25$. The normal fields are calculated using (2.13), and the lognormal fields using (2.14). All length dimensions are given in mm.

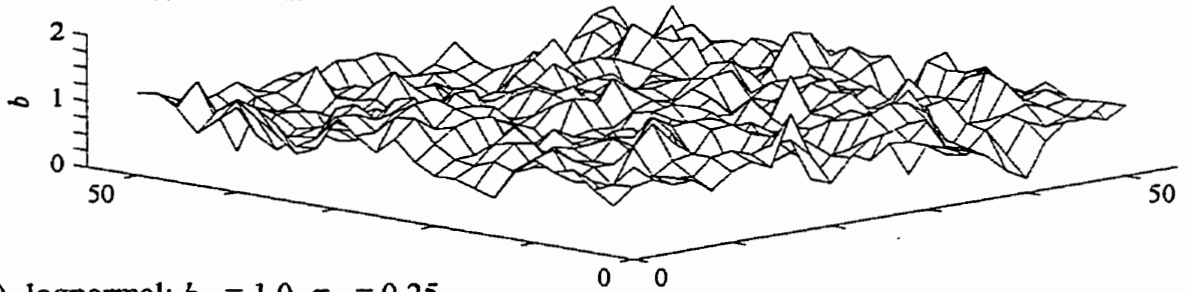
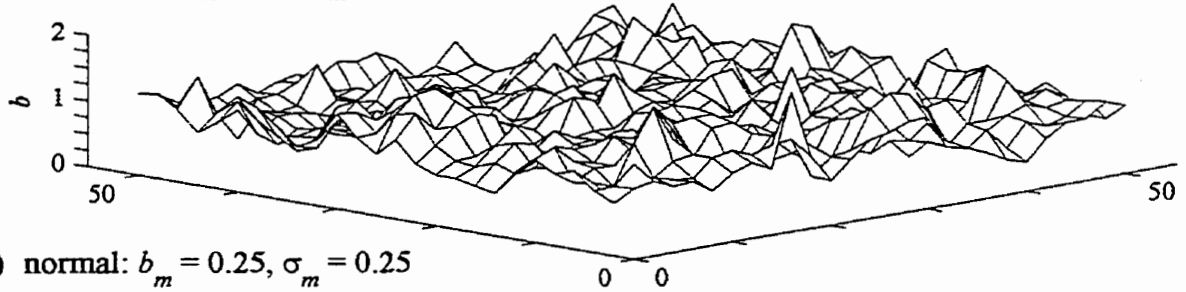
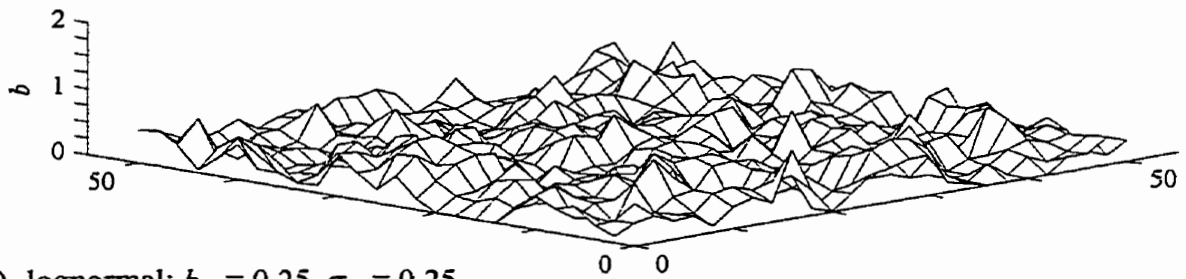
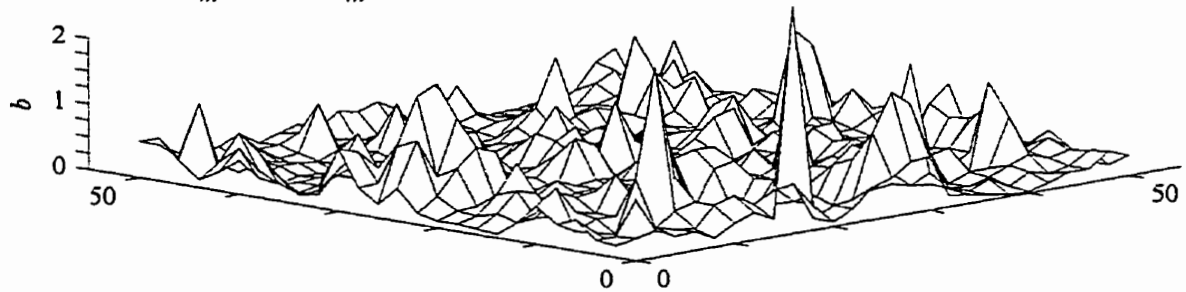
(a) normal: $b_m = 1.0, \sigma_m = 0.25$ (b) lognormal: $b_m = 1.0, \sigma_m = 0.25$ (c) normal: $b_m = 0.25, \sigma_m = 0.25$ (d) lognormal: $b_m = 0.25, \sigma_m = 0.25$ 

Figure 2.10. Surface plots of normally and lognormally distributed aperture fields shown in parts (b) and (c) of Figure 2.9. All length dimensions are given in mm.

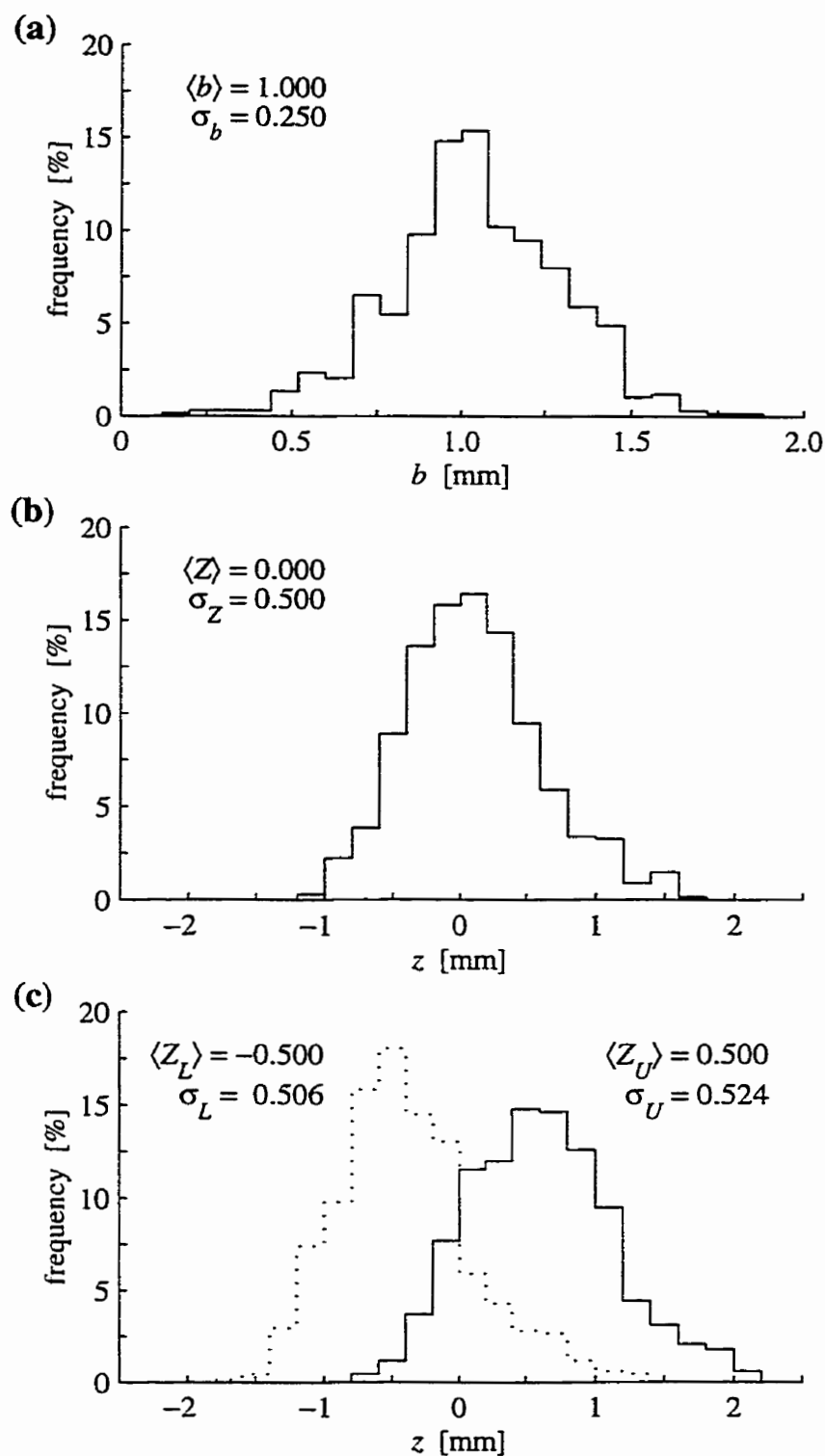


Figure 2.11. Histograms of (a) a normally distributed aperture field, (b) a normally distributed mid-surface field, and (c) the resulting upper and lower walls. The mid-surface and wall fields are calculated using (2.17) and (2.18), respectively. All length dimensions are given in mm.

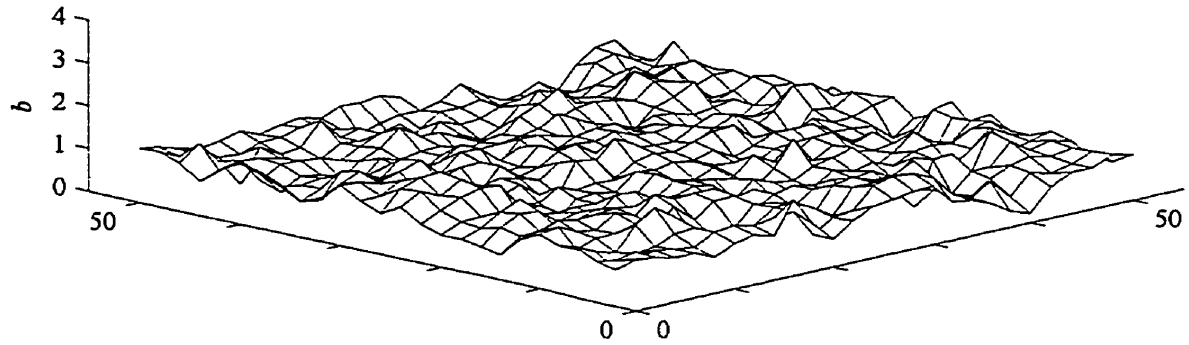
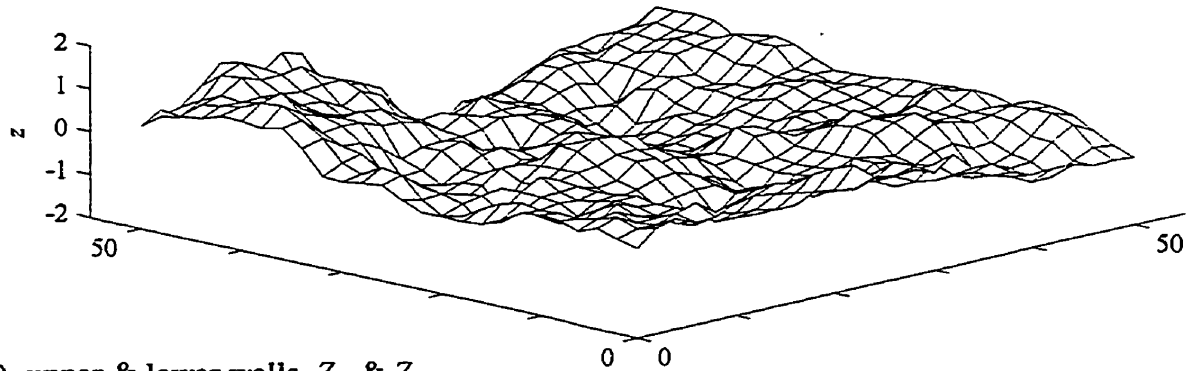
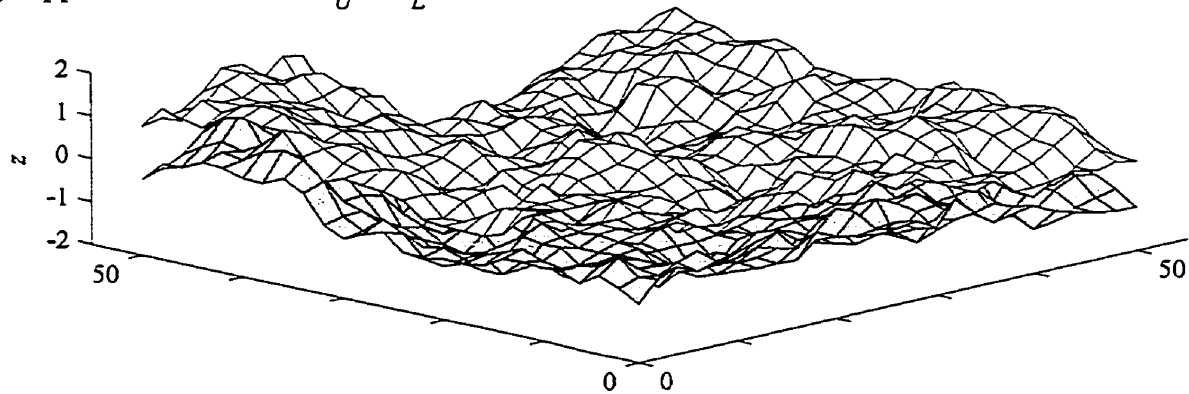
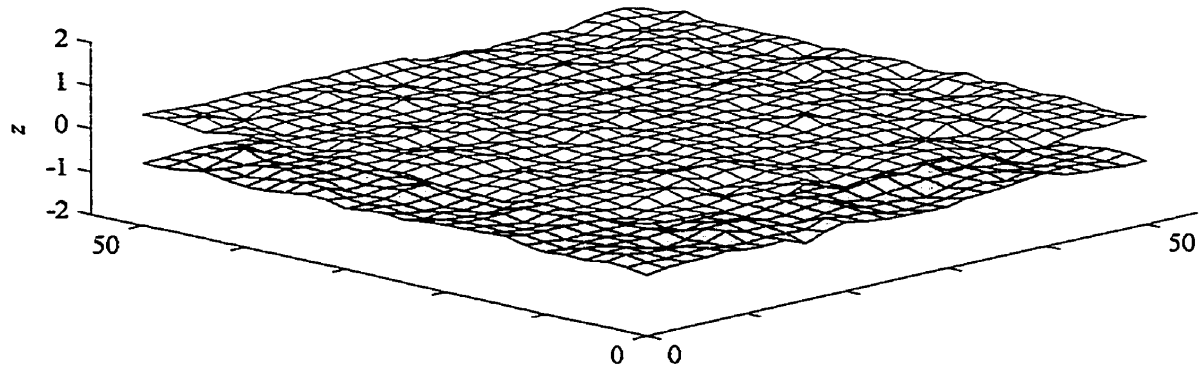
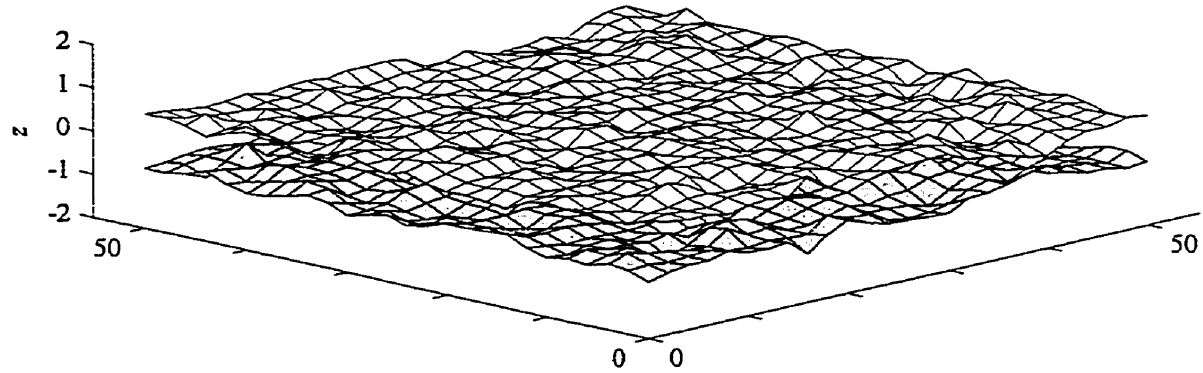
(a) aperture, b (b) mid-surface, Z (c) upper & lower walls, Z_U & Z_L 

Figure 2.12. Surface plots of (a) a normally distributed aperture field, (b) a normally distributed mid-surface field, and (c) the resulting upper and lower walls. These surface plots correspond to the histograms shown in Figure 2.11. All length dimensions are given in mm.

(a) $\sigma_m / b_m = 0.125$



(b) $\sigma_m / b_m = 0.25$



(c) $\sigma_m / b_m = 0.5$

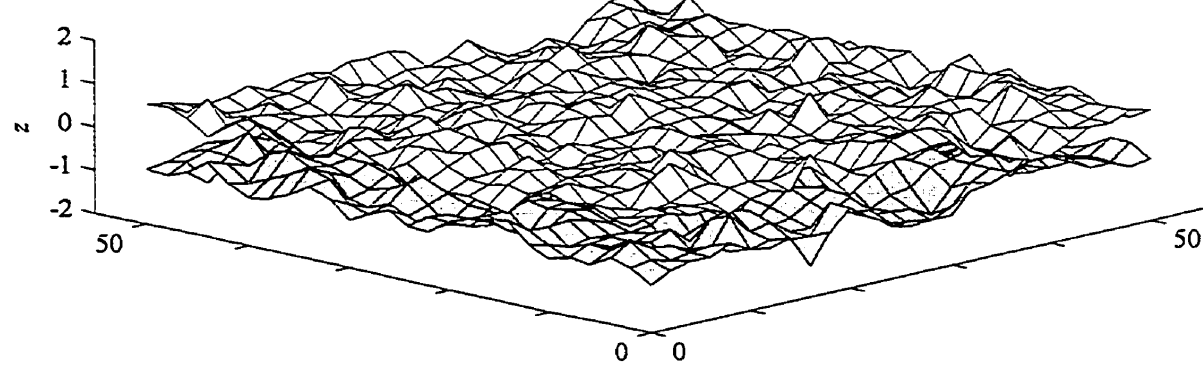
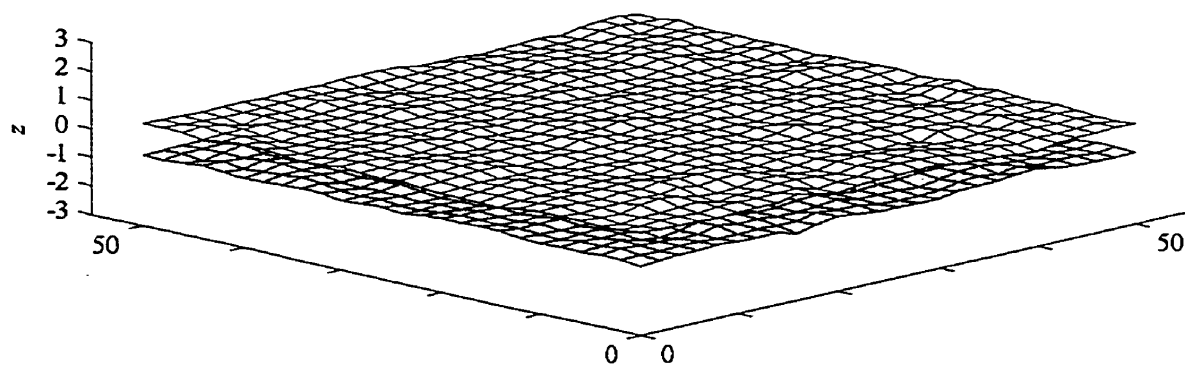
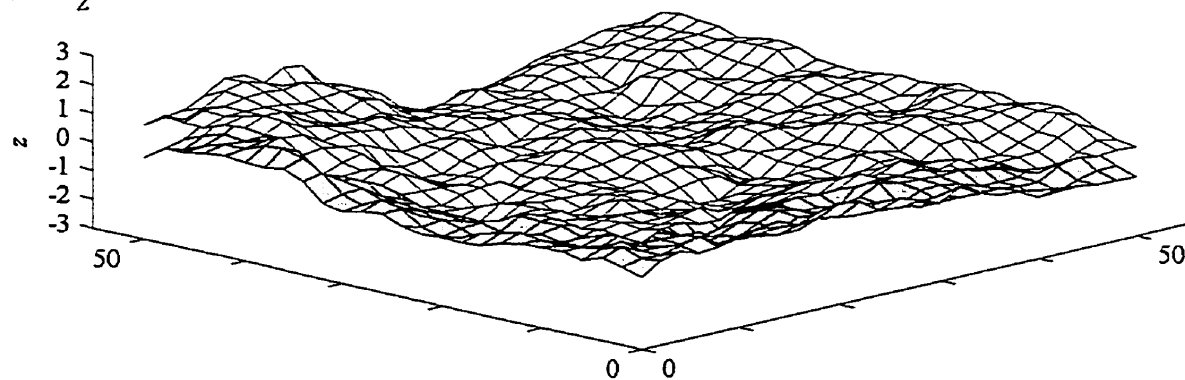
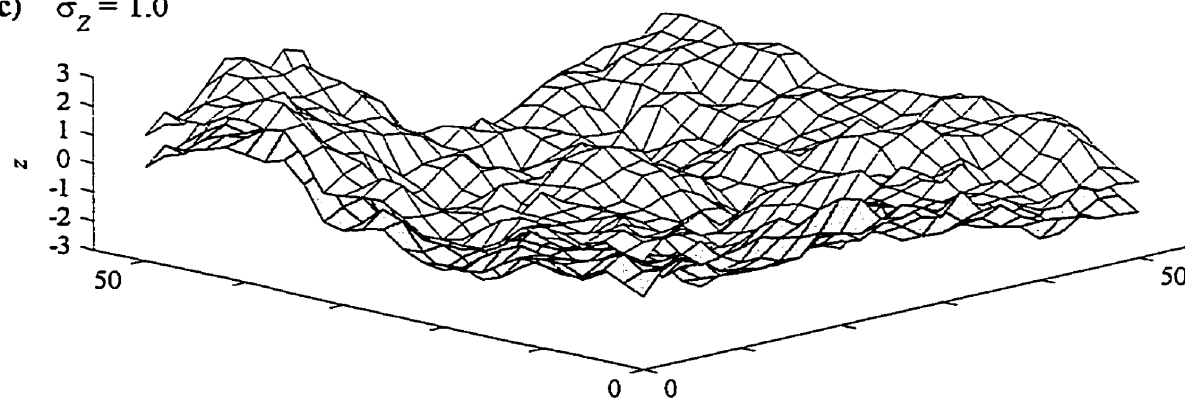


Figure 2.13. Examples of random fractures with $\sigma_z = 0$ and various values of σ_m / b_m .

(a) $\sigma_z = 0.0$ (b) $\sigma_z = 0.5$ (c) $\sigma_z = 1.0$ **Figure 2.14.** Examples of random fractures with $\sigma_m/b_m = 0.0625$ and various values of σ_z .

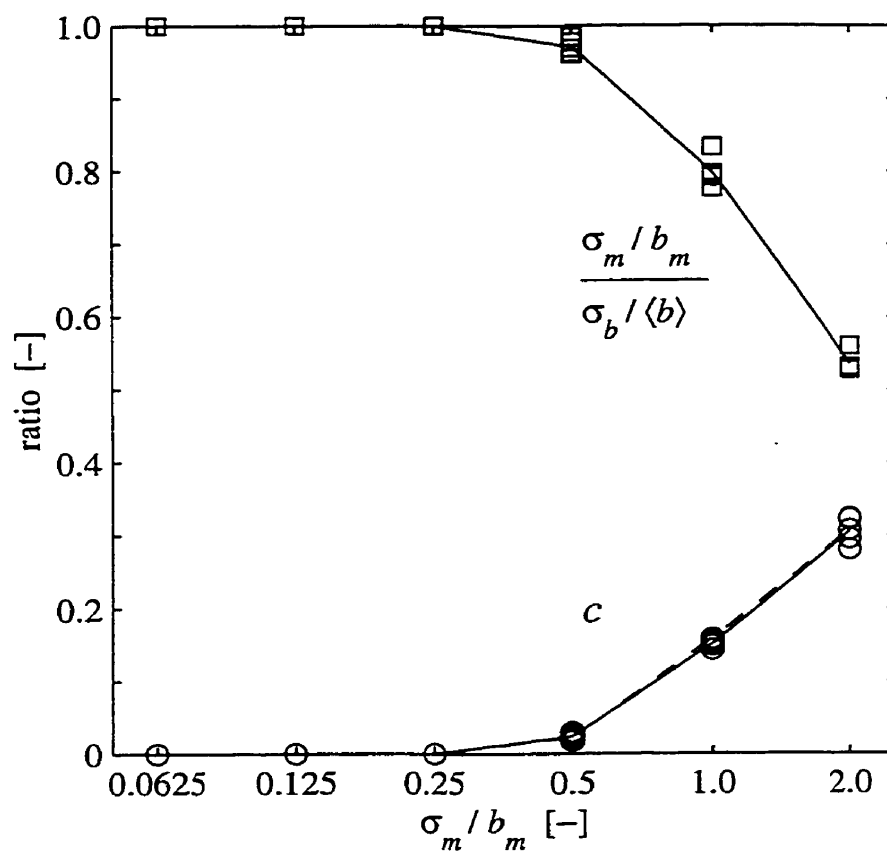


Figure 2.15. Plot of the relationship between the final relative roughness $\sigma_b / \langle b \rangle$ and fraction of contact c versus the initial relative roughness σ_m / b_m of the normally distributed random aperture fields used in this work. All the fields used are shown as symbols, and the line represents the mean. Also shown as a dashed line is the value of c as calculated with (2.15).

CHAPTER 3. Fluid Flow and Solute Transport in Single Fractures

3.1 Introduction

Single fractures have been widely studied because they form the building blocks for large fracture networks. Initially, single fractures were idealized as set of parallel plates in order to obtain a tractable mathematical description of fluid flow, namely the cubic law. However, it is now well established in the literature that single fractures are rough-walled conduits with variable aperture and points of contact. In fact, laboratory methods have been developed that directly map the void space of fracture samples (see Section 2.3). These methods have verified the rough-walled nature of single fractures, and more importantly, provide the unique opportunity of simulating flow and transport at the scale of these measurements. This in turn, allows for small scale phenomena to be directly simulated and compared to larger scale approximations. For example, much of the work presented in Section 3.3 focusses on comparing the small scale two-dimensional local cubic law (LCL) simulations to the large scale one-dimensional cubic law calculations. The work presented in this thesis goes a step further by simulating small scale flow and transport phenomena in three-dimensions with the Navier-Stokes equations and random walk particle method.

The next section (Section 3.2) presents the governing equations used in this thesis to simulate multi-dimensional fluid flow and three-dimensional solute transport through rough-walled fractures. Section 3.3 provides a review of empirical and theoretical studies of fluid flow and solute transport through single fractures.

3.2 Governing Equations

3.2.1 Fluid Flow

The most general description of fluid flow in single fractures is given by the Navier-Stokes (NS) equations which express momentum and mass conservation over the fracture void space. Considering the steady laminar flow of a Newtonian fluid with constant density and viscosity through a fracture with impervious walls, the NS equations may be written in vector form as [Bird *et al.*, 1960]

$$\rho (\mathbf{u} \cdot \nabla) \mathbf{u} = \mu \nabla^2 \mathbf{u} - \nabla p , \quad (3.1)$$

$$\nabla \cdot \mathbf{u} = 0 , \quad (3.2)$$

where ρ is the fluid density, μ is the fluid viscosity, $\mathbf{u}(u_x, u_y, u_z)$ is the velocity vector, and $p(x, y, z)$ is the hydrodynamic pressure. The hydrodynamic pressure at a point in the fracture is simply the difference between the total and static components of pressure [Milne-Thomson, 1968], which may be given as

$$p = p_T - \gamma d = \gamma h , \quad (3.3)$$

where $p_T(x, y, z)$ is the total pressure, γ is the fluid specific gravity, $d(x, y, z)$ is the depth below the free surface, and $h(x, y, z)$ is defined as the hydraulic head. Equation (3.1) is the momentum or force conservation equation and (3.2) is the mass conservation equation. The first term in (3.1) represents the inertial forces, the second viscous forces, and the third pressure forces.

The NS equations form a nonlinear system of partial differential equations that are difficult to solve in domains with complex geometry, such as a rough-walled fracture. Even in domains with simple geometry, such as a set of parallel plates, the computation burden of solving the three-dimensional system of equations is significant. It is therefore common practice to simplify the NS equations. This simplification may be performed in three successive levels.

The first level of simplification is to assume that the inertial forces in the flow field are negligibly small compared to the viscous and pressure forces. In this case, (3.1) reduces to

$$0 = \mu \nabla^2 \mathbf{u} - \nabla p , \quad (3.4)$$

which along with (3.2) form a linear system of equations called the Stokes or creeping flow equations. This linear system of equations is easier to solve than the non-linear NS equations; however, the inertial forces must be verified as being negligible. A common measure of the relative strength of inertial forces to viscous forces in flowing fluids is the Reynolds number. The Reynolds number for flow through a single fracture may be defined as

$$Re = \frac{\rho l_v U_i}{\mu} = \frac{\rho \langle b \rangle Q}{\mu \langle b \rangle W} = \frac{\rho Q}{\mu W} , \quad (3.5)$$

where l_v is the characteristic length of the viscous forces, and U_i is the characteristic velocity for the inertial forces. In this work, l_v is defined as mean fracture aperture $\langle b \rangle$ and U_i is defined as the bulk flow rate through the fracture Q divided by the average cross-sectional area ($\langle b \rangle W$).

Experimental observations of flow through smooth parallel plates have shown that the critical Reynolds number (as defined here) marking the beginning of turbulence and the dominance of inertial forces in the flow field is approximately 1200 [Lomize, 1951; Romm, 1968; Louis, 1968]. Considering typical values of subsurface hydraulic gradients, the value of Re in natural fractures will be much lower than this critical value; however, experimental observations using natural fracture samples have demonstrated that inertial forces may be non-dominant but significant at Re values above 1 to 10 [Sharp and Maini, 1972; Iwai, 1976; Schrauf and Evans, 1986].

Consequently, there have been several theoretical attempts to quantify the influence of inertial forces in single fractures. Zimmerman and Bodvarsson [1996] examined the perturbation analysis of Hasegawa and Izuchi [1983] for one-dimensional flow through a simple fracture with sinusoidal aperture variation. This approximate solution of the NS equations predicts the total flow rate through the fracture and has a correction term dependent on the amplitude (A) and wavelength (λ) of the sinusoidal aperture variation, $\langle b \rangle$, and Re . Constraints for a geometrical parameter ($\langle b \rangle / \lambda$, discussed in more detail below) and Re were determined by limiting the magnitude of this correction term. The contribution of inertial forces to the correction term was limited to 10% when Re was below unity. Using an order-of-magnitude analysis, Oron and Berkowitz [1998] estimated the magnitude of terms in the NS equations for two-dimensional flow through fracture profiles with random topography. They determined that the product of Re and σ_w / b_m should be significantly below unity for the Stokes equations to approximate the NS equations with second-order accuracy. Using a similar analysis, Zimmerman and Yeo [1998] suggested that the product of Re and $\langle b \rangle / \lambda_b$ should be significantly below unity. This result was also compared with the perturbation analysis of Hasegawa and Izuchi [1983] to provide a more practical evaluation of the condition. The contribution of inertial forces to the correction term was limited to 10% when $Re \langle b \rangle / \lambda_b$ was below 8.

The second level of simplification is to approximate the three-dimensional flow field given by the Stokes equations with a two-dimensional description. Assuming that the variability in the fracture aperture is gradual, then the velocity normal to the fracture walls will be approximately zero ($u_n \approx 0$) and the viscous forces in the flow field will be dominated by the shear forces acting normal to the fracture wall ($\nabla^2 \mathbf{u} \approx \partial^2 \mathbf{u} / \partial n^2$). Incorporating these velocity conditions into (3.4) and assuming that the fracture walls are approximately normal to the z -axis gives

$$0 = \mu \frac{\partial^2 \mathbf{u}}{\partial z^2} - \nabla p, \quad (3.6)$$

where $\mathbf{u}(u_x, u_y, 0)$ is a three-dimensional velocity vector with a direction parallel to the x - y plane. Incorporating the no-slip condition ($\mathbf{u} = 0$) at the fracture walls, (3.6) with (3.3) and (3.2) may be

integrated across the local aperture as [see *Zimmerman and Bodvarsson, 1996*]

$$\mathbf{U} = -\frac{b^2 \gamma}{12 \mu} \nabla H, \quad (3.7)$$

$$\nabla \cdot (b \mathbf{U}) = 0, \quad (3.8)$$

where $\mathbf{U}(U_x, U_y)$ is the average in-plane velocity vector, $H(x, y)$ is the average hydraulic head, and $b(x, y)$ is the local aperture parallel to the z -axis. Note that \mathbf{u} has a parabolic distribution along the z -axis, and that the change from lower to upper case in velocity and head symbols represents integration across the fracture aperture. Finally, (3.7) and (3.8) may be combined as

$$\nabla \cdot \left[\frac{b^3 \gamma}{12 \mu} \nabla H \right] = 0, \quad (3.9)$$

which is commonly known as the local cubic law (LCL) for fluid flow in a rough-walled fracture. It is also equivalent to a simplified form of the Reynolds equation (stationary walls and constant viscosity) used in field of hydrodynamic lubrication. It expresses the local force and mass conservation of fluid flow through a discrete portion of the fracture void space where all fluid flow vectors and pressure variables are integrated across the local aperture and are assumed to lie within the x - y plane. In the event that the fracture has a large degree of undulation (i.e., the mean wall topography or mid-surface is not approximately parallel the x - y plane), (3.9) may be recast using local orthogonal coordinates as

$$\frac{\partial}{\partial \xi_i} \left[\frac{b_\eta^3 \gamma}{12 \mu} \frac{\partial H}{\partial \xi_i} \right] = 0; \quad i = 1, 2 \quad (3.10)$$

where ξ_1 and ξ_2 are parallel to the local mid-surface, η is normal to the local mid-surface, $b_\eta(\xi_1, \xi_2)$ is the aperture defined normal to the local mid-surface, and $H(\xi_1, \xi_2)$ is the hydraulic head field. Alternatively, (3.10) may be shown to be equivalent to adding a correction term to (3.9) as

$$\nabla \cdot \left[\beta \frac{b^3 \gamma}{12 \mu} \nabla H \right] = 0, \quad (3.11)$$

where β is a correction tensor that adjusts the aperture and spatial dimensions of the local void space to reflect undulation in fracture mid-surface. Section 4.4 presents the development of a two-dimensional flow model that incorporates mid-surface corrections similar in form to (3.11).

As discussed in Chapter 1, the LCL has been widely applied and currently represents the state-of-the-art for simulating fluid flow in rough-walled fractures. Several of these applications are discussed in detail in Section 3.3. However, it is again important to delineate limits or constraints on the underlying assumptions used in the derivation of the LCL; the most crucial being that the aperture variation is gradual. *Brown [1987]* examined the velocity gradients calculated in LCL simulations in random fractures and suggested that λ_w should be at least 50 times larger than σ_w for the LCL to be a valid approximation to the Stokes equations. *Zimmerman et al. [1991]*,

Zimmerman and Bodvarsson [1996] and *Zimmerman and Yeo* [1998] examined the perturbation analysis of *Hasegawa and Izuchi* [1983] for one-dimensional flow through a simple fracture with sinusoidal aperture variation. As mentioned previously, this approximate solution of the NS equations predicts the total flow rate through the fracture and has a correction term dependent on A , λ , $\langle b \rangle$, and Re . By setting Re equal to zero, this perturbation solution approximates the Stokes equations, and the correction term may be shown to represent the relative discrepancy or error between the Stokes and LCL solutions. *Zimmerman et al.* [1991] determined that the error between the Stokes and LCL solutions was at most 10% when λ was 5 times greater than σ_b . *Zimmerman and Bodvarsson* [1996] and *Zimmerman and Yeo* [1998] found this same discrepancy when λ was approximately 2.6 to 3.3 times greater than $\langle b \rangle$.

The third and final level of simplification is to approximate the two-dimensional flow field given by the LCL with a one-dimensional description. The fracture may be conceptualized as a set of parallel plates by assuming that the fracture mid-surface is planar and that the variation in aperture is small relative to its mean value. Consequently, the flow field will be one-dimensional between the inlet and outlet boundaries of the fracture and may be described by integrating (3.7) over the length L of the fracture as

$$U = \frac{b^2 \gamma}{12 \mu} \frac{H_i - H_o}{L}, \quad (3.12)$$

where U is the average one-dimensional velocity, b is the constant plate aperture, H_i and H_o are the values of hydraulic head at the inlet and outlet boundaries, and $H_i - H_o / L$ is the hydraulic gradient applied across the fracture. In turn, this average velocity may be integrated over the aperture and width W of the fracture to obtain the total flow rate as

$$Q = \frac{b^3 \gamma W}{12 \mu} \frac{H_i - H_o}{L}, \quad (3.13)$$

which is the so-called cubic law for fluid flow between parallel plates. It is a simple linear flow law that predicts that the flow rate is proportional to the cube of the plate aperture. This behaviour has been experimentally verified using smooth parallel plates with apertures ranging from 1 cm to below 1 μm provided that Re was below the critical value of ~ 1200 [e.g., *Lomize*, 1951; *Romm*, 1968; *Louis*, 1969]. Equations (3.12) and (3.13) are analogous to forms of Darcy's law which describes one-dimensional fluid flow through traditional porous media. In comparing these two flow laws, the permeability and transmissivity of a parallel plate fracture (k and T) may be defined as $b^2/12$ and $W b^3/12$, respectively.

It is well known that the one-dimensional cubic law is unable to properly describe the complex internal flow fields through rough-walled fractures. Nonetheless, (3.13) is widely used to fit the observed relationship between the bulk flow rate and hydraulic gradient in single fractures, especially in field borehole tests. This empirical procedure defines effective flow parameters (aperture or transmissivity) for the fracture, which are commonly defined as hydraulic parameters

(b_H or T_H). For example, the hydraulic aperture of a single fracture with a linear flow field is defined by (2.1a), which is simply (3.13) rearranged in terms of the aperture. As discussed in Section 2.2, the hydraulic aperture is often used to characterize the void space of a single fracture, and is largely influenced by regions of high head loss within the flow field. Several theoretical studies have demonstrated that b_H depends on the mean and standard deviation of the aperture distribution, and the degree of fracture closure [e.g., *Tsang*, 1984; *Brown*, 1987]. These studies are discussed further in Section 3.3.

This section has presented the governing equations for fluid flow in single fractures at four levels of complexity. The first and most complex level is the three-dimensional Navier-Stokes equations given by (3.1) and (3.2). The second level is the three-dimensional Stokes equations given by (3.2) and (3.4). The third level is the two-dimensional local cubic law or Reynolds equation given by (3.9). Finally, the fourth and most basic level is the one-dimensional cubic law given by (3.13). The assumptions required to progressively simplify the NS equations to the cubic law are discussed. While the limitations of the cubic law have been clearly demonstrated and understood, the limitations of the LCL and Stokes equations are less clear. Table 3.1 summarizes several proposed kinematic and geometrical constraints for validity of these equations.

3.2.2 Solute Transport

A general description of solute transport in a single fracture may be given by the advection-diffusion equation [*Scheidegger*, 1974]:

$$\frac{\partial C}{\partial t} = - (\mathbf{u} \cdot \nabla) C + D_m \nabla^2 C, \quad (3.14)$$

where $C(x, y, z)$ is the solute concentration, and D_m is the molecular diffusivity of the solute. The first term in (3.14) represents the transient change in solute storage, the second term represents the advection of solute by the fluid flow field, and the third represents the molecular diffusion of solute. This equation is a subset of the general advection-dispersion equation for traditional porous media [see *Bear*, 1972], where the dispersion tensor has been simplified to the diffusion coefficient D_m and the porosity of the medium is set to unity. The simplification of the dispersion tensor is justified for the three-dimensional simulations in this thesis since the flow fields are fully mapped at the scale of the fracture void space. Therefore, the transport of solute by dispersion or mechanical mixing is directly captured by the flow field. Conversely, the typical flow fields in traditional porous media are volume averages at scales much larger than the pore space. Consequently, the dispersion tensor is required to account for solute transport by mechanical mixing of the pore space and various path lengths.

A common measure of the relative strength of solute advection to diffusion is the Péclet number. The Péclet number is a ratio of time-scales for each process and may be given as

$$Pe = \frac{t_{diff}}{t_{adv}} = \frac{l_{diff}^2 / D_m}{l_{adv} / U}, \quad (3.15)$$

where t_{diff} is the time-scale for diffusive transport defined as the square of the diffusion length l_{diff} over the diffusivity of the solute, and t_{adv} is the time-scale for advective transport defined as the advection length l_{adv} over the characteristic velocity U . A large Pe indicates that diffusion is significantly slower than advection, and consequently, that solute transport is dominated by advection. Conversely, a low Pe indicates that diffusion is significantly faster than advection, and that transport is dominated by diffusion. For traditional porous media, Pe is often used to compare hydrodynamic dispersion and advection over the length-scale and direction of the bulk flow. Applying this convention for a single fracture (3.15) may be given as

$$Pe = \frac{L^2 / D_m}{L / U} = \frac{L U}{D_m} = \frac{L Q}{W \langle b \rangle D_m}, \quad (3.16)$$

where the diffusion and advection lengths are both defined as the fracture length, and the advection velocity is defined as the bulk flow rate over the average cross-section area. This definition of Pe compares the time-scales of diffusion and advection across the fracture length. For the transport simulations performed in this thesis, Pe is always very large since the time-scale for diffusion across the fracture length is very large compared to advection in the bulk flow.

An alternative definition of the Péclet number for a single fracture may be given as

$$Pe_M = \frac{\langle b \rangle^2 / D_m}{L / U_a} = \frac{\langle b \rangle^2 U_a}{L D_m} = \frac{\langle b \rangle Q}{W L D_m}, \quad (3.17)$$

where the diffusion length is defined as the mean fracture aperture. This definition is referred to as the mixing Péclet number and compares the time-scales of diffusion across the fracture aperture and advection across the fracture length. A high Pe_M indicates that advective transport through the fracture will occur more quickly than the diffusive transport across the aperture. Consequently, the solute will experience a low degree of mixing across the fracture aperture. Conversely, a low Pe_M indicates that transverse diffusion will provide a high degree of mixing across the aperture relative to advection through the fracture.

A traditional numerical solution of (3.14) is potentially difficult because advection dominates diffusion along the length of the fracture (i.e., Pe is very large). This results in sharp solute concentration fronts that may introduce numerical instability and/or dispersion into the solution [see *Zheng and Bennet, 1995*]. A traditional cure to this numerical problem is to refine the spatial and temporal discretization of the solution; however, this is computationally expensive, especially in three-dimensions. An alternative approach, is to solve (3.14) using the random-walk particle method (RWPM) [Tompson and Gelhar, 1990]. This method transports a large number of marker particles through the fracture domain in such a way that the ensemble of particles satisfies (3.14). According to the RWPM, the advective-diffusive transport of a single particle may given

by [Kinzelback and Ufflink, 1991]

$$\mathbf{r}^t = \mathbf{r}^{t-\Delta t} + \mathbf{u}^{t-\Delta t} \Delta t + \mathbf{Z} \sqrt{2 D_m \Delta t} , \quad (3.18)$$

where $\mathbf{r}(x, y, z)$ is the position vector of the particle, $\mathbf{Z}(Z_x, Z_y, Z_z)$ is a vector of independent random numbers sampled from a standardized normal distribution (mean of zero and variance of unity), Δt is the time step, and the superscripts t and $t - \Delta t$ refer to the current and previous time step, respectively. The second term on the RHS of (3.18) represents advection by discretely tracking the particle within the flow field using Euler integration over the time step. The last term on the RHS of (3.18) represents diffusion by assigning a random Gaussian displacement to the particle. The variance of this Gaussian displacement is assigned $2 D_m \Delta t$, which is characteristic of a Fickian diffusive process [Bear, 1972; Scheidegger, 1974]. It is noteworthy that (3.18) is a subset of the general RWPM equation for solute transport by advection and dispersion, which includes additional terms associated with the dispersion tensor [see Kinzelback and Ufflink, 1991].

Effectively, (3.18) calculates the advective and diffusive transport of a particle independently, and then combines or superimposes these two components. In this way, the RWPM is not as susceptible to the numerical difficulties associated with large Pe values as are more traditional solution methods. In fact, provided that a suitable time step is selected, there will be a negligible amount of numerical dispersion in the solution of (3.18) [Kinzelback and Ufflink, 1991]. Finally, an obvious consideration in the RWPM is the number of particles required to properly characterize the ensemble behaviour of transport through the domain of interest.

3.3 Review of Previous Work

The purpose of this section is to provide the background material that shaped the development of this thesis and focuses on literature associated with the field of groundwater hydrology. For a more general review of fractures in the subsurface, the reader is referred to NRC [1996].

3.3.1 Empirical Studies of Fluid Flow and Solute Transport

Early empirical studies of fluid flow in single fractures conceptualized fractures as a set of rigid parallel plates with small scale wall roughness, which is analogous to the conceptual model used in pipe flow [see review by Iwai, 1976]. The most notable of these early studies are Lomize [1951] and Louis [1968]. These two studies used pipe flow techniques to examine the relationship between the friction factor and Reynolds number in laminar and turbulent flows through rough parallel plate fractures. The wall roughness was quantified using a relative roughness parameter, defined as the absolute roughness height over the hydraulic diameter of the parallel plates (ϵ/D). Note that the hydraulic diameter for a set of wide parallel plates may be shown to be equivalent to

twice the plate aperture ($D = 2b$). Under laminar flow conditions, the total flow rate through plates with ϵ/D less than or equal to 0.033 was observed to obey the cubic law. However, the total flow rate through plates with ϵ/D greater than 0.033 was observed to deviate from the cubic law.

These empirical observations may be represented as

$$\frac{Q_{obs}}{Q_{CL}} = \frac{b_H^3}{b^3} = \begin{cases} 1 & \epsilon/D \leq 0.033, \\ [1 + C(\epsilon/D)^{1.5}]^{-1} & \epsilon/D > 0.033, \end{cases} \quad (3.19)$$

where Q_{obs} is the observed flow rate, Q_{CL} is the flow rate predicted by the cubic law using the measured plate aperture, b_H is the observed hydraulic aperture of the plates, which is back-calculated from the cubic law using Q_{obs} , and C is a fitting parameter equal to 17.0 in *Lomize* [1951] and 8.8 in *Louis* [1968]. This equation indicates that Q_{obs}/Q_{CL} was less than unity when ϵ/D was greater than 0.033, and that this ratio decreased as the relative roughness increased. Interestingly, the RHS of (3.19) does not depend on the flow rate, which suggests that inertial effects did not influence the observed deviation. Equation (3.19) also demonstrates that the flow ratio may be given as the ratio of the hydraulic and measured plate apertures cubed. These studies concluded that rough plates with ϵ/D values less than or equal to 0.033 were hydraulically smooth. *Iwai* [1976] reviewed these studies along with measurements of ϵ made on natural fractures [*Romm*, 1966], and concluded that natural fractures with apertures above 20 μm may be regarded as hydraulically smooth. In other words, small scale wall roughness is not expected to influence the total flow rate through natural fractures with any appreciable aperture.

The next series of laboratory study examined fluid flow through fractures in rock samples under various degrees of normal stress [e.g., *Sharp*, 1970; *Gale*, 1975; *Iwai*, 1976]. The scale of roughness for these natural or induced rock fractures was larger than the simple roughened parallel plate model used previously. These fractures had variable aperture, points of contact, and undulation within their void space. The stress-strain behaviour of these rock samples was observed to be non-linear, hysteretic, and exhibit permanent deformation. However, the flow rate through these fractures was shown to be a unique function of the mechanical or volume aperture, defined by (2.6), (2.7), or (2.8). Nonetheless, the relationship between the total flow and measured aperture did not exactly follow the cubic law. Some studies suggested that the deviations from the cubic law were relatively small and concluded that the cubic law was valid [e.g., *Witherspoon et al.*, 1980]. This conclusion was probably influenced by the typically large uncertainties associated with estimating fluid flow in the subsurface. Other studies observed significant deviations which were attributed to tortuous channels in the flow field and concluded that the cubic law was invalid [e.g., *Raven and Gale*, 1985]. Furthermore, three of these studies [*Sharp and Maini*, 1972; *Iwai*, 1976; *Schrauf and Evans*, 1986] clearly observed a non-linear relationship between the total flow rate and the pressure gradient, which suggested that inertial forces in the flow field were significant.

Laboratory experiments of fluid flow and solute transport through single rough-walled fractures have also indicated that tortuous channels may control transport through the fractures. *Neretnieks et al.* [1982] and *Moreno et al.* [1985] observed breakthrough curves of conservative tracers through natural fractures that contained sudden jumps or steps which suggested that channels with different flow pathways and velocities contributed to the breakthrough at different times. The breakthrough curves also displayed long tails indicating that a portion of the tracer mass was transported along slow moving channels or zones. Figure 3.1 shows the experimental breakthrough curves of *Moreno et al.* [1985]. *Hakami and Barton* [1990] mapped the flow pathways of dye injected at various locations at the inlet boundary of transparent fracture replicas and found that the average pathway tortuosity (pathway length over fracture length) ranged from 1.01 to 1.34. The fracture with the largest relative roughness $\sigma_b/\langle b \rangle$ was observed to have the largest tortuosity. *Brown et al.* [1998] used a nuclear magnetic resonance technique to map the average in-plane velocity field for fluid flow through a transparent fracture replica. The velocity components in the direction of the bulk flow were found to vary over several orders-of-magnitude, with a maximum 5 times larger than the mean. Photographs of dye transport through the fracture showed that the dye initially travelled through large aperture channels, and at a later time appeared in the lower aperture regions. The geometry of the dye channels was dependent on the imposed flow rate and the interplay between advection and diffusion processes. The tortuosity along several flow channels was estimated to range from 1.05 to 1.37.

Field studies examining fluid flow and solute transport in large single fractures and fracture networks have demonstrated that channelling also occurs at larger scales. *Raven et al.* [1988] and *Novakowski and Lapcevic* [1994] performed in situ hydraulic and tracer tests in large horizontal fractures accessed with boreholes. The bulk aperture values determined (see Table 2.1) at various borehole locations clearly demonstrated aperture variability. Breakthrough curves at extraction or observation boreholes were fit to various one-dimensional advection-dispersion models. *Raven et al.* [1988] suggested that the tracer transport was largely influenced by mass transfer between fast and slow moving zones within the fracture. *Novakowski and Lapcevic* [1994] required tortuosity factors (as defined here) ranging from 1.03 to 1.9 to fit the observed data. *Birgersson et al.* [1993] examined the distribution of fluid flow and tracer transport through a intensely fractured rock zone that intersected the Stripa underground research laboratory in Sweden. The majority of groundwater and tracer influx was observed in only a few sampling areas (e.g., 90% of groundwater was collected in 8 of 150 collection areas).

Laboratory measurements of the fracture aperture distribution have been used with the cubic or LCL to predict the total flow rate through the fractures. *Hakami and Barton* [1990] observed fluid flow through transparent fracture replicas and sampled the aperture distribution using a visualization technique. Cubic law calculations using $\langle b \rangle$ overestimated the observed flow rate by a factor of 1.3 to 5. *Keller et al.* [1995] observed bulk fluid flow and solute transport

through a rock fracture with an aperture distribution characterized using a CAT X-ray scanning technique. The cubic law transmissivity $Wb^3/12$ was estimated using the geometric mean of $b(x, y)^3$ and underestimated the observed total flow rate by 13%. *Hakami and Larsson* [1996] measured fluid flow through a natural rock fracture and the aperture distribution of the fracture using an injection method. A LCL simulation using the measured aperture field predicted a flow rate through the fracture 2.4 times greater than the measured flow rate. *Yeo et al.* [1998] performed flow experiments on a transparent fracture analogue that was formed by replicating the wall of a sandstone fracture and then creating a mate from its own negative cast. The aperture distribution of the fracture under different mating conditions was measured using a casting technique. Using these measured aperture fields, LCL simulations predicted flow rates through the fracture 1.3 to 2 times higher than those measured. *Nicholl et al.* [1999] examined fluid flow through a set of roughed glass plates and measured the aperture distribution using a visible light transmission technique. LCL simulations using the measured aperture distribution with various geometrical corrections (discussed in Section 4.2) predicted a total flow rate 1.2 to 1.3 times greater than the measured flow rate. The relationship between the flow rate and hydraulic gradient was observed to be slightly non-linear at highest flow rate, which corresponded to a Re of ~ 4 .

Table 3.2 provides a detailed summary of various empirical studies which compared measured flow rates through single fracture to values predicted using aperture measurements with the cubic law (CL) or local cubic law (LCL). The rectangular dimensions of linear flow experiments ($W \times L$) and radial dimension of radial flow experiments ($r_o - r_i$ which is the difference in the radial position of the outlet or observation well and the radius of the injection well) are included. The bulk aperture or aperture statistics are also given, including estimates of contact fraction c and Re . In general, the CL and LCL predicted flow rates through the fractures on the order of 1.5 to 10 times greater than those measured. The largest deviations were observed for the CL predictions, which are likely caused by flow channelling within the void space, as observed directly by *Hakami and Barton* [1990] and *Brown et al.* [1998]. However, even the LCL simulations using the measured aperture distribution over-predicted flow rates by a factor of 1.2 to 2.4. Of the five studies listed in Table 3.2 with reported or estimated Re values above 1, only two [*Iwai*, 1976 and *Schrauf and Evans*, 1986] clearly observed non-linear inertial effects.

It is noteworthy to re-examine the bulk apertures presented and discussed in Section 2.2. The most common definitions are the hydraulic, tracer, and mass balance apertures (b_H , b_T , and b_B), which are often observed to follow (2.4), as shown in Table 2.1. Using (2.4) and assuming that b_B is a good approximation of $\langle b \rangle$ [*Tsang*, 1992], suggests that

$$\langle b \rangle \geq b_H \quad \rightarrow \quad \langle b \rangle^3 \geq b_H^3 \quad \rightarrow \quad Q_{CL} \geq Q_{obs} \quad , \quad (3.20)$$

which indicates that cubic law calculations using $\langle b \rangle$ will be equal to or greater than the measured flow rate. This statement is in agreement with the results from these empirical studies.

3.3.2 Theoretical Studies of Fluid Flow

Theoretical studies of fluid flow through single fractures have conceptualized the fracture void space using two general methods: the first method places asperities or columns of contact between two parallel plates [e.g., Walsh, 1981; Zimmerman *et al.*, 1992], and the second method defines voids with variable geometry between rough walls in potential contact [e.g., Tsang, 1984; Brown, 1987]. The work presented in this thesis follows the second method (see Section 2.5) and therefore this section will focus on theoretical studies that conceptualize fractures with rough walls.

Local Cubic Law

Patir and Cheng [1978] examined the flow of lubricating fluids between rough-walled bearings using the Reynolds equation or LCL. The topography of the each bearing wall was generated independently using a Gaussian distribution with zero mean and specified standard deviation σ_w . The spatial correlation of each wall was modelled using a simple linear auto-correlation function, although the correlation length was not reported. The local film thickness or aperture field $b(x, y)$ between the walls was defined as

$$b = \max(b_m + Z_U - Z_L, b_c) \quad (3.21)$$

where b_m is the mechanical aperture, $Z_U(x, y)$ and $Z_L(x, y)$ are the random surfaces of the upper and lower walls, respectively, and b_c is the contact aperture equal to zero. Equation (3.21) creates a normally distributed aperture field that is truncated at b_c , where b_c represents contact between the walls. The total flow rate through various aperture fields was simulated using the LCL (Q_{LCL}) and compared to cubic law calculations (Q_{CL}) using $\langle b \rangle$. The differences between these predictions were described by

$$\frac{Q_{LCL}}{Q_{CL}} = \frac{b_H^3}{\langle b \rangle^3} = 1 - 0.9 \exp(-0.56 b_m / \sigma_m), \quad (3.22)$$

where σ_m is the standard deviation of b without truncation, which may be shown to be equivalent to $2^{1/2} \sigma_w$ since Z_U and Z_L are independent. The flow ratio predicted by (3.22) is plotted against b_m / σ_m in Figure 3.2(a) as originally presented by *Patir and Cheng* [1978]. Figure 3.2(b) shows the flow ratio from (3.22) versus σ_m / b_m using a semi-logarithmic plot, which represents the format used in this thesis. It is clear that the cubic law over-predicts the flow rate as compared to the LCL, and that their relative difference increases as the relative roughness (defined by σ_m / b_m) of the aperture field increased. The authors noted, that points of contact in the aperture fields were expected when σ_m was greater than $3 b_m$. This is a result of sampling from Gaussian distributions with a finite range of 3 standard deviations on each side of the mean. The fraction of contact c in these finite aperture fields may be estimated using (2.15). Figure 3.2 displays (2.15) and shows that c increases exponentially as σ_m / b_m increases above 3. Interestingly, the original numerical data

points and (3.22) vary smoothly as the walls come into contact, and do not exhibit a clear discontinuity in slope. It is important to note that *Patir and Cheng* [1978] state that the cubic law calculations used b_m ; however, the relationship depicted by (3.22) suggests that $\langle b \rangle$ was used. If b_m had been used in the cubic law calculations, the flow ratio would not continue to decay with increasing σ_m/b_m as predicted by (3.22), but would eventually approach and perhaps exceed unity. This is because the value of b_m is unaffected by truncation in the aperture field and eventually becomes a conservative estimate of the hydraulic aperture as the fracture closes. An example of this behaviour is clearly shown in Figure 11 of *Brown* [1987].

Brown [1987] performed LCL simulations of flow through rough-walled fractures using a method similar to *Patir and Cheng* [1978]. The topography of the each fracture wall was generated independently using a Gaussian distribution with zero mean and specified standard deviation σ_w . However, the spatial correlation of each wall was modelled using a fracture correlation structure quantified by the fractal dimension. The fractal dimension D is a measure of the wall texture and has been found to range from 2 (smooth) to 2.5 (jagged) for natural rock surfaces [*Brown and Scholz*, 1985]. The fracture aperture field of each fracture was defined using (3.21) with b_c set equal to a small positive value (e.g., $0.01 b_m$). Once again, the flow rate through various aperture fields was simulated using the LCL and compared to cubic law calculations using $\langle b \rangle$. The differences between these predictions were fit to a slight variation of (3.22):

$$\frac{Q_{LCL}}{Q_{CL}} = \frac{b_H^3}{\langle b \rangle^3} = 1 - A \exp(-B b_m / \sigma_w), \quad (3.23)$$

where A and B equal 0.807 and 0.478 when D equals 2, and 0.697 and 0.459 when D equals 2.5. The flow ratio from (3.23) is plotted for these two bounding values of D in Figure 3.2 against b_m/σ_m and σ_m/b_m where σ_m equals $2^{1/2} \sigma_w$. The figure shows that (3.23) for both D values are very similar, especially for smooth surfaces, which indicates that flow rate deviations using fractal surfaces are not very sensitive to the fracture dimension D of each surface. Interestingly, the smoother surfaces (D equals 2) had larger discrepancies than the jagged surfaces. Furthermore, comparing (3.23) to (3.22) suggests that flow rate deviations using the fractal surfaces are less than those observed in *Patir and Cheng* [1978]. Note however, that if σ_m and σ_w are assumed to be equivalent [*Brown*, 1987; *Zimmerman and Bodvarsson*, 1996] then (3.22) and (3.23) are in better agreement. In a later study, *Thompson and Brown* [1991] demonstrated that anisotropy within the structure of the fractal surfaces was more important in predicting fluid flow than the degree of roughness (b_m/σ_m). Surface roughness oriented parallel to the primary direction of flow was found to enhance fluid flow, and roughness oriented perpendicular to the primary flow direction inhibited fluid flow. Consequently, the deviations between the LCL and cubic law for fractures with an anisotropic correlation structure were found to be very different than (3.23).

Tsang [1984] created rough-walled fractures by randomly generating two-dimensional planar aperture fields. These fields were spatially uncorrelated and sampled from normal and gamma

distributions. Fracture closure was simulated by truncating the original aperture fields $b_o(x, y)$ according to

$$b = \max(b_m - b_o, 0) \quad (3.24)$$

where b_m is the mechanical aperture. LCL simulations using an aperture-resistor analogue predicted flow rates one to three orders-of-magnitude smaller than the cubic law using $\langle b \rangle$ when the fraction of contact was 15 to 35%. These large deviations were likely due to the absence of spatial correlation within the aperture fields, and consequently, the absence of persistent flow channels [Brown, 1987]. Later work by Tsang and co-workers added spatial correlation to the fracture aperture fields [e.g., Tsang and Tsang, 1987, 1989; Moreno *et al.*, 1988; Tsang *et al.*, 1988]. These studies used LCL simulations to map the flow channels through the variable aperture field and did not compare the total flow rates to the cubic law. However, the bulk of the total flow was observed to follow a few preferred pathways. These studies also used particle tracking to simulate solute transport along these preferred pathways (see Section 3.3.3).

Renshaw [1995] examined the relationship between b_m and b_H in rough-walled fractures using a statistical analysis. The fracture aperture fields were assumed to be two-dimensional, planar, isotropic, uncorrelated, and log-normally distributed. These fields were not truncated, and therefore, b_m was always equivalent to $\langle b \rangle$. Using a well-known result of stochastic theory for isotropic log-normal fields, b_H was approximated as the geometric mean of aperture field ($b_G = \exp(\langle \ln b \rangle)$ which is equivalent to b_m^* in the notation used in this work). Finally, the following ratios were determined:

$$\frac{b_H^3}{\langle b \rangle^3} = \frac{b_H^3}{b_m^3} = \exp\left(-\frac{1}{2} \sigma_m^{*2}\right)^3, \quad (3.25a)$$

$$\frac{b_m}{\sigma_m} = \frac{\exp\left(\frac{1}{2} \sigma_m^{*2}\right)}{\left[\exp(\sigma_m^{*2}) \left(\exp(\sigma_m^{*2}) - 1\right)\right]^{\frac{1}{2}}}, \quad (3.25b)$$

which depend only on the variance of the log-aperture field σ_m^{*2} . These ratios are plotted in Figure 3.2 for various values of σ_m^* . It is interesting to observe that for $b_m/\sigma_m > 2$ (or $\sigma_m/b_m < 0.5$) that the functions (3.25) and (3.22) are very similar.

Zimmerman and Bodvarsson [1996] reviewed several analytical treatments of the LCL and two-dimensional flow through heterogeneous porous media. They concluded that b_H^3 for any variable aperture field was limited to the following constraint:

$$\langle b^{-3} \rangle^{-1} \leq b_H^3 \leq \langle b^3 \rangle \quad (3.26)$$

where the bounds are the harmonic and arithmetic means of the $b(x, y)^3$ field. They also compared various estimates of b_H^3 from stochastic and equivalent medium theory to the laboratory flow data of Hakami [1989] and Gale *et al.* [1990]. The best estimates of the observed b_H^3 values were

given by an expression developed by the authors:

$$\frac{b_H^3}{\langle b \rangle^3} = \left[1 - 1.5 \frac{\sigma_b^2}{\langle b \rangle^2} \right] (1 - 2c) , \quad (3.27)$$

which is the product of a stochastic solution for isotropic log-normal aperture fields and a contact area correction term. Equation (3.27) is plotted on Figure 3.2 by approximating $\sigma_b/\langle b \rangle$ and c with a truncated standardized normal distribution. The expression is shown to be equivalent to (3.25) for small values of c , and predicts the lowest flow ratio as c increases.

Navier-Stokes Equations

The Navier-Stokes equations are difficult to solve in rough-walled fractures. For example, *Coakley et al.* [1987] attempted to solve the NS equations in a realistic variable aperture fracture, but were forced to use a simple fracture with four saw-tooth constrictions because the computational burden of the numerical solution was too large. Consequently, there are apparently no published studies solving the NS equations in a realistic three-dimensional rough-walled fracture. The closest efforts have been made by *Mourzenko et al.* [1995] and *Brown et al.* [1995].

Mourzenko et al. [1995] solved the three-dimensional Stokes equations in three-dimensional rough-walled fractures formed using the method of *Patir and Cheng* [1978] and *Brown* [1987]. The total flow rate predicted by the Stokes equations Q_s was compared to the total flow rate predicted by the LCL Q_{LCL} in order to evaluate the LCL approach. Figure 3.3 shows the predicted flow ratio versus a relative roughness parameter σ_w/b_m for fractures with independent and dependent walls. The wall topography was sampled from a Gaussian distribution with a quadratic correlation structure. Figure 3.3 displays significant deviations between the Stokes and LCL simulations; however, there are two unusual properties in the figure that are noteworthy. The first is that the deviation in the flow rates is significantly larger for the dependent fractures for a given σ_w/b_m value, and the second is that the flow ratio levels off as σ_w/b_m becomes large. The opposite of these properties is expected since the degree of closure and tortuosity increase for the independent fractures and increasing values of σ_w/b_m , and therefore, the two-dimensional LCL is expected to be less viable.

Brown et al. [1995] performed Stokes (defined as Re equal to zero) and Navier-Stokes simulations based on a lattice-gas automaton method in two-dimensional fracture profiles formed from several cycles of a sinusoid. These simulations showed that the fluid velocity distribution perpendicular to the fracture plane was not parabolic at all locations and the NS simulations predicted zones of recirculation at high Reynolds number. Figure 3.4(a) shows the predicted flow ratios between Stokes and LCL simulations through fracture profiles illustrated in Figure 3.4(b). Two parameters were used to quantify the roughness of these profiles: the amplitude over the minimum aperture A/b_{min} , and the amplitude over the wavelength A/λ . The first parameter

measures the relative roughness of the profile and the second measures the rate of change in the roughness or the roughness slope. The Stokes simulations are shown to be significantly lower than the LCL as A/b_{\min} increases, and are also lower for the steeply sloped profiles. Figure 3.4(b) also shows the predicted flow ratios between NS and Stokes simulations versus the Reynolds number for the steeply sloped fracture profiles, and demonstrates that the inertial forces become significant for Re values above 10.

This subsection discussed theoretical studies which have clearly demonstrated that cubic law calculations based on $\langle b \rangle$ significantly deviate from LCL simulations for large values of the relative roughness $\sigma_b/\langle b \rangle$. Figure 3.2 illustrates several expressions that quantify these deviations for different types of synthetic rough-walled fractures. In Section 5.4.1 these expressions are compared with simulations performed in the present research. These expressions are potentially useful to correct large scale network problems which often employ the cubic law to simulate flow through single fractures. However, these corrections are based directly on LCL simulations or statistical arguments assuming that the LCL is valid. This reliance on the LCL has prompted several researchers to investigate its validity using approximate techniques (see Section 3.2.1). A more direct numerical method of validating the LCL is to solve the complete Navier-Stokes equations; however, this is a difficult task, and is the main objective of this thesis. The results of two numerical studies discussed above suggest that the LCL may significantly overestimate the total flow rate through rough-walled fractures as compare to NS or Stokes simulations. These deviations were generally shown to increase as the relative roughness and roughness slope of the fracture increased. Finally, the work of *Brown et al.* [1995] demonstrated that inertial forces can significantly influence the fracture flow field.

3.3.3 Theoretical Studies of Solute Transport

Parallel Plates

As with fluid flow, the most basic conceptual model of solute transport through a single fracture is transport between a set of parallel plates. Using this conceptual model it is possible to analytically describe the bulk transport between the parallel plates at two extreme time scales that may be quantified by Pe_M (see (3.17) in Section 3.2.2). Note that for this discussion it is assumed that Pe as defined in (3.16) is always large.

The first time scale occurs when Pe_M is much greater than unity, which indicates that diffusion across the fracture aperture is insignificant compared to the advective transport across the fracture length. Consequently, solute transport at high Pe_M values may be approximated as purely advective, and therefore, is described by the velocity distribution between the parallel plates, which may be given as [*Zimmerman and Bodvarsson*, 1996]

$$u = -\frac{\gamma \Delta H}{8 \mu L} (4 z^2 - b^2) , \quad (3.28)$$

where $u(z)$ is the longitudinal velocity parallel to walls, b is the plate aperture, and z is the local coordinate perpendicular to the walls. This z -coordinate defines layers or sheets of fluid flowing at a same velocity parallel to the walls, and it ranges from $-b/2$ at the lower plate to $b/2$ at the upper plate. The velocity distribution given by (3.28) is parabolic with a maximum value at the z -origin, and values of zero at the lower and upper plates. Note that the average velocity through the plates may be obtained by integrating (3.28) as

$$U = -\int_{-b/2}^{b/2} \frac{\gamma \Delta H}{8 \mu L} (4 z^2 - b^2) dz = -\frac{b^2 \gamma \Delta H}{12 \mu L} , \quad (3.29)$$

which is simply the velocity form of the cubic law. Furthermore, (3.28) and (3.29) may be used to estimate the time required for solute to travel by advection along the plate length L . The travel time $t(z)$ for solute mass flowing along a specific fluid layer is given by

$$t = \frac{L}{u} = \frac{8 \mu L^2}{\gamma |\Delta H| (4 z^2 - b^2)} , \quad (3.30)$$

and the average travel time t_R for the entire plate cross-section may be given by

$$t_R = \frac{L}{U} = \frac{12 \mu L^2}{\gamma |\Delta H| b^2} . \quad (3.31)$$

These travel times may be combined to define a dimensionless travel time for solute flowing along a specific fluid layer as

$$\frac{t}{t_R} = \frac{2}{3} \frac{b^2}{4 z^2 - b^2} . \quad (3.32)$$

The mass flux $m(z)$ of solute crossing the outlet boundary may be estimated as an integral of fluid layers according to

$$m = C_i 2 W \int_0^z u dz , \quad (3.33)$$

where C_i is the inlet concentration, and the travel time for each fluid layer is given implicitly by (3.32). The relative concentration at the outlet may then be defined as

$$\frac{C}{C_i} = \frac{m}{m_T} = \frac{C_i 2 W \int_0^z u dz}{C_i W U b} = \frac{4 z^3 - 3 z b^2}{b^3} , \quad (3.34)$$

which is the ratio of (3.33) to the total mass flux m_T after complete breakthrough. Finally, (3.32) and (3.34) may be evaluated for z values between 0 and $b/2$ to obtain the dimensionless breakthrough curve for advective transport through parallel plates [for a similar development for

advective transport through a pipe see *Bear, 1972*]. Figure 3.5 plots this characteristic breakthrough curve (defining Pe_M and Pe to equal ∞), which displays a sudden and steep rise at early times and a long tail at later times. This sudden rise is a characteristic of plug-flow transport, and the large, steep increase in C/C_i indicates that a large portion of solute mass is transported along the high velocity (or high flux) layers in the middle ($z=0$) of the plates. The tail indicates that a portion of the solute mass transported in the low velocity layers next to the plate walls.

The second time scale for solute transport through a set of plates occurs when Pe_M is much lower than unity, which indicates that transverse diffusion is significant and effectively mixes the solute across the fracture aperture. This transverse mixing introduces dispersion in the longitudinal direction as the solute moves to different fluid layers within the parabolic velocity distribution between the plate. Therefore, the bulk transport may be described by the traditional one-dimensional advection-dispersion equation, given as

$$\frac{\partial c}{\partial t} + U \frac{\partial c}{\partial x} - D_e \frac{\partial^2 c}{\partial x^2} = 0 \quad (3.35)$$

where x -axis defines the longitudinal direction, and D_e is the effective longitudinal dispersion coefficient, which has been determined analytically for parallel plates by *Aris [1956]* as

$$D_e = D_m + \frac{U^2 b^2}{210 D_m} \quad (3.36)$$

where D_m is the molecular diffusion coefficient, and the second term on the RHS is often referred to the Taylor dispersion term. Equation (3.36) shows that D_e is analogous to the hydrodynamic dispersion coefficient used in one-dimensional transport through porous media, given as

$$D_e = D_m + \alpha U, \quad (3.37)$$

where α is the dispersivity of the medium. Both (3.36) and (3.37) have a diffusion component and a mixing component that depends on velocity. The effective dispersion coefficient may be used to redefine (3.16) as

$$Pe^* = \frac{L U}{D_e} = \frac{L Q}{W \langle b \rangle D_e}, \quad (3.38)$$

which describes the strength of advection to the effective dispersion across the length of the fracture. The analytical solution of (3.35) for parallel plates of finite length with no solute initially present within the fracture, constant solute injection at the inlet boundary, and no concentration gradient at the outlet boundary, is given by *van Genuchten and Alves [1982]*. This solution is displayed in Figure 3.5 for several values of Pe and Pe_M (the values of Pe^* given by (3.38) are also shown), and clearly display classical Fickian or Gaussian s -shaped breakthrough curves. In contrast to the curve with no mixing ($Pe_M = \infty$), these curves have gradual transitions at both the head and tail of the curves, and have larger median arrival times.

Rough-Walled Fractures

Empirical studies of fluid flow and solute transport through rough-walled fractures have clearly demonstrated that the bulk of flow and transport occurs along tortuous channels. This property has led to the development of the channel model for solute transport through single fractures. According to this model, the solute travels by advection along independent channels from the fracture inlet to the outlet. These channels behave as ducts with equal lengths and widths, but have different apertures that may vary along the channel length. This channel model is attractive because the advective transport along each channel is simulated as one-dimensional plug-flow, and the bulk transport is simply described by summing the independent contributions of each channel. This approach is analogous to the one used to develop (3.30) and (3.33), and results in equations that are easy to invert or fit to measured laboratory data. *Neretnieks et al.* [1982] used the channel model with lognormally distributed apertures that persisted along the channel lengths to simulate the breakthrough of conservative tracers through a rough-walled fracture. This channel model reproduced the general shape of the observed breakthrough curves, but could not reproduce the stair-step behaviour. Interestingly, the value of Pe_M for the experimental data may be estimated to range from 0.001 to 0.01, which suggests that mixing across the fracture should have smoothed out the observed stair-step features. *Tsang and Tsang* [1987] used the channel model with lognormally distributed apertures that varied along the length of the channels, and found that the model could reproduce the steep initial rise, long tailing, and stair-step features observed in experimental work of *Moreno et al.* [1985] (see Figure 3.1). The value of Pe_M for these experimental data may be estimated to range from 6 to 19.

An alternative to the channel model is to simulate transport through the entire void space of a rough-walled fracture. *Moreno et al.* [1988] randomly generated planar aperture fields that were lognormally distributed with a spatial correlation structure given by the exponential autocorrelation function. The fluid flow field was simulated using the LCL, and advective transport was simulated using particle tracking through the two-dimensional flow field. These high Pe_M simulations confirmed the presence of dominant flow and transport channels across the fractures, and produced particle breakthrough curves with steep rise, long tailing, and subtle stair-step features. *Thomson and Brown* [1991] simulated flow and transport through two-dimensional aperture fields formed by the method of *Brown* [1987]. Fluid flow was simulated with the LCL and solute transport simulations used a modified form of the two-dimensional advection-diffusion equation used in porous media. The solute concentration breakthrough curve for an isotropic aperture field displayed a fairly steep rise and long tail, but was smoother than the diffusion-free particle tracking method and did not exhibit stair-step features. The value of Pe_M for the simulation may be estimated to be on the order of 0.001. *Meakin et al.* [1998] examined three-dimensional fluid flow and solute transport through a fracture formed by mating random surfaces with fractal correlation. Fluid flow was simulated using the Stokes equations and solute transport

was simulated using the advection-diffusion equation (3.14). Shaded contour plots showed that a transport simulations with low Pe produced homogeneous plumes with smooth fronts, whereas simulations with high Pe produced heterogeneous or channelled plumes with sharp fronts. Finally, *James and Chrysikopoulos* [2000] examined three-dimensional transport of variable diameter colloids through parallel plates and rough-walled fractures using the RWPM under low Pe_M conditions. Fluid flow was simulated using a quasi-three-dimensional approach: the LCL was used to simulate the average two-dimensional velocity field, and then a parabolic velocity distribution (e.g., see (3.28) and (3.29)) was assigned across each local aperture region. The colloid breakthrough curves displayed the traditional s -shaped Gaussian characteristics (see Figure 3.5); however, the median arrival time and tailing significantly increased as the aperture variability increased. This increased spreading of the colloid plume was attributed to the increased heterogeneity in the flow field caused by the aperture variability.

In summary, solute transport through a single rough-walled fracture occurs primarily along tortuous channels. For conditions where there is low degree of mixing across the fracture aperture (i.e., high values of Pe_M) the channels cause the breakthrough curves to exhibit a sudden and steep initial rise, intermediate stair-step features, and long tailing. Conversely, the breakthrough curves for conditions where there is appreciable mixing across the fracture aperture (i.e., low values of Pe_M) tend to resemble more traditional Gaussian s -shaped curves with long tails. These characteristics have been observed in laboratory experiments and numerical simulations using one-dimensional channel models, two-dimensional variable aperture models, and three-dimensional fracture models.

Table 3.1 Summary of constraints for the LCL

source	geometric constraint	kinematic constraint
<i>Brown</i> [1987]	$\sigma_w / \lambda_w < 0.02$	—
<i>Zimmerman et al.</i> [1991] ^a	$\sigma_b / \lambda_b < 0.2$	—
<i>Zimmerman and Bodvarsson</i> [1996] ^a	$\langle b \rangle / \lambda_b < 0.39$	$Re < 1$
<i>Oron and Berkowitz</i> [1998]	$\sigma_w / b_m \ll 1$	$Re \sigma_w / b_m \ll 1$
<i>Zimmerman and Yeo</i> [1998]	$\langle b \rangle / \lambda_b < 0.3$	$Re \langle b \rangle / \lambda_b < 8$

^a λ_b was originally defined as the wavelength of a sinusoid A

Table 3.2. Summary of various studies that measured and predicted fluid flow through single rough-walled fractures.

source	flow experiment and fracture type [dimensions in mm]	aperture measurements [mm]	fraction of contact, c [%]	Reynolds number, Re [-]	predicted flow equation	flow ratio Q_{calc}/Q_{obs} [-]
<i>Iwai [1976]; Witherspoon et al. [1980]</i>	linear (121 × 207) and radial (128) flow through induced granite, basalt and marble fractures	b_M 0.004 - 0.250	0.1 - 35	0.015 - 150	CL	1.04 - 1.65
<i>Raven and Gale [1985]</i>	radial (100-294) flow through natural granite fractures	b_M 0.010 - 0.100			CL	1 - 10
<i>Schrauf and Evans [1986]</i>	linear (282 × 254) and radial (~114) air flow through a natural granite fracture	b_V 0.200 - 0.600	<10	1.8 - 255	CL	3.9 - 15
<i>Hakami and Barton [1990]</i>	linear (59-159 × 148-208) water flow through transparent replicas of natural leucite, quartz monzonite, and granite fractures	$\langle b \rangle$ 0.161 - 0.462 σ_b 0.075 - 0.273	0	—	CL	1.3 - 5
<i>Durham and Bonner [1994]</i>	linear (136 × 142) flow through induced well-mated and offset granite fractures	b_m 0.008 - 0.600	0 - 100	—	CL	1 - >100
<i>Keller et al. [1995]</i>	linear (52 × 100) flow through a natural granite fracture	$\langle \ln b \rangle$ 0.38 $\sigma_{\ln b}$ 1.6	—	0.04 - 0.9	CL [†]	0.87
<i>Hakami and Larsson [1996]</i>	linear (190 × 410) flow through a natural granite fracture	$\langle b \rangle$ 0.360 σ_b 0.150	<5	61	LCL	2.4
<i>Yeo et al. [1998]</i>	linear (200 × 200) and radial (~94) water flow through a natural granite fracture	$\langle b \rangle$ 0.607 - 1.024 σ_b 0.160 - 0.332	<0.1	9 - 30	LCL	1.3 - 2
<i>Nicholl et al. [1999]</i>	linear (148 × 302) water flow through glass fracture analog	$\langle b \rangle$ 0.226 σ_b 0.062	0	0.063 - 4.3	LCL	1.2 - 1.3

Notes: see Sections 2.2 and 2.3 for aperture definitions; CL = cubic law; LCL = local cubic law; [†]calculation used geometric mean of $b(x,y)$ ³

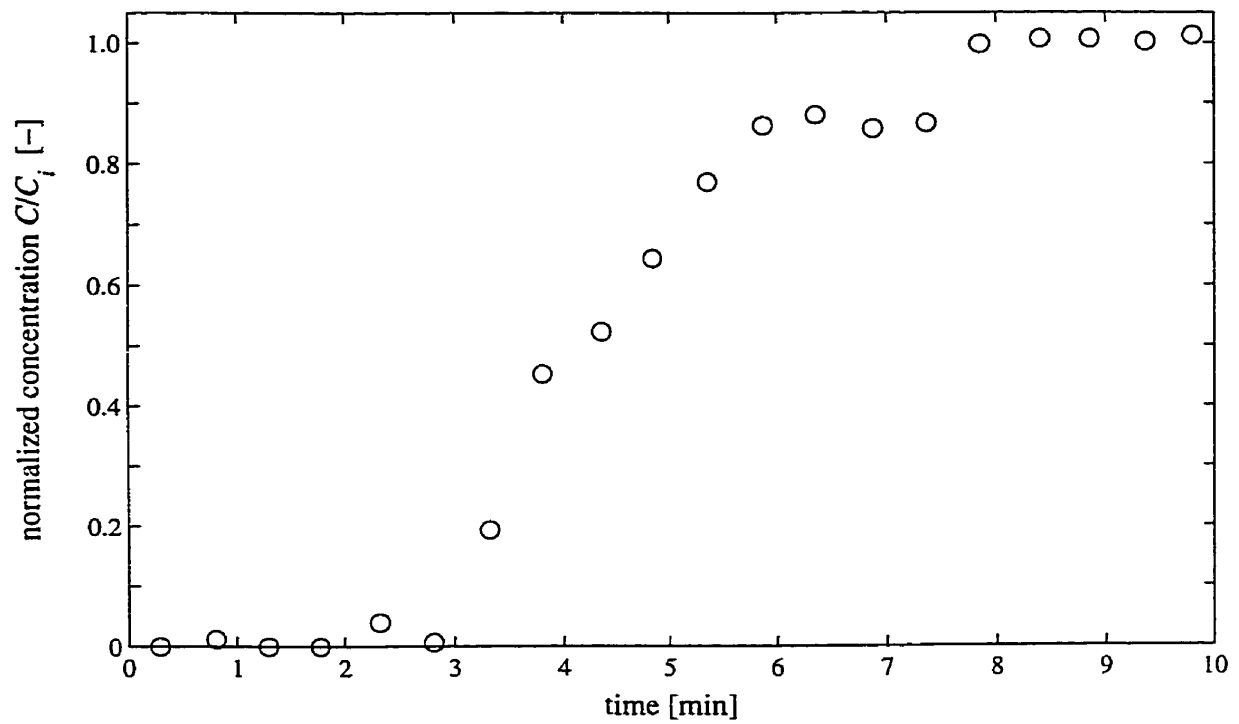


Figure 3.1. Breakthrough curve (normalized concentration C/C_i versus time) of a conservative tracer through a single rough-walled fracture. Laboratory data extracted from *Moreno et al.* [1985]. The fracture length and width were 185 and 100 mm. The mean aperture and Péclet number were estimated to be 0.14 mm and 14, respectively.

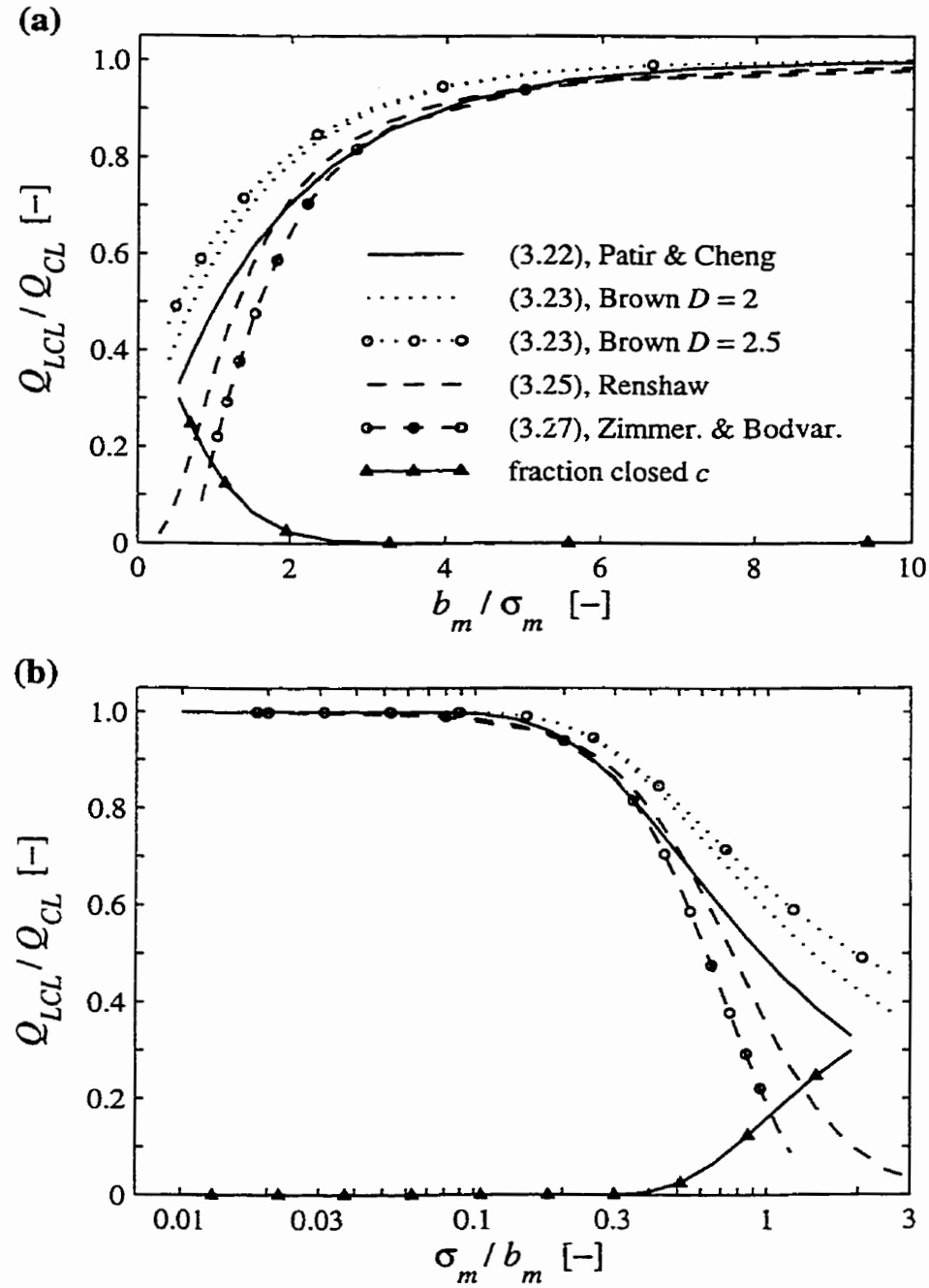


Figure 3.2. The total flow rate from LCL simulations Q_{LCL} compared to the cubic law Q_{CL} using (a) relative smoothness b_m/σ_m , (b) and relative roughness σ_m/b_m . The legend refers to both (a) and (b), and gives the equation number for each curve.

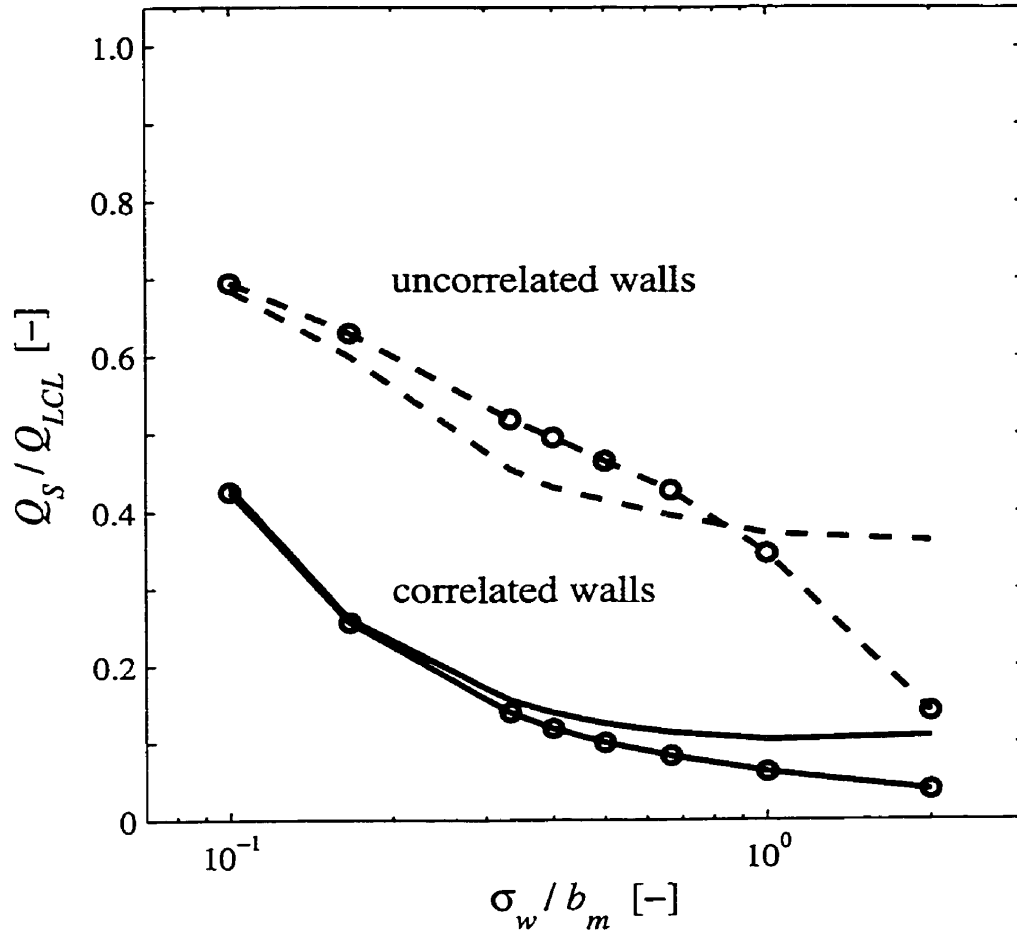


Figure 3.3. The total flow rate from Stokes simulations Q_S compared to LCL simulations Q_{LCL} for various values of relative roughness σ_w / b_m from Mourzenko *et al.* [1995]. The dashed lines correspond to fractures with uncorrelated walls, and the solid lines correspond to correlated walls. The lines without symbols represent fracture walls with $\sigma_w / \lambda_w = 1/3$, and the lines with symbols represent walls with $\sigma_w / \lambda_w = 1$. Note that σ_w and λ_w are the standard deviation and correlation length of the wall roughness (where $\sigma_w = \sigma_U = \sigma_L$ and $\lambda_w = \lambda_U = \lambda_L$).

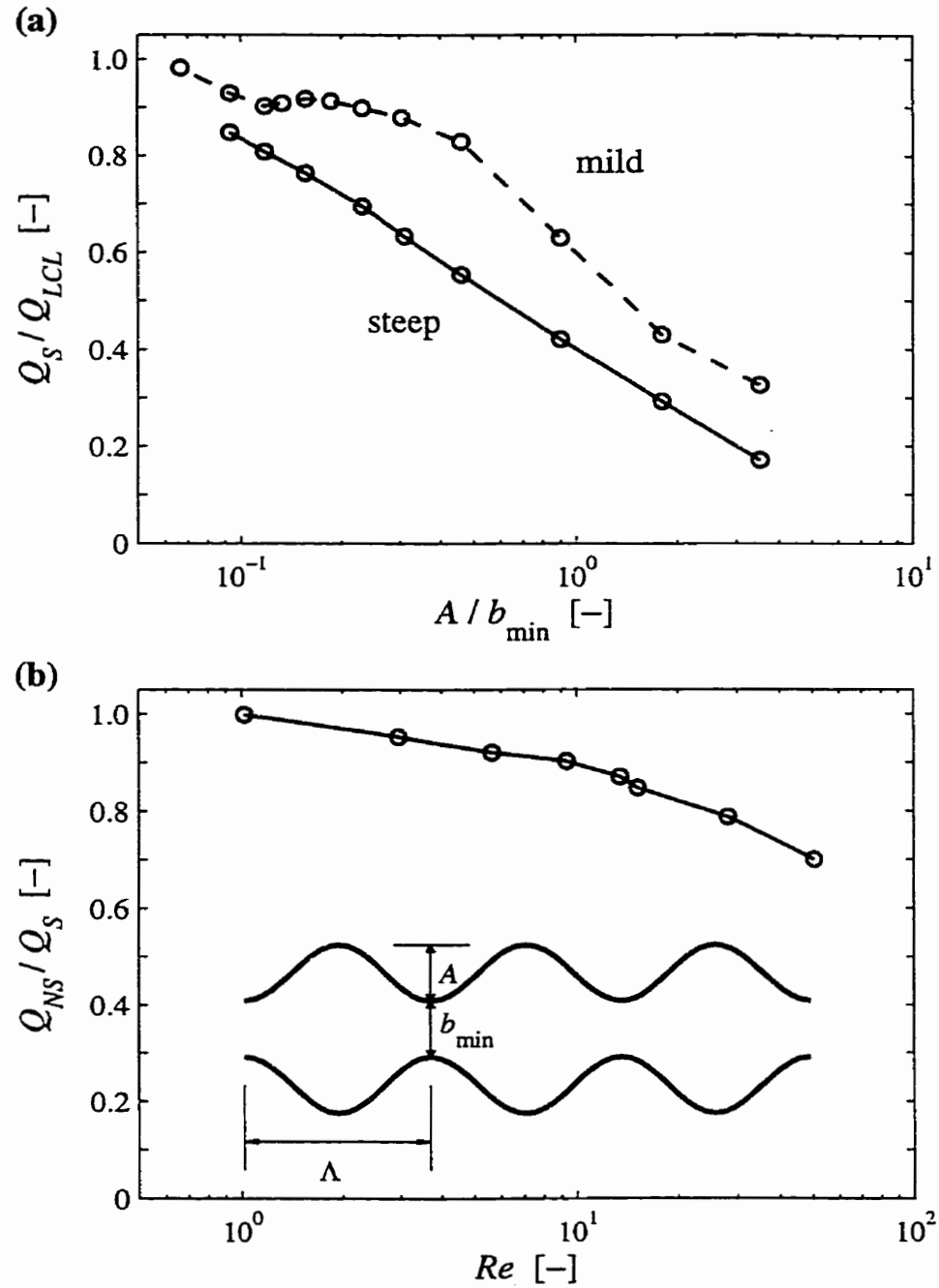


Figure 3.4. Results of various simulations through sinusoidal fracture profiles (see schematic in part (b)) from *Brown et al.* [1995]. (a) The total flow rate from Stokes simulations Q_S compared to the LCL Q_{LCL} for various values of relative roughness A / b_{\min} . The dashed line represents profiles with mild slopes ($A/\Lambda = 0.11$), and the solid line represents profiles with steep slopes ($A/\Lambda = 0.43$). (b) The total flow rate from Navier-Stokes simulations Q_{NS} compared to Stokes Q_S for various values of Reynolds number Re . These simulations used steeply sloped profiles ($A/\Lambda = 0.43$).

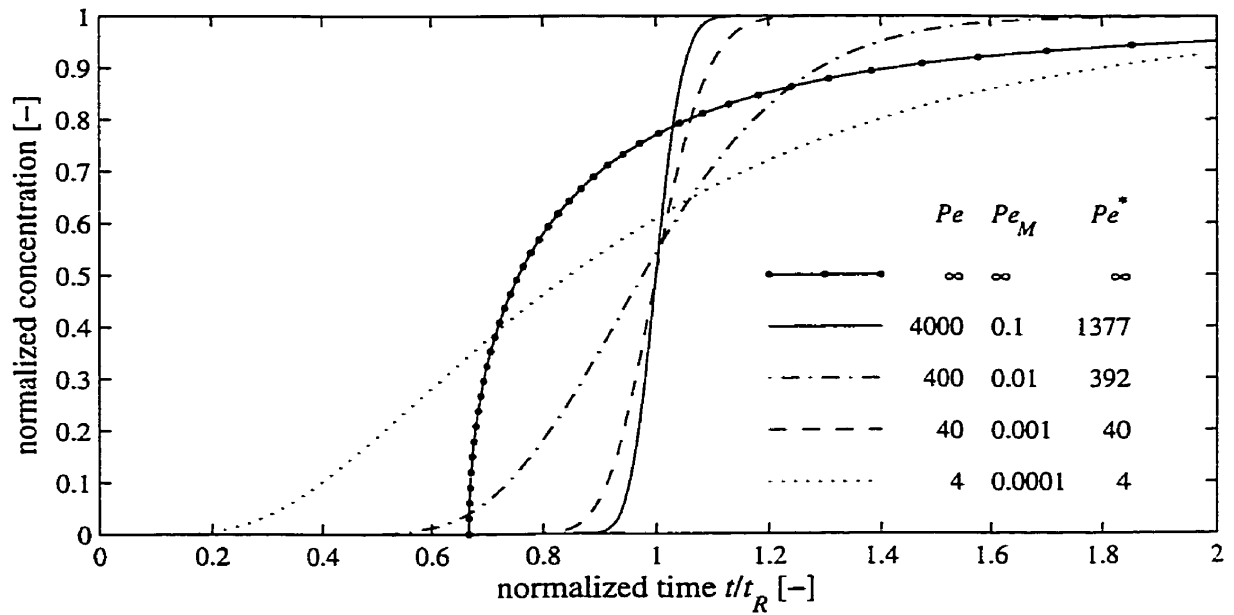


Figure 3.5. Dimensionless breakthrough curves of solute transport through a set of parallel plates for various values of Péclet numbers: Pe , Pe_M , and Pe^* (see text for description). Concentration C is normalized by the inlet concentration C_i , and time t is normalized by the hydraulic residence or plug-flow travel time t_R .

CHAPTER 4. Development of Fluid Flow and Solute Transport Models

4.1 Introduction

The formulation of two- and three-dimensional models for predicting fluid flow and solute transport through rough-walled fractures are presented in this chapter. The flow models employ the Finite Volume (FV) method to approximate the governing differential equations over the fracture void space or domain. The model domains are formed by subdividing the fracture void space into a structured grid of closed two-dimensional polygons or three-dimensional prisms which are called Control Volumes (CVs). The FV method integrates the governing differential equations over each CV, and transforms the resulting volume integrals of flux terms into surface integrals by applying Gauss' divergence theorem. Furthermore, the method specifies that all flux terms must be consistent across neighbouring CVs. In other words, all terms defined at a CV surface must be equivalent for both of the CVs sharing that surface. This property ensures that the FV method is inherently conservative over each single CV, and additionally over the sum of all the CVs in the domain.

The three-dimensional flow model solves the steady-state incompressible Navier-Stokes equations and is presented in Section 4.3. This model features a structured non-orthogonal CV grid with co-location of the primary variables (velocity and pressure) at the cell-centre of the CVs and is largely based on the work of *Ferziger and Perić* [1999]. The two-dimensional flow model solves the local cubic law or Reynolds equation and is presented in Section 4.4. This model features a traditional structured orthogonal CV grid with a single primary variable (pressure) located at the cell-centre of the CVs.

This chapter also presents the formulation of a three-dimensional model for solute transport through rough-walled fractures (Section 4.5). The model is based on the random walk particle method (RWPM) and uses the velocity field determined by the three-dimensional flow model. The RWPM simulates advective transport by tracking particles through the fracture velocity field and diffusive transport by randomly displacing the particles. This model uses the same CV grid as the three-dimensional flow model, but interpolates the velocity field to the CV vertices.

The next section (Section 4.2) discusses the discretization of the fracture void space for the flow and solute transport models.

4.2 Discretization of Fracture Void Space

Section 2.5.1 described the methodology employed in this work to generate random three-dimensional fractures. The fracture void space is represented as two-dimensional fields of aperture and mid-surface elevation that are defined over $N_x \times N_y$ uniformly spaced grid points. The two-dimensional grid is defined parallel to the x - y plane, and the aperture and mid-surface elevation fields are defined perpendicular to the x - y plane. Figure 4.1(a) presents an example of the synthetic fracture generated on a 11×11 grid. A consequence of creating the fracture over the uniform planar grid is that the dimensions Δ_x and Δ_y of the local voids formed between the grid points are constant, whereas $b(x,y)$ and $Z(x,y)$ vary at each grid point location. This variability along the z -axis causes the geometry of the local voids to be non-orthogonal.

In order to simulate three-dimensional fluid flow and solute transport through the synthetic or real fractures the void space was subdivided or discretized into $n_i \times n_j \times n_k$ non-orthogonal CVs. Figure 4.1(b) presents an example of a three-dimensional CV grid formed by discretizing the fracture void space shown in Figure 4.1(a). Globally, the i - and j -directions of the CVs correspond to the x - and y -axes, however, locally the i - and j -directions are generally non-parallel to the x - and y -axes. The values of n_i and n_j are defined as $(N_x - 1)n_{sub}$ and $(N_y - 1)n_{sub}$ where n_{sub} is the number of subdivisions in the original x - y grid. The k -direction is defined parallel to the z -axis since the aperture and elevation fields are defined perpendicular to the x - y plane. The resulting dimensions δ_x , δ_y , and δ_z of the CVs are given as Δ_x/n_{sub} , Δ_y/n_{sub} , and $b(x,y)/n_k$, respectively. Section 4.3.1 provides a detailed discussion of the 3D CVs used in fluid flow simulations and Section 4.5.1 describes the 3D CVs used for solute transport simulations.

For the two-dimensional fluid flow simulations the three-dimensional void space was discretized into $n_i \times n_j$ orthogonal CVs where the i - and j -directions correspond to the x - and y -axes. Figure 4.1(c) shows an example of a the two-dimensional CV grid formed by discretizing the fracture void space shown in Figure 4.1(a). As in the three-dimensional discretization, the values of n_i and n_j are defined as $(N_x - 1)n_{sub}$ and $(N_y - 1)n_{sub}$ resulting in CV dimensions δ_x , δ_y given by Δ_x/n_{sub} and Δ_y/n_{sub} .

4.3 Three-Dimensional Flow Model Based on the Navier-Stokes Equations

4.3.1 Description of the Three-Dimensional Control Volume

A useful starting point in the development of the three-dimensional flow model is a detailed description of a typical three-dimensional CV used in this work. Figure 4.2 shows a typical CV from the interior of a discretized fracture domain (see Figure 4.1(b)). The CV is a hexahedron which has six sides or faces and is defined by the Cartesian coordinates of its eight corners. This hexahedral CV has constant dimensions along the x - and y -axes (δ_x and δ_y) and variable dimensions along z -axis (δ_z). These dimensions are a consequence of subdividing the original fracture void space which has uniform spacing in the x - y plane and variable spacing along the z -axis. Since the values of δ_x and δ_y are constant, the volume of the CV indexed as P may be estimated using mid-point integration as

$$V_P = \int_V dV = \int_z \delta_x \delta_y dz \approx \delta_x \delta_y (z_t - z_b) , \quad (4.1)$$

where z_t and z_b are the elevation values at centre or integration points of the top and bottom faces. The computational node or cell-centre of the CV is defined as

$$\mathbf{r}_P = \frac{1}{8} \sum_{c=1}^8 \mathbf{r}_c , \quad (4.2)$$

which is the mean position of the eight CV corners where \mathbf{r}_P and \mathbf{r}_c are Cartesian position vectors of the CV node and CV corners. Also shown are the nodes of the neighbouring CVs that share faces with the CV of interest. These nodes are indexed relative to the central node P using the following local directions: east, west, north, south, top, and bottom [Pantankar, 1980]. The neighbouring nodes in each of these local directions are represented with the upper case symbols: E , W , N , S , T , and B . As shown in Figure 4.2, the local directions are simply defined by connecting each neighbouring node to the node P . East and west correspond to the positive and negative i -directions, north and south correspond to the positive and negative j -directions, and finally top and bottom correspond to the positive and negative k -directions.

The compass method is also used to index the centres or integration points of CV faces. The integration points on faces in each local direction are represented by the lower case symbols: e , w , n , s , t , and b . Figure 4.3(a) shows a more detailed view of the east-face taken from the CV in Figure 4.2. The surface of the face is defined by bi-linear interpolation of the four corners coordinates, and consequently, the position of the integration point is defined as the mean position of the four corners, or

$$\mathbf{r}_e = \frac{1}{4} \sum_{c=1}^4 \mathbf{r}_c , \quad (4.3)$$

where \mathbf{r}_e is the position vector of the integration point on the east-face. Two local vectors may be defined tangential to the bi-linear surface of the east-face as

$$\chi_e = \frac{1}{2}(\mathbf{r}_2 + \mathbf{r}_3 - \mathbf{r}_4 - \mathbf{r}_1), \quad (4.4a)$$

$$\zeta_e = \frac{1}{2}(\mathbf{r}_3 + \mathbf{r}_4 - \mathbf{r}_1 - \mathbf{r}_2), \quad (4.4b)$$

where the four corners are indexed with the right-hand convention as shown in Figure 4.3(a).

These two local surface vectors intersect at point e and may be used to approximate the normal surface area vector of the face as

$$\mathbf{S}_e = \chi_e \times \zeta_e, \quad (4.5)$$

which is defined using the positive outward sign convention. Given this approximation for \mathbf{S}_e , the unit outward normal of the face may be defined as

$$\hat{\mathbf{n}}_e = \frac{\mathbf{S}_e}{|\mathbf{S}_e|} = \frac{\mathbf{S}_e}{S_e}. \quad (4.6)$$

A local vector along the east-direction may be defined by connecting the nodes on either side of the east-face as

$$\xi_e = \mathbf{r}_E - \mathbf{r}_P, \quad (4.7)$$

where the point of intersection between the vector and face is defined as point e' , and a corresponding unit vector may be defined as

$$\hat{\xi}_e = \frac{\xi_e}{|\xi_e|}. \quad (4.8)$$

For the CV grid used in this work, the position of e' was determined using

$$\mathbf{r}_{e'} = \mathbf{r}_P + \frac{1}{2}\xi_e = \frac{1}{2}(\mathbf{r}_E + \mathbf{r}_P), \quad (4.9)$$

which is simply the mid-point of ξ_e and is a consequence of the method used to define and discretize the fracture void space.

Figure 4.3(b) shows that an addition local vector may be defined across the east-face as

$$\eta_e = \mathbf{r}_{E'} - \mathbf{r}_{P'}, \quad (4.10)$$

which is parallel to $\hat{\mathbf{n}}_e$ and passes through the integration point e . The location of points P' and E' are given by [Ferziger and Perić, 1999]

$$\mathbf{r}_{P'} = \mathbf{r}_e - [(\mathbf{r}_e - \mathbf{r}_P) \cdot \hat{\mathbf{n}}_e] \hat{\mathbf{n}}_e, \quad (4.11a)$$

$$\mathbf{r}_{E'} = \mathbf{r}_e - [(\mathbf{r}_e - \mathbf{r}_E) \cdot \hat{\mathbf{n}}_e] \hat{\mathbf{n}}_e, \quad (4.11b)$$

which define the intersection of the normal line passing through point e with two planes that are also normal to the line (or parallel to the face) and contain nodes P and E , respectively. As shown in Figure 4.3(b), normal lines may be projected from the face corners onto the planes passing

through nodes P' and E' to define a CV that is orthogonal to the east-face. Using mid-point integration the volume of this interfacial CV may be given as

$$V_e = \int_V dV = \int_n S_e dn \approx S_e |\boldsymbol{\eta}_e| . \quad (4.12)$$

The points P' and E' , and volume V_e are used to calculate gradients and mass fluxes normal to the CV face.

Equations (4.3) to (4.12) are defined using the east-face of the CV shown in Figure 4.3; however, these equations may be easily adapted for each of the remaining CV faces. For a general CV face f and adjacent CV node F , (4.3) to (4.12) may be generalized by replacing the indices e , e' , and E with f , f' , and F .

Interface Interpolation

The value of a generic variable ϕ may be defined at the integration point of a general CV face f as [Ferziger and Perić, 1999]

$$\phi_f = \phi_{f'} + \nabla \phi_{f'}^o \cdot (\mathbf{r}_f - \mathbf{r}_{f'}) , \quad (4.13)$$

where $\phi_{f'}$ is the value of ϕ at point f' and $\nabla \phi_{f'}^o$ is the *lagged* gradient of ϕ at point f' . The value and gradient of $\phi_{f'}$ are interpolated between the nodes P and F as

$$\phi_{f'} = w_P \phi_P + w_F \phi_F , \quad (4.14a)$$

$$\nabla \phi_{f'}^o = w_P \nabla \phi_P^o + w_F \nabla \phi_F^o , \quad (4.14b)$$

where w_P and w_F are linear weights of interpolation given by

$$w_P = \frac{|\mathbf{r}_F - \mathbf{r}_{f'}|}{|\mathbf{r}_F - \mathbf{r}_P|} = \frac{1}{2} , \quad w_F = \frac{|\mathbf{r}_{f'} - \mathbf{r}_P|}{|\mathbf{r}_F - \mathbf{r}_P|} = \frac{1}{2} . \quad (4.15)$$

The numerical values for the CV grid used in this work are shown in (4.15), and predict that the interface value is the mid-point or arithmetic average of nodes P and F . For this general condition, (4.13) may be expanded as

$$\phi_f = \frac{1}{2} (\phi_P + \phi_F) + \frac{1}{2} (\nabla \phi_P^o + \nabla \phi_F^o) \cdot (\mathbf{r}_f - \mathbf{r}_{f'}) . \quad (4.16)$$

Equations (4.13) and (4.16) simply interpolate between ϕ_P and ϕ_F , and add a lagged correction term based on the interpolated nodal gradient. Note that if the point f' coincides with the integration point f the correction term vanishes.

Nodal Gradients

The gradient of a generic variable ϕ defined at the CV node P may be expanded as

$$\nabla \phi_P = \left(\frac{\partial \phi}{\partial x}, \frac{\partial \phi}{\partial y}, \frac{\partial \phi}{\partial z} \right)_P, \quad (4.17)$$

where each Cartesian component may be estimated using a volume average given by

$$\left. \frac{\partial \phi}{\partial x_i} \right|_P = \frac{1}{V_P} \int_V \frac{\partial \phi}{\partial x_i} dV, \quad (4.18)$$

where V_P is the volume of the CV. The volume integral in (4.18) may be transformed into a surface integral using Gauss' divergence theorem as [Ferziger and Perić, 1999]

$$\left. \frac{\partial \phi}{\partial x_i} \right|_P = \frac{1}{V_P} \int_S \phi \hat{x}_i \cdot \hat{n} dS, \quad (4.19)$$

where S is the surface of the CV, \hat{x}_i is the Cartesian direction vector, and \hat{n} is the outward unit normal vector to the surface. Given that the CV is comprised of a number of discrete faces, (4.19) may be approximated as

$$\left. \frac{\partial \phi}{\partial x_i} \right|_P = \frac{1}{V_P} \sum_f \phi_f S_{i,f}, \quad (4.20)$$

where ϕ_f is the interpolated value of ϕ on each face f , and $S_{i,f}$ is the Cartesian component of the outward surface area vector. Finally, (4.13) may be substituted into (4.20) yielding

$$\left. \frac{\partial \phi}{\partial x_i} \right|_P \approx \frac{1}{V_P} \sum_f \left[\phi_{f'} + \nabla \phi_{f'}^o \cdot (\mathbf{r}_f - \mathbf{r}_{f'}) \right] S_{i,f}. \quad (4.21)$$

Examination of (4.21) shows that the nodal gradient is dependent on the lagged or old nodal gradient field. This dependency may be removed by zeroing the old gradient field and iteratively solving the current gradient field according to [Ferziger and Perić, 1999]

$$\left. \frac{\partial \phi}{\partial x_i} \right|_P^m \approx \frac{1}{V_P} \sum_f \left[\phi_{f'}^m + \nabla \phi_{f'}^{m-1} \cdot (\mathbf{r}_f - \mathbf{r}_{f'}) \right] S_{i,f}, \quad (4.22)$$

where m refers to the iteration number. In this work (4.21) is used to calculate the gradient of the primary variables (velocity and pressure) and (4.22) (with $m = 2$) is used to calculate the gradient of the pressure correction.

Normal Interfacial Gradients

The gradient of a generic variable normal to a CV face may be approximated using the *central difference scheme* (CDS) between the points F' and P' (see Figure 4.3) as [Ferziger and Perić, 1999]

$$\left. \frac{\partial \phi}{\partial n} \right|_f \approx \frac{\phi_{F'} - \phi_{P'}}{|\mathbf{r}_{F'} - \mathbf{r}_{P'}|} = \frac{\phi_{F'} - \phi_{P'}}{(\mathbf{r}_F - \mathbf{r}_P) \cdot \hat{\mathbf{n}}_f}, \quad (4.23)$$

where the values of ϕ at the points P' and F' are interpolated from the nodal values with

$$\phi_{P'} = \phi_P + \nabla \phi_P^o \cdot (\mathbf{r}_{P'} - \mathbf{r}_P), \quad (4.24a)$$

$$\phi_{F'} = \phi_F + \nabla \phi_F^o \cdot (\mathbf{r}_{F'} - \mathbf{r}_F), \quad (4.24b)$$

where the position vectors of P' and F' are given by (4.11). Finally, (4.24) may be substituted into (4.23) to yield

$$\left. \frac{\partial \phi}{\partial n} \right|_f \approx \frac{\phi_F - \phi_P}{(\mathbf{r}_F - \mathbf{r}_P) \cdot \hat{\mathbf{n}}_f} + \frac{\nabla \phi_F^o \cdot (\mathbf{r}_{F'} - \mathbf{r}_F) - \nabla \phi_P^o \cdot (\mathbf{r}_{P'} - \mathbf{r}_P)}{(\mathbf{r}_F - \mathbf{r}_P) \cdot \hat{\mathbf{n}}_f}, \quad (4.25)$$

where the first term represents the implicit part of the gradient and the second represents the explicit part. The second term may be considered as a non-orthogonal correction factor that disappears when the vectors ξ_f and η_f coincide.

4.3.2 Approximation of the Mass Conservation Equation

The mass conservation equation (3.2) may be integrated over an arbitrary CV as

$$\int_V \rho \nabla \cdot \mathbf{u} \, dV = 0, \quad (4.26)$$

or alternatively, as

$$\int_S \rho \mathbf{u} \cdot \hat{\mathbf{n}} \, dS = 0, \quad (4.27)$$

where the volume integral in (4.26) is transformed into a surface integral using Gauss' divergence theorem. This surface integral represents the divergence of mass flux over the CV by summing the normal mass flux to the CV surface. Given that a CV is comprised of a number of discrete faces, (4.27) may be approximated as

$$\sum_f \dot{m}_f = 0, \quad (4.28)$$

where \dot{m}_f is the mass flux normal to each face f . For the hexahedral CVs used in this work, (4.28) may be expanded by setting f equal to e , n , t , w , s , and b , and noting that the outward normal sign convention is used so that positive terms are mass fluxes in the direction of the outward normal of the face. Or in other words, positive mass fluxes are outflows from the CV and negative mass

fluxes are inflows. In this work, the normal mass flux is defined using mid-point integration of the velocity normal to the CV face, which may be given for a general face f as

$$\dot{m}_f = \rho \mathbf{u}_f \cdot \mathbf{S}_f = \sum_i \rho u_{i,f} S_{i,f} , \quad (4.29)$$

where $i = (1, 2, 3)$ or (x, y, z) , \mathbf{S}_f is the outward normal surface area vector with Cartesian components $S_{i,f}$, and \mathbf{u}_f is the interface velocity vector with Cartesian components $u_{i,f}$ which are interpolated using (4.13). Finally, (4.28) and (4.29) may be combined as

$$\sum_f \sum_i \rho u_{i,f} S_{i,f} = 0 , \quad (4.30)$$

which is the discrete FV approximation of the mass conservation equation. Note however, that since the NS equations (i.e., both mass and momentum conservation) are being solved on a co-located grid, (4.29) will be altered in Section 4.3.3 to suppress oscillations in the velocity and pressure fields.

4.3.3 Approximation of the Momentum Conservation Equation

The momentum conservation equation (3.1) may be written in summation notation and integrated over an arbitrary CV as

$$\int_V \rho \mathbf{u} \cdot \nabla u_i \, dV - \int_V \mu \nabla^2 u_i \, dV + \int_V \nabla p \cdot \hat{\mathbf{x}}_i \, dV = 0 , \quad (4.31)$$

which represents three equations conserving momentum in each Cartesian direction ($i = 1, 2, 3$). The first term in (4.31) represents the inertial forces acting over the CV, the second term viscous forces and the third pressure forces. Once again, Gauss' divergence theorem may be used to transform these volume integrals into surface integrals, resulting in

$$\int_S \rho u_i \mathbf{u} \cdot \hat{\mathbf{n}} \, dS - \int_S \mu \nabla u_i \cdot \hat{\mathbf{n}} \, dS + \int_S p \hat{\mathbf{x}}_i \cdot \hat{\mathbf{n}} \, dS = 0 , \quad (4.32)$$

which may be approximated over a discrete CV as

$$\sum_f F_{i,f}^a + \sum_f F_{i,f}^d + \sum_f F_{i,f}^p = 0 , \quad (4.33a)$$

$$F_{i,P}^a + F_{i,P}^d + F_{i,P}^p = 0 , \quad (4.33b)$$

where $F_{i,f}^a$, and $F_{i,f}^d$ are the Cartesian components of the advective and diffusive momentum fluxes crossing normal to the f face, and $F_{i,f}^p$ is the Cartesian component of the pressure force acting on the f face. Equation (4.33b) shows that the sum of these surface forces may also be expressed as $F_{i,P}^a$, $F_{i,P}^d$, and $F_{i,P}^p$ which are the Cartesian components of the advective or inertial force, the diffusive or viscous force, and the pressure force acting on the CV P . For the hexahedral CVs used in this work, each term in (4.33) may be expanded by setting f equal to e , n , t , w , s , and b , and noting that the outward normal sign convention is used so that positive terms are momentum fluxes or pressure forces in the direction of the outward normal of the face. The formulation use for each

of these terms is presented below.

Advection Term

The advection term for a general CV face is approximated as

$$F_{i,f}^a = \dot{m}_f u_{i,f}^a, \quad (4.34)$$

where $u_{i,f}^a$ is the *advected* Cartesian component of the velocity vector crossing the face. Although the mass flux does not carry the superscript o , it is defined using the previous or lagged velocity field in order to linearize this advection term. The advected velocity component is approximated as

$$u_{i,f}^a = \begin{cases} u_{i,P} & \text{if } \dot{m}_f > 0 \\ u_{i,F} & \text{if } \dot{m}_f < 0 \end{cases}, \quad (4.35)$$

which is the *upstream difference scheme* (UDS). The UDS is known to be very stable at the expense of introducing numerical diffusion into the solution. Substituting (4.35) into (4.34) yields the final form of the advection term as

$$F_{i,f}^a = \max(\dot{m}_f, 0) u_{i,P} + \min(\dot{m}_f, 0) u_{i,F}. \quad (4.36)$$

This work employed the UDS after attempts of using a higher order blended scheme proposed by [Ferziger and Perić, 1999] resulted in oscillatory solutions for the fracture systems investigated.

Diffusion Term

The diffusion term for a general CV face f is defined as

$$F_{i,f}^d = -\mu S_f \left. \frac{\partial u_i}{\partial n} \right|_f, \quad (4.37)$$

which may be approximated using (4.25) as

$$F_{i,f}^d \approx -\mu S_f \left[\frac{u_{i,F} - u_{i,P}}{(\mathbf{r}_F - \mathbf{r}_P) \cdot \hat{\mathbf{n}}_f} + \frac{\nabla u_{i,F}^o \cdot (\mathbf{r}_F - \mathbf{r}_F) - \nabla u_{i,P}^o \cdot (\mathbf{r}_P - \mathbf{r}_P)}{(\mathbf{r}_F - \mathbf{r}_P) \cdot \hat{\mathbf{n}}_f} \right]. \quad (4.38)$$

Note that the first term in the brackets is the implicit part of the gradient and the second term is the explicit part.

Pressure Term

The pressure term for a general CV face is approximated as

$$F_{i,f}^p = p_f S_{i,f} , \quad (4.39)$$

where p_f is the interfacial pressure interpolated using (4.13). Note that the total pressure force acting on the CV P is given by the sum shown in (4.29) as

$$F_{i,P}^p = \sum_f F_{i,f}^p = \sum_f p_f S_{i,f} , \quad (4.40)$$

which may be shown to be equivalent to

$$F_{i,P}^p = V_P \left. \frac{\partial p}{\partial x_i} \right|_P = \sum_f p_f S_{i,f} , \quad (4.41)$$

where the nodal pressure gradient is calculated using (4.20).

General Algebraic Equation

A general algebraic equation of momentum conservation for an interior CV P may be obtained by substituting the interfacial terms defined above into (4.33a), yielding

$$A_P^u u_{i,P} = \sum_F A_F^u u_{i,F} + B_{i,P}^u , \quad (4.42)$$

where A_F^u are the velocity coefficients at the neighbouring nodes, and A_P^u and $B_{i,P}^u$ are the velocity coefficient and source term at node P . The velocity coefficients and source term may be expanded as

$$\begin{aligned} A_E^u &= D_e - \min(\dot{m}_e, 0) , & A_W^u &= D_w - \min(\dot{m}_w, 0) , \\ A_N^u &= D_n - \min(\dot{m}_n, 0) , & A_S^u &= D_s - \min(\dot{m}_s, 0) , \\ A_T^u &= D_t - \min(\dot{m}_t, 0) , & A_B^u &= D_b - \min(\dot{m}_b, 0) , \\ A_P^u &= A_E^u + A_N^u + A_T^u + A_W^u + A_S^u + A_B^u = \sum_F A_F^u , \end{aligned} \quad (4.43)$$

$$\begin{aligned} B_{i,P}^u &= -F_{i,P}^p + B_{i,e}^d + B_{i,n}^d + B_{i,t}^d + B_{i,w}^d + B_{i,s}^d + B_{i,b}^d \\ &= -\sum_f p_f S_{i,f} + \sum_f B_{i,f}^d , \end{aligned}$$

where D_f is the interface conductance defined as

$$D_f = \frac{\mu S_f}{(\mathbf{r}_F - \mathbf{r}_P) \cdot \hat{\mathbf{n}}_f} , \quad (4.44)$$

and $B_{i,f}^d$ is the explicit part of the diffusion term defined as

$$B_{i,f}^d = D_f \left(\nabla u_{i,F}^o \cdot (\mathbf{r}_F - \mathbf{r}_F) - \nabla u_{i,P}^o \cdot (\mathbf{r}_P - \mathbf{r}_P) \right) . \quad (4.45)$$

Equations (4.42) to (4.45) may be applied to each interior CV over the discrete domain to form a linearized set of algebraic equations that are solved iteratively using the strongly implicit procedure (see Section 4.3.6). However, the non-linearity present in the advection terms require under-relaxation between subsequent steps or outer iterations in the steady state solution [Patankar, 1980]. Consequently, (4.42) may be altered to include under-relaxation as

$$\frac{A_P^u}{\alpha_u} u_{i,P} = \sum_F A_F^u u_{i,F} + B_{i,P}^u + \frac{1 - \alpha_u}{\alpha_u} A_P^u u_{i,P}^o, \quad (4.46a)$$

$$A_P^{u*} u_{i,P} = \sum_F A_F^u u_{i,F} + B_{i,P}^{u*}, \quad (4.46b)$$

where α_u is the velocity under-relaxation factor, and A_P^{u*} and $B_{i,P}^{u*}$ are the altered velocity coefficient and source term at CV P .

It is important to note that the velocity coefficients are equivalent for each Cartesian component of velocity. This is a convenient property of the co-located grid and is incorporated into the iterative solution of the velocity field. To preserve this property requires that certain boundary conditions be implemented explicitly (see Section 4.3.4).

4.3.4 Coupling the Momentum and Mass Conservation Equations

The solution of the steady incompressible NS equations with co-located variables is complicated by two factors. The first is that an independent equation coupling the velocity and pressure fields is absent for incompressible flows. A traditional solution to this problem is the semi-implicit-pressure-linked-equations (SIMPLE) algorithm [see Patankar, 1980]. Essentially, this algorithm provides coupling by constructing a pressure field that satisfies the mass conservation equation. The second complicating factor has to do with the co-located variable arrangement. It is well known that solving the NS equations on a co-located grid is susceptible to oscillations or so-called checker-boarding in the velocity and pressure fields, whereas a solution based on a traditional staggered grid is not [see Patankar, 1980]. A solution to this problem is the pressure-weighted-interpolation (PWI) method which is often attributed to Rhie and Chow [1983]. The PWI method mimics the desirable properties of a staggered grid on a co-located grid by interpolating the velocity/mass flux to the face of a CV in a special way. The implementations of the SIMPLE algorithm and the PWI method in this work are discussed below.

PWI Method

The PWI method begins by solving the momentum equations based on initial estimates of the velocity, pressure and mass flux fields. Then the influence of the pressure terms is removed from the resulting velocity field to define a *pseudo*-velocity field. This is performed by rearranging the general algebraic momentum equation (4.42) in terms of the nodal velocity as

$$u_{i,P} = \frac{1}{A_P^u} \left[\sum_F A_F^u u_{i,F} - V_P \frac{\partial p}{\partial x_i} \Big|_P + \sum_f B_{i,f}^d \right], \quad (4.47)$$

where the source term is expanded and the pressure term given by (4.41). The pseudo-velocity field is then defined as

$$\tilde{u}_{i,P} = \frac{1}{A_P^u} \left[\sum_F A_F^u u_{i,F} + \sum_f B_{i,f}^d \right] = u_{i,P} + \frac{V_P}{A_P^u} \frac{\partial p}{\partial x_i} \Big|_P, \quad (4.48)$$

where the pressure term is simply removed from (4.47). Equation (4.48) may be used to define the pseudo-velocity value at the CV face. The interfacial velocity for a general CV face f may be given as

$$u_{i,f} = \frac{1}{2} u_{i,P} + \frac{1}{2} u_{i,F} + \nabla u_{i,f}^o \cdot (\mathbf{r}_f - \mathbf{r}_{f'}), \quad (4.49)$$

where the first two terms are the implicit part of the interpolation and the gradient term is the explicit part resulting from the non-orthogonality of the grid. An interfacial pseudo-velocity may be defined by removing the influence of the pressure terms from the implicit terms of (4.49) yielding

$$\tilde{u}_{i,f} = \frac{1}{2} \tilde{u}_{i,P} + \frac{1}{2} \tilde{u}_{i,F} + \nabla u_{i,f}^o \cdot (\mathbf{r}_f - \mathbf{r}_{f'}), \quad (4.50)$$

which may also be given as

$$\tilde{u}_{i,f} = u_{i,f} + \frac{1}{2} \frac{V_P}{A_P^u} \frac{\partial p}{\partial x_i} \Big|_P + \frac{1}{2} \frac{V_F}{A_F^u} \frac{\partial p}{\partial x_i} \Big|_F. \quad (4.51)$$

The next step in PWI is to reintroduce a pressure term into (4.51) that is local to the CV face, yielding

$$\hat{u}_{i,f} = u_{i,f} + \frac{1}{2} \frac{V_P}{A_P^u} \frac{\partial p}{\partial x_i} \Big|_P + \frac{1}{2} \frac{V_F}{A_F^u} \frac{\partial p}{\partial x_i} \Big|_F - \frac{V_f}{A_f^u} \frac{\partial p}{\partial x_i} \Big|_f, \quad (4.52)$$

where $\hat{u}_{i,f}$ is commonly defined as the *advecting* velocity, V_f is the volume of the interface CV (see Figure 4.3(b)) defined by (4.12), and A_f^u is the interface velocity coefficient defined by

$$\frac{1}{A_f^u} = \frac{w_P}{A_P^u} + \frac{w_F}{A_F^u} = \frac{1}{2 A_P^u} + \frac{1}{2 A_F^u}. \quad (4.53)$$

Finally, the advecting velocity is used to define the mass flux normal to the face as

$$\dot{m}_f = \sum_i \rho \hat{u}_{i,f} S_{i,f}, \quad (4.54)$$

which may be expanded and simplified as

$$\dot{m}_f = \sum_i \rho \left[u_{i,f} + \frac{1}{2} \frac{V_P}{A_P^u} \frac{\partial p}{\partial x_i} \Big|_P + \frac{1}{2} \frac{V_F}{A_F^u} \frac{\partial p}{\partial x_i} \Big|_F \right] S_{i,f} - \rho \frac{V_f}{A_f^u} \frac{\partial p}{\partial n} \Big|_f, \quad (4.55)$$

where the local pressure term is a function of the normal pressure gradient defined by (4.25).

Effectively, (4.55) mimics a staggered grid definition of mass flux since the local pressure term is

staggered or offset from the interface velocity. Consequently, the mass flux calculation is able to detect local pressure oscillations and properly influence the momentum and conservation equations to suppress checkerboarding in the nodal velocity and pressure fields.

It is noteworthy that \dot{m}_f was originally defined as [Ferziger and Peric, 1999]

$$\dot{m}_f = \sum_i \rho u_{i,f} S_{i,f} - \rho \frac{S_f V_f}{A_f^u} \left[\left. \frac{\partial p}{\partial n} \right|_f - \overline{\left. \frac{\partial p}{\partial n} \right|_f} \right] \quad (4.56)$$

where the over-bar indicates that the pressure gradient normal to the face is interpolated from the nodal values. Equation (4.56) is a more eloquent version of (4.55) where the nodal pressure gradients and coefficients at P and F are approximated with a single interpolated pressure gradient and interfacial coefficients at f . Nonetheless, for the flow simulations performed in this study (4.55) provided a more robust numerical solution than (4.56).

SIMPLE Algorithm

The SIMPLE algorithm begins by defining corrections for pressure, velocity and mass flux as

$$p_P = p_P^o + p_P', \quad (4.57a)$$

$$u_{i,P} = u_{i,P}^o + u_{i,P}', \quad (4.57b)$$

$$\dot{m}_f = \dot{m}_f^o + \dot{m}_f', \quad (4.57c)$$

where the superscript o indicates the previous or old value, and $'$ indicates the correction. After solving the momentum equations, (4.57) may be substituted into the implicit terms of (4.42) to yield

$$A_P^u u_{i,P}' = \sum_F A_F^u u_{i,F}' - V_P \left. \frac{\partial p'}{\partial x_i} \right|_P, \quad (4.58)$$

where the old values of velocity and pressure already satisfy the momentum equation. The SIMPLE algorithm approximates (4.58) as

$$A_P^u u_{i,P}' \approx - V_P \left. \frac{\partial p'}{\partial x_i} \right|_P, \quad (4.59)$$

which couples the nodal velocity correction and the nodal pressure correction gradient. Similarly, after calculating the mass flux, (4.57) and (4.59) may be substituted into the implicit terms of (4.55) to yield

$$\dot{m}_f' \approx - \rho \frac{V_f}{A_f^u} \left. \frac{\partial p'}{\partial n} \right|_f S_f, \quad (4.60)$$

which may be expanded using (4.12) and (4.25) as

$$\dot{m}'_f \approx - \frac{\rho S_f^2}{A_f^u} \left(p'_F - p'_P + \nabla p_{F'}' \cdot (\mathbf{r}_{F'} - \mathbf{r}_F) - \nabla p_{P'}' \cdot (\mathbf{r}_{P'} - \mathbf{r}_P) \right). \quad (4.61)$$

The expression may be simplified by neglecting the explicit part of the normal pressure correction gradient as

$$\dot{m}'_f \approx - \frac{\rho S_f^2}{A_f^u} (p'_F - p'_P) = - c_f (p'_F - p'_P), \quad (4.62)$$

where c_f is defined as the interface redistribution coefficient. Equation (4.62) couples the mass flux and pressure corrections through the CV face and may be used to update the pressure field to satisfy mass conservation over the adjacent CVs.

In general, the initial solutions of the momentum equations and subsequent calculation of interface mass fluxes will not satisfy mass conservation since the initial pressure field is incorrect. This mass conservation error may be represented as

$$\sum_f \dot{m}_f = \Delta \dot{m}_P, \quad (4.63)$$

where $\Delta \dot{m}_P$ is the mass flux residual over the CV P . Finally, the SIMPLE pressure correction equation may be formed by substituting (4.57c), (4.62), and (4.63) into (4.28) as

$$\sum_f -c_f (p'_F - p'_P) = -\Delta \dot{m}_P. \quad (4.64)$$

General Algebraic Equation

The general algebraic equation of the pressure correction equation (4.64) for a CV P may be given as

$$A_P^p p'_P = \sum_F A_F^p p'_F + B_P^p \quad (4.65)$$

where A_F^p are the pressure coefficients at the neighbouring nodes, and A_P^p and B_P^p are the pressure coefficient and source term at node P . The pressure coefficients and source term are defined as

$$\begin{aligned} A_E^p &= c_e, & A_N^p &= c_n, & A_T^p &= c_t, \\ A_W^p &= c_w, & A_S^p &= c_s, & A_B^p &= c_b, \\ A_P^p &= \sum_F A_F^p, & B_P^p &= -\Delta \dot{m}_P. \end{aligned} \quad (4.66)$$

Equations (4.65) and (4.66) may be applied to each interior CV over the discrete domain to form a linear set of algebraic equations that are solved iteratively using a SIP solver. Once the pressure correction field is obtained, the pressure correction gradient field is determined using (4.22) with m equalling 2. Then the velocity field is updated using (4.57b) and (4.59), and mass flux field is updated using (4.57c) and (4.62). However, it is important to note, that the pressure field is

updated using [Pantankar, 1980]

$$p_P = p_P^o + \alpha_p p_P' , \quad (4.67)$$

where α_p is the pressure correction under-relaxation factor. Equation (4.67) under-relaxes the updating of the pressure field, since (4.59) tends to significantly overestimate the pressure correction field, and consequently, the momentum equations become susceptible to oscillations (over acceleration/deceleration) in the velocity field.

4.3.5 Boundary Conditions

There are three types of boundaries defined over the fracture domain (see Figure 4.4): the fracture inlet and outlet are flow boundaries where the pressure is prescribed, the sides of the fracture are symmetry boundaries, and the fracture walls are impermeable boundaries. These boundaries influence the algebraic equations of CVs that have a single or multiple faces that coincide with the boundaries. As mentioned in Section 4.3.2, a benefit of using a co-located grid, is that the velocity coefficients for each Cartesian component are equivalent. In this work, the boundary conditions are implemented so that this property is maintained for CVs with boundary faces. It is important to note, that before the boundary conditions are implemented in this section their influence on the general algebraic equations ((4.42) and (4.65)) is removed. Accordingly, the following coefficients and variables are set to zero, depending on which boundary or boundaries the CV lies on:

$$\begin{aligned} \text{west inlet boundary: } A_W^u &= B_{i,w}^D = p_w = A_W^p = 0 , \\ \text{east outlet boundary: } A_E^u &= B_{i,e}^D = p_e = A_E^p = 0 , \\ \text{south side boundary: } A_S^u &= B_{i,s}^D = p_s = A_S^p = 0 , \\ \text{north side boundary: } A_N^u &= B_{i,n}^D = p_n = A_N^p = 0 , \\ \text{bottom wall boundary: } A_B^u &= B_{i,b}^D = p_b = A_B^p = 0 , \\ \text{top wall boundary: } A_T^u &= B_{i,t}^D = p_t = A_T^p = 0 . \end{aligned} \quad (4.68)$$

Effectively, (4.68) initializes the momentum fluxes and pressure forces at boundary faces as zero. The formulation of the three boundary types and further modifications to the general algebraic momentum and pressure correction equations are presented below.

Boundary Interface Extrapolation

An important component to all three types of boundary conditions is the extrapolation of velocity and pressure from the CV centre to the boundary face(s) of boundary CVs. Figure 4.5(a) shows a general boundary face with its adjacent node P and the next interior node PP . The integration point of the boundary face is indexed as bf and local vectors may be defined between P

and bf as

$$\xi_{bf} = \mathbf{r}_{bf} - \mathbf{r}_P, \quad \hat{\xi}_{bf} = \frac{\xi_{bf}}{|\xi_{bf}|}. \quad (4.69)$$

In general, the value of a generic variable at the boundary face (ϕ_{bf}) may be extrapolated from interior nodes P and PP as

$$\phi_{bf} = w_P \phi_P + w_{PP} \phi_{PP} \quad (4.70)$$

where w_P and w_{PP} are the linear weights of the extrapolation. Two options for evaluating these weights are used in this work. The first is to simply approximate the boundary face value with nodal value at P , which corresponds to the following weights:

$$w_P = 1, \quad w_{PP} = 0. \quad (4.71)$$

This option was used for the velocity vector on the inlet and outlet boundaries to ensure numerical stability. The second option is to linearly extrapolate using both nodes, and corresponds to the following weights:

$$w_P = \frac{(\mathbf{r}_{bf} - \mathbf{r}_{PP}) \cdot \hat{\xi}_{bf}}{|\mathbf{r}_P - \mathbf{r}_{PP}|}, \quad w_{PP} = \frac{(\mathbf{r}_P - \mathbf{r}_{bf}) \cdot \hat{\xi}_{bf}}{|\mathbf{r}_P - \mathbf{r}_{PP}|}. \quad (4.72)$$

This second option was used for pressure on the wall and side boundaries and the velocity vector on the side boundaries.

Inlet and Outlet Boundaries

The inlet and outlet of the fracture domain have prescribed pressures and are flow boundaries to mass and momentum transport. This pressure condition may be given as

$$P_{bf} = P_{\text{prescribed}}, \quad (4.73)$$

or in terms of a boundary pressure force as

$$F_{i,bf}^P = P_{\text{prescribed}} S_{i,bf}, \quad (4.74)$$

which drives the momentum transport through the interior of the fracture domain through the velocity source terms of CVs with inlet or outlet faces. The velocity vector at these faces is approximated with the nodal velocity of the CV holding the boundary face ((4.70) with (4.71)).

This boundary velocity vector may be used to calculate the mass flux at a boundary face as

$$\dot{m}_{bf} = \sum_i \rho u_{i,bf} S_{i,bf}, \quad (4.75)$$

and both of these conditions may be incorporated into the boundary advection term as

$$F_{i,bf}^a = \max(\dot{m}_{bf}, 0) u_{i,P} + \min(\dot{m}_{bf}, 0) u_{i,bf}^o. \quad (4.76)$$

The diffusion term at the boundary interface may be approximated with a one-sided difference

between the auxiliary node P' and integration point bf (see Figure 4.5(b)) as

$$F_{i,bf}^d \approx -\mu S_{bf} \left[\frac{u_{i,bf}^o - u_{i,P'}}{(\mathbf{r}_{bf} - \mathbf{r}_P) \cdot \hat{\mathbf{n}}_{bf}} \right], \quad (4.77)$$

and may be expanded using (4.25a) as

$$F_{i,bf}^d \approx -\mu S_{bf} \left[\frac{u_{i,bf}^o - u_{i,P}}{(\mathbf{r}_{bf} - \mathbf{r}_P) \cdot \hat{\mathbf{n}}_{bf}} - \frac{\nabla u_{i,P}^o \cdot (\mathbf{r}_{bf} - \mathbf{r}_P)}{(\mathbf{r}_{bf} - \mathbf{r}_P) \cdot \hat{\mathbf{n}}_{bf}} \right], \quad (4.78)$$

where the position of P' is given by (4.11a) with the index bf replacing e .

The above terms may be incorporated into the algebraic momentum equation ((4.42) initialized with (4.68)) as

$$\begin{aligned} A_P^u &= A_P^{u,old} + (D_{bf} - \min(\dot{m}_{bf}, 0)), \\ B_{i,P}^u &= B_{i,P}^{u,old} + (D_{bf} - \min(\dot{m}_{bf}, 0)) u_{i,bf}^o + p_{bf} S_{i,bf} + B_{i,bf}^d, \end{aligned} \quad (4.79)$$

where D_{bf} is the boundary face conductance defined as

$$D_{bf} = \frac{\mu S_{bf}}{(\mathbf{r}_{bf} - \mathbf{r}_P) \cdot \hat{\mathbf{n}}_{bf}}, \quad (4.80)$$

$B_{i,bf}^d$ is the explicit part of the boundary diffusion term defined as

$$B_{i,bf}^d = -D_{bf} \nabla u_{i,P}^o \cdot (\mathbf{r}_{bf} - \mathbf{r}_P), \quad (4.81)$$

and the superscript old refers to the initialized or cumulative (i.e., after sequential boundary modifications) values of the central coefficient and source term.

The prescribed pressure at the boundary faces indicate that

$$p'_{bf} = 0 \quad (4.82)$$

and the mass flux correction at these faces may be approximated from (4.61) as

$$\dot{m}'_{bf} \approx -\frac{\rho S_{bf}^2}{A_P^u} (p'_{bf} - p'_P) = -c_f (p'_{bf} - p'_P) = c_f p'_P. \quad (4.83)$$

Finally, (4.83) may be incorporated into the algebraic pressure correction equation ((4.64) initialized with (4.67)) as

$$A_P^p = A_P^{p,old} + c_{bf}. \quad (4.84)$$

Wall Boundaries

The wall boundaries of the fracture domain are impermeable no-slip boundaries which means that only diffusive momentum fluxes in the form of viscous shear stresses act tangentially on the boundary faces, while the wall velocity, mass flux, advective and normal diffusive momentum fluxes are zero. This is the dominant boundary condition for resisting flow through the fracture domain and may be represented as

$$\mathbf{u}_{bf} = u_{i,bf} = 0, \quad (4.85a)$$

$$\dot{m}_{bf} = F_{i,bf}^a = 0, \quad (4.85b)$$

$$F_{n,bf}^d = 0, \quad (4.85c)$$

where $F_{n,bf}^d$ is the normal diffusive momentum flux, and pressure is extrapolated from the interior to the wall boundary using (4.70) and (4.72). The first condition may be easily satisfied by setting the wall velocity to zero, and the second condition is already satisfied by (4.68), but the third requires some manipulation of the local velocity vector next to the wall boundary in order to properly zero the normal diffusive flux.

First the velocity vector is interpolated to the boundary auxiliary node P' (see Figure 4.5(b)) using (4.25a). Then the normal component of this velocity vector may be calculated as

$$u_{n,P'} = \mathbf{u}_{P'} \cdot \hat{\mathbf{n}}_{bf}, \quad (4.86)$$

which in turn may be used to define a Cartesian normal velocity vector as

$$u_{i,P'}^n = u_{n,P'} \hat{n}_{i,bf}. \quad (4.86)$$

Then a tangential velocity vector may be defined at P' as

$$u_{i,P'}^t = u_{i,P'} - u_{i,P'}^n = u_{i,P'} + \nabla u_{i,P}^o \cdot (\mathbf{r}_{P'} - \mathbf{r}_P) - u_{i,P'}^n, \quad (4.87)$$

which simply removes the normal velocity component from the interpolated velocity. This tangential velocity vector is then used to approximate the diffusive flux at the wall boundary, and effectively zeroes the normal component of the diffusive flux. Using a one-sided difference between the auxiliary node P' and integration point bf , the diffusion term at the wall may be given as

$$F_{i,bf}^d \approx -\mu S_{bf} \left[\frac{0 - u_{i,P'}^t}{(\mathbf{r}_{bf} - \mathbf{r}_P) \cdot \hat{\mathbf{n}}_{bf}} \right], \quad (4.88)$$

and may be expanded using (4.87) and simplified as

$$F_{i,bf}^d \approx -\frac{\mu S_{bf}}{(\mathbf{r}_{bf} - \mathbf{r}_P) \cdot \hat{\mathbf{n}}_{bf}} \left[u_{i,P'} + \nabla u_{i,P}^o \cdot (\mathbf{r}_{P'} - \mathbf{r}_P) - u_{i,P'}^n \right], \quad (4.89)$$

where the Cartesian component of the normal velocity is lagged. Equation (4.89) is similar to

(4.77) except that an addition term removing the normal component of the flux is present.

Incorporating (4.89) into the algebraic momentum equations results in the following modification to the central velocity coefficient and source term:

$$\begin{aligned} A_p^u &= A_p^{u,old} + D_{bf}, \\ B_{i,p}^u &= B_{i,p}^{u,old} + D_{bf} u_{i,p}^{n,o} + p_{bf} S_{i,bf} + B_{i,bf}^d, \end{aligned} \quad (4.90)$$

where D_{bf} and $B_{i,bf}^d$ are given by (4.80) and (4.81), and p_{bf} is the extrapolated boundary pressure.

Finally, the impermeable condition, (4.85b), indicates that

$$\dot{m}_{bf}' = 0 \quad (4.91)$$

which does not introduce modifications to the algebraic pressure correction equation.

Side Boundaries

The side boundaries of the fracture domain are symmetry boundaries which means that only the normal component of the diffusive momentum flux is allowed to cross the boundary faces, while the mass, advective and tangential diffusive fluxes are all zero. These conditions are simplified since the side boundaries are normal to the y -axis, and may be represented as

$$u_{n,bf} = u_{y,bf} = 0, \quad (4.92a)$$

$$\dot{m}_{bf} = F_{i,bf}^a = 0, \quad (4.92b)$$

$$F_{t,bf}^d = F_{x,bf}^d = F_{z,bf}^d = 0, \quad (4.92c)$$

where $u_{n,bf}$ is the normal velocity component, and $F_{t,bf}^d$ is the tangential diffusive flux. The first condition is satisfied by setting the y -component of velocity to zero at the boundary and the remaining velocity components, along with pressure, may be extrapolated from the interior using (4.70) and (4.72). The second and third conditions are satisfied by initializing the algebraic equations with (4.68), and the normal (y -axis) diffusive flux may be approximated with a one-sided difference as

$$F_{y,bf}^d \approx - \frac{\mu S_{bf}}{(\mathbf{r}_{bf} - \mathbf{r}_p) \cdot \hat{\mathbf{n}}_{bf}} \left((0 - u_{y,p}^o) - \nabla u_{y,p}^o \cdot (\mathbf{r}_{p'} - \mathbf{r}_p) \right). \quad (4.93)$$

This term is fully lagged and was directly implemented into the general algebraic equations without significantly affecting the convergence of the numerical solution. This is not surprising since the magnitude of (4.93) is typically small compared to the balance of the momentum fluxes passing through the side boundary CVs. This diffusive flux term and the pressure force term acting normal to the boundary were added to the y -axis source terms of algebraic momentum equations as

$$B_{y,p}^u = B_{y,p}^{u,old} + p_{bf} S_{y,bf} + F_{y,bf}^d. \quad (4.94)$$

Finally, the mass flux condition (4.92b) indicates that

$$\dot{m}'_{bf} = 0, \quad (4.95)$$

and does not introduce modifications to the algebraic pressure correction equation.

4.3.6 Segregated Solution Algorithm

The momentum equations (one for each Cartesian direction) and the pressure correction equation are solved separately and sequentially. This is referred to as the segregated solution of the Navier-Stokes equations, and the algorithm used in this work is summarized in Table 4.1. The main or outer loop of the algorithm occurs over steps 2 to 10. There are several minor or inner loops that are implicit to steps 4, 7 and 8; however, there are no formal inner loops that are required for transient solutions of the Navier-Stokes equations. These inner loops enforce convergence after each outer (time) iteration, but are not required for the steady-state solution. In this thesis work, convergence is determined when the solution satisfies the following criteria:

$$\text{norm}_F = \frac{\frac{1}{n_i} \sum_{CV} |\Delta F|}{F_{\text{inlet}}^P - F_{\text{outlet}}^P} \leq \text{tol}_F, \quad (4.96a)$$

$$\text{norm}_m = \frac{\frac{1}{n_i} \sum_{CV} |\Delta \dot{m}|}{\dot{m}_{\text{inlet}}} \leq \text{tol}_m, \quad (4.96b)$$

$$\text{norm}_s = \max \left(\left| 1 - \frac{\dot{m}_{\text{inlet}}^o}{\dot{m}_{\text{inlet}}} \right|, \left| 1 - \frac{\dot{m}_{\text{outlet}}^o}{\dot{m}_{\text{outlet}}} \right| \right) \leq \text{tol}_s, \quad (4.96c)$$

where norm_F and norm_m are normalized parameters for measuring the force and mass balance over the domain, norm_s is a normalized parameter for indicating when steady-state across the domain has been achieved, and tol refers to specified tolerances for each normalized parameter. The numerator of (4.96a) determines the average absolute sum of force residuals along the x -axis (the direction of the bulk flow) and the denominator is the difference in total pressure forces acting on the inlet and outlet boundaries. The numerator of (4.96b) determines the average absolute sum of mass residuals along the x -axis and the denominator is the total mass flux crossing the inlet boundary. Equation (4.96c) measures the absolute fractional difference between the old and current total mass fluxes crossing the inlet and outlet boundaries.

Typically, (4.96c) was the limiting condition for obtaining a converged solution. In fact, the force and mass balance conditions were satisfied early in the simulations, while the steady-state condition marked the end of the simulations. This is a common situation when pressure boundary conditions are used at inlet boundaries of Navier-Stokes simulations [Ferziger and Peric, 1999]. The pressure force terms acting on these boundaries influence the velocity field explicitly through

the momentum source terms. However, the net pressure force across the CVs along inlet boundary depends on the nodal pressure gradient, which in turn depends on the evolution of the internal flow field. Consequently, the velocity field accelerates slowly, as compared to the traditional velocity boundary condition, to satisfy the pressure boundary condition.

4.3.7 Solution of the General Algebraic Equations

A general algebraic equation for a generic variable may be given as

$$A_P \phi_P = \sum_F A_F \phi_F + B_P, \quad (4.97)$$

and may also be represented over the entire domain as

$$\begin{aligned} A_{ijk}^P \phi_{ijk} = & A_{ijk}^E \phi_{i+1jk} + A_{ijk}^N \phi_{ij+1k} + A_{ijk}^T \phi_{ijk+1} \\ & + A_{ijk}^W \phi_{i-1jk} + A_{ijk}^S \phi_{ij-1k} + A_{ijk}^B \phi_{ijk-1} + B_{ijk}, \end{aligned} \quad (4.98)$$

where (i, j, k) are the indices of the CV grid. Equation (4.98) is a three-dimensional matrix equation that may be solved iteratively using Stone's [1968] method of incomplete factorization, often referred to as the strongly implicit procedure (SIP). This method may be divided into two steps: the calculation of SIP coefficients, and the calculation of the correction.

The coefficients in the SIP form the lower (L) and upper (U) triangular matrices of the incomplete factorization. In this work, these coefficients are defined as seven three-dimensional matrices with the same structure as the coefficients shown in (4.98). The recursive equations defining the seven SIP coefficient matrices are shown in Appendix A. Once these SIP coefficient matrices are defined, they need to be redefined only when the coefficients in (4.98) change. Therefore, for the sequential solution of the momentum equations (u_x , u_y , and u_z), the SIP coefficients are defined only once since the velocity coefficients for each component are equivalent. Incorporated within the definition of the SIP coefficients is the SIP parameter (α_S), which influences the convergence properties the algorithm. For all simulations, the SIP parameter was set equal to 0.92.

The correction step of the SIP begins by calculating the residual of (4.98) as

$$\begin{aligned} R_{ijk} = & A_{ijk}^E \phi_{i+1jk} + A_{ijk}^N \phi_{ij+1k} + A_{ijk}^T \phi_{ijk+1} \\ & + A_{ijk}^W \phi_{i-1jk} + A_{ijk}^S \phi_{ij-1k} + A_{ijk}^B \phi_{ijk-1} \\ & - A_{ijk}^P \phi_{ijk} + B_{ijk}, \end{aligned} \quad (4.99)$$

and then forward and backward substitution loops (see Appendix A) involving the SIP coefficient matrices are used to solve an estimate of the correction matrix. This estimate may be refined by repeating the correction step over a specified number of iterations. Note again that the SIP coefficients remain fixed over these correction iterations. Convergence of the correction step may be monitored by comparing the current absolute sum of the residuals to its initial value.

In this thesis, the multigrid method is used to accelerate the convergence of the SIP. The

method is based on the additive correction approach [Hutchinson and Raithby, 1986] and uses the V-cycle algorithm which may be divided into two steps: the restriction or passing of residuals to coarser grids, and the prolongation or injection of corrections to the finer grids.

The restriction step begins by using the SIP to solve (4.99) over the original CV grid, which is defined as the level-1 or fine grid. The residual field and coefficients from this level-1 grid are then passed to a coarser level-2 grid, which is formed by agglomerating the CVs into $2 \times 2 \times 2$ blocks if possible. This results in a level-2 grid with $(n_i + 1)/2 \times (n_j + 1)/2 \times (n_k + 1)/2$ CVs. The level-2 residual field is formed by summing the level-1 residuals over the agglomerated CVs. The level-2 coefficients are formed by removing the level-1 coefficients of faces contained within the interior of the agglomerated CVs, and summing the level-1 coefficients that share a common exterior face. Level-2 SIP coefficients may then be defined, and the SIP may be used to solve a correction field. This level-2 correction field has an associated residual that in turn may be passed, along with the level-2 coefficients, to a coarser level-3 grid. A level-3 correction field may be obtained in a similar manner as the level-2 grid. This restriction may be repeated over a specified number of levels.

The prolongation step begins at the coarsest grid level. The correction field determined from the SIP is injected into the finer grid of the previous level using a simple block correction. Then the SIP is used to smooth the resulting correction field on the finer grid. This prolongation is repeated on subsequently finer grid levels until the level-1 grid is reached, which marks the end of the V-cycle.

The SIP-multigrid solver developed in this work is summarized in Table 4.2. For all three-dimensional simulations, the solver used 1 V-cycle with 5 grid levels and 1 iteration per SIP call (i.e., $n_V = 1$, $n_L = 5$, and $n_S = 1$). These solver parameters reduced the residual fields moderately during each call to the solver. This was desirable in terms of the overall efficiency of the segregated solution algorithm, since the convergence was limited by the slow acceleration of the flow field. Therefore, by the time that the flow field had obtained steady-state, the residual force and mass flux fields were reduced to acceptable levels.

4.4 Two-Dimensional Flow Model Based on the Local Cubic Law

4.4.1 Description of the Two-Dimensional Control Volume

An example of a two-dimensional CV grid or domain extracted from a three-dimensional fracture is shown in Figure 4.1(c). The grid spacing along the x - and y -axes are uniform and equal, and consequently, the CVs are orthogonal and square. Figure 4.6(a) displays a single CV from the interior of the domain along with its central node, integration points, and neighbouring nodes. As displayed in the figure, the lines connecting neighbouring nodes pass through the integration points of each CV face. The aperture field is defined at each corner, and using bilinear interpolation, the average aperture for the CV may be defined as

$$b_p = \frac{1}{4} \sum_{i=1}^4 b_c \quad (4.100)$$

where b_c is the aperture at the CV corners indexed from 1 to 4. Figure 4.6(b) displays a general CV face between the nodes P and F that contains the integration point f . The dashed line defines a square interfacial CV with point f at its centre. The aperture at the integration point is simply defined as

$$b_f = \frac{1}{2} (b_1 + b_2) \quad (4.101)$$

where b_1 and b_2 are the corner aperture values associated with the face. As noted in Section 3.2.1, the LCL assumes that the mean wall topography or mid-surface of the fracture is approximately planar. This situation is illustrated in Figure 4.7(a) which is a cross-section or profile through the nodes P and F in Figure 4.6(b). Even though the CV grid is formally two-dimensional, the profile reveals the underlying geometry used to define the effective flow parameters through the CV grid. As shown the mid-surface of the profile is planar and perpendicular to the definition of aperture used in this thesis. Figure 4.7(b) displays a profile with the same aperture values but undulation in the mid-surface. Consequently, the definition of aperture is not perpendicular to the mid-surface, and the distances between the nodes and integration point are larger than the grid spacing. Considering this situation, an aperture may be defined perpendicular to the mid-surface b_η as

$$b_\eta \approx b \hat{n}_z \quad (4.102)$$

where b is the vertical aperture, and \hat{n}_z is the z -component of the unit normal of the mid-surface (see Figure 4.7(c)). For a planar fracture \hat{n}_z equals unity and for a undulating fracture \hat{n}_z falls below unity. Furthermore, a tortuosity factor for the distance between the node P and integration point f may be defined as

$$\tau_{fp} = \frac{|\mathbf{r}_f - \mathbf{r}_p|}{\delta_{L,fp}} \quad (4.103)$$

which yields a value of unity for planar fractures, and a value above unity for undulating fractures. In the next section (4.102) and (4.103) are used to correct the LCL to reflect fracture undulation.

4.4.2 Approximation of the Local Cubic Law

The LCL (3.9) may be integrated over an arbitrary CV as

$$\int_V \rho \nabla \cdot \left[\frac{b^3 \gamma}{12 \mu} \nabla H \right] dV = 0 , \quad (4.104)$$

or alternatively, as

$$\int_S \rho \left[\frac{b^3 \gamma}{12 \mu} \nabla H \right] \cdot \hat{\mathbf{n}} dS = 0 , \quad (4.105)$$

where the volume integral is transformed into a surface integral. The discrete approximation of (4.105) is given by

$$\sum_f \dot{m}_f = 0 , \quad (4.106)$$

where \dot{m}_f is the mass flux normal to each face f defined as

$$\dot{m}_f = \frac{\bar{b}_f^3 \delta_{w,f} \rho \gamma}{12 \mu} \left[\frac{H_P - H_F}{\delta_{L,f}} \right] = \frac{\bar{b}_f^3 \delta_{w,f} \rho \gamma}{\delta_{L,f} 12 \mu} (H_P - H_F) , \quad (4.107)$$

where \bar{b}_f^3 is a characteristic average of b^3 defined over the CV centred around f (see Figure 4.7(b)), $\delta_{w,f}$ and $\delta_{L,f}$ are width and length of the interface CV, and H is hydraulic head at each node.

Equation (4.107) is simply a local application of the one-dimensional cubic law between nodes P and F . In this study the value of $\bar{b}_f^3 / \delta_{L,f}$ is defined using a weighted harmonic mean as

$$\frac{\bar{b}_f^3}{\delta_{L,f}} = \left[\frac{\delta_{L,fP}}{\beta_{fP} \bar{b}_{fP}^3} + \frac{\delta_{L,fF}}{\beta_{fF} \bar{b}_{fF}^3} \right]^{-1} , \quad (4.108)$$

where the subscripts fP and fF indicate values defined over adjacent halves of the interface CV, and β is a term correcting the aperture and spatial step values to reflect undulation. The characteristic values of b^3 for each half CV are defined using three methods. Using the half CV associated with node P , the first method is given as

$$\bar{b}_{fP}^3 = \left[\frac{1}{2} (b_f + b_P) \right]^3 , \quad (4.109)$$

which is simply the cube of the arithmetic mean aperture defined over the half CV [Brown, 1987, as reported by Nicholl *et al.*, 1999]. The second method is derived from the analytical solution of the LCL for one-dimensional flow between mildly tapered plates [Iwai, 1976] and is given as

$$\bar{b}_{fP}^3 = \frac{2 b_f^2 b_P^2}{b_f + b_P} . \quad (4.110)$$

The third method is derived from the analytical solution of the Stokes equations for two-dimensional radial flow through tapered plates (i.e., Hamel's problem) [Nicholl *et al.*, 1999] and is given as

$$\bar{b}_{fP}^3 = \frac{2 b_f^2 b_P^2}{b_f + b_P} \frac{3 (\tan \theta_{fP} - \theta_{fP})}{\tan^3 \theta_{fP}} , \quad (4.111)$$

where the angle θ_{fP} measures the relative slope of the tapered plates (see Figure 4.7(c)), given as

$$\tan \theta_{fP} = \kappa_{fP} \frac{|b_f - b_P|}{\delta_{L fP}} , \quad (4.112)$$

where κ is a term correcting the aperture and spatial step values to reflect undulation. Finally, the correction terms β and κ may be defined as

$$\beta_{fP} = \frac{\hat{n}_{z,P}^3 \delta_{L fP}}{|\mathbf{r}_f - \mathbf{r}_P|} , \quad (4.113)$$

$$\kappa_{fP} = \frac{\hat{n}_{z,P} \delta_{L fP}}{|\mathbf{r}_f - \mathbf{r}_P|} , \quad (4.114)$$

which are unity when the fracture is planar and below unity with fracture undulation.

The algebraic equation of the LCL for a single CV P may be given as

$$A_P^H H_P = \sum_F A_F^H H_F + B_P^H , \quad (4.115)$$

where A_F^H are the head coefficients at the neighbouring nodes, and A_P^H and B_P^H are the head coefficient and source term at node P . In general, the head coefficients and source term are defined as

$$A_F^H = \frac{\bar{b}_f^3}{\delta_{L f}} \frac{\delta_{w,f} \rho \gamma}{12 \mu} , \quad A_P^H = \sum_F A_F^H , \quad B_P^H = 0 , \quad (4.116)$$

where $\bar{b}_f^3 / \delta_{L f}$ is given by (4.108) to (4.114) depending on the method used to approximate \bar{b}_{fP}^3 . Equations (4.115) and (4.116) may be applied to each CV over the domain to form a linear set of algebraic equations. As with the three-dimensional flow model, the coefficients of CVs lying on a boundary are defined in order to initially remove the influence of the boundary. The following coefficients are set to zero, depending on which boundary or boundaries the CV lies on:

$$\begin{aligned} \text{west inlet boundary: } A_W^H &= 0 , \\ \text{east outlet boundary: } A_E^H &= 0 , \\ \text{south side boundary: } A_S^H &= 0 , \\ \text{north side boundary: } A_N^H &= 0 . \end{aligned} \quad (4.117)$$

Effectively, (4.117) sets the coefficients of all boundary faces to be no-flow boundaries, which is the desired boundary condition for the side boundaries. The inlet and outlet boundaries are flow boundaries with prescribed pressure, and therefore, the coefficients of CVs lying on the inlet and outlet must be modified according to

$$A_P^H = A_P^{H_{old}} + \frac{\bar{b}_{bf}^3}{\delta_{L,bf}} \frac{\delta_{w,bf} \rho \gamma}{12 \mu}, \quad (4.118)$$

$$B_P^H = H_{prescribed},$$

where *bf* refers to boundary faces, old refers to the cumulative value of the central coefficient. The mass flux through these boundaries is given by

$$\dot{m}_{bf} = \frac{\bar{b}_{bf}^3}{\delta_{L,bf}} \frac{\delta_{w,bf} \rho \gamma}{12 \mu} (H_P - H_{prescribed}). \quad (4.119)$$

After incorporating the boundary conditions, the set of algebraic equations are solved iteratively using a two-dimensional version of the SIP-multigrid solver presented in Section 4.3.6 (see Table 4.2). For all two-dimensional simulations, the solver used 5 V-cycles with 5 grid levels and 5 iterations per SIP call ($n_v = 5$, $n_L = 5$, and $n_S = 5$). The SIP solver was called successively until the convergence criteria (4.96b) and (4.96c) fell below 10^{-6} .

4.5 Three-dimensional Solute Transport Model Based on the Random Walk Particle Method

4.5.1 Description of the Three-Dimensional Control Volume

The three-dimensional solute transport simulations employ the velocity fields from the three-dimensional flow simulations, and therefore, use the same CV grid, except that the nodal velocity field is interpolated from the CV nodes to the CV corners. An inverse distance scheme was employed (see Figure 4.8(a)) to interpolate the velocity vector at the CV corners \mathbf{u}_c as

$$\mathbf{u}_c = \sum_F w_F \mathbf{u}_F, \quad (4.120a)$$

$$w_F = \frac{|\mathbf{r}_c - \mathbf{r}_F|^{-1}}{\sum_F |\mathbf{r}_c - \mathbf{r}_F|^{-1}}, \quad (4.120b)$$

where the subscripts *c* and *F* refer to the CV corner of interest and surrounding nodes involved in the interpolation, and *w* is the inverse distance weight for each node. This scheme used a maximum of 8 nodes for interior CV corners, and a minimum of 4 interpolation points for boundary CV corners. The velocity at any point within the fracture domain was defined by first identifying

the CV which holds the point and then tri-linearly interpolating from the CV corners to the point of interest. The tri-linear interpolation scheme for a specific CV may be given as (see Figure 4.8(b))

$$\mathbf{u}_p = \frac{1}{8} \sum_{c=1}^8 (1 + T_i^c w_i) (1 + T_j^c w_j) (1 + T_k^c w_k) \mathbf{u}_c, \quad (4.121a)$$

where \mathbf{u}_p is the velocity vector at a point $\mathbf{r}_p(x, y, z)$ with trilinear weights (w_i, w_j, w_k) , and T_i^c, T_j^c , and T_k^c are local coordinates for each corner which may be defined as

$$\begin{aligned} T_i &= \{-1, +1, +1, -1, -1, +1, +1, -1\}, \\ T_j &= \{-1, -1, +1, +1, -1, -1, +1, +1\}, \\ T_k &= \{-1, -1, -1, -1, +1, +1, +1, +1\}, \end{aligned} \quad (4.121b)$$

where each row vector is indexed from corner 1 to 8 as displayed in Figure 4.8(b).

4.5.2 Approximation of the Advection-Diffusion Equation

As presented in Section 3.2.2, the three-dimensional advection-diffusion equation is approximated by the RWPM which simulates transport of a large number of particles n_p through the fracture domain. The transport of each individual particle is governed by

$$\mathbf{r}^t = \mathbf{r}^{t-\Delta t} + \mathbf{u}^{t-\Delta t} \Delta t + \mathbf{Z} \sqrt{2 D_m \Delta t}, \quad (4.122)$$

where the advective term tracks the particle within the predetermined steady state flow field, and the diffusive term displaces the particle randomly with a variance $2 D_m \Delta t$ that is characteristic of Fickian diffusion. Each particle is introduced or injected into the domain at random locations on CV faces lying on the inlet boundary. Each CV boundary face is assigned a number of particles n_p^{bf} as a fraction of n_p , according to

$$n_p^{bf} = n_p \frac{\dot{m}_{bf}}{\dot{m}_{inlet}}, \quad (4.123)$$

where $\dot{m}_{bf}/\dot{m}_{inlet}$ is the ratio of mass flux passing through boundary face bf to the total mass flux through the inlet. Equation (4.122) explicitly describes the transport of each injected particle through the fracture domain over sequential time steps. The spatial history of each particle was stored, and the end or breakthrough time of the simulation was determined as the particles crossed the outlet boundary.

The main boundary condition used with (4.122) is the reflection boundary. This boundary satisfies the no-flow and symmetry requirements of the wall and side boundaries, and is also used at the inlet boundary after the particles are injected. It ensures that particles that are assigned positions that are outside of the fracture domain are reassigned positions within the domain using a simple reflection property. Figure 4.9(a) illustrates this property for a particle with an initial location \mathbf{r}_1 and a new location \mathbf{r}_2 , which is outside of the domain. The reflection boundary assigns

the new position \mathbf{r}_2 , by setting the distance δw to equal $\delta w'$. Figure 4.9(b) illustrates the same principle used for a non-horizontal wall. In this situation, the particle is also assumed to be reflected by setting the distance δw to equal $\delta w'$. This clear approximation was implemented since it reduces the computational burden of finding the actual point of intersection between the bilinear wall faces and the pathway of the particle. For fractures with very rough walls this approximation may influence the particle transport; however, this influence may be reduced by choosing a suitably small time step. Finally, a secondary boundary condition sets the minimum distance that a particle may approach a wall. In the event of very low or zero diffusive transport, this condition prevents particles from becoming trapped along the walls with velocity components that approach zero (see Figure 4.9(c)). The minimum distance was specified as a fraction of the CV dimension along the z -axis as

$$\delta_{w \min} = F_w \delta_z \quad (4.124)$$

where the fraction F_w equalled 0 or 0.1 for all transport simulations.

Table 4.1. Summary of the segregated solution algorithm.

step	description	equations
1	initialize velocity, pressure and mass flux fields	$u_i = p = m_f = 0$
2	calculate velocity and pressure gradients	(4.21)
3	assemble algebraic momentum equations and incorporate boundary conditions	(4.42), (4.43), (4.67), (4.78), (4.89), (4.93)
4	solve momentum equations sequentially with $\alpha_u = 0.75$ to 0.95	(4.46)
5	calculate mass flux and mass residual fields	(4.55), (4.62)
6	assemble algebraic pressure correction equation and incorporate boundary conditions	(4.64), (4.65), (4.67), (4.83)
7	solve pressure correction equation	(4.64)
8	calculate pressure correction gradient with $m = 2$	(4.22)
9	correct velocity, mass flux, and pressure with $\alpha_p = 0.10$	(4.56b), (4.56c), (4.66)
10	check convergence criteria with $\text{tol}_F = \text{tol}_m = \text{tol}_S = 10^{-4}$, if criteria are met then end solution, otherwise go to step 2	(4.95)

Table 4.2. Summary of SIP-multigrid solver algorithm.

-
- define A coefficients[†] on grid levels 2 to n_L
 - calculate SIP coefficients[†] on all grid levels
 - V-cycle loop: $i = 1$ to n_V
 - SIP solve level _{i} grid using n_S iterations
 - restriction loop: $j = 2$ to n_L
 - calculate residual[†] on level _{$j-1$} grid
 - pass residual to level _{j} grid
 - SIP solve level _{j} grid using n_S iterations
 - prolongation loop: $j = n_L$ to 2 by -1
 - inject level _{j} correction[†] into level _{$j-1$} grid
 - SIP solve level _{$j-1$} grid using n_S iterations
-

[†] all coefficients, residuals, and corrections on levels 2 to n_L were stored in three-dimensional matrices with dimensions:

$$n_i^I \times n_j^I \times n_k^I = (n_i^{I-1} - 1)/2 \times (n_j^{I-1} - 1)/2 \times (n_k^{I-1} - 1)/2$$

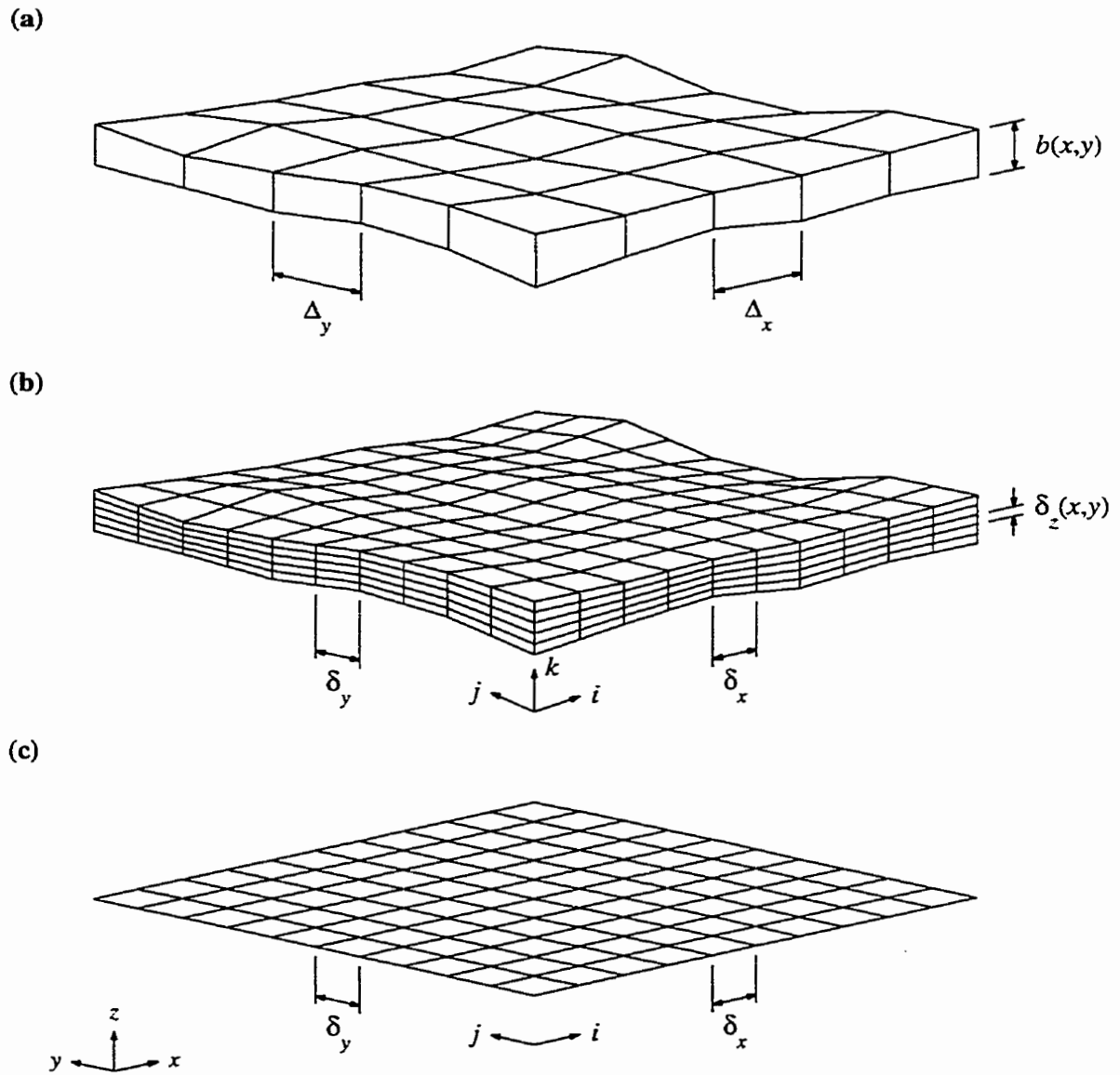


Figure 4.1. Examples of fracture domains: (a) 3D void space generated over an x - y grid with uniform spacing Δ_x and Δ_y , and variable aperture $b(x,y)$, (b) 3D CV domain formed by subdividing void space into uniform x - y increments δ_x and δ_y , and variable z increments $\delta_z(x,y)$, (c) 2D CV domain formed by subdividing void space into uniform x - y increments δ_x and δ_y .

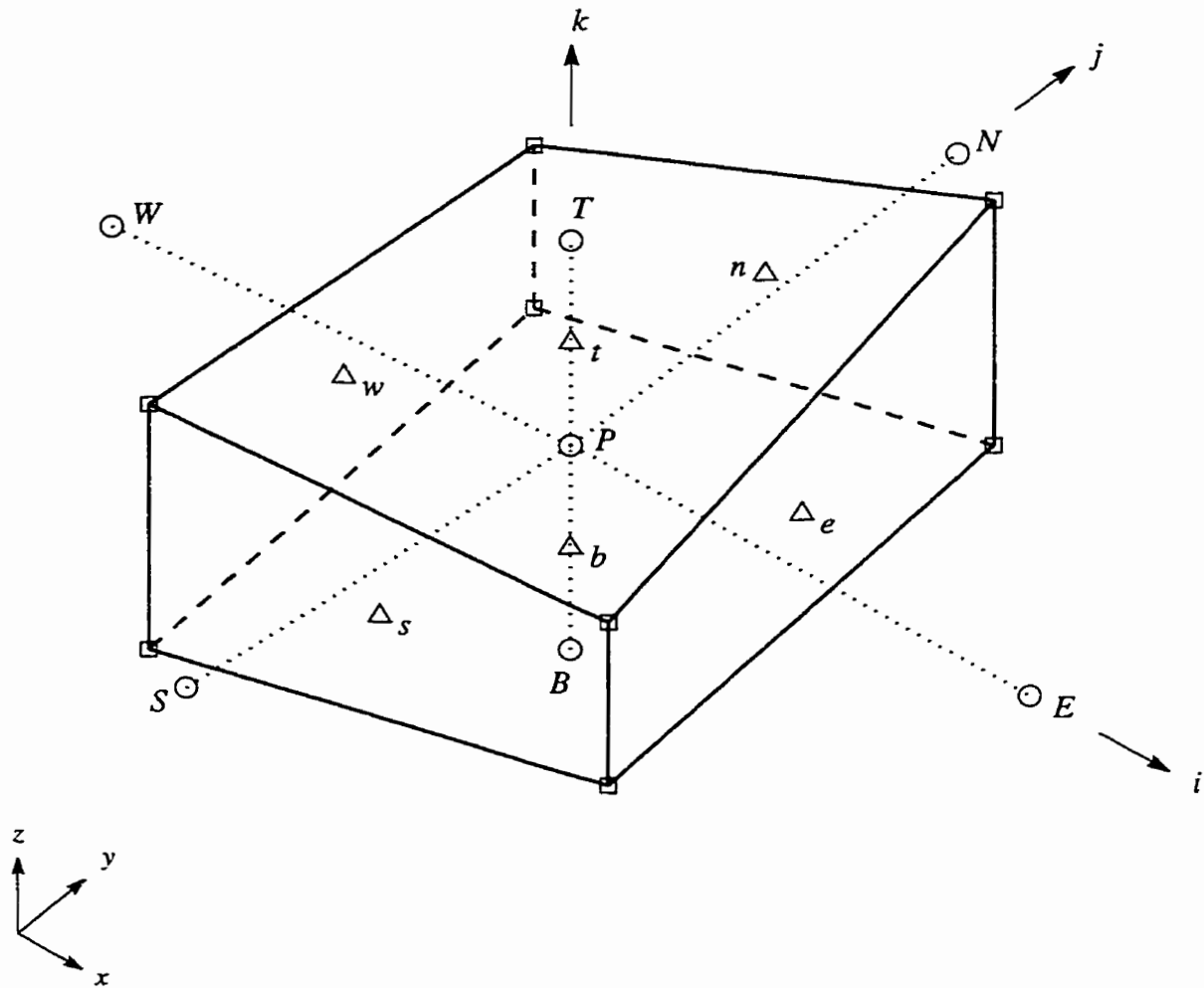


Figure 4.2. Example of a 3D CV from the interior of the 3D domain shown in Figure 4.1(a). The compass method is used to index nodes (circles) and integration points (triangles). The indices or corners of the CV are represented with square symbols.

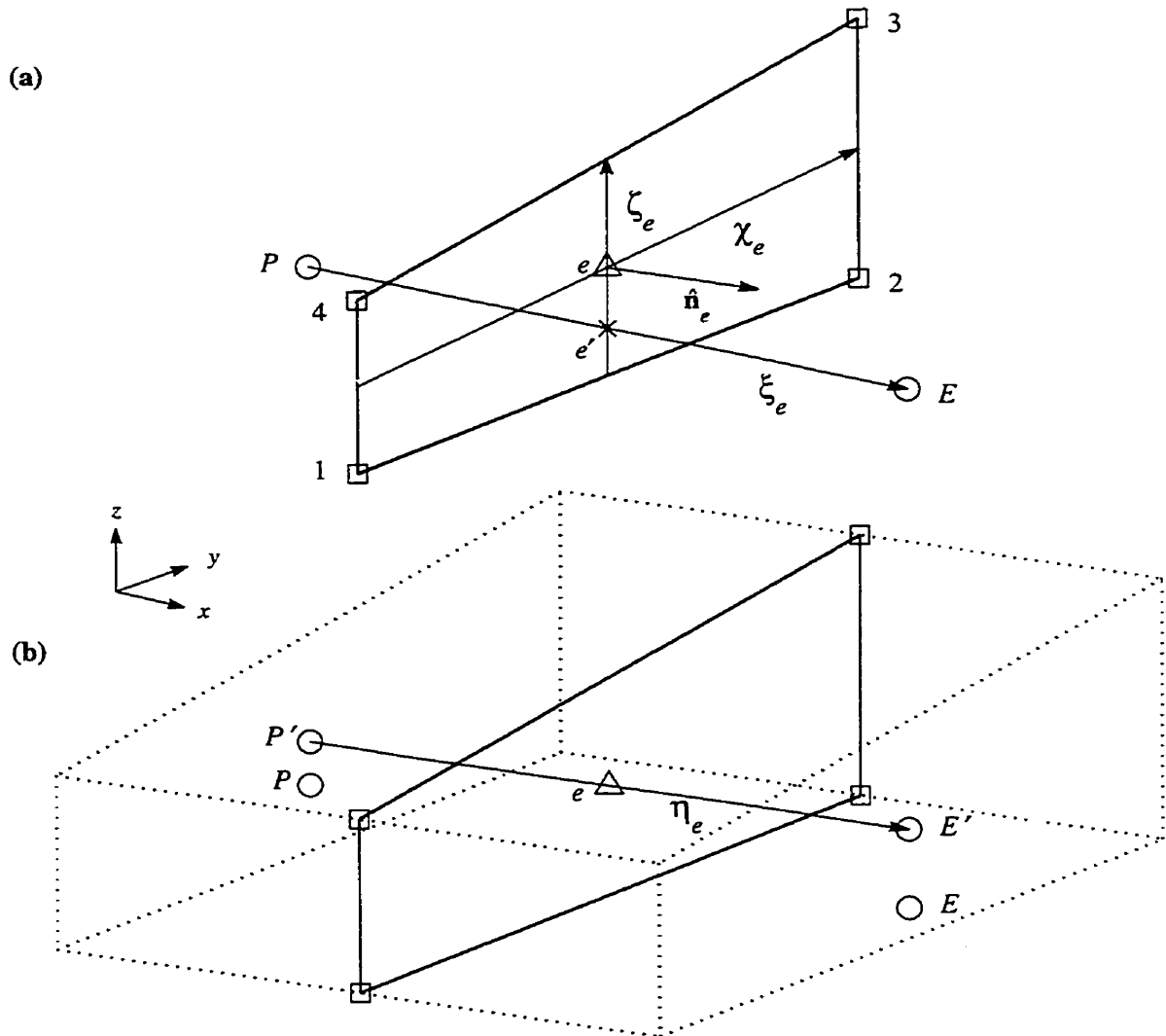


Figure 4.3. Details of the east face from the 3D CV shown in Figure 4.2. (a) Definition of tangential vectors ζ_e and χ_e , unit normal vector \hat{n}_e , and the local vector ξ_e which connects nodes P and E . (b) Definition of normal vector η_e passing through integration point e connecting auxiliary nodes P' and E' , and the outline (dotted line) of the CV associated with the face.

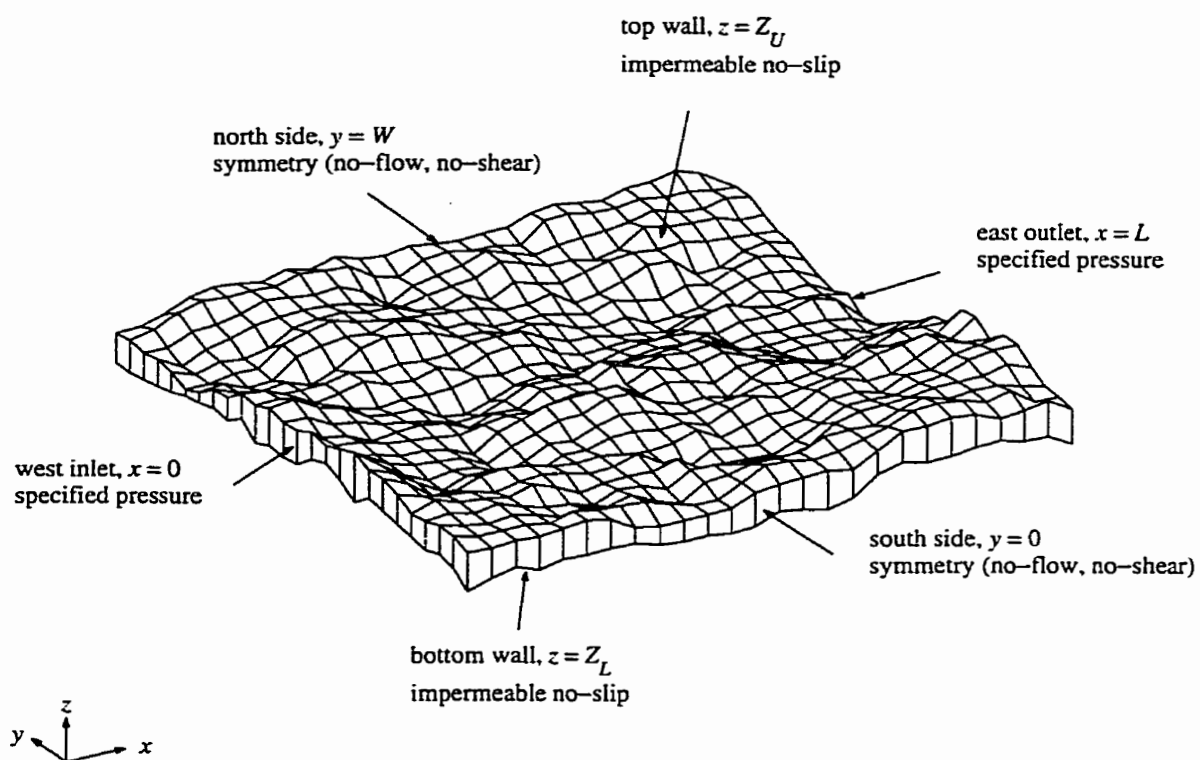
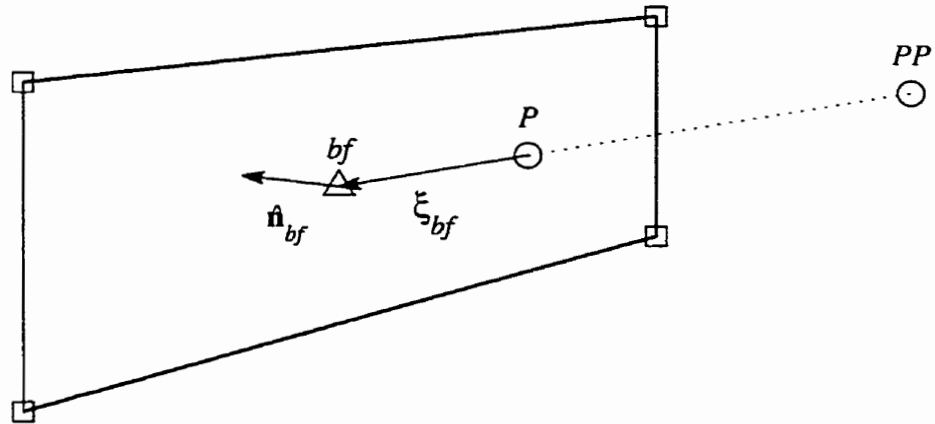


Figure 4.4. General boundary conditions used for the 3D simulations. The 2D simulations used the inlet, outlet, and side boundary conditions.

(a)



(b)

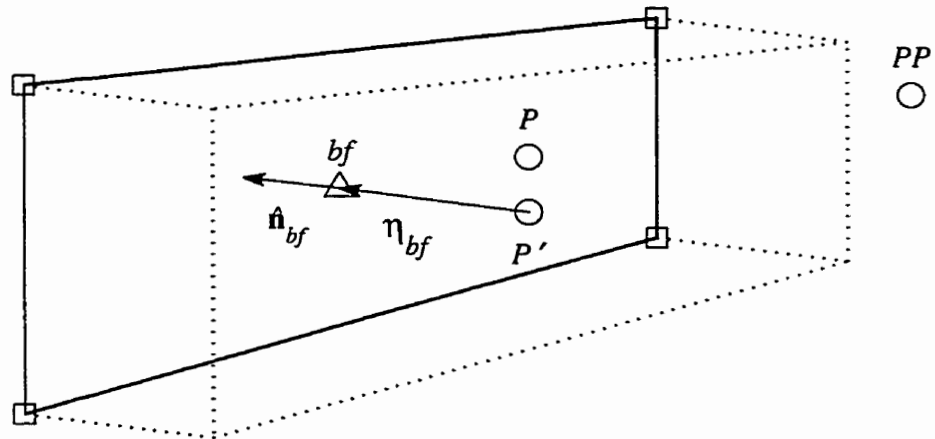


Figure 4.5. Details of a general 3D CV boundary face bf . (a) Definition of unit normal vector \hat{n}_{bf} and the local vector ξ_{bf} which connects node P to integration point bf . (b) Definition of normal vector η_{bf} connecting auxiliary node P' to integration point bf , and the boundary interface CV (dotted line).

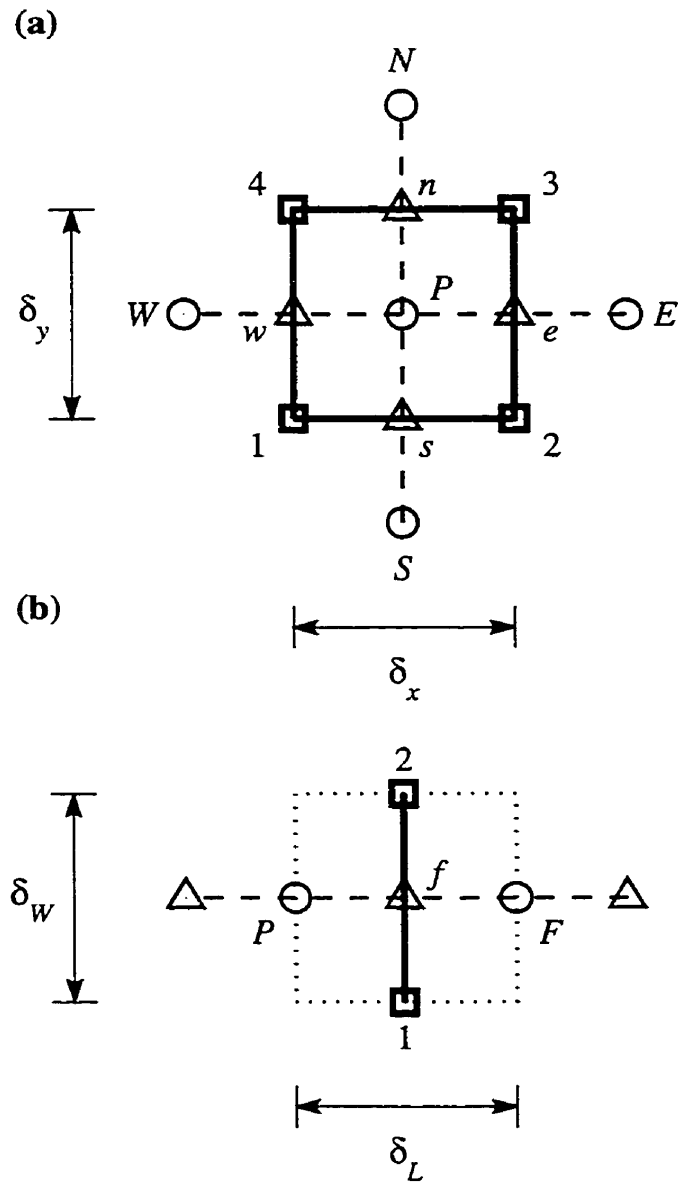


Figure 4.6. (a) An example of a 2D CV from the interior of the 2D domain shown in Figure 4.1(c). The corners (rectangles) are indexed 1 to 4, and the compass method is used to index the nodes (circles) and integration points (triangles). (b) Detail of a general 2D face and the outline (dotted line) of the CV associated with the face.

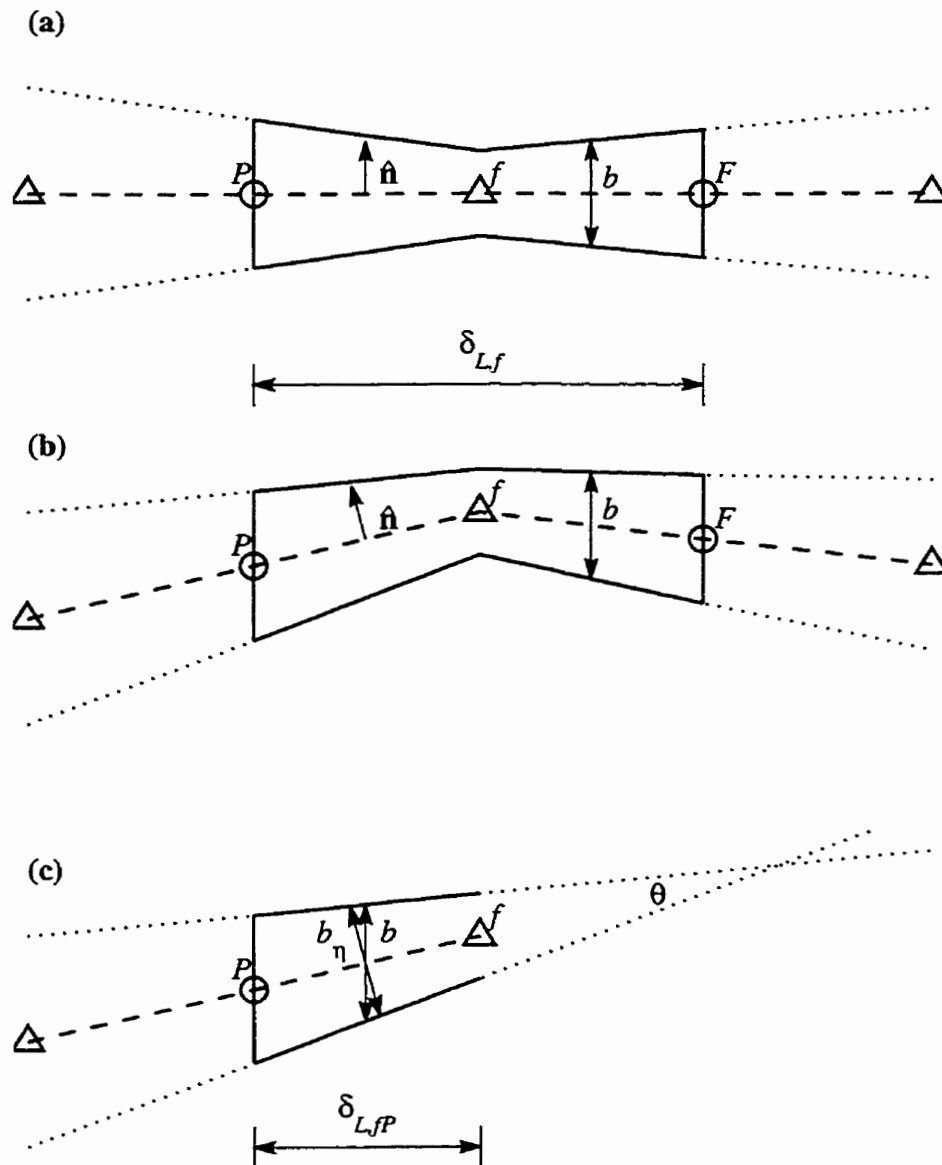


Figure 4.7. Profiles through nodes P and F shown in Figure 4.6(b) with: (a) planar mid-surface (dashed line), and (b) undulating mid-surface. The solid line delineates the portion of the profiles associated with the interface f , the circles represent nodes, and the triangles represent integration points. (c) Detail of profile shown in Part (b).

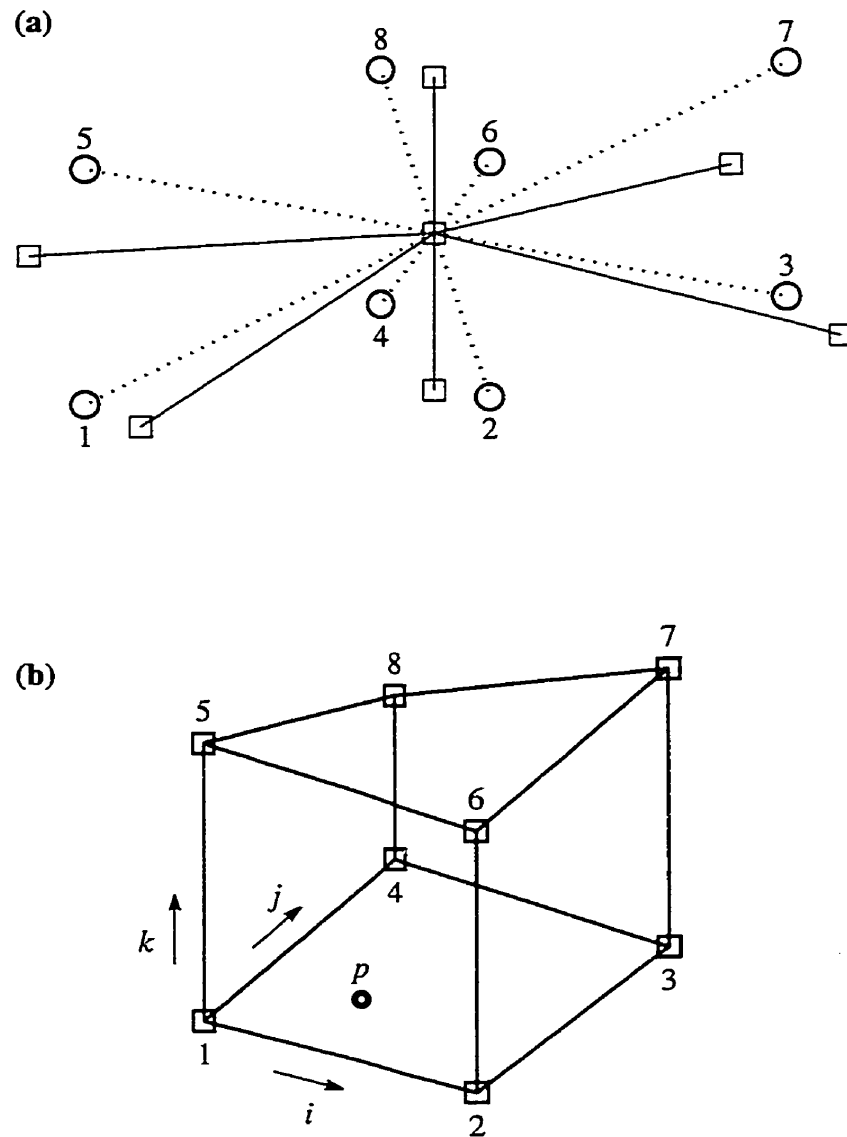


Figure 4.8. (a) Layout of nodes (circles) used to interpolate velocity at CV corner (square). The solid lines represent CV edges, and the dotted lines represent the distance between the corner and nodes used in (4.120). (b) Layout of CV corners used to interpolate velocity at a general point p within the CV.

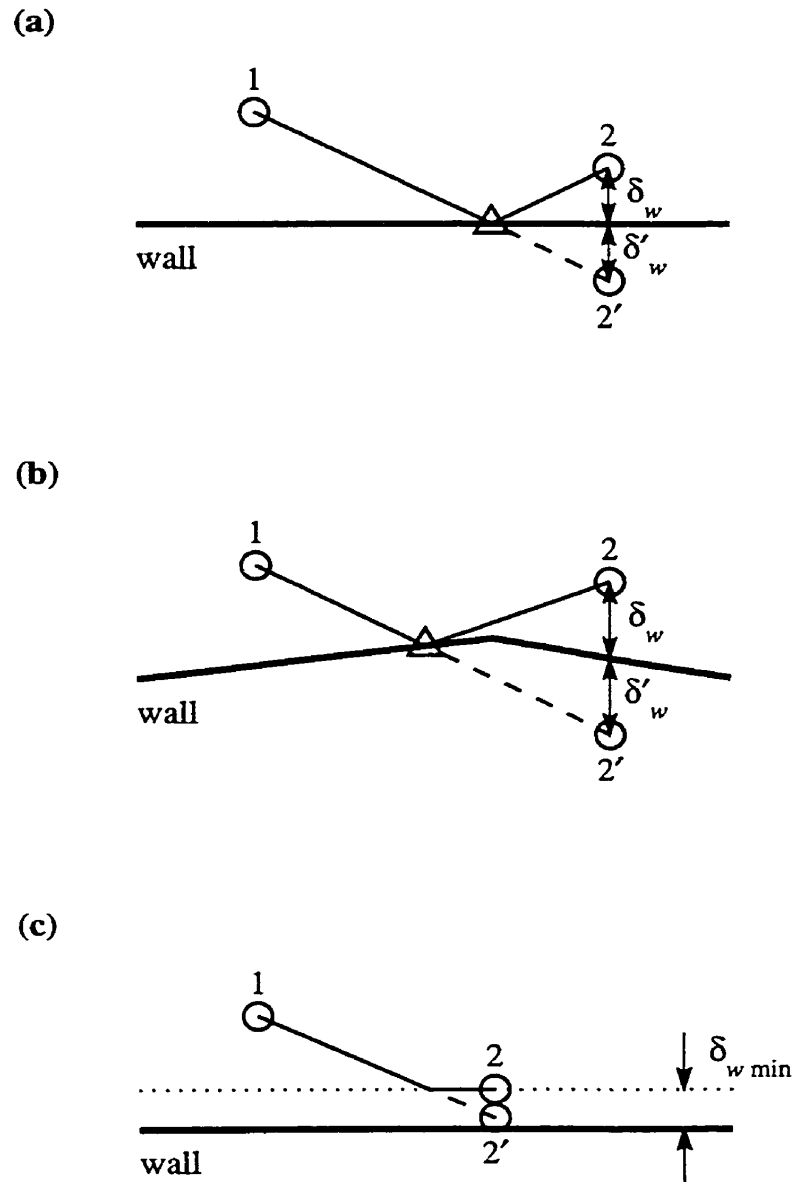


Figure 4.9. Illustration of RWPM wall boundary conditions for various situations: (a) particle reflection off a planar wall, (b) particle reflection off an undulating wall, and (c) particle adjustment for the minimum wall separation distance. The dashed line represents the unadjusted pathway of the particles, and the solid represents the final or adjusted pathways. The circles are the particle positions at the beginning (point 1) and end (point 2) of a time step, and the triangles are points of reflection.

CHAPTER 5. Simulation Results and Discussion

5.1 Introduction

The primary purpose of this chapter is to present and discuss the results of various fluid flow simulations performed on progressively more complex domains. The simulations begin with flow through parallel plates, move to flow through sinusoidal surfaces, and end with flow through synthetic rough-walled fractures. The first two ideal domains are used to verify the three-dimensional and two-dimensional flow models presented in Chapter 4. The rough-walled fracture domains are used to demonstrate the complex nature of fracture flow, and to compare the total flow rate predicted from the developed models under different conditions. By comparing the predicted total flow rates, geometric and kinematic constraints on the usage of the LCL and Stokes simulations are presented. Numerical accuracy, errors, and variability in the observed numerical simulations are also presented.

It is important to note that numerical simulations referred to as Stokes simulations in this thesis differ from the NS simulations only in that all the inertial terms (see (4.36)) are set to zero. Otherwise, the three-dimensional NS and Stokes simulations use the same discretization, boundary conditions, and solution methods. However, in general, the linear Stokes simulations were numerically more stable than the non-linear NS simulations. This property allowed for larger relaxation parameters to be used in the iterative solution of the Stokes equations, and consequently, led to a greater rate of convergence than the NS equations.

This chapter also presents and discusses the results of solute transport simulations performed on parallel plates, and two laboratory samples of rough-walled fractures. The parallel plates simulations are used to verify the RWPM model presented in Chapter 4. The laboratory rough-walled fracture simulations serve to verify the physics and numerical solution methods for both the flow and transport models developed in this thesis by matching experimental hydraulic and tracer tests.

5.2 Fluid Flow through Parallel Plates

Fluid flow through parallel plates was simulated using the three-dimensional Navier-Stokes model and compared to the exact solution given by (3.13) or (3.28). For this domain the two-dimensional LCL model reduces to the exact solution and hence will not be further discussed in this section. The parameters for the three-dimensional parallel plate simulations are summarised in Table 5.1, and several simulation results are presented in Figure 5.1. These simulations employed the boundary conditions presented in Section 4.3.4. Figure 5.1(a) shows the velocity field between the plates oriented in the direction of flow for the simulation with 20 CVs along the vertical axis (i.e., n_z equals 20). The velocity vectors are parallel to the plate walls and their magnitudes vary parabolically along the vertical axis. Figure 5.1(b) displays the normalized velocity profile between the plates predicted by the model and the exact solution. As shown, the model compares very well with the exact solution. In addition, a normalized pressure profile is shown to match the pressure profile that is implicit to the exact solution. It is important to emphasize here that the Navier-Stokes and Stokes simulations were identical even though the Reynolds number of the flow field was high ($Re = 0.8$). This occurred since the velocity vector at a specific vertical position z was one-dimensional and constant throughout the domain, and consequently, fluid inertial forces remained negligible. Figure 5.1(c) displays the observed relationship between the relative error e_Q of the numerical solution and the vertical grid spacing δ_z . The relative error e_Q is defined as

$$e_Q = \frac{|Q_{CL} - Q_{\delta_z}|}{Q_{CL}} \quad (5.1)$$

where Q_{CL} is the exact flow rate from the cubic law, and Q_{δ} is the flow rate from NS simulations using a specific δ_z value. As expected, the relative error decreases as the vertical grid spacing decreases, or in other words, the relative error decreases as the number of CVs in the vertical direction increase. The regressed power relationship between the relative error and grid spacing is also displayed, yielding an exponent of approximately 2. This indicates that the numerical system of equations display second-order accuracy in approximating the exact solution. This result is expected since the accuracy of the viscous and pressure forces terms used in the CV formulation are also second-order.

5.3 Fluid Flow through Sinusoidal Fractures

Fluid flow through fractures with sinusoidal walls was simulated using the three-dimensional Navier-Stokes and the two-dimensional LCL models. The profile of a general sinusoidal fracture is shown in Figure 5.2(a) while Table 5.2 summarizes the model parameters used in these simulations. These simulations used the standard boundary conditions presented Sections 4.3.4 and 4.4.2. Two important parameters describing the aperture variability in the sinusoidal profile are the relative roughness A/b_{\min} , and the roughness slope A/λ . Various values of relative roughness were examined and two values of the roughness slope, 0.1 and 0.4, were used to represent mild and steep roughness variations.

Figures 5.2(b) and (c) present the velocity field through the middle oscillation of a relatively rough ($A/b_{\min} = 1$) and steeply sloped ($A/\lambda = 0.4$) fracture profile as predicted by Stokes and Navier-Stokes simulations for a gradient equal to 0.033. The flow solution is symmetric about the centre line, however, the vectors below the centre line of the profiles are transformed by taking the quad root of their magnitude to reveal the flow pattern in the low velocity region. Figure 5.2(b) displays a vector distribution at the constriction that is qualitatively parabolic and parallel to the x -axis. The direction of the vectors spread or fan out as the aperture of the profile increases so that the vectors next to the walls become parallel to the wall and vectors travelling along the vertical centre of the profile remain parallel to the x -axis. Essentially the direction of the vector field conforms to the shape of the fracture profile. It is also clear that the magnitude of the vectors is largest in the constriction and smallest in the large aperture portion of the profile. Figure 5.2(c) displays similar behaviour to Figure 5.2(b) except that the vectors tend to remain parallel to the x -axis, and the magnitude of the vectors close to the vertical centre of the profile are larger. Additionally, vectors in the large aperture region recirculate due to separation in the flow field. These properties indicate that inertial forces significantly influence the flow field by resisting changes in magnitude and direction. Figures (c) and (b) are in good agreement with Figure 6 in work of *Brown et al.* [1995].

Figure 5.3 displays vertical profiles of two velocity components u_x and u_z , and pressure p for three locations (P1, P2, and P3) along the x -axis as indicated on Figure 5.2. The vertical position is normalized by the aperture value at the profile locations, and the velocity components and pressure are normalized by the maximum value of u_x and p observed along the profile. Also included are the ideal velocity and pressure profiles assumed by the LCL approximation. It is clear that both simulations display non-parabolic profiles for u_x and, non-vertical profiles of u_z and p , with the NS simulation displaying the largest deviations. This behaviour suggests the LCL approximation may be invalid for predicting the bulk flow through this sinusoidal fracture and hydraulic gradient.

Figure 5.4 displays the ratio of bulk flow rates predicted by the Stokes and LCL simulations

Q_S/Q_{LCL} for sinusoidal fractures with various values of A/b_{min} , and mild and steep values of A/λ . Also displayed on the figure are data from *Brown et al.* [1995]. The LCL simulations used three different definitions of \bar{b}_{fp}^3 given by (4.109), (4.110), and (4.111). According to *Nichols et al.* [1999], (4.109) was the definition used in LCL model developed in the work of *Brown* [1987] and subsequently applied in the work of *Brown et al.* [1995]. Therefore, the flow ratios represented as square symbols should be in agreement with the data from *Brown et al.* [1995]. The flow ratios for the mild sloped fractures are in good agreement, but the flow ratios for the steep sloped fractures significantly deviate as the relative roughness of the fracture decreases. This suggests that there are differences in the Stokes simulations performed in this work and those performed in *Brown et al.* [1995] using a lattice-gas automaton method. This also suggests that for steeply sloped sinusoidal aperture variations the LCL with (4.109) will overestimate the flow rate by a factor greater than 2 even for a small relative roughness. The flow ratios using the LCL simulations with (4.111) are shown to be quite different from the data of *Brown et al.* [1995]; however, these ratios are close to unity which indicate very good agreement with the Stokes simulations. Therefore, the LCL with (4.111) closely approximated the Stokes equations for fluid flow through the sinusoidal fracture with mildly and steeply sloped aperture variation. Equation (4.111) incorporates the effects of non-orthogonal flow into the LCL approximation which is demonstrated to be important for the sinusoidal fractures examined.

Figure 5.5(a) displays the ratio of flow rates predicted by the NS and Stokes simulations Q_{NS}/Q_S for a steeply sloped sinusoidal fracture with a relative roughness of unity and various values of Re . Again data from *Brown et al.* [1995] are included on this figure. Interestingly, even though there are apparent differences in the Q_S/Q_{LCL} data presented in this thesis work and the work of *Brown et al.* [1995], the relationship between Q_{NS}/Q_S and Re for a single sinusoidal fracture are in good agreement.

Figure 5.5(b) displays the observed relationship between the relative error e_Q of the numerical solution and the number of subdivisions applied to a CV grid originally containing $60 \times 1 \times 20$ CVs. For example, subdividing the domain by a factor of 2 creates $120 \times 2 \times 40$ CVs with reduced grid spacing. The relative error for each simulation was defined as

$$e_Q = \frac{|Q_S - Q_{n_{sub}}|}{Q_S} \quad (5.2)$$

where Q_S is the total flow rate from a reference simulation using n_{sub} equal to 5. The sinusoidal fracture examined is steeply sloped and has a relative roughness of unity (see Figure 5.3). The relative error decreases as n_{sub}^{-1} decreases or as the number of CVs increases. The regressed power relationship between e_Q and n_{sub}^{-1} is also displayed, yielding exponents of approximately 2.1 and 1.3 for the Stokes and NS simulations, respectively. For this fracture flow scenario, the exponents indicate that the accuracy of the numerical system of equations is higher for the Stokes equations. This result is expected since the viscous and pressure forces terms used in the CV formulation are

second-order accurate, whereas the inertial force terms are first-order accurate. Consequently, as the influence of the inertial terms increases in the system of equations, the overall accuracy will fall below second-order and approach first-order.

5.4 Fluid Flow through Synthetic Rough-Walled Fractures

Synthetic rough-walled fractures were generated using the method presented in Section 2.6. Fluid flow through these synthetic fractures was simulated using the two-dimensional LCL and three-dimensional Navier-Stokes models. The parameters for these simulations are summarised in Table 5.3 and the boundary conditions are presented in Sections 4.3.4 and 4.4.2 (see Figure 4.4). The following subsections discuss the comparison of the LCL simulations to published results, the comparison of the LCL to the Stokes simulations, and finally, the comparison of the Navier-Stokes and Stokes simulations. In addition, example simulations are presented of fluid flow through relatively smooth and rough fractures (σ_m/b_m equals 0.125 and 1.0, respectively) with moderate undulation (σ_z equal to 0.5 mm). These smooth and rough fracture examples have the same mechanical aperture (b_m equalling 0.5 mm) and are shown in Figures 5.6 and 5.7.

5.4.1 LCL Simulations versus Cubic Law Calculations

Figure 5.8 displays the two-dimensional fluid flow fields through each example fracture predicted by the LCL simulations using (4.109) with β_p set to unity (i.e., no correction for undulation, which is equivalent to assuming $\sigma_z = 0$). The fluid flow vectors for the smooth fracture vary mildly in magnitude and direction over the domain, whereas the vectors for the rough fracture exhibit strong heterogeneity and form distinct flow channels across the domain. This channelling behaviour is characteristic of fluid flowing through persistent or correlated large aperture pathways across the domain. In addition, the total flow rate through the rough fracture is only two thirds of the flow through the smooth fracture even though they have identical b_m values. This decrease in total flow is caused by a reduction in the cross sectional area available to flow, and then forcing the flow field through the small aperture regions along the channels. In this situation, the local velocity must increase, which leads to larger internal head losses and smaller total flow rates for a given hydraulic gradient. As discussed in Section 3.3, this channelling and hydraulic behaviour has been well documented in theoretical [e.g., Brown, 1987] and experimental [e.g., Brown *et al.*, 1998] studies.

Section 3.3.2 discussed the results of various theoretical studies examining fluid flow through random or synthetic rough-walled fractures. Figure 3.2 presents the functional relationships (equations (3.22), (3.23), (3.25), and (3.27)) that were observed between the total flow rate predicted by the LCL and the parallel plate cubic law using the arithmetic mean aperture $\langle b \rangle$ of the

fracture. Note that this flow ratio Q_{LCL}/Q_{CL} may be shown to be equivalent to the cube of the hydraulic aperture over the arithmetic mean $(b_H/\langle b \rangle)^3$. The figure displays that the LCL, under-predicts the total flow rate as compared to the cubic law when the relative roughness σ_m/b_m of the fracture is high (or alternatively b_m/σ_m is small). These functional relationships were determined using different theoretical models of rough-walled fractures and predict a range of Q_{LCL}/Q_{CL} values that diverge as σ_m/b_m increases.

Figure 5.9 superimposes the results of LCL simulations using (4.109) performed in this thesis work onto Figure 3.2 for fractures with various values of mid-surface variation or undulation. The symbols represent fractures with normal or lognormal aperture distributions with two correlation length λ_b values. The equation and source of the functional relationships from Figure 3.2 are also shown. Figure 5.9(a) displays the results for fractures with planar mid-surfaces ($\sigma_z = 0$) and represents the common situation where fracture undulation is neglected in the LCL approach. The LCL results for all the fracture types are shown to fall within the range of the previously determined relationships. The results for the fractures with normally distributed aperture fields behaved most like the relationships of *Petir and Cheng* [1978] and *Brown* [1987] which also produced normally distributed aperture fields. The results for the fractures with lognormally distributed aperture fields are shifted downward along the flow ratio-axis toward the relationship of *Renshaw* [1995] which is based on statistical arguments for lognormally distributed aperture fields. Additionally, for both normal and lognormal distributions there was a shift downward for the smaller correlation lengths. The magnitude of the shift was consistent with *Brown* [1987] who observed a second-order difference between fractures with smoothly and roughly textured aperture fields with fractal correlation. However, *Brown* [1987] observed that Q_{LCL}/Q_{CL} shifted upwards for the fractures with roughly textured aperture fields, or in other words, the LCL and cubic law were in better agreement for the roughly textured fractures. Conversely, this thesis work observed that the LCL and cubic law were in better agreement for fractures with milder spatial variation in aperture as quantified by the traditional correlation length.

Figures 5.9(b) and 5.9(c) display the LCL results for fractures with two values of undulation ($\sigma_z = 0.5$ and 1.0 mm), superimposed on the functional relationships from Figure 3.2. These figures show a shift downward in Q_{LCL}/Q_{CL} for low σ_m/b_m values as σ_z increases. Essentially, the undulation decreases the local aperture field and reduces the flow predicted by the LCL. This aperture field reduction seems to be more important when the fracture is smooth, or the relative roughness σ_m/b_m is low.

This subsection has presented two-dimensional flow fields (see Figure 5.8) from LCL simulations on the smooth and rough example fractures. These results are consistent with other published data [e.g., *Brown*, 1987] and clearly illustrate that σ_m/b_m is an important parameter for describing the distribution of flow in a rough-walled fracture. Furthermore, the total flow rates from LCL simulations on many synthetic fractures were compared to the total flow rate from the

cubic law using $\langle b \rangle$ (see Figure 5.9). In other words, the LCL total flow rate was compared to the total flow through a set of parallel plates with a constant aperture equal to the arithmetic mean of the synthetic fracture. Figure 5.9(a) shows that the results of this work are within the range of several published correlations and again that σ_m / b_m is an important parameter in terms of predicted the total flow. Figure 5.9(c) illustrates that large values of mid-surface variability or fracture undulation reduce the effective aperture for smooth fractures and should be included into the LCL approach.

5.4.2 Stokes versus LCL Simulations

Figure 5.10 displays two-dimensional vector plots of the integrated fluid flux field within each fracture predicted by the three-dimensional Stokes simulations. Qualitatively, these results are identical to the LCL simulations shown in Figure 5.8. The fluid flux vectors for the smooth fracture vary mildly in magnitude and direction over the domain, and the vectors for the rough fracture form distinct tortuous channels that convey the majority of the fluid across the domain. Quantitative differences are displayed in Figure 5.11 which was formed by subtracting the Stokes integrated flux fields from the LCL flux fields. This figure shows that the largest flux difference vectors are located along the highest flux pathways with maximum values equal to 10 and 23% of each total flow difference. These total flow differences indicate that the Stokes simulations predict total flows 3% and 14% lower than the LCL simulations for the smooth and rough fracture examples, respectively.

Figure 5.12 displays velocity fields over a two-dimensional cross-section through the centre of the fracture domains and parallel to the x - z plane (see Section C-C on Figure 5.10). The variability of the fracture geometry along each cross-section is clearly displayed, with the rough fracture cross-section displaying two points of contact. The resulting velocity fields are not entirely parallel with the fracture walls, and qualitatively, do not agree with an ideal parabolic profile between parallel plates. Figure 5.13 displays vertical velocity profiles through each cross-section in Figure 5.12 at the points labelled P1, P2, and P3. These profiles are normalized by the local aperture and the ideal maximum x -axis velocity for the integrated local flow rate. Additionally, the velocity distribution is resolved into its x - and z -components, and includes the corresponding ideal velocity profiles. Interestingly, the x -velocity is shown to be very close to the ideal parabola, whereas the z -velocity is different from the ideal value of zero. This non-zero z -velocity reflects the radial or converging-diverging nature of the flow field, and is shown to be more significant, and even asymmetric, for the rough fracture example. A consequence of this non-zero z -velocity is that larger viscous shear stresses are produced within the flow field as compared to the LCL approximation. Therefore, the Stokes simulation for the rough fracture example predicts a total flow rate 14% lower than the LCL simulation.

The fracture examples discussed so far have demonstrated small to moderate (second order)

differences between the fluid flux fields and total flow rates predicted by the LCL and Stokes equations. In order to generalize this observation, many LCL and Stokes simulations were performed on synthetic fractures with various values of relative roughness σ_m/b_m and mid-surface variability σ_z (see Table 5.3). Figure 5.14 displays the ratio of the total flow predicted from Stokes and LCL simulations Q_S/Q_{LCL} versus the fracture relative roughness. These results used synthetic fractures with σ_m/b_m values ranging from 0.0625 to 2, σ_z values of 0, 0.5, and 1.0 mm, and normally distributed aperture fields with a correlation length of 2 mm. The corresponding LCL simulations used (4.109), (4.110), and (4.111) with β_{JP} and κ_{JP} set to unity so that no geometric correction for undulation was included. Each part of Figure 5.14 displays flow ratios that decrease exponentially in response to increases in the relative roughness. This response is similar to the response of the Q_{LCL}/Q_{CL} shown in Figure 5.9 except that the magnitude of the decrease is smaller. Figure 5.14(a) shows that the total flow predicted by LCL simulations using (4.109), (4.110), and (4.111) were all very close to the Stokes simulations up to a relative roughness value of 0.25. Above 0.25 the flow ratio began to decrease exponentially with the LCL simulations using (4.110) and (4.111) predicting total flows within 10% of the Stokes simulations. The LCL simulations using (4.109) predicted slightly larger flow rates within 15% of the Stokes simulations. Parts (b) and (c) of Figure 5.14 display uniform decreases of approximately 5 and 15% across the entire range of relative roughness values in response to increases in the mid-surface variability. Interestingly, these simulations demonstrate that mid-surface undulation may be an important component of fracture roughness even when the relative roughness is low. Furthermore, the constant shift downward in Q_S/Q_{LCL} for the given mid-surface standard deviations suggests that geometric corrections based on the mid-surface fields may be effective in correcting the LCL simulations.

Figure 5.15 displays Q_S/Q_{LCL} results for the same fractures used in Figure 5.14 except that the LCL simulations incorporate the mid-surface correction terms. Figure 5.14(a) and 5.15(a) are identical since the correction terms are equal to unity when the mid-surface is a plane (i.e., σ_z equals 0). Parts (b) and (c) of Figure 5.15 clearly demonstrate that the correction terms effectively remove the downward shift in Q_S/Q_{LCL} in response to mid-surface variability. As a result, the relationship in Part (c) is very similar to Part (a) except that Q_S/Q_{LCL} levels off at a value of 1.02 instead of 1.0. In other words, the LCL with mid-surface corrections slightly under-predicts the total flow as compared to the Stokes simulations.

Figure 5.16 presents the results of Stokes and LCL simulations using (4.111) with mid-surface corrections for three different fracture types. These fracture types include normally distributed aperture fields with correlation lengths of 2 and 5 mm, and lognormally distributed aperture fields with a correlation length of 2 mm. Figure 5.16(a) shows that Q_S/Q_{LCL} for all three fracture types are identical for relative roughness values up to 0.25. Above 0.25, the Q_S/Q_{LCL} values decrease exponentially to a minimum value of 0.9. The Q_S/Q_{LCL} values for the fractures with

a correlation length of 2 mm are very similar and the Q_S/Q_{LCL} values for fractures with a correlation length of 5 mm are slightly closer to unity. Once again the effectiveness of the correction terms is demonstrated in that Parts (b) and (c) are very similar to Part (a). Effectively, the corrections have removed the influence of the mid-surface variability.

Figure 5.17 presents the Q_S/Q_{LCL} values from Figure 5.16 for the normally distributed aperture fractures with λ_b equalling 2 mm versus three roughness parameters: the actual relative roughness $\sigma_b/\langle b \rangle$, the actual roughness slope σ_b/λ_b , and the mean aperture aspect ratio $\langle b \rangle/\lambda_b$. These actual parameters are different from σ_m/b_m , σ_m/λ_b , and b_m/λ_b when the fracture aperture field is truncated during closure (see Figure 2.15). These three parameters are presented in order to examine geometric constraints on the LCL to approximate the Stokes equations (see Section 3.2.1 and Table 3.1). Following the work of *Zimmerman et al.* [1991], an acceptable level of error between the Stokes and LCL is set to be 10%, which corresponds to a minimum Q_S/Q_{LCL} value of 0.9. This minimum value is shown as a dotted line in Figure 5.17 and clearly demonstrates that all of the simulation data are within the acceptable range of error. The trend in Figure 5.17(a) suggests that $\sigma_b/\langle b \rangle$ should be limited to values below 1.0 to maintain this property. This also corresponds to a σ_m/b_m value of 2.0. These limits contrast the recommendation of *Oron and Berkowitz* [1998] to limit σ_w/b_m to values an order of magnitude below 1.0. The trend in Figure 5.17(b) suggests that σ_b/λ_b should be limited to values below 0.2 which is identical to the limit proposed by *Zimmerman et al.* [1991]. Although Figure 5.17(c) does not display a definite trend, the results are not as expected. According to the work of *Zimmerman and Bodvarsson* [1996], the value of Q_S/Q_{LCL} should approach unity as the value of $\langle b \rangle/\lambda_b$ decreases. Conversely, the numerical simulations performed in this work predict values of Q_S/Q_{LCL} that approach unity as the value of $\langle b \rangle/\lambda_b$ increases. *Zimmerman and Yeo* [1998] proposed that $\langle b \rangle/\lambda_b$ be limited to values below 0.3, and this work demonstrates acceptable error levels for values up to 0.5.

Finally, a portion of the flow ratio results from this thesis work are compared with the work of *Mourzenko et al.* [1995] in Figure 5.18. The hollow symbols are the lowest flow ratios observed in Figures 5.14 and 5.15 and the σ_m/b_m values have been transformed into σ_w/b_m using (2.20) where σ_w is the standard deviation of the wall topography which equals σ_U and σ_L . It is very clear that the discrepancy between the LCL and Stokes simulations was much smaller in this work than observed in the results of *Mourzenko et al.* [1995]. One cause of this discrepancy may be that different methods were used to represent the synthetic fracture geometry in each work. In this study the synthetic fractures are formed by combining two-dimensional random fields of aperture and mid-surface elevation that are point values (see Section 2.6). The resulting fracture walls are two-dimensional fields of elevation point values that are inter-connected with bilinear surfaces. Thus, each fracture wall may be described as a piece-wise continuous surface. *Mourzenko et al.* [1995] generated two-dimensional random elevation fields for each fracture wall as an array of horizontal plates inter-connected by vertical steps. Thus, these fracture walls are stair-stepped

fields of block elevation values, which form piece-wise discontinuous surfaces. And upon mating the fracture walls, the resulting aperture fields have the same stepped block value structure. Consequently, the fracture geometry used by *Mourzenko et al.* [1995] has an additional component of roughness due to the stair-stepped structure and the block value fields are statistically different than point value fields. Moreover, plotting the flow ratio data from Figure 5.18 against the roughness slope σ_m/λ_b , and aperture aspect ratio b_m/λ_b (see Figure 5.19) demonstrates that *Mourzenko et al.* [1995] used more steeply sloped fractures with larger aspect ratios. Note that the uncorrelated data from *Mourzenko et al.* [1995] was transformed by assuming that σ_m equals $2^{1/2} \sigma_w$. This transformation is appropriate since *Mourzenko et al.* [1995] defined b as Z_U minus Z_L , and therefore, σ_m^2 is approximately equal to $\sigma_U^2 + \sigma_L^2$ or $2 \sigma_w^2$. Interestingly, the unclear trend observed in Figure 5.17 is clearly observed in Figure 5.19(b), where the value of Q_S/Q_{LCL} approaches unity for as b_m/λ_b increases, rather than decreases.

This section compared Stokes and LCL simulations using various aperture definitions and aperture corrections. Simulations using synthetic example fractures demonstrated that the integrated fluid flux fields from the Stokes simulations were qualitatively identical to the fluid flux field from the LCL simulations. Differencing these fields revealed some qualitative differences along the high flow pathways which corresponded to significant vertical components in the velocity field. Simulations using many synthetic fractures demonstrated that total flow rate predicted by the LCL with geometric corrections were within 2% of Stokes for σ_m/b_m values below 0.25 and within 10% for σ_m/b_m values above 0.25 and below 2. These results clearly demonstrate the utility of LCL and were used to set limits on two roughness parameters for its validity. Observing trends in Q_S/Q_{LCL} suggests that $\sigma_b/\langle b \rangle$ and σ_b/λ_b be limited to values below 1.0 and 0.2, so that Q_S and Q_{LCL} are within 10%. The observed trend in Q_S/Q_{LCL} versus $\langle b \rangle/\lambda_b$ was the inverse of what is predicted in theoretical work of *Zimmerman and Bodvarsson* [1996], and suggests that $\langle b \rangle/\lambda_b$ may not be useful as a single parameter to limit the validity of the LCL. Finally, the values of Q_S/Q_{LCL} in this thesis work were much closer to unity than the work of *Mourzenko et al.* [1995] which used synthetic fractures with stair-stepped features and larger values of σ_m/λ_b and b_m/λ_b .

5.4.3 Navier-Stokes versus Stokes Simulations

Figure 5.20 displays two-dimensional vector plots of the integrated fluid flux field within each example fracture predicted by the three-dimensional NS simulations. Qualitatively, these results are identical to the LCL and Stokes simulations shown in Figures 5.8 and 5.10. Once again, the fluid flux vectors for the smooth fracture vary mildly in magnitude and direction over the domain, and the vectors for the rough fracture form distinct tortuous channels that convey the majority of the fluid across the domain. However, the vectors in Figure 5.20 are more concentrated in the flow channels and define smoother pathways of fluid flux as compared to Figure 5.10. This indicates that inertial forces are resisting changes in direction and magnitude within the velocity field.

Figure 5.21 clearly quantifies these differences by subtracting the integrated flux fields from the NS simulations from the Stokes simulations. The largest flux difference vectors are located along the highest flux pathways with maximum values equal to 8 and 22% of each total flow difference. These total flow differences indicate that the NS simulations predict total flows 8% and 36% lower than the Stokes simulations for the smooth and rough fracture examples, respectively.

Figure 5.22 displays velocity vector plots over a two-dimensional cross-section through the centre of the fracture domains and parallel to the x - z plane (see Section C-C on Figure 5.20). As with the Stokes simulations (see Figure 5.12), the resulting velocity fields are not entirely parallel with the fracture walls, and qualitatively, do not agree with an ideal parabolic profile between parallel plates. Given the wide range in vector magnitude displayed in Figures 5.12 and 5.22, it is difficult to observe differences in the NS and Stokes profiles. Figure 5.23 displays vertical velocity profiles through each cross-section in Figures 5.12 and 5.22 at the points labelled P1, P2, and P3. These profiles are normalized by the local aperture and the ideal maximum x -axis velocity for the local integrated flow rate. This normalization allows for differences in the x and z -components of the velocity profiles to be clearly observed and compared to the ideal situation. As stated previously, the Stokes x -velocity profiles follow the ideal profile very closely, and the z -velocity is non-zero to reflect the radial or converging-diverging nature of the flow field. Relative to the Stokes profiles, all the NS profiles are skewed in the direction of mean local flow, or in other words, resist changing direction as imposed by the fracture walls. Interestingly, several NS profiles have flatter peaks or noses which indicates the formation of an inertial core between the walls. Once again these properties reflect that the inertial forces are significant and resist changes in direction and magnitude in the flow field. Consequently, viscous shear stresses are altered by the skewed velocity profiles, and most importantly, a portion of the hydraulic (pressure plus gravity) forces are balanced by inertial forces so that the forces driving the flow field are reduced. Therefore, the total flow rate may be significantly reduced. For example, the NS simulations for the smooth and rough fracture examples predicted total flow rates 8 and 36% less than the Stokes simulations.

In order to generalize the influence of inertial forces on the total flow rate through rough-walled fractures many NS simulations were performed on synthetic fractures and compared with corresponding Stokes simulations (see Table 5.3). Figure 5.24 displays the ratio of the total flow predicted from NS and Stokes simulations Q_{NS}/Q_S versus the fracture relative roughness. Since the only difference between the NS and Stokes simulations is the presence of the inertial force terms, Q_{NS}/Q_S values below unity reflect the influence of inertial forces alone. As with the LCL and Stokes simulations presented in Figure 5.14, these results used synthetic fractures with σ_m/b_m values ranging from 0.0625 to 2, σ_z values of 0, 0.5, and 1.0 mm, and normally distributed aperture fields with a correlation length of 2 mm. In addition, these results are delineated into three values of mechanical aperture b_m (0.25, 0.5, and 1.0 mm) and hydraulic gradients i (0.01, 0.1, and

1.0). Both of these parameters influence the magnitude of inertial forces within the flow field since they directly influence the fracture conductivity and the driving forces across the fracture. Figure 5.24 clearly demonstrates the influence of inertial forces on the total flow rate and the interrelation between b_m and i . The simulations using the smallest values of b_m and i have Q_{NS}/Q_S values close to unity even as the relative roughness increases. However, increasing b_m and/or i causes Q_{NS}/Q_S to fall well below unity and decrease exponentially with increases in σ_m/b_m . Clearly the simulations using the largest values of b_m and i have the lowest Q_{NS}/Q_S values at approximately 0.4. Interestingly, increases in the mid-surface variability σ_z shifts Q_{NS}/Q_S downward for the lower σ_m/b_m values, and slightly shifts Q_{NS}/Q_S upward for the higher values of σ_m/b_m . Again, this indicates that mid-surface variation or fracture undulation is an important component of fracture roughness when the relative roughness is low. Figures 5.25 and 5.26 display the results for fractures with normally and lognormally distributed aperture fields with λ_b equalling 5 mm and 2 mm, respectively. These figures are very similar to Figure 5.24, especially in response to increases in σ_z at lower values of σ_m/b_m . This is not surprising because at low values of σ_m/b_m all three aperture distributions are very similar (e.g., see Figure 2.9(b)). However, there are subtle differences at higher σ_m/b_m values, where the normally distributed aperture fractures display more decay in Q_{NS}/Q_S as σ_m/b_m increases, and the lognormally distributed aperture fractures display less decay. In the normally distributed aperture fractures with λ_b equalling 5 mm this behaviour reflects that more dominant channels formed as σ_m/b_m increases or the fracture closes, and that these channels have a greater influence on the inertial forces. In the lognormally distributed aperture fractures with λ_b equalling 2 mm this behaviour reflects differences in σ_m/b_m and σ_m^*/b_m^* as the fracture closes and the distribution becomes positively skewed (e.g., see Figure 2.9(c)).

Figures 5.24, 5.25, and 5.26 present many NS simulations with significant inertial forces that predict total flow rates that are substantially less than the Stokes simulations. However, these figures also demonstrate that there are situations when the NS and Stokes simulations are in close agreement. Given that the numerical solution of the linear Stokes equations is more straight forward than the non-linear NS equations, it is important to identify the situations where the NS equations can be replaced by the Stokes equations with minimal error. In other words, it is important to delineate the kinematic constraints of ignoring the inertial terms in the NS simulations. In addition, the previous section demonstrated that the total flow rate from Stokes and corrected LCL simulations were within 10% for the all synthetic fractures used in this thesis work. Therefore, delineating kinematic constraints by comparing the total flow rates from NS and Stokes simulations will also be applicable to LCL simulations. Table 3.1 presents three dimensionless kinematic constraints for the LCL that are discussed in Section 3.2.1 and are based on approximate analytical solutions of fluid flow through ideal fracture geometries.

Figure 5.27 displays Q_{NS}/Q_S values for all three fracture types versus the Reynolds number Re of the bulk flow across the synthetic fractures. In this work Re is defined as (3.5) and

represents the strength of inertial forces relative to viscous forces through the fractures. The Q_{NS}/Q_S values for all three fracture types are shown to be very close to unity for Re values below 1. At Re values above 1, the values of Q_{NS}/Q_S decrease exponentially with similar rates of decay. Comparing Parts (a), (b), and (c) of the figure displays a leftward shift in the data to lower Re values as σ_z increases. Furthermore, data points with Q_{NS}/Q_S values close to unity and high Re values are shifted downward to lower Q_{NS}/Q_S values as σ_z increases. These data that are shifted downward represent fractures with low σ_m/b_m , and high b_m and i values which were shown to be very sensitive to σ_z in Figures 5.24 to 5.26. Overall these data demonstrate for Re values above 1 to 10, that the inertial forces become more significant as the fracture undulation increases. Conversely, for Re values below 1, the influence of inertial forces is negligible so that Q_{NS}/Q_S is close to unity. This limiting value of Re corresponds exactly with the constraint proposed by *Zimmerman and Bodvarsson* [1996].

Figure 5.28 displays Q_{NS}/Q_S values for all three fracture types versus the parameter $Re \langle b \rangle / \lambda_b$, which was proposed by *Zimmerman and Yeo* [1998] (see Table 3.1). The distribution of the data for each value of σ_z is very similar to Figure 5.27, except that the Q_{NS}/Q_S values are skewed toward the lower $Re \langle b \rangle / \lambda_b$ values. For $Re \langle b \rangle / \lambda_b$ values below 0.1, the influence of inertial forces is shown to be small so that Q_{NS}/Q_S is close to unity. This limiting value of $Re \langle b \rangle / \lambda_b$ is significantly lower than the constraint proposed by *Zimmerman and Yeo* [1998] equal to 8.

Figure 5.29 displays Q_{NS}/Q_S values for all three fracture types versus the parameter $Re \sigma_b / \langle b \rangle$, which is a modified version of $Re \sigma_w / b_m$ proposed by *Oron and Berkowitz* [1998] (see Table 3.1). As shown in the figure, this parameter concentrates the Q_{NS}/Q_S data into a narrower range and a clearer trend. Again, the data respond to increases σ_z in a similar manner to Figures 5.27 and 5.28. For $Re \sigma_b / \langle b \rangle$ values below 1, the influence of inertial forces is shown to be negligible so that Q_{NS}/Q_S is close to unity. This limiting $Re \sigma_b / \langle b \rangle$ value is substantially higher than the proposal of *Oron and Berkowitz* [1998] to constrain $Re \sigma_w / b_m$ to be much less (i.e., one to two orders-of-magnitude) than 1.

This subsection has compared NS and Stokes simulations of fluid flow through synthetic rough-walled fractures. Velocity vector and profile plots from the example fracture simulations demonstrated that the velocity field resisted changes in direction and magnitude when the inertial forces became significant. In addition, the increase in inertial forces balanced a portion of the driving hydraulic forces, thus reducing the overall flow rate through the example fractures. The results of many synthetic fracture simulations clearly demonstrated that Q_{NS}/Q_S may fall significantly below unity for larger values of σ_m/b_m , b_m , and i . Furthermore, increases in the fracture mid-surface variability σ_z were shown to reduce Q_{NS}/Q_S , especially for low σ_m/b_m values. Finally, several dimensionless kinematic constraints were determined by limiting Q_{NS}/Q_S to be close to unity.

5.4.4 Navier-Stokes Simulations versus Cubic Law Calculations

Up to this point in Section 5.4, LCL simulations have been compared to cubic law calculations, Stokes to LCL simulations, and NS to Stokes simulations. This comparison has focussed on total flow rates and has demonstrated for certain flow and fracture properties that the LCL, Stokes, and NS simulations predicted very similar values. This subsection takes this comparison to the logical endpoint by directly comparing the NS simulations to cubic law calculations. The NS simulations represent the most complete and complex flow solution and the cubic law based on the arithmetic mean aperture of the fracture represents the most straight forward and simplest flow solution.

Figure 5.30 displays Q_{NS}/Q_{CL} versus σ_m/b_m for the normal type fractures with λ_b equalling 2 mm. The results for the lowest i and b_m values are very similar to the Q_{LCL}/Q_{CL} data displayed in Figure 5.9, that is, the decrease in Q_{NS}/Q_{CL} is controlled by σ_m/b_m . This demonstrates that the differences between the LCL, Stokes, and NS models are small compared to the base difference between all these models and the cubic law. However, for the larger i and b_m values the influence of inertial forces becomes clear and Q_{NS}/Q_{CL} is shifted significantly downward, especially for low σ_m/b_m values. This demonstrates that inertial forces may significantly reduce the total flow rate through rough-walled fractures, even when the fractures are relatively smooth.

The final exercise of this subsection is to transform the flow ratio Q_{NS}/Q_{CL} data in Figure 5.30 into the common form, $b_H/\langle b \rangle$, which is the ratio of the hydraulic aperture to the arithmetic aperture mean aperture. This transformation is performed by taking the cube root of the Q_{NS}/Q_{CL} data since Q_{NS}/Q_{CL} may be shown to be equivalent to $(b_H/\langle b \rangle)^3$. Figure 5.31 displays $b_H/\langle b \rangle$ values that range from 1 to 0.5 for the range of σ_m/b_m considered in this work. This figure demonstrates that b_H is an appropriate estimate of $\langle b \rangle$ over a limited range of σ_m/b_m when i and b_m are low. Otherwise, b_H under-estimates $\langle b \rangle$ for larger values of σ_m/b_m , b_m , and i . This numerical result supports the common laboratory or field observation that the measured hydraulic aperture is smaller than the estimated arithmetic mean aperture (see Section 2.2).

5.4.5 Accuracy, Errors, and Variability of Synthetic Fracture Simulations

Sections 4.3 and 4.4 presented the numerical formulation of the Navier-Stokes and LCL models. These models used the FV method to approximate the governing equations and the majority of the FV terms had second-order spatial accuracy. The exceptions were the first-order UDS approximations of the inertial force terms (see (4.36)) and extrapolation of velocity vector to the inlet and outlet boundaries (see (4.72)) in the three-dimensional model. Also, it is important to note that the method of fracture discretization was an additional component of the numerical accuracy in each model. In this work, the fracture walls were approximated as piece-wise

continuous bi-linear curved surfaces, interpolated over a uniform x - y grid of point values which defined the fracture. Consequently, refining the discretization of the fracture domain increases the accuracy of both the governing equations and the fracture geometry, and thus, the numerical solution and physical domain are smoothed.

Figure 5.32 displays the relative error in the total flow rate e_Q (see (5.2)) predicted by LCL, Stokes, and NS simulations versus the inverse number of subdivisions n_{sub}^{-1} applied to base CV grids originally containing 25×25 CVs in 2D or $25 \times 25 \times 10$ CVs in 3D. These simulations used a smooth and rough fracture (σ_m/b_m equalling 0.0625 and 0.5) with b_m , σ_z , and i values equal to 1.0 mm, 1.0 mm, and 1.0, respectively. As expected, e_Q for each model and fracture type decreased as n_{sub}^{-1} decreased, or alternatively, as the number of CVs increased. The LCL simulations displayed the smallest e_Q values, ranging from 0.0001 to 0.03, the Stokes simulations displayed values ranging from 0.0009 to 0.07, and the NS simulations display the largest e_Q values, ranging from 0.02 to 0.2, where Re equalled ~ 220 . For the LCL and Stokes simulations, the relative error for the smooth fracture was lower than the rough fracture, whereas the NS simulations predicted similar values. The regressed power relationships between e_Q and n_{sub}^{-1} are displayed in the figure and yield exponents ranging from 1.9 to 3.7. These exponents reflect the spatial accuracy of the numerical simulations. All of the exponents are equal to approximately 2 or greater. The fact that many of these exponents are significantly greater than 2 demonstrates the importance of domain smoothing on the simulations.

It is important to discuss the magnitude of e_Q for the synthetic fracture simulations used in Sections 5.4.1 to 5.4.3. For these simulations n_{sub} equalled 2, which corresponds to e_Q values ranging from 0.001 to 0.02 for the LCL and Stokes simulations, and values of 0.1 and 0.13 for the NS simulations. These e_Q values suggest that the total flow rates from LCL and Stokes simulations are within 2% of the reference simulation, and that the large Re NS simulations are greater than 10% different. Therefore, the NS results with large Re values discussed in Section 5.4.3 must be qualified with at least a 10% error envelope. Incidentally, the absolute value used in (5.2) masks the direction of the errors. In general, the NS simulations under-predicted the total flow rate as compared with the reference simulations. Therefore, the figures in Section 5.4.3 overestimate the reduction in Q_{NS}/Q_S for large Re values by greater than 10%. However, considering that the overall reduction in Q_{NS}/Q_S is much greater than 10%, the influence of inertial forces on the flow field is still clearly demonstrated. Furthermore, the kinematic constraints are determined at values of Q_{NS}/Q_S close to unity, and more importantly, at Re values 2 orders-of-magnitude lower than in Figure 5.30(c). Therefore, the magnitude of errors associated with these constraints is likely to be on the order of 1% rather than 10%.

To illustrate the variability of the synthetic fractures simulations, Figure 5.33 displays all the realizations (as symbols) used to estimate the mean behaviour (solid lines) of Q_S/Q_{LCL} and Q_{NS}/Q_S versus σ_m/b_m for the normal fractures with λ_b , σ_z , and i values equal to 2 mm, 1 mm, and 1,

respectively. For most values of σ_m/b_m the mean values are calculated with 5 realizations. Obviously, more realizations and variation in fractures parameters are required to rigorously generalize the mean behaviour of Q_S/Q_{LCL} and Q_{NS}/Q_S ; however, the variability is quite low for the limited number of realizations performed in this work. The variability in Q_S/Q_{LCL} is shown to increase with σ_m/b_m , whereas the variability in Q_{NS}/Q_S does not clearly show this property. In both cases, the values are within 0.05 from the mean values; however, this magnitude may be large compared to the overall trends in Q_S/Q_{LCL} and the value of 0.9 used to determine the geometric constraints in Figure 5.17. Conversely, this magnitude is small compared to the overall trends observed in Q_{NS}/Q_S . Furthermore, Figure 5.33 demonstrates that the variability associated with the kinematic constraints (values of Q_{NS}/Q_S approximately equal to 1 and Re below 1) is small.

5.5 Solute Transport through Parallel Plates

Two-dimensional solute transport through parallel plates was simulated using the RWPM and a parabolic velocity distribution given by the cubic law. Figure 5.34 displays a schematic diagram of the two-dimensional domain that is characterized by the plate length L and aperture b . Two types of boundary conditions used with the RWPM are also displayed in the figure. Figure 5.34(a) shows reflection boundaries at the plate walls, and one-way boundaries at the plate inlet and outlet. The term one-way indicates that particles are only permitted to cross the boundary in the positive x -direction. Once a particle enters the domain, the inlet boundary becomes a reflection boundary, and as soon as a particle crosses the outlet boundary, the transport simulation of that particle terminates. The boundary conditions displayed Figure 5.34(b) are very similar to Figure 5.34(a) except that a two-way boundary is used at the inlet. Particles are injected along the line at the inlet boundary, and are allowed to move in the positive and negative x -directions (i.e., they may cross the inlet boundary more than once).

Table 5.4 presents the transport parameters for 7 simulations which correspond to a wide range of Pe and Pe_M values. For all of these simulations the values of L and b are held constant and the value of the average velocity U is varied. The final simulation T7 represents the very ideal situation where the solute is transported by advection alone. Table 5.4 also displays the time-scales of advection t_{adv} , diffusion t_{dif} , and mixing t_{mix} within the domain, the time step Δt employed by each simulation, and the effective dispersion coefficient D_e given by (3.36).

Figure 5.35 displays particle positions for simulation T1 at three time values for the two sets of boundary conditions shown in Figure 5.34. The time values are normalized by the hydraulic residence time of the parallel plates ($t_R = L / U$). Simulation T1 has the lowest Pe value of the parallel plate simulations and represents solute transport with a significant diffusive component. The figure illustrates the strength of diffusion in the simulation where particles diffuse in all

directions to fill the entire domain. Additionally, the one-way boundary is shown to enhance the transport of the particles toward the outlet boundary by reflecting diffusive particle displacements in the positive x -direction. Or conversely, the two-way boundary retards transport toward the outlet boundary by allowing particles to move in the negative x -direction across the inlet boundary.

Figure 5.36(a) displays particle positions from simulation T4 for three values of normalized time using the boundary conditions shown in Figure 5.34(a). Simulation T4 has a Pe value 1000 times greater than simulation T1, and consequently, the magnitude of diffusive transport in the longitudinal direction is much smaller than in simulation T1. Instead of filling the entire domain, the particles stay more concentrated around the plug-flow front. Consequently, the one-way inlet boundary does not influence the transport of the particles toward the outlet boundary. Note however, that the particles are uniformly distributed between the plates, or in other words, are well-mixed across the plate aperture. As discussed in Section 3.2.2, this mixing behaviour is expected when t_{mix} is less than t_{adv} , or equivalently, when Pe_M is below unity.

Figure 5.36(b) displays particle positions from simulation 7 for three values of normalized time. This simulation demonstrates that in the absence of diffusion the vertical position of each particle remains constant and the longitudinal transport is totally controlled by the parabolic velocity distribution.

Figure 5.37 displays the particle breakthrough curves (BTCs) for simulations T1 to T7 using the one-way inlet boundary condition. Part (a) of the figure displays the simulations with sufficient diffusion to mix the particles across the aperture, and consequently, may be compared to the exact solutions shown in Figure 3.5 (shown as hollow symbols). The BTC for simulation T1 clearly displays the influence of the one-way boundary on the diffusive transport where breakthrough is significantly earlier than the exact solution. The results of the remaining simulations are shown to be in greater agreement with the exact solution as the value of Pe increases and the front of the BTCs sharpen. Figure 5.37(b) displays the BTCs for the simulations where the particles are no longer well-mixed across the aperture. In other words, advection overwhelms diffusion so that the particles are no longer uniformly distributed across the plates. The BTCs are shown to move between the limiting well-mixed simulation T4 to the advection only simulation T7 as the value of Pe increases. Note that the BTC for simulation 7 is shown to match the exact solution given by (3.32) and (3.34).

Figure 5.38 displays the particle BTCs for simulations T1 to T7 using the two-way inlet boundary condition. Comparing the BTCs for simulations T1 to T3 with the corresponding simulations in Figure 5.37 indicates that the two-way inlet boundary condition better represents the exact solution. This was expected since the exact solution represents diffusion or dispersion as a two-way process in the longitudinal direction. It is important to note that for simulations T4 to T7 that the BTCs in Figures 5.37 and 5.38 are identical.

Figure 5.39 displays the particle BTCs for simulations T1, T2, and T4 using different values of the time step Δt , and number of particles n_p . These BTCs are relatively insensitive to the halving and doubling of the base Δt and n_p values, which indicates that these base values are adequate to simulate particle transport through the domain.

This subsection has presented the results of two-dimensional solute transport simulations through parallel plates using the RWPM. These results demonstrate that the developed transport model was able to accurately represent advective and dispersive transport through parallel plates. The model results were shown to agree with exact solutions for solute transport when Pe was between 400 and 4000. For Pe values below 400, the model and exact solutions were shown to disagree; however, this discrepancy was related to the inlet and outlet boundary conditions rather than the underlying transport processes. In the ideal simulation where diffusive transport was neglected, the transport model matched the exact solution for advective transport between parallel plates. The flexibility of the RWPM was clearly demonstrated in these simulations since the model was applicable for the entire range of Pe and Pe_M values considered.

5.6 Fluid Flow and Solute Transport through Laboratory Fractures

This section presents the results of three-dimensional fluid flow and solute transport simulations through two laboratory fracture samples that were characterized by measuring the topography of the fracture walls on a 2×2 mm grid (see Section 2.5). Figures 2.1 and 2.2 display the wall topography of the fractures, and Figures 2.3 and 2.4 display the raw aperture fields that are formed by differencing the walls. Figures 2.6 and 2.7 display the actual aperture fields formed by adding the mechanical aperture b_m and truncating aperture values below the contact aperture b_c . These figures use values of b_m that were estimated from exterior measurements on the assembled fracture samples. In this section, the laboratory fracture characterization data presented in Section 2.5 is altered in two ways. Firstly, the topographic and aperture fields have been averaged to form fields defined on a 4×4 mm grid. Secondly, the value of b_m was adjusted so that the total flow rate given by fluid flow simulations matched those observed in laboratory tests. At this point, it is also important to note that the laboratory tests involving Fracture II were performed on a transparent replica of Fracture II, whereas the fracture characterization used the actual fracture.

Figure 5.40 displays a schematic diagram of the laboratory apparatus used to conduct hydraulic/tracer tests on the two fracture samples. The sides of the fractures were sealed and the inlet and outlet boundaries were capped with semi-cylindrical cells. These cells provided pressure equalization and fluid/tracer accessibility along the entire width of the fracture, and more importantly, incorporated a recirculation system to ensure that the inlet and outlet boundaries were

well-mixed. The test was initialized by introducing a known concentration of tracer (bromide) into the reservoir, feed line, and inlet cell. Then a fixed flow rate was pumped through each fracture sample and the head loss across the fracture, and the tracer concentration in the inlet and outlet cells was measured over time. Figure 5.40(b) displays a conceptual cross section of the apparatus and illustrates the direction of the bulk flow Q , and several tracer concentration values defined at the inlet cell C_i , outlet cell C_o , and the end of the fracture C_f . Assuming that the outlet cell is completely and continuously mixed, the average tracer concentration at the end of the fracture may be estimated by the mixing cell equation

$$\frac{V_o}{Q} \frac{dC_o}{dt} = t_o \frac{dC_o}{dt} = C_f - C_o \quad (5.3)$$

where V_o and t_o are the volume and average residence time of the outlet cell. Figure 5.41 displays the values of C_i and C_o observed over time during a tracer test on each fracture. The value of C_i was not constant at early time because it was difficult to initialize the cell to a known concentration without allowing tracer to enter the fracture. The value of C_o is shown to increase smoothly over time, and levels as C_o approaches C_i . The breakthrough of tracer occurs more quickly in Fracture I since it has a lower hydraulic residence time than Fracture II (t_R equalled 8.6 versus 14 min). Also displayed in Figure 5.41 is the estimate of C_f using C_o and (5.3) for each fracture. These C_f estimates are very sensitive to small variations in dC_o/dt since the residence time of the outlet cells was quite high relative to the residence time of the fractures (t_o equalled 67 and 42 min for Fracture I and II, respectively). Consequently, C_f displays significant variation, especially at early time as the value of C_f approaches C_i ; however, the initial breakthrough front of solute from the fractures is clearly delineated.

Table 5.5 lists the various parameters used to simulate fluid flow and solute transport through the three-dimensional void space of each laboratory fracture. The goal of these simulations was to directly compare the predictions of the developed models to the observed flow and transport behaviour. The first step of this comparison required the calibration of the flow fields for each fracture. As noted above, the mechanical aperture b_m was adjusted so that the predicted total flow rate matched the observed value for the given hydraulic boundary conditions. In other words, b_m was used as a fitting parameter to calibrate the flow fields. These flow simulations employed the boundary conditions presented in Section 4.3.4, except that the side boundaries were treated as wall boundaries. Fracture I required a b_m value of 0.13 mm so that the simulated flow rate matched the observed flow rate of 0.5 mL/min under a hydraulic gradient of 0.12, and Fracture II required a b_m value of 0.585 mm to match the observed flow rate of 1.3 mL/min under a hydraulic gradient of 0.002. In both cases the fitted values of b_m were reduced from the original values estimated from external measurements on the assembled fractures (0.20 and 0.74 mm for Fractures I and II, respectively). Figures 5.42 and 5.43 display the calibrated aperture fields of each fracture and the integrated flow field predicted by the NS model. These flow fields are very heterogeneous

throughout the fractures with the primary flow pathways following tortuous channels of high aperture.

Figures 5.44 and 5.45 display the x - y position of 10,000 particles predicted by the transport model using the flow fields displayed in Figures 5.42 and 5.43. The one-way inlet boundary was employed for these simulations since the values of Pe were very high (5.6×10^4 and 3×10^4). The parameters used in these simulations are listed in Table 5.5. These figures are instantaneous snapshots at three values of normalized time (0.1, 0.25, and 0.5) defined as a fraction of the hydraulic residence time. The particle distributions display fingering along the primary flow channels and trapped particles in low-flow regions with small aperture or near the side boundaries. In examining the evolution of the particles over time, it is clear that particles moving along different fingers or channels will breakthrough the fracture outlet at different times. This is especially evident in the particle distribution for Fracture I at a normalized time of 0.5 where channels in the upper half of the fracture have transported particles much closer to the outlet as compared to the lower half. These figures also demonstrate that the front of particles in Fracture II display more spreading or dispersion as compared to Fracture I. In other words, the particles in Fracture II move in a thicker line, which is clearly displayed at the normalized time of 0.1. This discrepancy in front thickness is caused by the differences in the overall magnitude of the aperture fields and the strength of advection in the flow fields. As reported in Table 5.5, the effective Peclet numbers Pe^* of Fractures I and II were 11,000 and 1,000, respectively. While this calculation assumes that the fractures behave as parallel plates, it indicates that on average the longitudinal dispersive transport along a particular channel in Fracture II is an order of magnitude larger than Fracture I.

Figure 5.46 displays the simulated and observed breakthrough curves for each fracture. The observed concentration data were normalized with C_i values of 107.3 and 75.6 mg/L for Fracture I and II, respectively. These C_i values reflect trends or levelling at early time (see Figure 5.41). The transport model predicted the breakthrough curves for C_f and the corresponding C_o curve was determined using (5.3). As displayed in Figure 5.46(a), the simulated and observed results for Fracture I are in very good agreement. Two parameter adjustments were performed to achieve this agreement. The first is the calibration of b_m to the observed flow rate, and the second is the normalization of the observed concentration data. Interestingly, the simulated C_f breakthrough curve displays a stair-stepped feature which indicates the late contribution of the lower half of the fracture to the particle breakthrough (see Figure 5.44). Figure 5.46(b) shows that the simulated breakthrough curves for Fracture II did not match those observed. In particular, the simulated curves are shown to breakthrough in approximately half the time as those observed. One possible explanation for this discrepancy is that the overall dimensions of the transparent replica fracture (245×160 mm) used in the laboratory test were significantly larger than those used in the simulation (224×140 mm). This difference occurred because the method used to characterize the

actual fracture could not cover the entire fracture wall. Consequently, the hydraulic residence time of the simulation domain was approximately 25% less than the residence time of the transparent replica fracture.

Figure 5.47 displays the same simulated and observed breakthrough curves presented in Figure 5.46 except that the time axis has been normalized. Time for the simulated curves is normalized by the hydraulic residence time, and time for the observed curves is normalized by the median arrival time of the C_f front (i.e., the time where C_f/C_i equals 0.5). It is clear that this normalization has little effect on the results for Fracture I since Figures 5.46(a) and 5.47(a) are essentially identical. Comparing Figures 5.46(b) and 5.47(b) shows that this normalization brings the C_f results for Fracture II into better agreement. However, if the initial discrepancy between the simulated and observed results for Fracture II were primarily due to the difference in overall dimensions (residence times), then this normalization should be successful in bringing both C_f and C_o curves into better agreement. Therefore, the continued disagreement of the C_o curves suggests that there are other factors contributing to the differences between the simulations and observations. The most probable explanation is that the void space of the transparent fracture replica is markedly different than the void space characterized on the actual fracture.

Also displayed in Figure 5.47 are C_f breakthrough curves for parallel plates with an aperture equal to the mean aperture of the fracture samples and Pe^* values equal to those estimated in Table 5.5. These ideal breakthrough curves are obviously much sharper than those observed or simulated. The differences are attributed to the channelling and fingering of the solute along the various flow paths, and provide a clear example of macroscopic dispersion over the fracture [Russell *et al.*, 2000].

Figure 5.48 displays the simulated particle breakthrough for Fracture I using two values of the minimum wall distance fraction ($F_w = 0.1$, and 0.0). This transport parameter was presented in Section 4.5.2 to set the minimum vertical distance between a particle and the fracture walls (see equation (4.124)) so that particles do not become artificially trapped along the walls. The simulated Fracture I BTCs are not very sensitive to F_w , and demonstrate that the strength of diffusion is sufficient to keep particles from becoming trapped along the walls.

This section directly compared simulated and observed tracer breakthrough curves for two laboratory fracture samples. The flow field for each simulation was calibrated by adjusting the mechanical aperture of the fracture void space until the total flow rate matched the observed value. The resulting flow fields, typical for rough walled fractures, displayed tortuous high-flow pathways along large aperture channels and low-flow zones in small aperture regions. The tracer transport simulations predicted particle distributions that exhibited channelling or fingering along the high-flow pathways, and particle entrapment in the low-flow zones. For Fracture I the simulated breakthrough of particles was shown to be in very good agreement with the observed solute breakthrough curve. In fact, the simulation displayed a stair-step feature that matches the

observed data, and has been previously observed in other laboratory studies (e.g., see Figure 3.1). The simulated particle breakthrough for Fracture II was not successful in matching the observed tracer breakthrough curve. It is likely that the fracture characterization data used for the flow and transport simulations do not match the transparent fracture replica used in the experiments.

Table 5.1. Parameters used in three-dimensional parallel plate simulations.

parameter	value(s)	units
<i>x-y grid:</i>		
total dimensions L, W	40, 40	mm
control volumes n_i, n_j	20, 20	—
uniform spacing δ_x, δ_y	2, 2	mm
<i>z grid:</i>		
aperture b	0.1	mm
control volumes n_k	5, 10, 20, 40	—
uniform spacing δ_z	0.02, 0.01, 0.005, 0.0025	mm
<i>fluid properties:</i>		
density ρ	1000	kg/m ³
viscosity μ	0.001	Pa-s
hydraulic gradient i	1	—

Table 5.2. Parameters used in sinusoidal fracture flow simulations.

parameter	value(s)	units
<i>x-y</i> grid:		
length L	7.5, 30	mm
width W	2.5, 10	mm
control volumes n_i, n_j	60, 20	—
uniform spacing δ_x	0.125, 0.5	mm
uniform spacing δ_y	0.125, 0.5	mm
sinusoid:		
aperture $b(x)$	$b_{\min} + A \left[1 - \cos \left(\frac{x}{A} \pi \right) \right]$	mm
amplitude A	1	mm
wave length λ	2.5, 10	mm
relative roughness A/b_{\min}	0.125, 0.25, 0.5, 1, 2, 4	—
3D z grid:		
control volumes n_k	20	—
non-uniform spacing $\delta_z(x)$	$b(x)/20$	mm
2D characteristic aperture cubed \bar{b}_{fp}^3	Eq. (4.109), (4.111)	mm ³
fluid properties:		
density ρ	1000	kg/m ³
viscosity μ	0.001	Pa-s
hydraulic gradient i	0.001, 0.033, 0.01, 0.033, 0.1	—

Table 5.3. Parameters used in synthetic fracture flow simulations.

parameter	value(s)	units
<i>x-y</i> grid:		
length L , width W	50, 50	mm
number subdivisions n_{sub}	2	—
control volumes n_i, n_j	50, 50	mm
uniform spacing δ_x, δ_y	1, 1	mm
aperture field:		
correlation length λ_b	2.5, 10	mm
initial aperture b_m	0.25, 0.5, 1.0	mm
initial standard deviation σ_m	0.125, 0.25, 0.5, 1, 2, 4	mm
roughness slope σ_m / λ_b		—
relative roughness σ_m / b_m		—
distribution	normal, lognormal	—
contact aperture b_c	$b_m / 100$	mm
mid-surface field:		
correlation length λ_z	10	mm
standard deviation σ_z	0, 0.5, 1.0	mm
3D z grid:		
control volumes n_k	25	—
non-uniform spacing $\delta_z(x, y)$	$b(x, y) / 25$	mm
2D characteristic aperture cubed \bar{b}_{fp}^3	Eq. (4.109), (4.110), (4.111)	mm ³
fluid properties:		
density ρ	1000	kg/m ³
viscosity μ	0.001	Pa-s
hydraulic gradient i	0.01, 0.1, 1.0	—

Table 5.4. Parameters used in the parallel plate transport simulations.

(a) constant parameters		value	units
total length L		20	mm
aperture b		0.1	mm
number of particles n_p		1000	—
minimum wall distance fraction F_w		0	—

(b) simulation specific parameters										
	¹ U [mm/s]	² D_m [mm ² /s]	³ t_{adv} [s]	⁴ t_{dif} [s]	⁵ t_{mix} [s]	⁶ Δt [s]	⁷ Pe [-]	⁸ Pe_M [-]	⁹ D_e [mm ² /s]	¹⁰ Pe^* [-]
T1	4×10^{-4}	2×10^{-3}	5×10^4	2×10^5	5	5×10^{-3}	4	1×10^{-4}	2×10^{-3}	4
T2	4×10^{-3}	2×10^{-3}	5×10^3	2×10^5	5	5×10^{-3}	40	1×10^{-3}	2×10^{-3}	40
T3	4×10^{-2}	2×10^{-3}	5×10^2	2×10^5	5	5×10^{-3}	4×10^2	1×10^{-2}	2.04×10^{-3}	393
T4	4×10^{-1}	2×10^{-3}	5×10^1	2×10^5	5	5×10^{-3}	4×10^3	1×10^{-1}	5.81×10^{-3}	1377
T5	4	2×10^{-3}	5	2×10^5	5	5×10^{-3}	4×10^4	1	—	—
T6	40	2×10^{-3}	0.5	2×10^5	5	5×10^{-4}	4×10^5	10	—	—
T7	4×10^{-3}	0	5×10^3	∞	∞	1	∞	∞	—	—

¹ average velocity² molecular diffusion coefficient, typical for bromide ion at 20°C³ time-scale of advective transport along plate length = L / U ⁴ time-scale of diffusive transport along plate length = L^2 / D_m ⁵ time-scale of diffusive transport across plate aperture = b^2 / D_m ⁶ time step of simulation⁷ Peclet number (t_{dif} / t_{adv})⁸ mixing Peclet number (t_{mix} / t_{adv})⁹ effective dispersion coefficient from (3.36)¹⁰ effective Peclet number from (3.38)

Table 5.5. Parameters used in laboratory fracture flow and transport simulations.

parameter	Fracture I	Fracture II	units
¹ Aperture:			
length L , width W	240, 140	224, 140	mm
number of points N_i, N_j	61, 36	57, 36	—
mechanical b_m	0.130	0.585	mm
mean $\langle b \rangle$	0.128	0.584	mm
standard deviation σ_b	0.159	0.456	mm
relative roughness $\sigma_b/\langle b \rangle$	1.24	0.78	—
fraction closed c	0.6	2.1	%
Flow:			
length L , width W	240, 140	224, 140	mm
number subdivisions n_{sub}	2	2	—
control volumes n_i, n_j, n_k	120, 70, 20	112, 70, 20	—
fluid density ρ	1000	1000	kg/m ³
fluid viscosity μ	0.001	0.001	Pa-s
hydraulic gradient i	0.12	0.002	—
total flow rate Q	0.5	1.3	mL/min
hydraulic residence time t_R	8.6	14	min
Reynolds number Re	0.05	0.15	—
Transport:			
diffusivity D_m	0.002	0.002	mm ² /s
time step Δt	0.01	0.01	s
number of particles n_p	10,000	10,000	—
wall distance fraction F_ω	0.5	0.5	—
Peclet number Pe	5.6×10^4	3.0×10^4	—
mixing Peclet Pe_M	0.016	0.2	—
effective dispersion coef. D_e	0.01	0.06	mm ² /s
effective Peclet Pe^*	1.1×10^4	1.0×10^3	—

¹ Aperture and mid-surface fields in these simulations were defined on a 4×4 mm grid by averaging the original fields measured on a 2×2 mm grid.

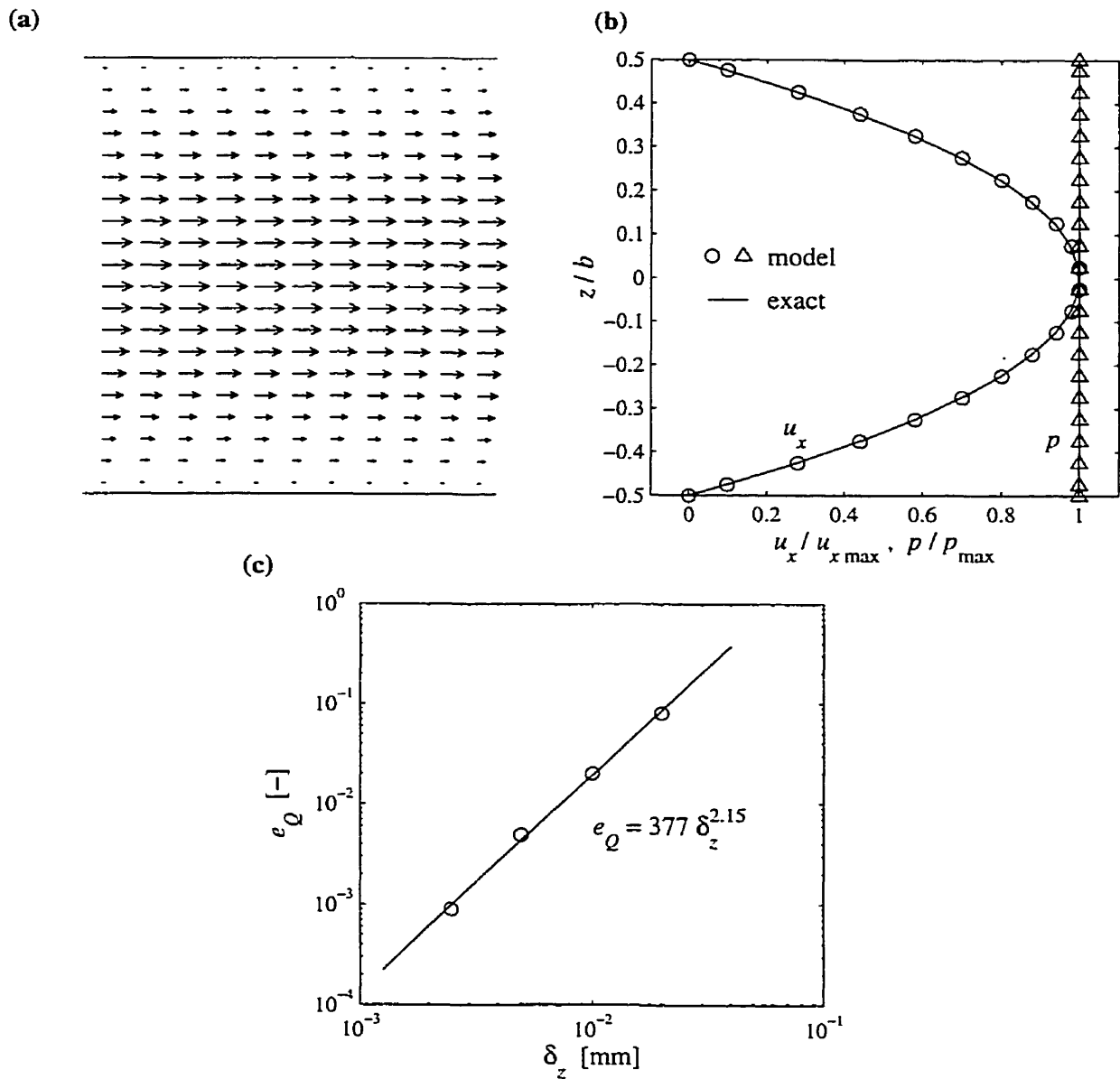


Figure 5.1. Navier-Stokes simulations through parallel plates: (a) cross-sectional velocity vector plot, (b) normalized velocity and pressure profiles, and (c) relative error e_Q versus vertical grid spacing δ_z . The trend line and equation display the regressed power relationship for the data set.

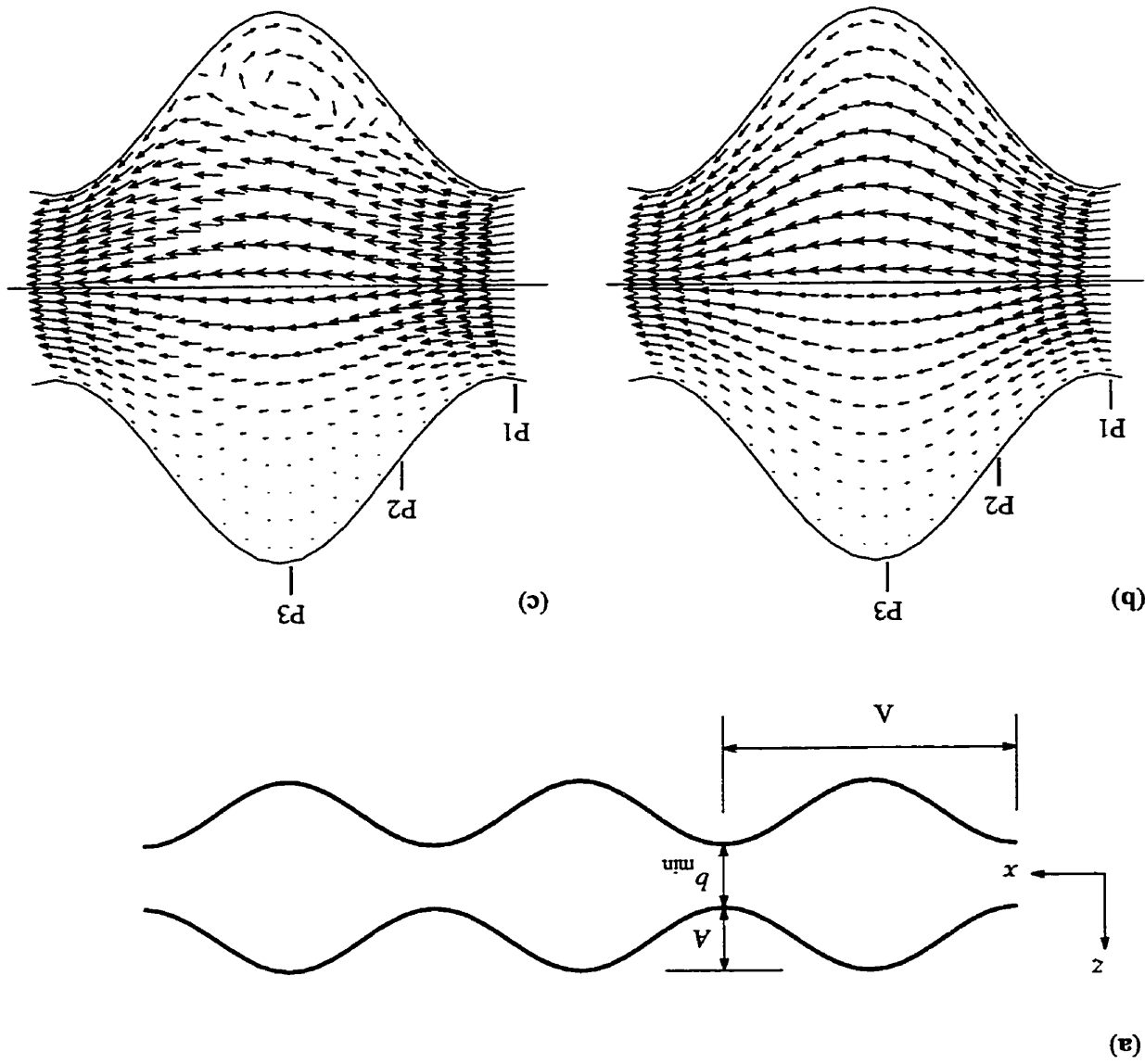


Figure 5.2. Stokes and Navier-Stokes simulations through sinusoidal surfaces: (a) schematic profile of sinusoidal surfaces, (b) velocity field from Stokes simulations through the middle oscillation, and (c) velocity field from NS simulations through the middle oscillation. These simulations used relatively rough ($A/b_{\min} = 1$) and steeply sloped ($A/\lambda = 0.4$) sinusoidal surfaces. Note that the velocity vectors below the line of symmetry are transformed by taking the quad root of their magnitude to reveal the flow pattern in the low velocity region.

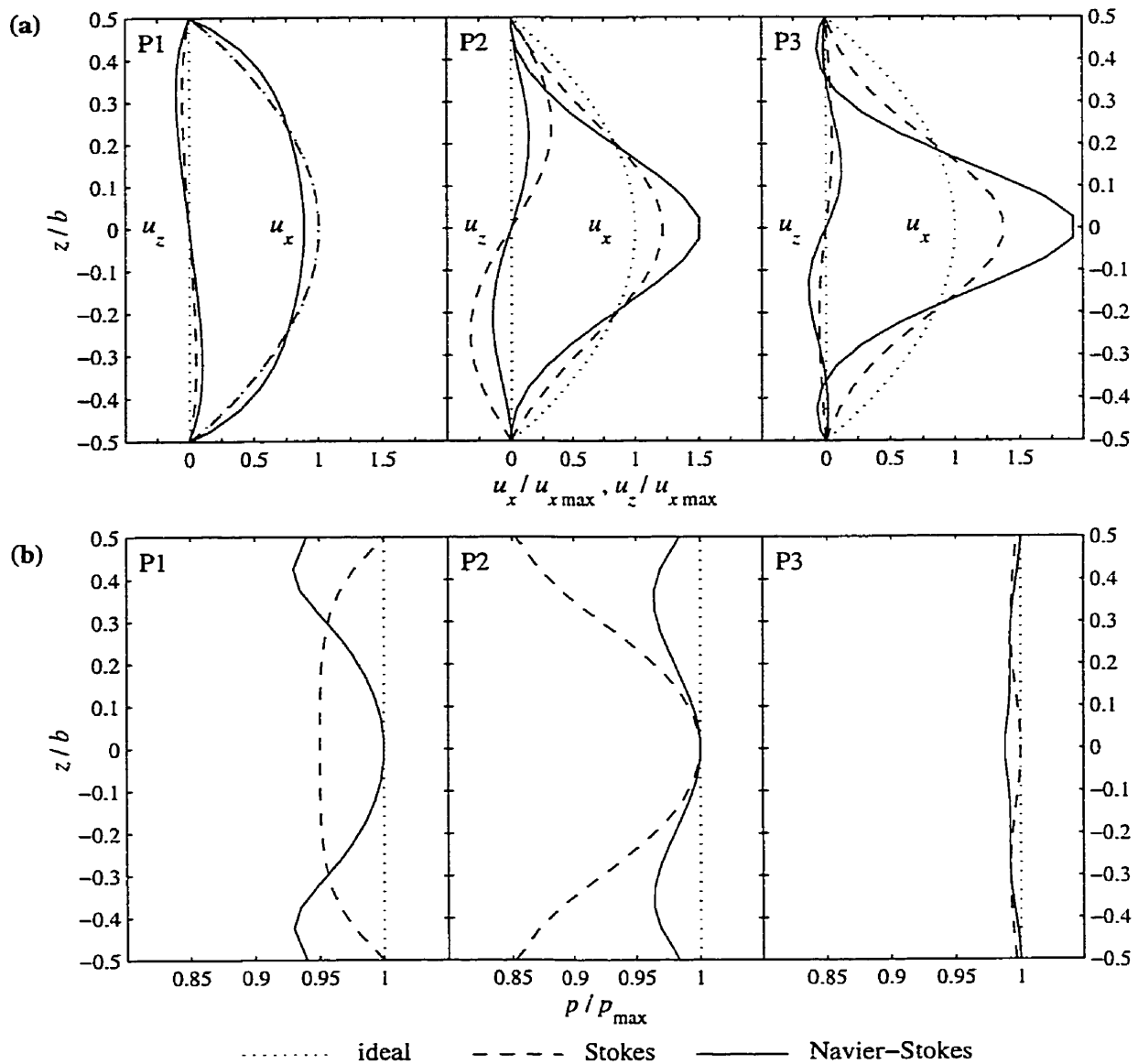


Figure 5.3. Stokes and Navier-Stokes simulations through sinusoidal surfaces: vertical profiles of (a) velocity components, and (b) pressure, at vertical locations P1, P2, and P3 in Parts (b) and (c) of Figure 5.2. The ideal profiles are included. The vertical location z is normalized by the local aperture b , the velocity components u_x and u_z are normalized by the ideal maximum u_x for the vertically integrated flow rate at each location, and pressure p is normalized by the maximum pressure.

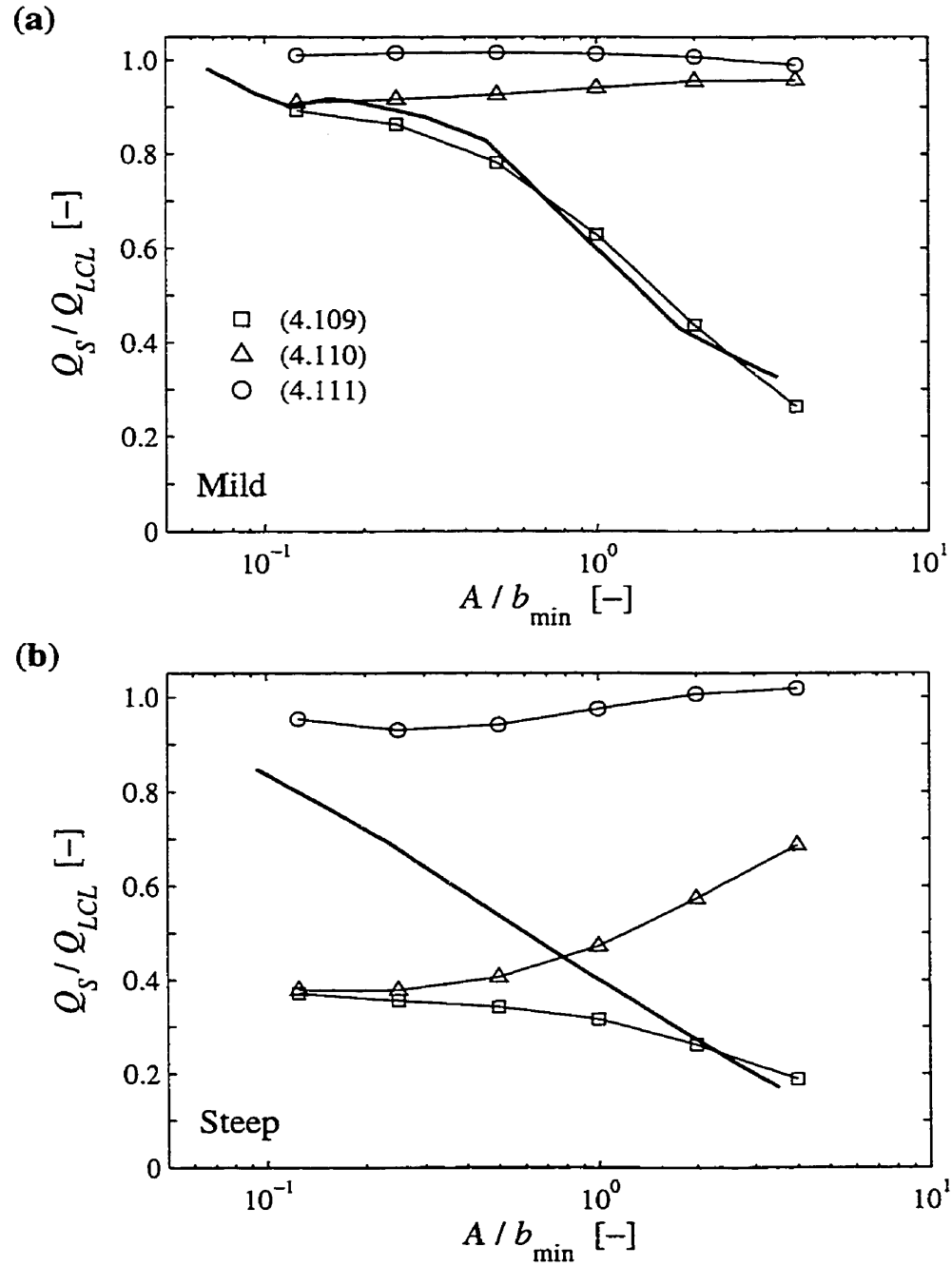


Figure 5.4. Stokes and LCL sinusoidal surface simulations: total flow ratio Q_S/Q_{LCL} versus the sinusoidal relative roughness A/b_{min} for (a) mildly sloped $A/\lambda = 0.1$, and (b) steeply sloped $A/\lambda = 0.4$ surfaces. The heavy solid lines are numerical data from Brown et al. [1995], and the lines with symbols are data from this work using three definitions of \bar{b}_{fp}^3 in the LCL simulations given by (4.109), (4.110), and (4.111).

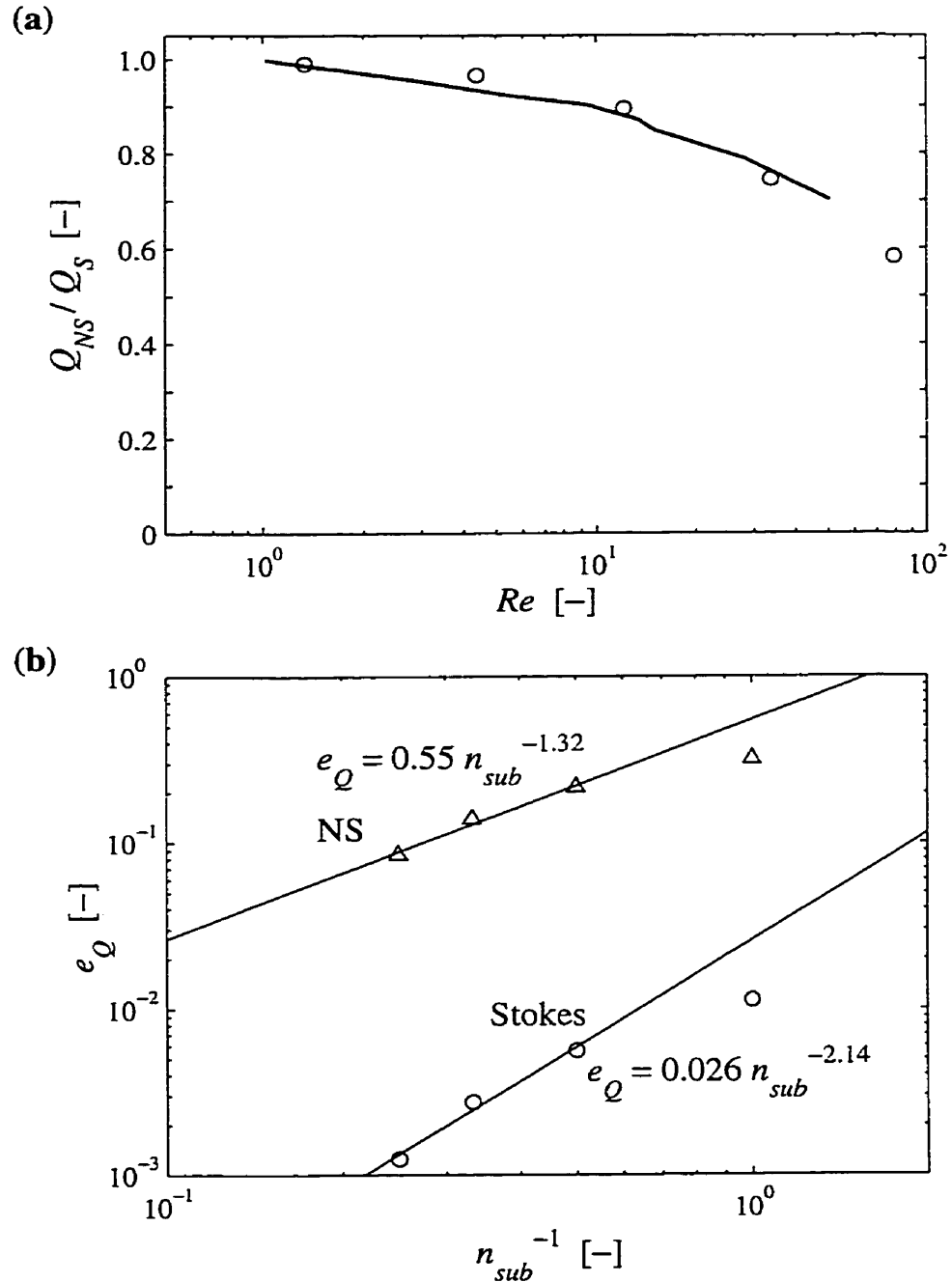
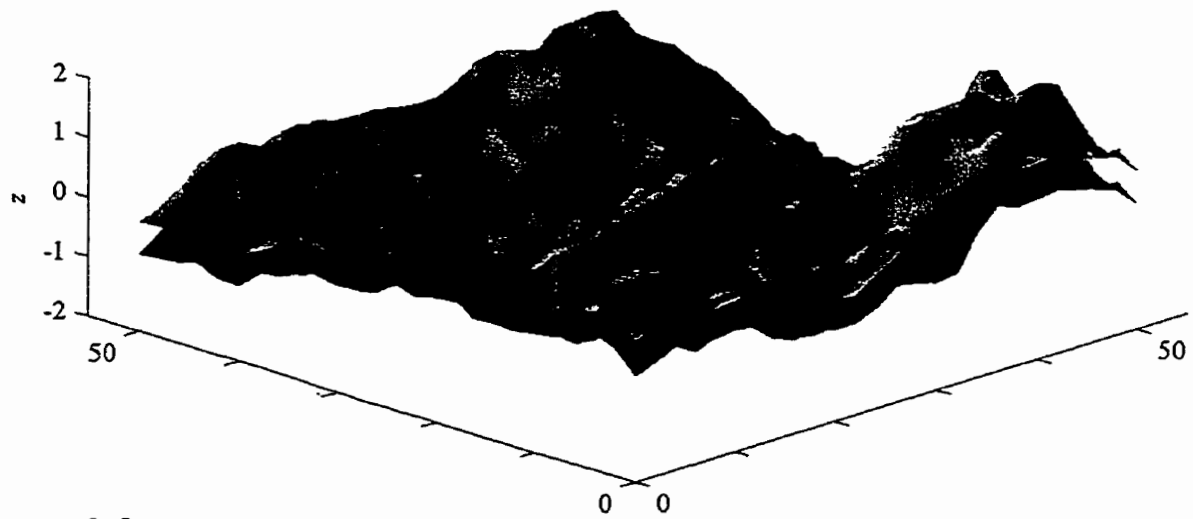


Figure 5.5. Navier-Stokes and Stokes simulations through steeply sloped ($A/\lambda = 0.4$) sinusoidal surfaces: (a) Total flow ratio Q_{NS}/Q_S versus the Reynolds number Re of the flow field. The heavy solid lines are numerical data from *Brown et al.* [1995] and the lines with symbols are data from this thesis work. (b) Relative error e_Q in the simulations versus the inverse number of subdivisions n_{sub}^{-1} applied to the base grid of $60 \times 1 \times 20$ CVs. The trend lines and equations display the regressed power relationship for each data set.

(a) smooth fracture



(b) rough fracture

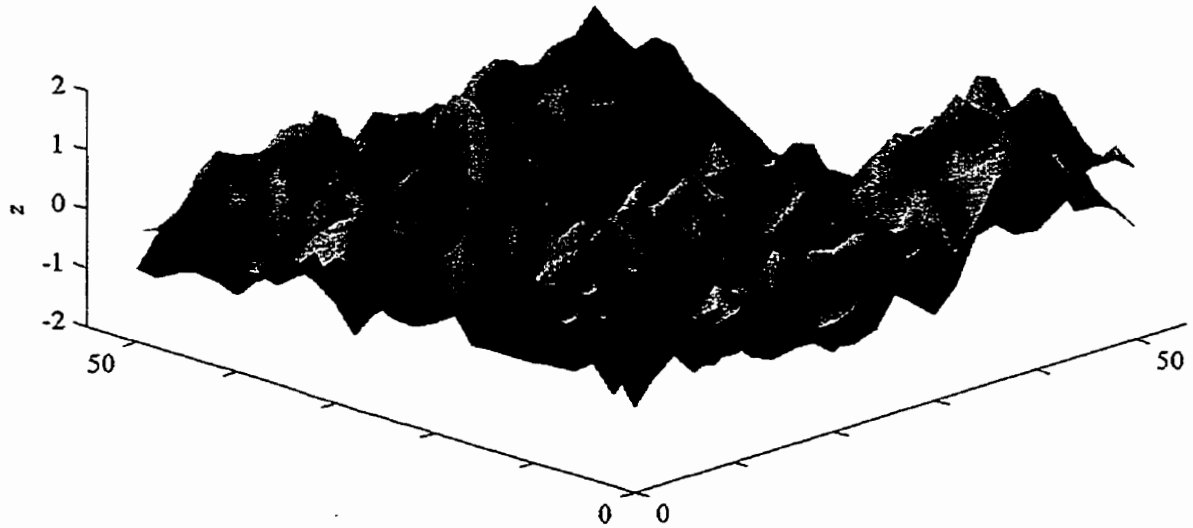


Figure 5.6. Example fracture geometry: three-dimensional surfaces plots of (a) smooth fracture with $\sigma_m/b_m = 0.125$, and (b) rough fracture with $\sigma_m/b_m = 1.0$. These fractures were randomly generated over a 26×26 grid using a uniform 2×2 mm spacing, normally distributed aperture ($\lambda_b = 2$ mm), moderate undulation ($\sigma_z = 0.5$ mm), and moderate mechanical aperture ($b_m = 0.5$ mm).

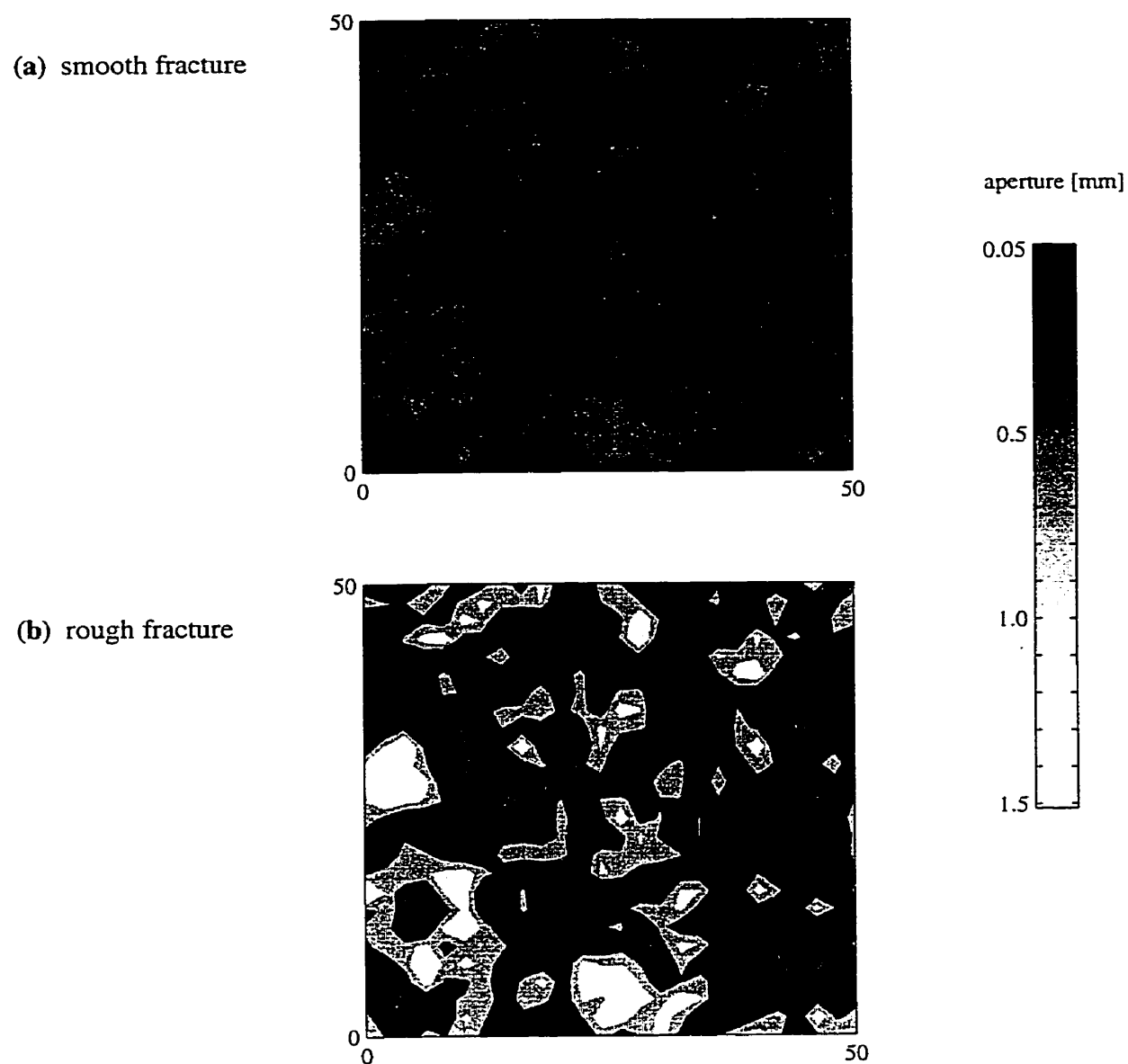


Figure 5.7. Example fracture geometry: aperture contour plots of (a) smooth fracture with $\sigma_m/b_m = 0.125$, and (b) rough fracture with $\sigma_m/b_m = 1.0$.

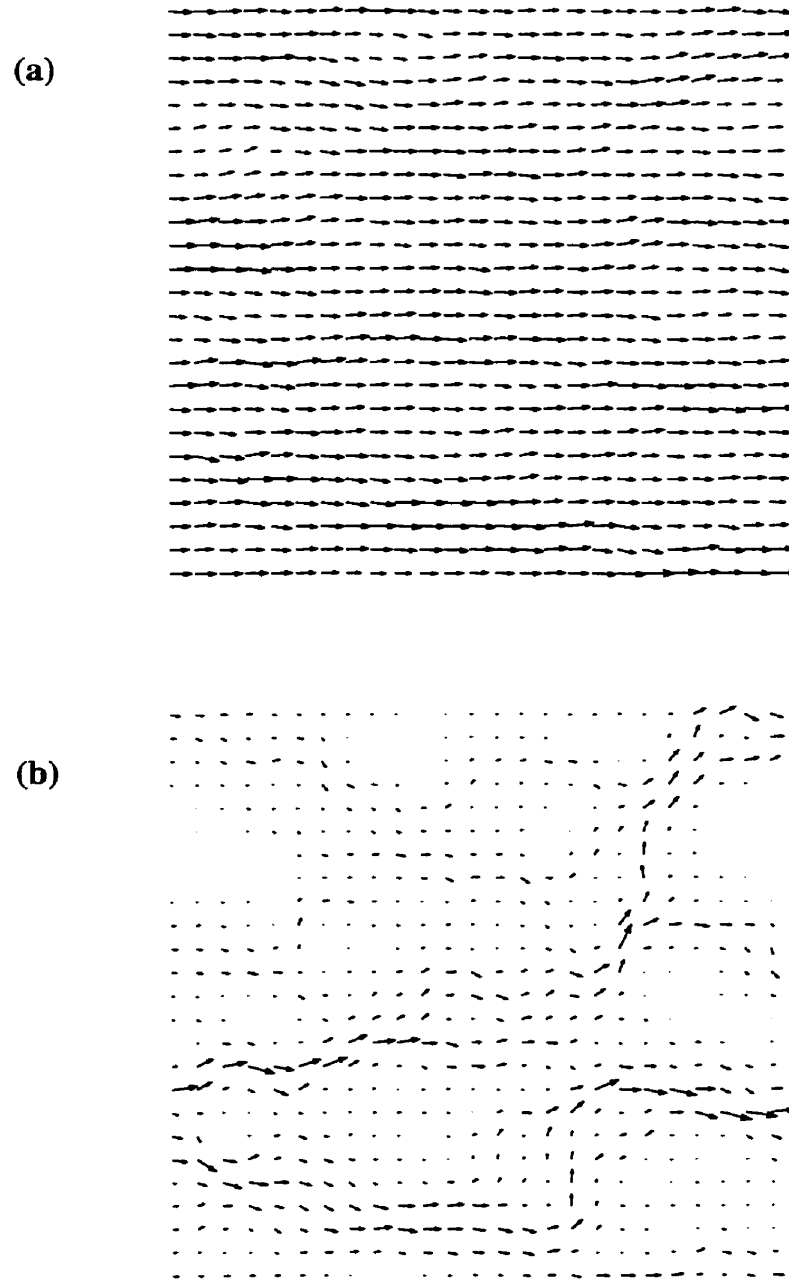


Figure 5.8. LCL example fracture simulations: flow fields using (4.109) without corrections ($\beta_p = 1$) for (a) the smooth fracture with a total flow rate of 5.0 mL/s and a maximum vector of 0.16 mL/s, and (b) the rough fracture with a total flow rate of 3.1 mL/s and a maximum vector of 0.47 mL/s.

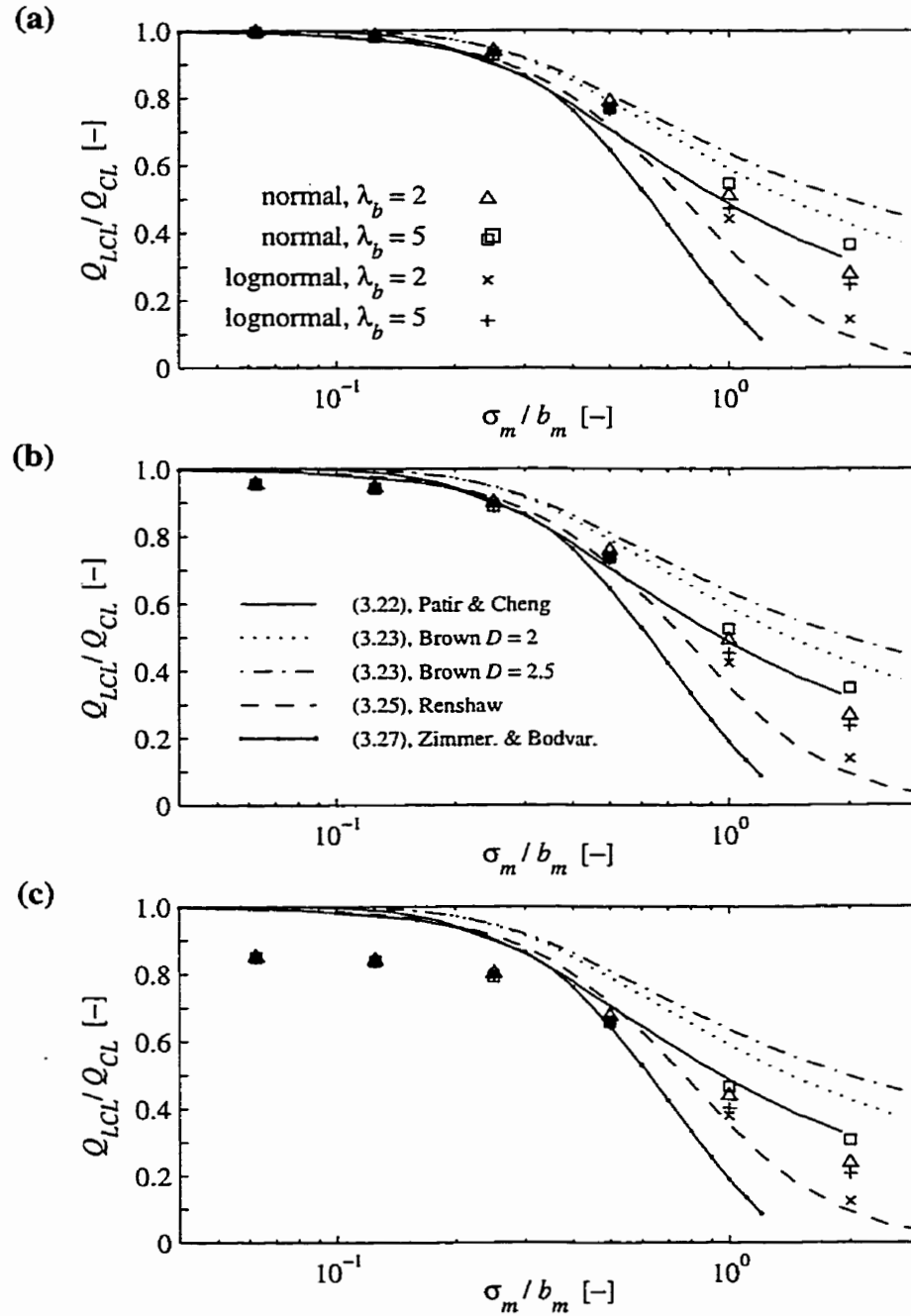


Figure 5.9. LCL simulations and cubic law calculations for synthetic fractures: total flow ratio Q_{LCL}/Q_{CL} versus the relative roughness σ_m/b_m for three values of mid-surface variability: (a) $\sigma_z = 0$, (b) $\sigma_z = 0.5$, and (c) $\sigma_z = 1$ mm. The LCL simulations used (4.109) without corrections ($\beta_P = 1$). The symbols represent four different fracture types and each data point is the mean of ~5 realizations. The lines are published functional relationships presented in Section 3.3.2.

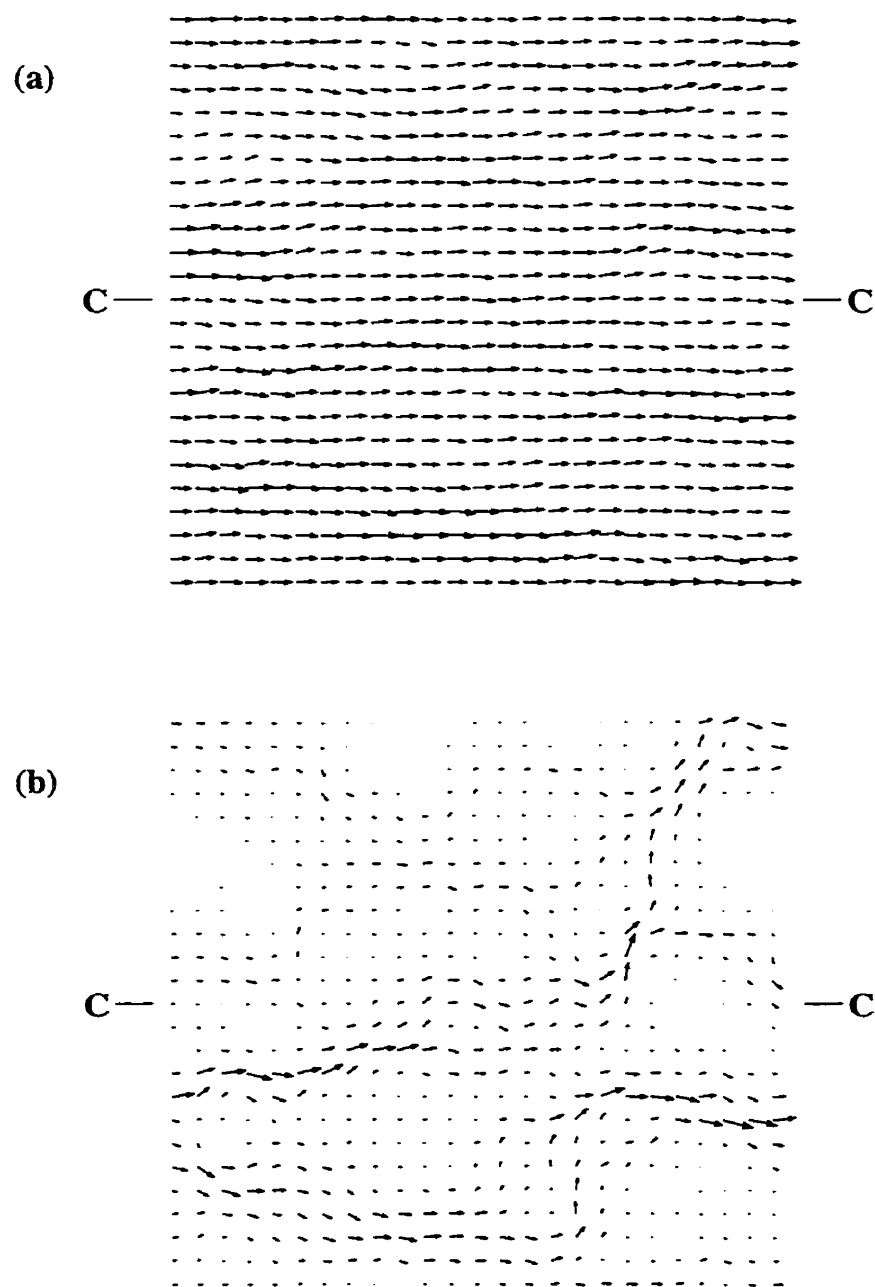


Figure 5.10. Stokes example fracture simulations: vertically integrated flow fields for (a) the smooth fracture with a total flow rate of 4.85 mL/s and a maximum vector of 0.16 mL/s, and (b) the rough fracture with a total flow rate of 2.7 mL/s and a maximum vector of 0.40 mL/s. The line C-C defines the cross-sectional view displayed in Figure 5.12.

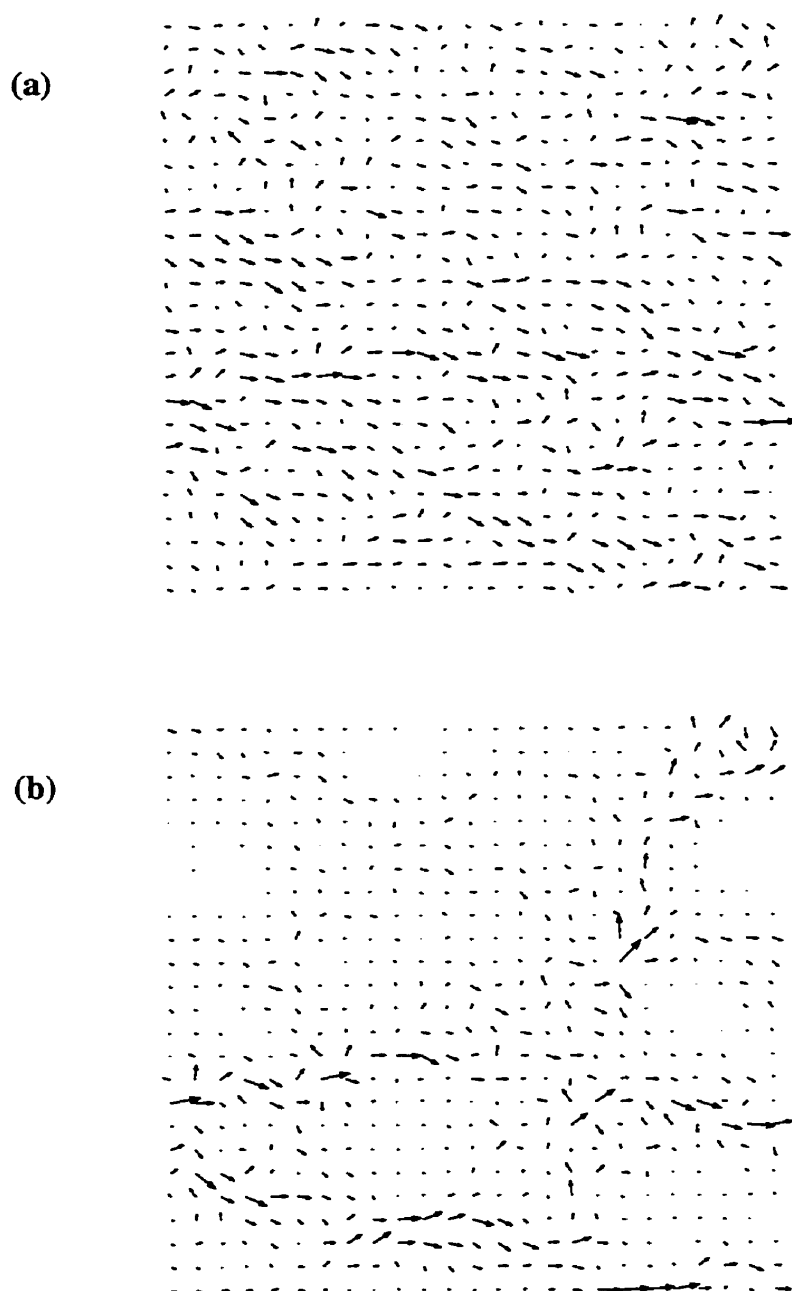


Figure 5.11. Stokes and LCL example fracture simulations: LCL flow field (Figure 5.8) minus Stokes flow field (Figure 5.10) for (a) the smooth fracture with a total flow difference of 0.16 mL/s and the maximum difference vector of 0.016 mL/s (10% of maximum vector in Figure 5.10), and (b) the rough fracture with a total flow difference of 0.44 mL/s and the maximum difference vector of 0.10 mL/s (25% of maximum vector in Figure 5.10).

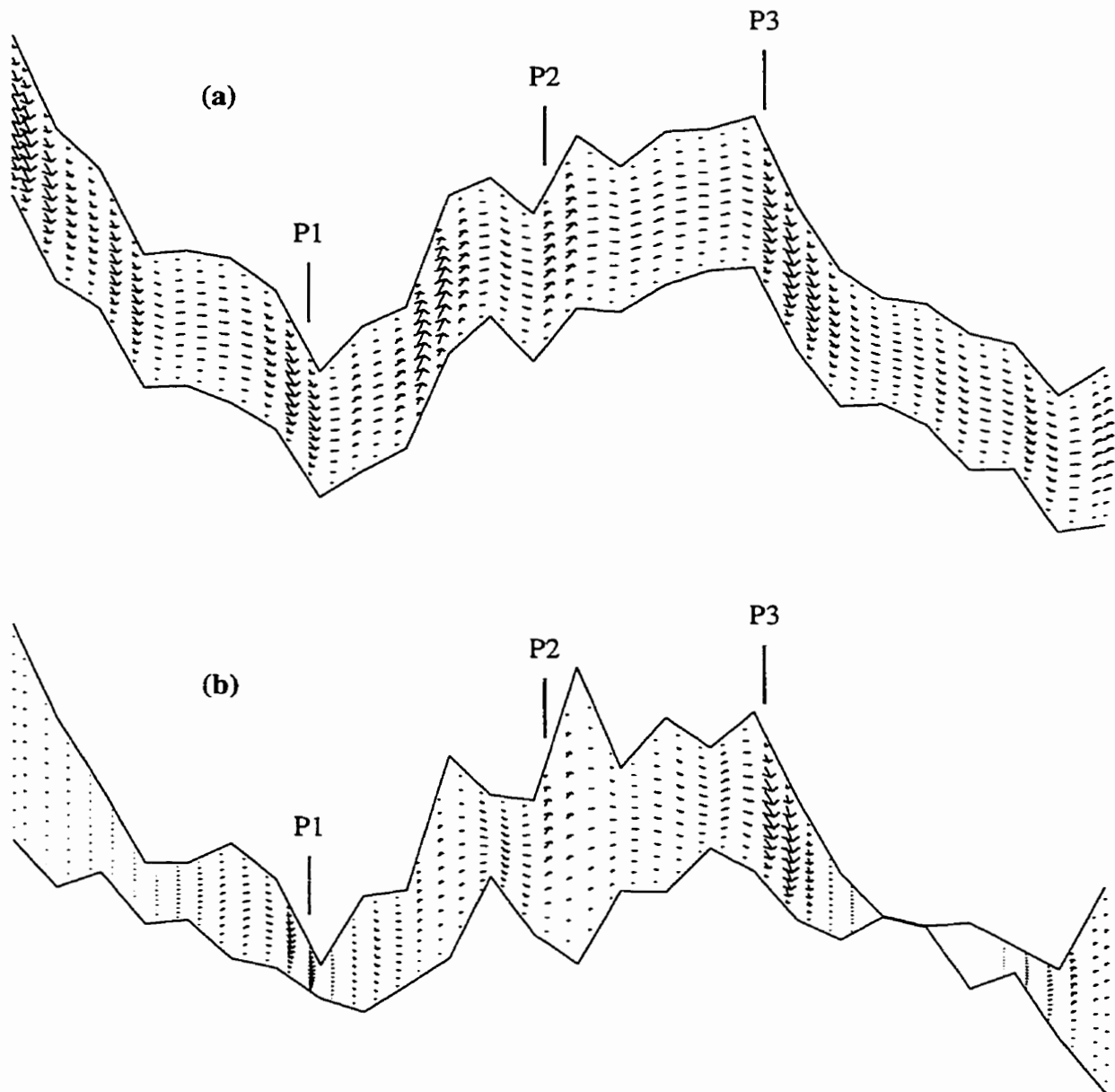


Figure 5.12. Stokes example fracture simulations: cross-sectional velocity field for (a) the smooth fracture with a maximum velocity vector of 2.9 m/s, and (b) the rough fracture with a maximum velocity vector of 3.2 m/s. The position of this cross-section view is defined by line C-C in Figure 5.10. The positions P1, P2, and P3 define the locations of the vertical profiles displayed in Figure 5.13.

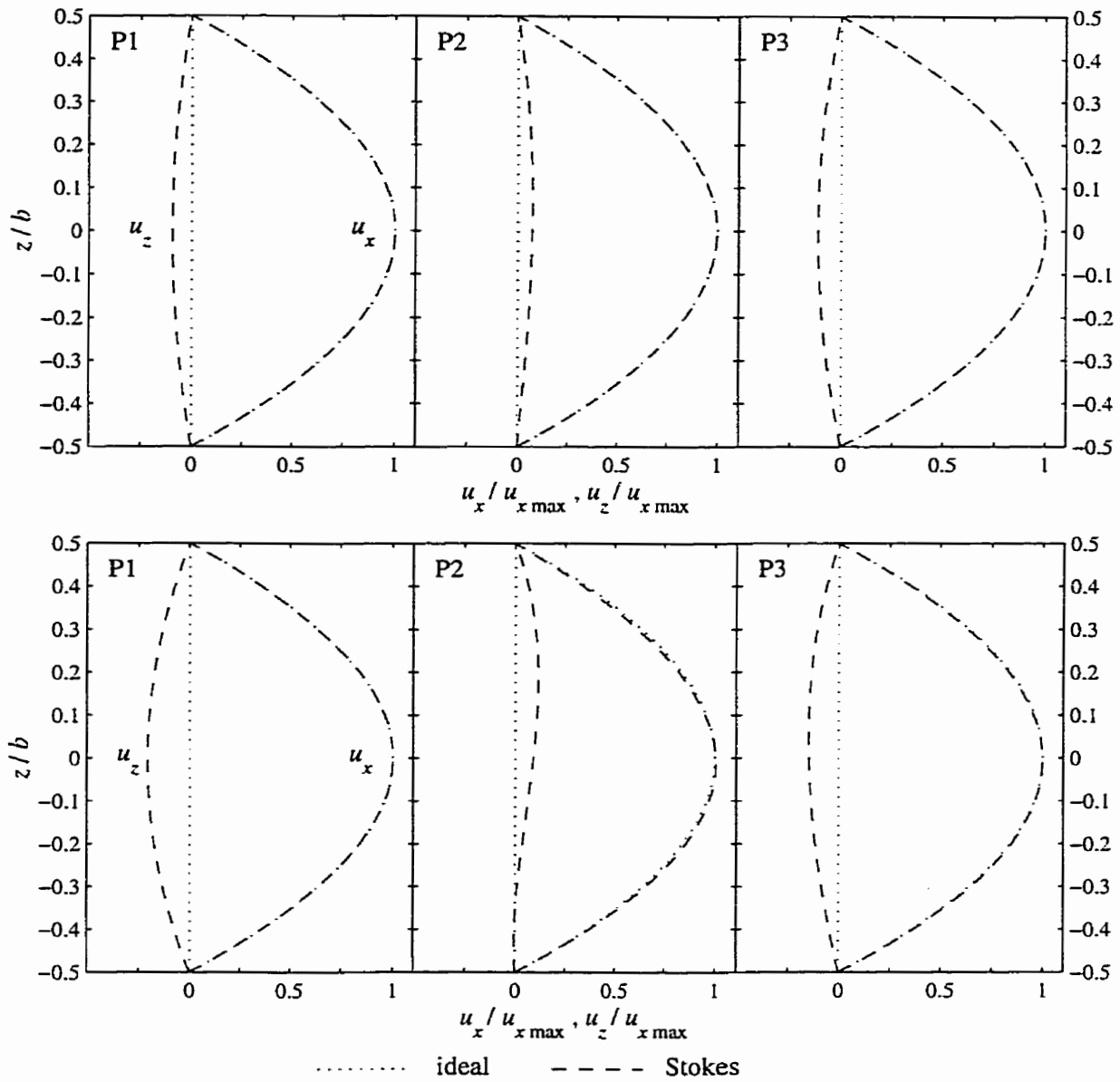


Figure 5.13. Stokes example fracture simulations: vertical profiles of the x- and z-components of velocity at the locations P1, P2, and P3 defined in Figure 5.12. The ideal profiles are included. The vertical location z is normalized by the local aperture b , and the velocity components u_x and u_z are normalized by the ideal maximum u_x for the vertically integrated flow rate at each location.

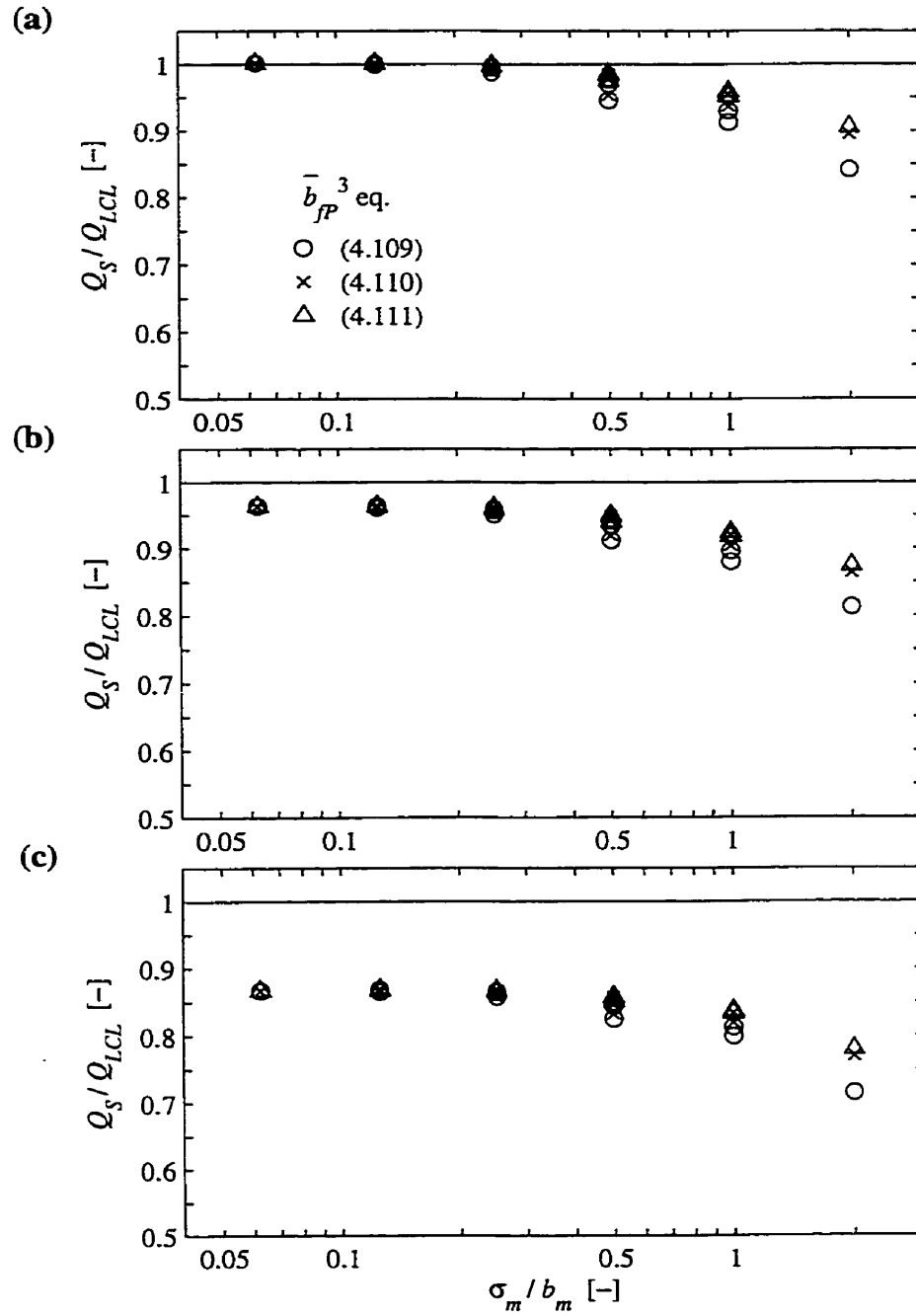


Figure 5.14. Stokes and LCL synthetic fracture simulations: total flow ratio Q_s/Q_{LCL} versus the relative roughness σ_m/b_m for fractures with (a) $\sigma_z = 0$, (b) $\sigma_z = 0.5$, and (c) $\sigma_z = 1$ mm. The symbols represent LCL simulations using (4.109), (4.100), and (4.111) without corrections ($\beta_{fP} = 1$ and $\kappa_{fP} = 1$). Each data point is the mean of ~ 5 fracture realizations.

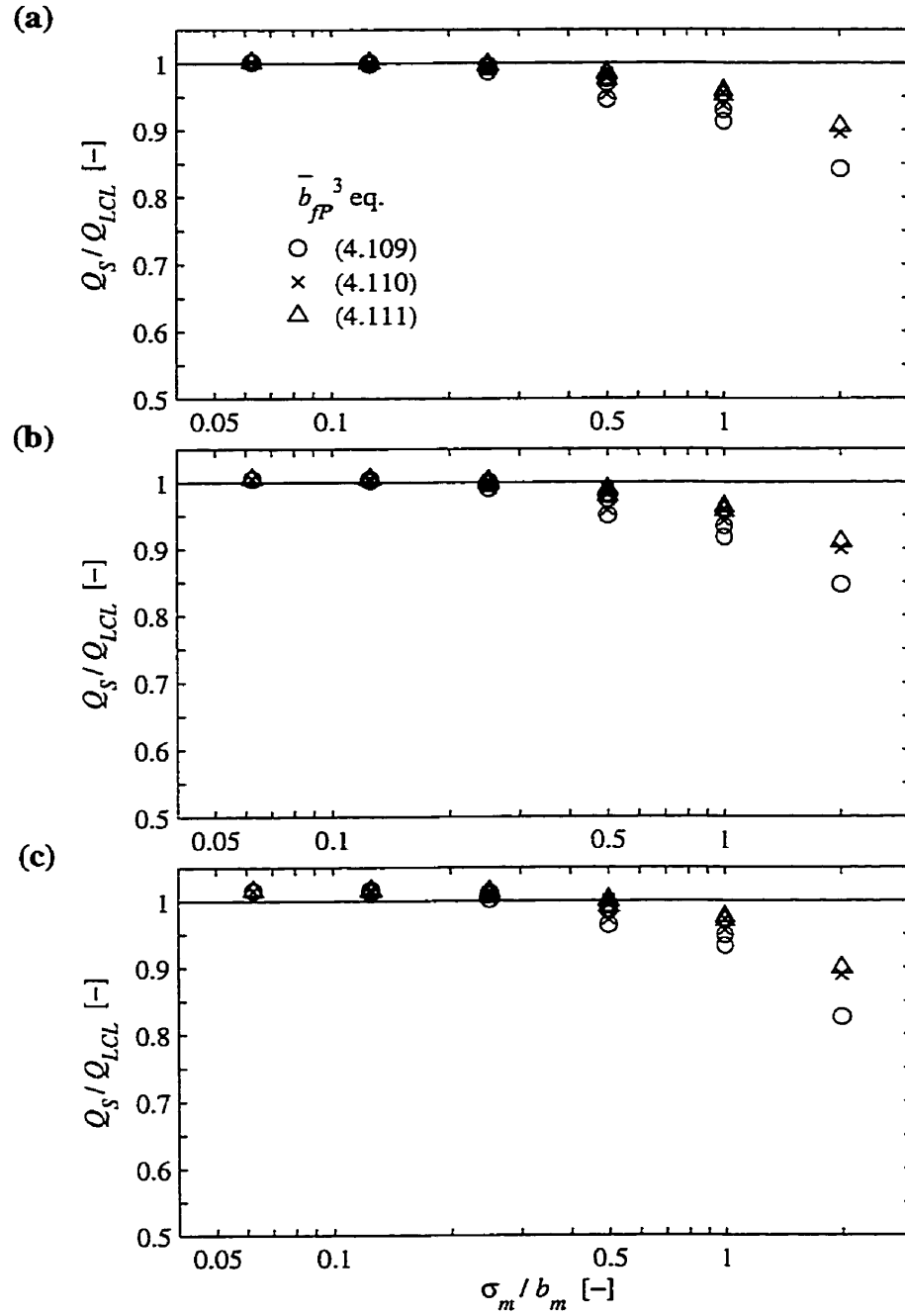


Figure 5.15. Stokes and corrected LCL synthetic fracture simulations: total flow ratio Q_S/Q_{LCL} versus the relative roughness σ_m/b_m for fractures with (a) $\sigma_z = 0$, (b) $\sigma_z = 0.5$, and (c) $\sigma_z = 1$ mm. The symbols represent LCL simulations using (4.109), (4.100), and (4.111). Each data point is the mean of ~ 5 fracture realizations.

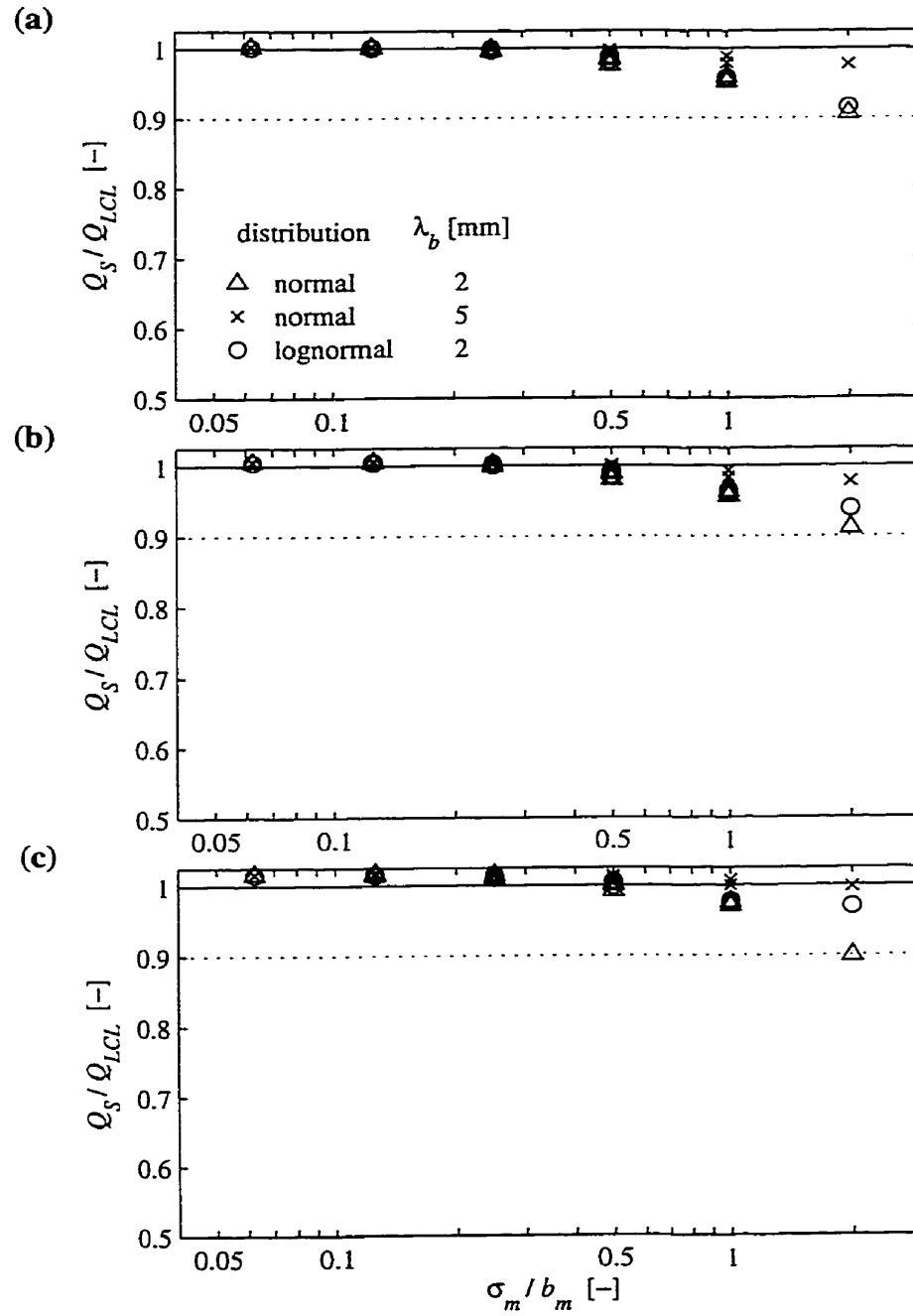


Figure 5.16. Stokes and corrected LCL synthetic fracture simulations: total flow ratio Q_S/Q_{LCL} versus the relative roughness σ_m/b_m for fractures with (a) $\sigma_z = 0$, (b) $\sigma_z = 0.5$, and (c) $\sigma_z = 1$ mm. The symbols represent three fracture types and the LCL simulations used (4.111). Each data point is the mean of ~5 fracture realizations.

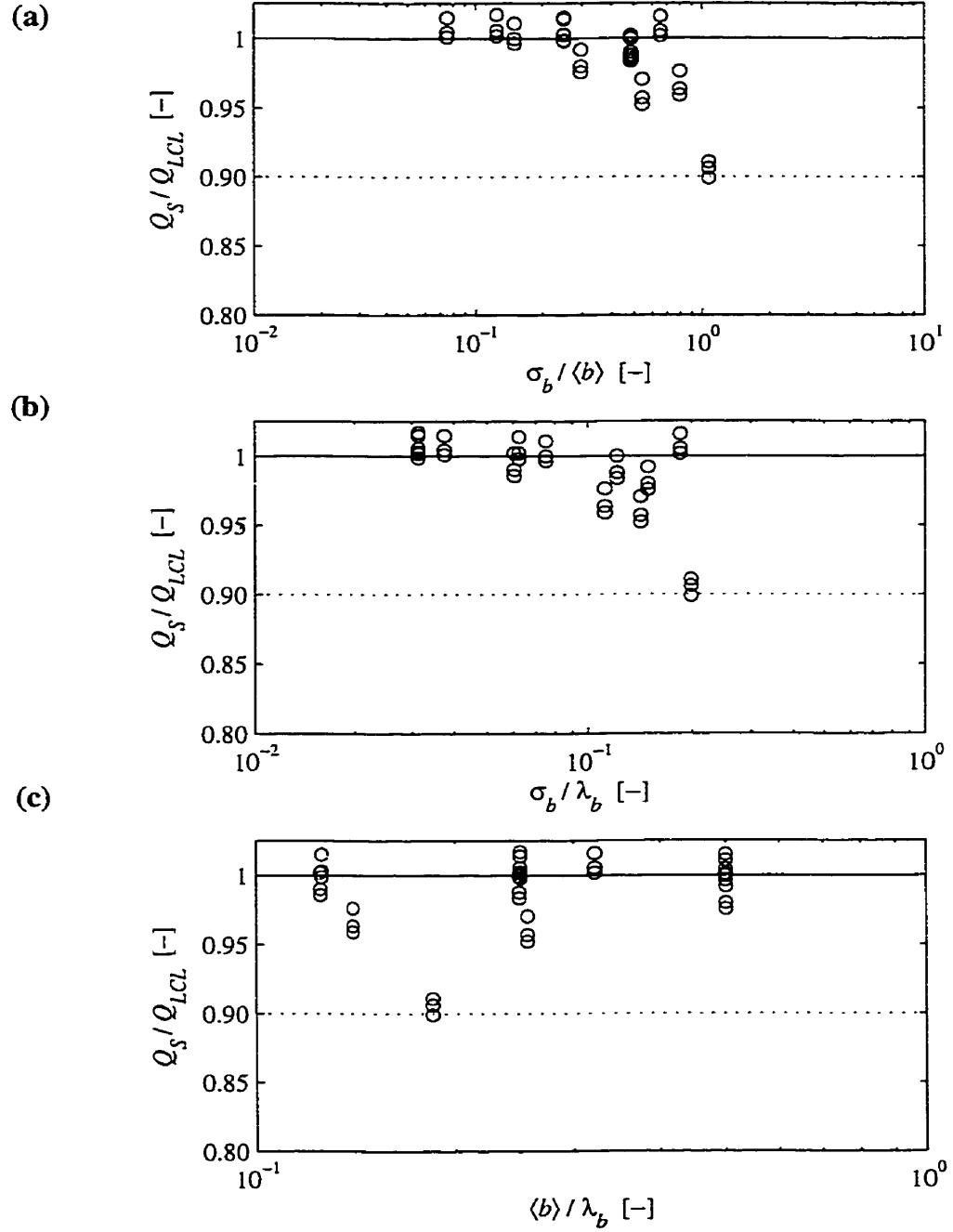


Figure 5.17. Stokes and corrected LCL synthetic fracture simulations: total flow ratio Q_S/Q_{LCL} versus (a) the actual relative roughness $\sigma_b/\langle b \rangle$, (b) the actual roughness slope σ_b/λ_b , and (c) the mean aperture aspect ratio $\langle b \rangle/\lambda_b$. The LCL simulations used (4.111) and the fractures used normally distributed aperture with $\lambda_b = 2$ mm, and all values of mid-surface variability ($\sigma_z = 0, 0.5, 1$ mm). Each data point is the mean of ~ 5 fracture realizations.

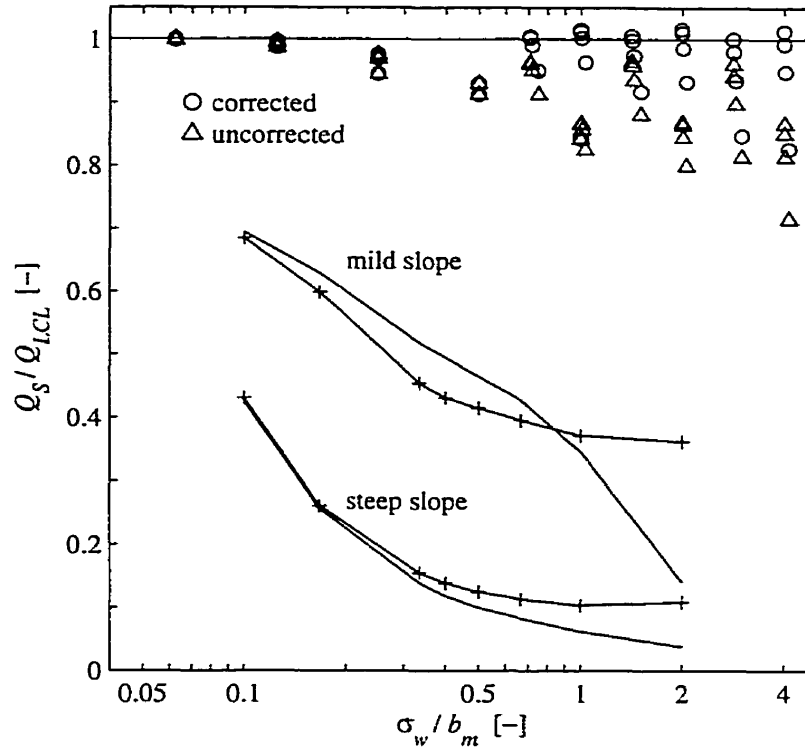


Figure 5.18. Stokes and LCL synthetic fracture simulations: total flow ratio Q_S/Q_{LCL} versus the wall relative roughness σ_w/b_m . The hollow symbols represent results from LCL simulations using (4.109) with and without corrections for fractures with normally distributed aperture ($\lambda_b = 2$ mm) and three values of mid-surface variability ($\sigma_z = 0, 0.5, 1$ mm). The solid lines represent the numerical data of Mourzenko *et al.* [1995] for mildly and steeply sloped ($\sigma_w/\lambda_w = 1/3$ and 1, respectively) fracture surfaces. The lines without symbols represent fractures formed by mating correlated surfaces, and the lines with symbols represent fractures formed by mating uncorrelated surfaces.

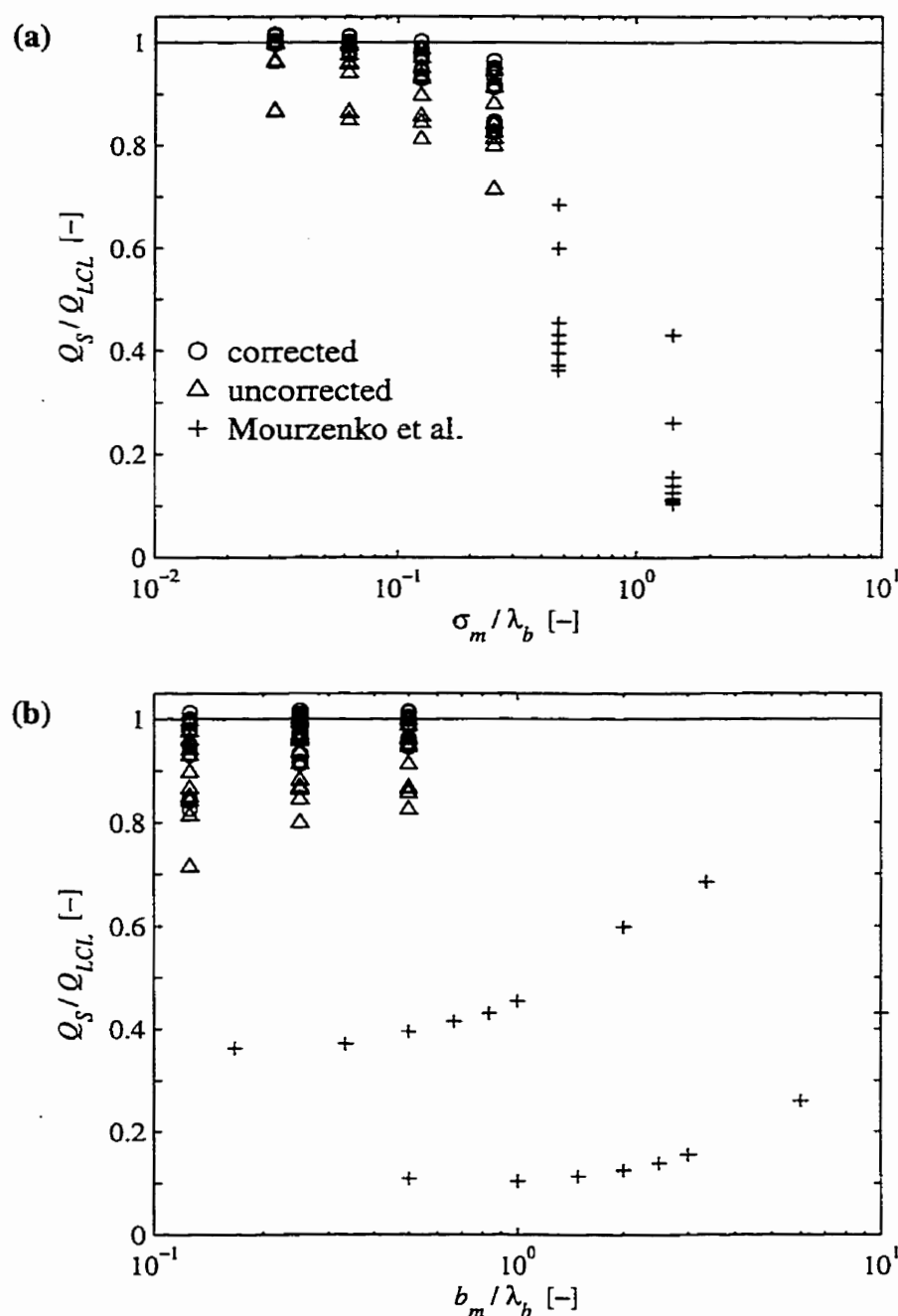


Figure 5.19. Stokes and LCL synthetic fracture simulations: total flow ratio Q_s/Q_{LCL} versus (a) the mechanical roughness slope σ_m/λ_b , and (b) the mechanical aspect ratio b_m/λ_b . The hollow symbols represent results from LCL simulations using (4.109) with and without corrections (see legend) for fractures with normally distributed aperture ($\lambda_b = 2$ mm) and three values of mid-surface variability ($\sigma_z = 0, 0.5, 1$ mm). The “+” symbols represent the numerical data of Mourzenko et al. [1995] for mildly and steeply sloped ($\sigma_w/\lambda_w = 1/3$ and 1, respectively) fracture surfaces that are uncorrelated. Note that the uncorrelated data from Mourzenko et al. [1995] was transformed by assuming that σ_m equals $2^{1/2} \sigma_w$.

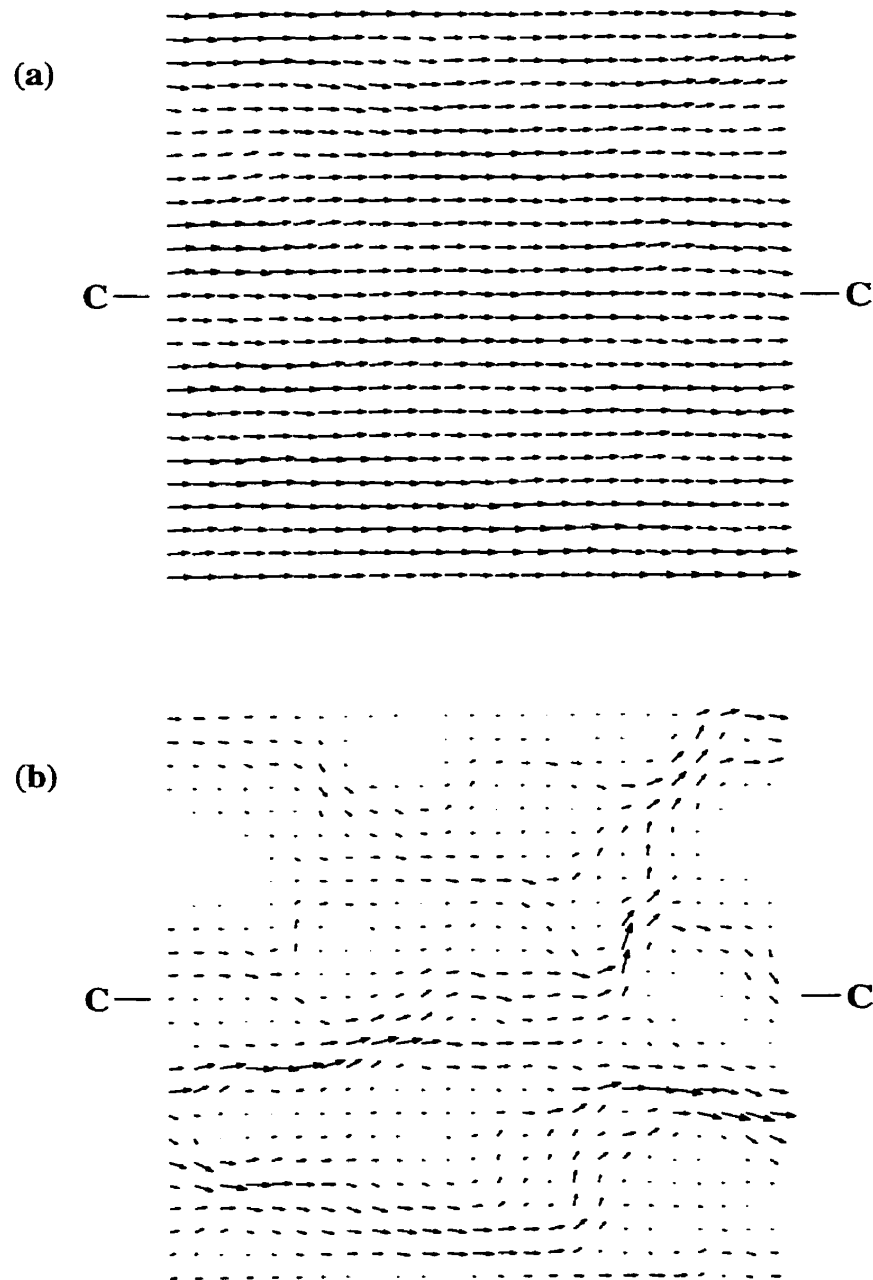


Figure 5.20. Navier-Stokes example fracture simulations: vertically integrated flow field for (a) the smooth fracture with a total flow rate of 4.5 mL/s and a maximum vector of 0.13 mL/s, and (b) the rough fracture with a total flow rate of 1.7 mL/s and a maximum vector of 0.180 mL/s. The line C-C defines the cross-section displayed in Figure 5.22.

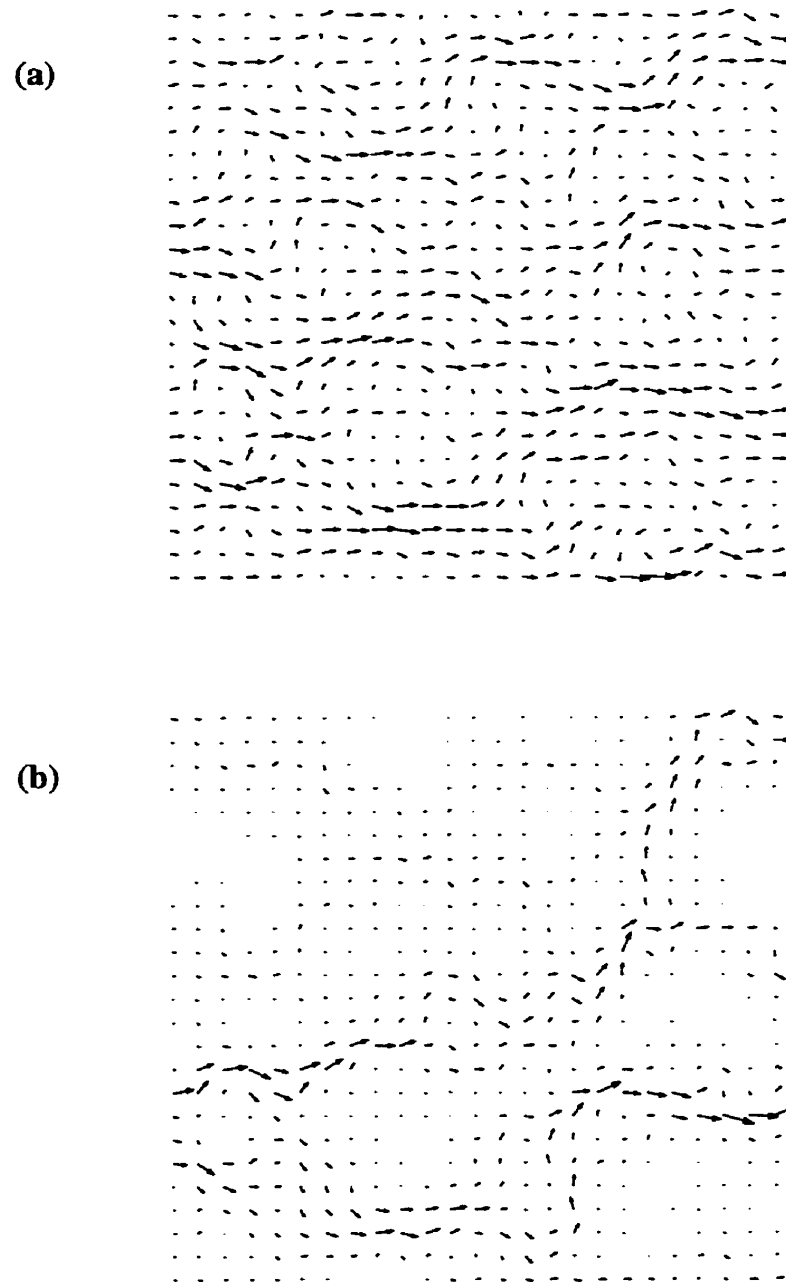


Figure 5.21. Navier-Stokes and Stokes example fracture simulations: Stokes flow field (Figure 5.10) minus NS flow field (Figure 5.20) for (a) the smooth fracture with a total flow difference of 0.39 mL/s and a maximum difference vector of 0.033 mL/s (25% of maximum vector in Figure 5.20), and (b) the rough fracture with a total flow difference of 0.95 mL/s and a maximum difference vector of 0.21 mL/s (120% of maximum vector in Figure 5.20).

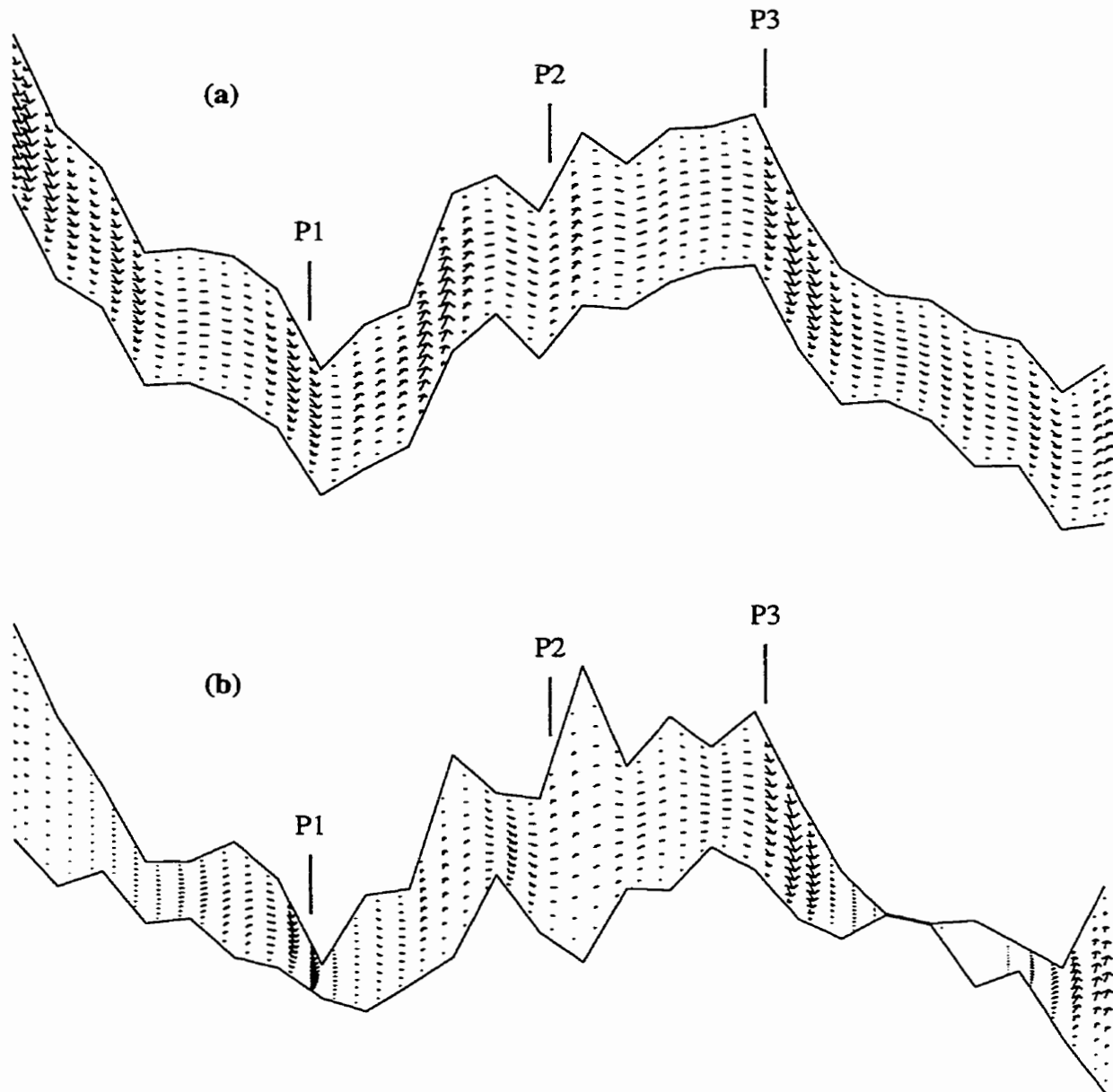


Figure 5.22. Navier-Stokes example fracture simulations: cross-section velocity field for (a) the smooth fracture with a maximum velocity vector of 2.7 m/s, and the rough fracture with a maximum velocity vector of 1.8 m/s. The position of this cross-section view is defined by line C-C in Figure 5.20. The positions P1, P2, and P3 define the locations of the vertical profiles displayed in Figure 5.23.

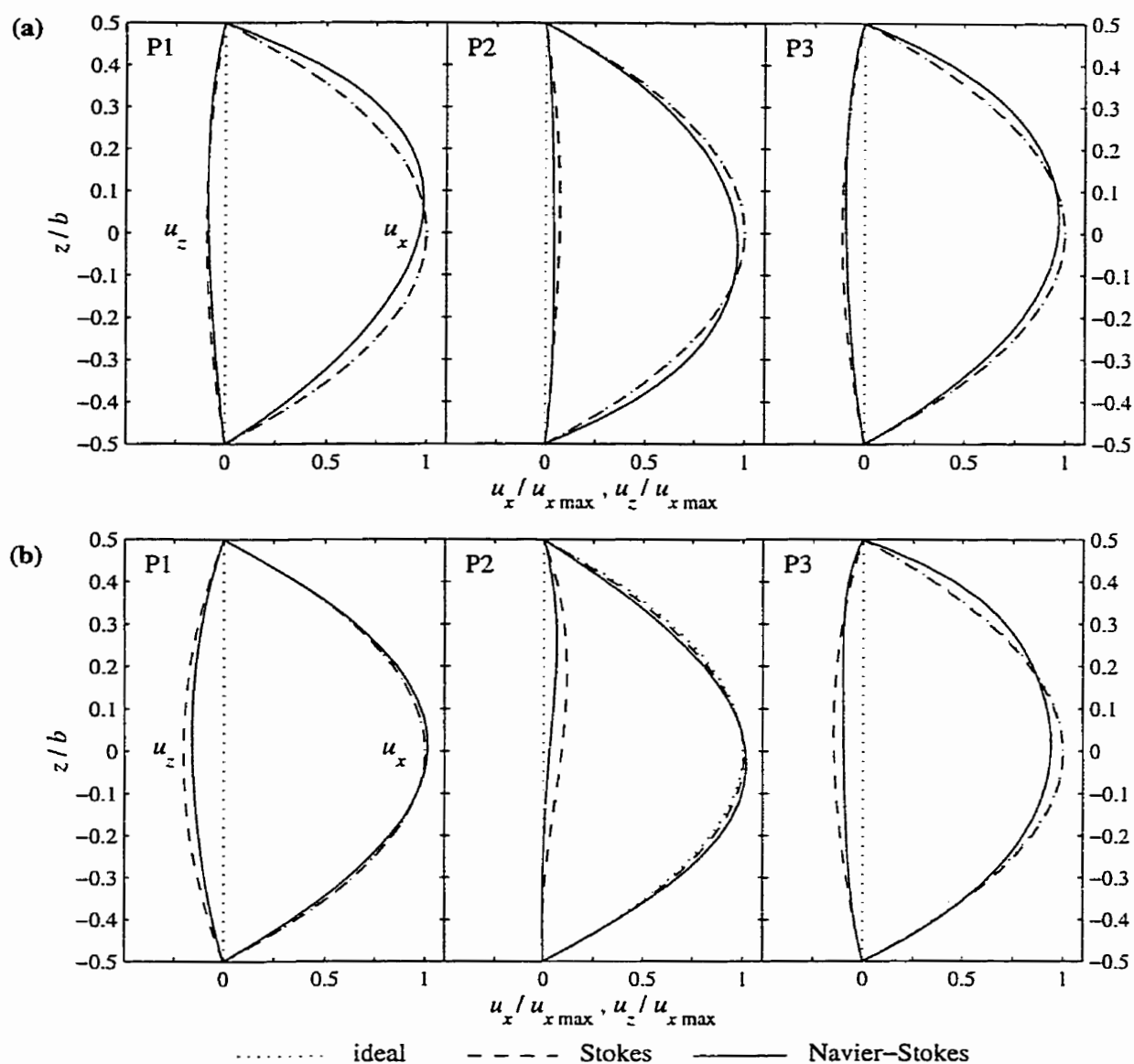


Figure 5.23. Navier-Stokes and Stokes example fracture simulations: vertical profiles of the x - and z - components of velocity at the locations P1, P2, and P3 defined in Figure 5.22. The ideal profiles are included. The vertical location z is normalized by the local aperture b , and the velocity components u_x and u_z are normalized by the ideal maximum u_x for the vertically integrated flow rate at each location.

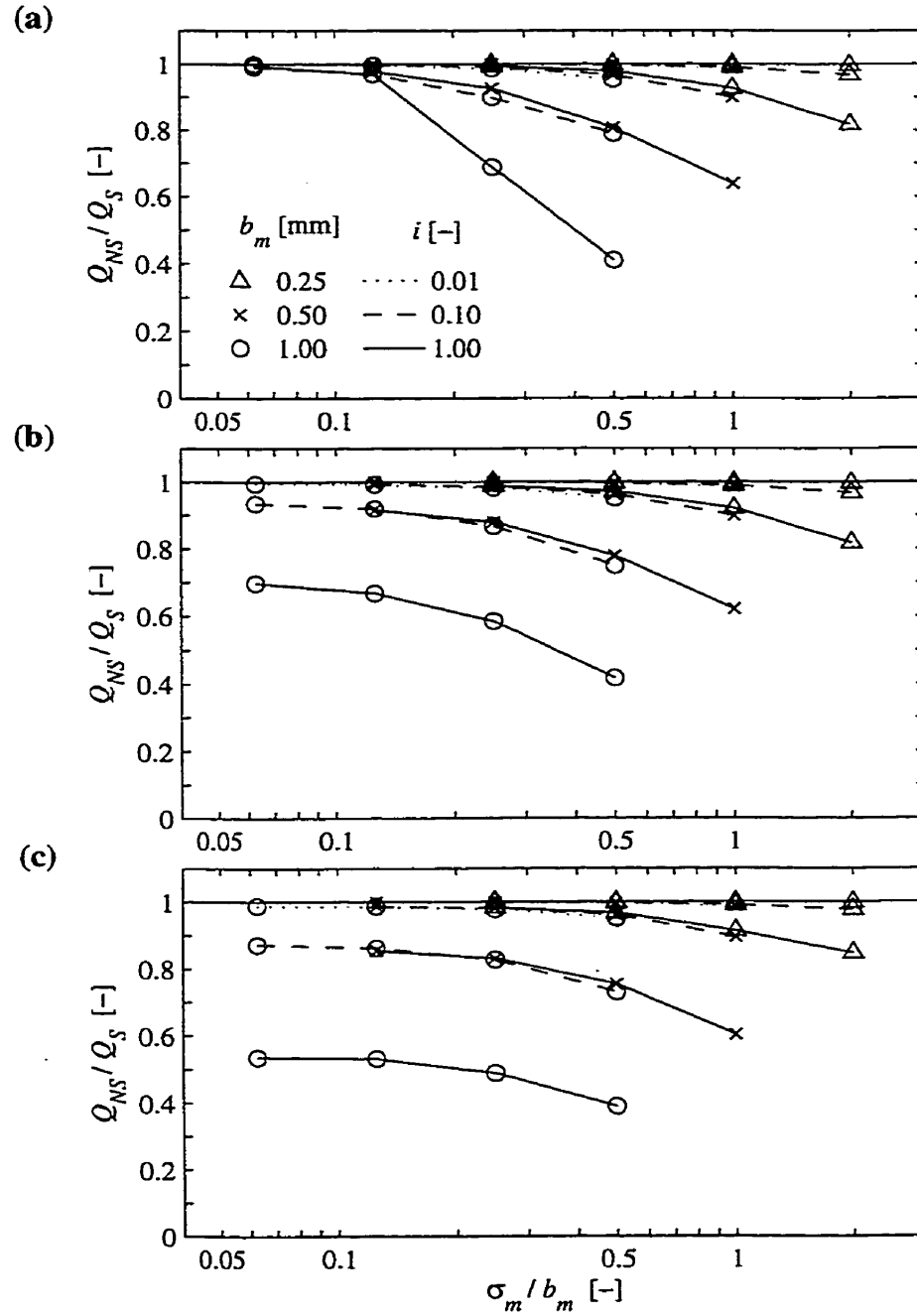


Figure 5.24. Navier-Stokes and Stokes synthetic fracture simulations: total flow ratio Q_{NS}/Q_S versus the relative roughness σ_m/b_m for fractures with (a) $\sigma_z = 0$, (b) $\sigma_z = 0.5$, and (c) $\sigma_z = 1$ mm. The synthetic fractures used normally distributed aperture with $\lambda_b = 2$ mm. The symbols represent three values of mechanical aperture b_m and the lines represent three values of hydraulic gradient i . Each data point is the mean of ~ 5 fracture realizations.

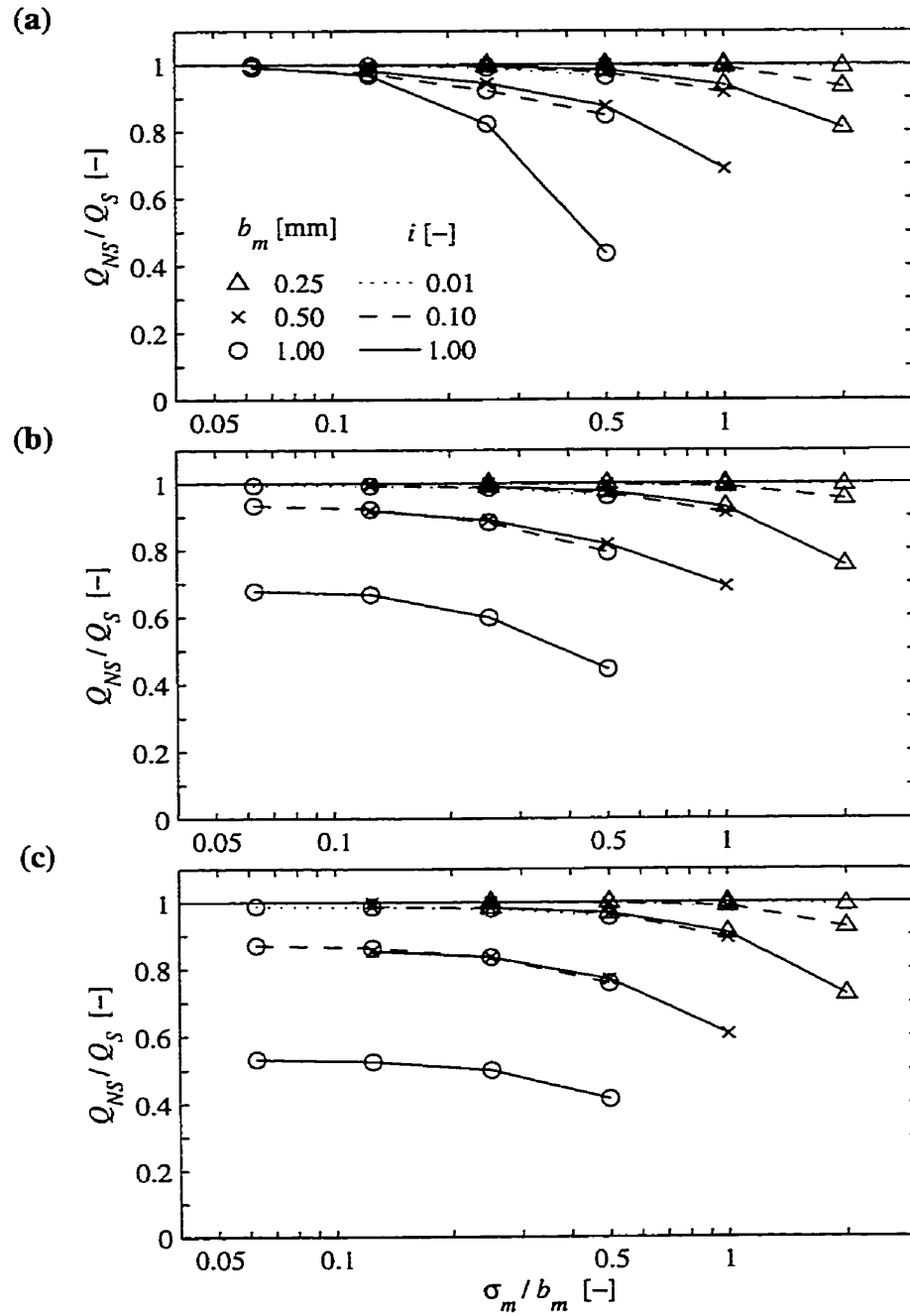


Figure 5.25. Navier-Stokes and Stokes synthetic fracture simulations: total flow ratio Q_{NS}/Q_S versus the relative roughness σ_m/b_m for fractures with (a) $\sigma_z = 0$, (b) $\sigma_z = 0.5$, and (c) $\sigma_z = 1$ mm. The synthetic fractures used normally distributed aperture with $\lambda_b = 5$ mm. The symbols represent three values of mechanical aperture b_m and the lines represent three values of hydraulic gradient i . Each data point is the mean of ~ 5 fracture realizations.

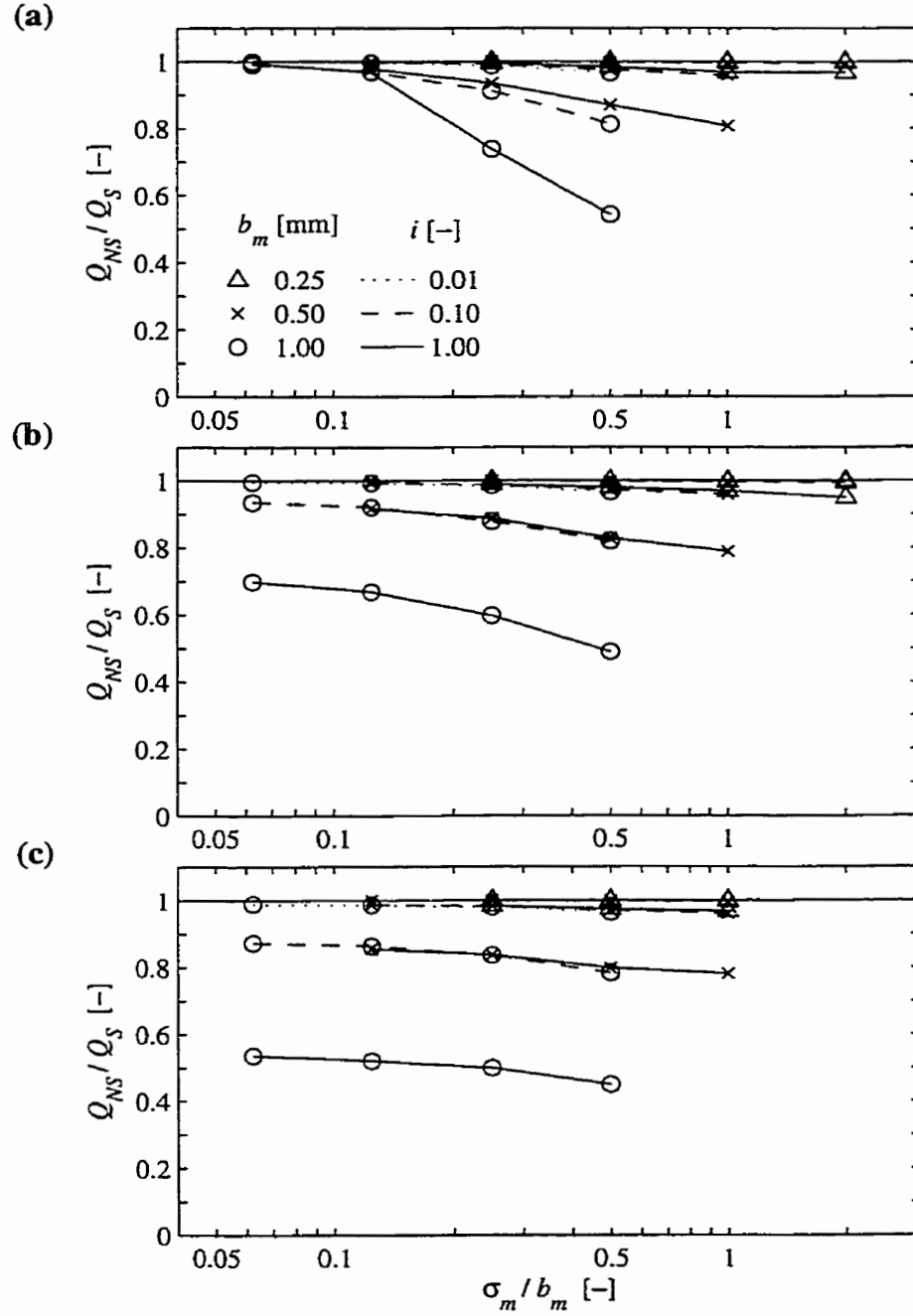


Figure 5.26. Navier-Stokes and Stokes synthetic fracture simulations: total flow ratio Q_{NS}/Q_S versus the relative roughness σ_m/b_m for fractures with (a) $\sigma_z = 0$, (b) $\sigma_z = 0.5$, and (c) $\sigma_z = 1$ mm. The synthetic fractures used lognormally distributed aperture with $\lambda_b = 2$ mm. The symbols represent three values of mechanical aperture b_m and the lines represent three values of hydraulic gradient i . Each data point is the mean of ~ 5 fracture realizations.

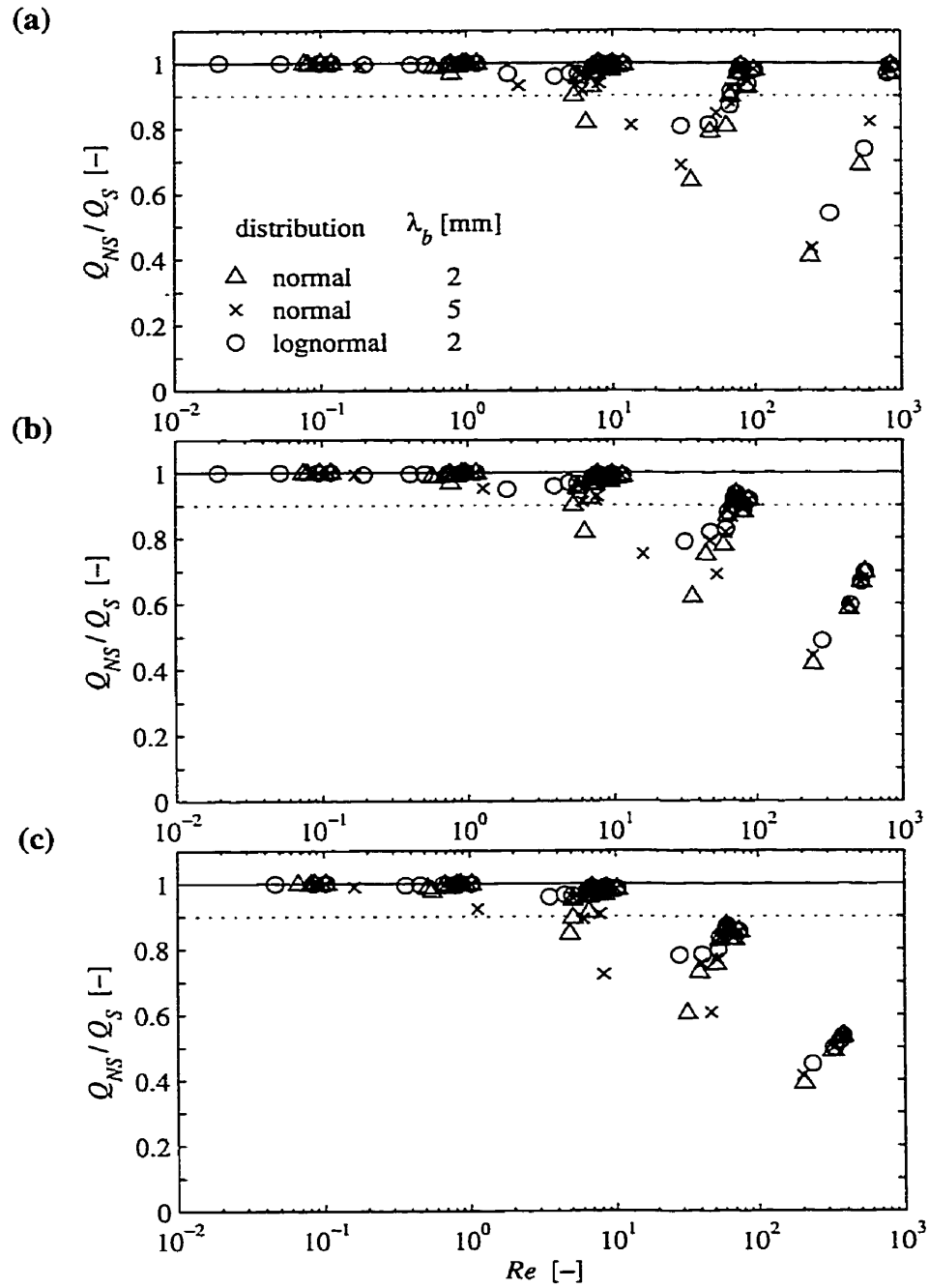


Figure 5.27. Navier-Stokes and Stokes synthetic fracture simulations: total flow ratio Q_{NS}/Q_S versus the Reynolds number Re for fractures with (a) $\sigma_z = 0$, (b) $\sigma_z = 0.5$, and (c) $\sigma_z = 1$ mm. The symbols represent three fracture types. Each data point is the mean of ~5 fracture realizations.

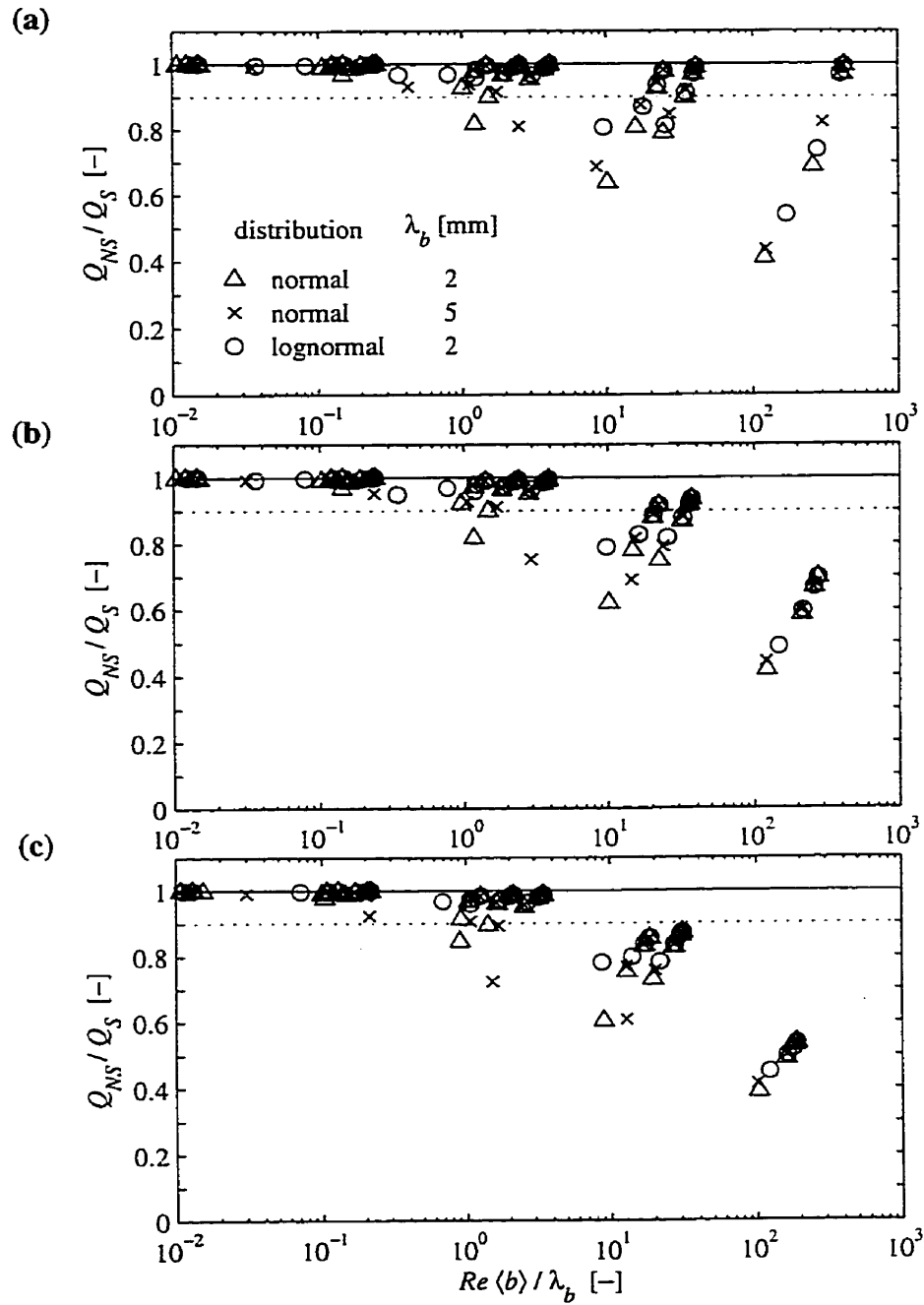


Figure 5.28. Navier-Stokes and Stokes synthetic fracture simulations: total flow ratio Q_{NS}/Q_S versus the kinematic parameter $Re(b)/\lambda_b$ for fractures with (a) $\sigma_z = 0$, (b) $\sigma_z = 0.5$, and (c) $\sigma_z = 1$ mm. The symbols represent three fracture types. Each data point is the mean of ~ 5 fracture realizations.

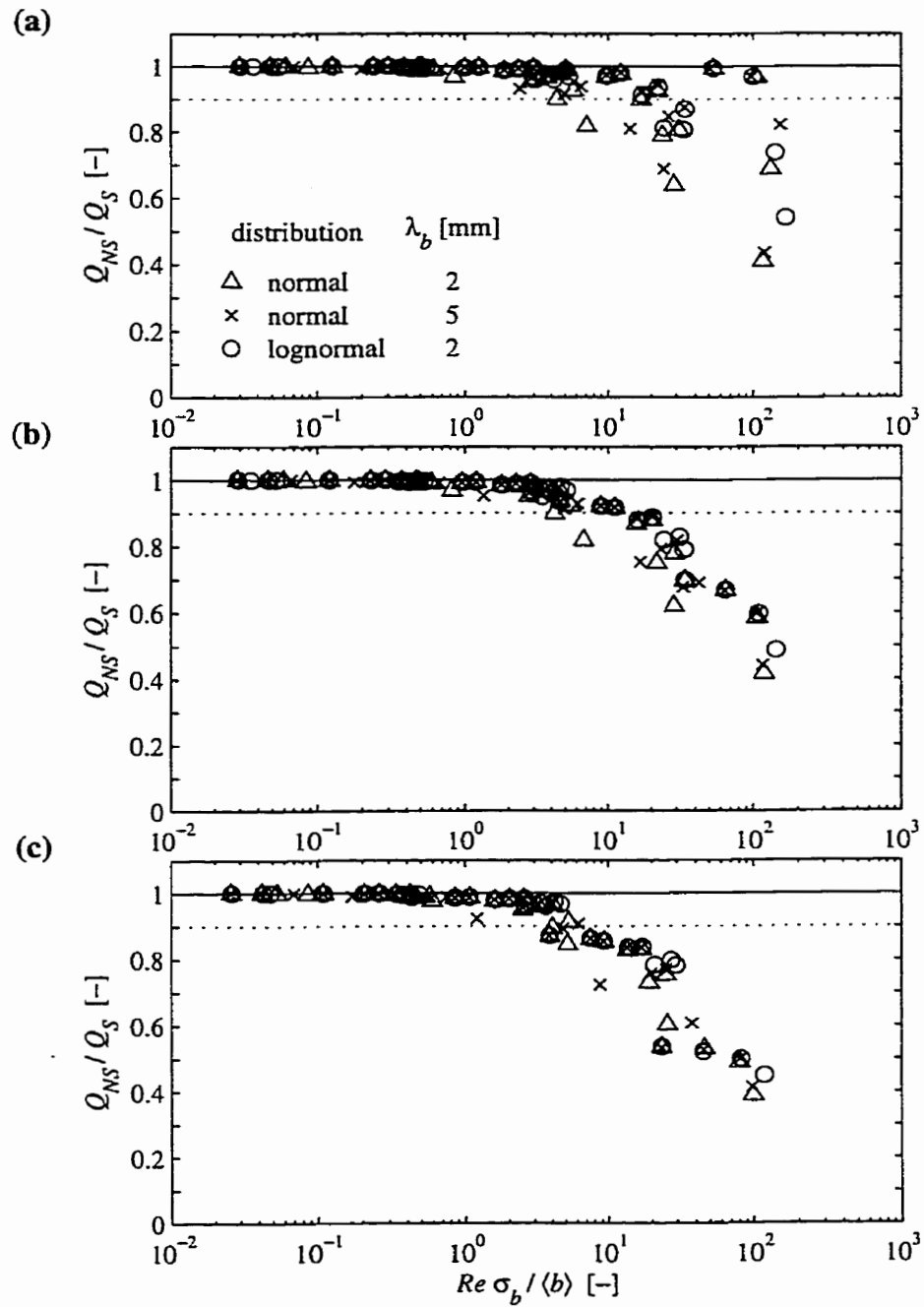


Figure 5.29. Navier-Stokes and Stokes synthetic fracture simulations: total flow ratio Q_{NS}/Q_S versus the kinematic parameter $Re \sigma_b / \langle b \rangle$ for fractures with (a) $\sigma_z = 0$, (b) $\sigma_z = 0.5$, and (c) $\sigma_z = 1$ mm. The symbols represent three fracture types. Each data point is the mean of ~5 fracture realizations.

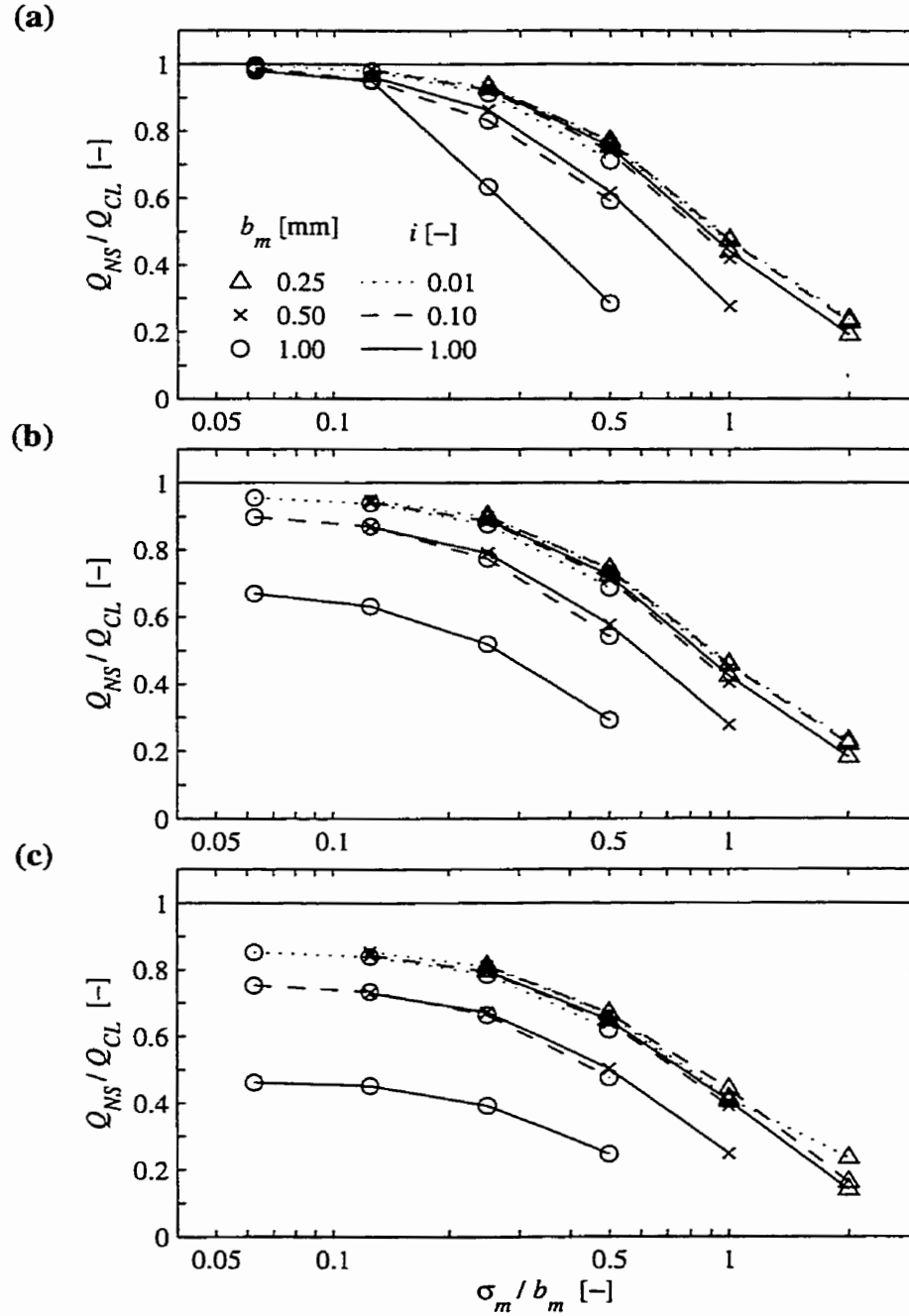


Figure 5.30. Navier-Stokes simulations and cubic law calculations for synthetic fractures: total flow ratio Q_{NS}/Q_{CL} versus the relative roughness σ_m/b_m for fractures with (a) $\sigma_z = 0$, (b) $\sigma_z = 0.5$, and (c) $\sigma_z = 1$ mm. The synthetic fractures used normally distributed aperture with $\lambda_h = 2$ mm. The symbols represent three values of mechanical aperture b_m , and the lines represent three values of hydraulic gradient i . Each data point is the mean of ~ 5 fracture realizations.

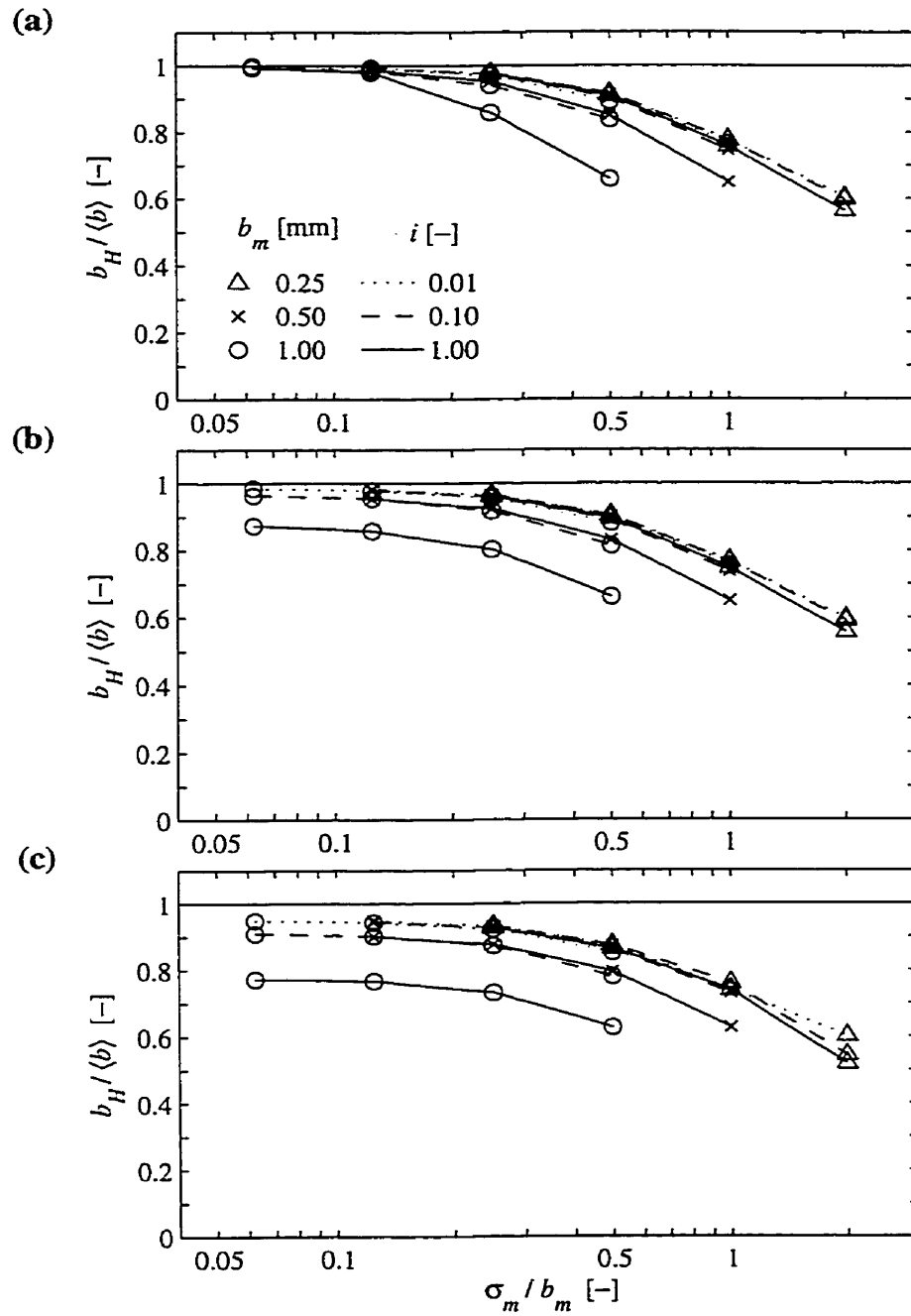


Figure 5.31. Navier-Stokes simulations and cubic law calculations for synthetic fractures: ratio of hydraulic aperture to the arithmetic mean aperture $b_H / \langle b \rangle$ versus the relative roughness σ_m / b_m for fractures with (a) $\sigma_z = 0$, (b) $\sigma_z = 0.5$, and (c) $\sigma_z = 1$ mm. The synthetic fractures used normally distributed aperture with $\lambda_b = 2$ mm. The symbols represent three values of mechanical aperture b_m , and the lines represent three values of hydraulic gradient i . Each data point is the mean of ~ 5 fracture realizations.

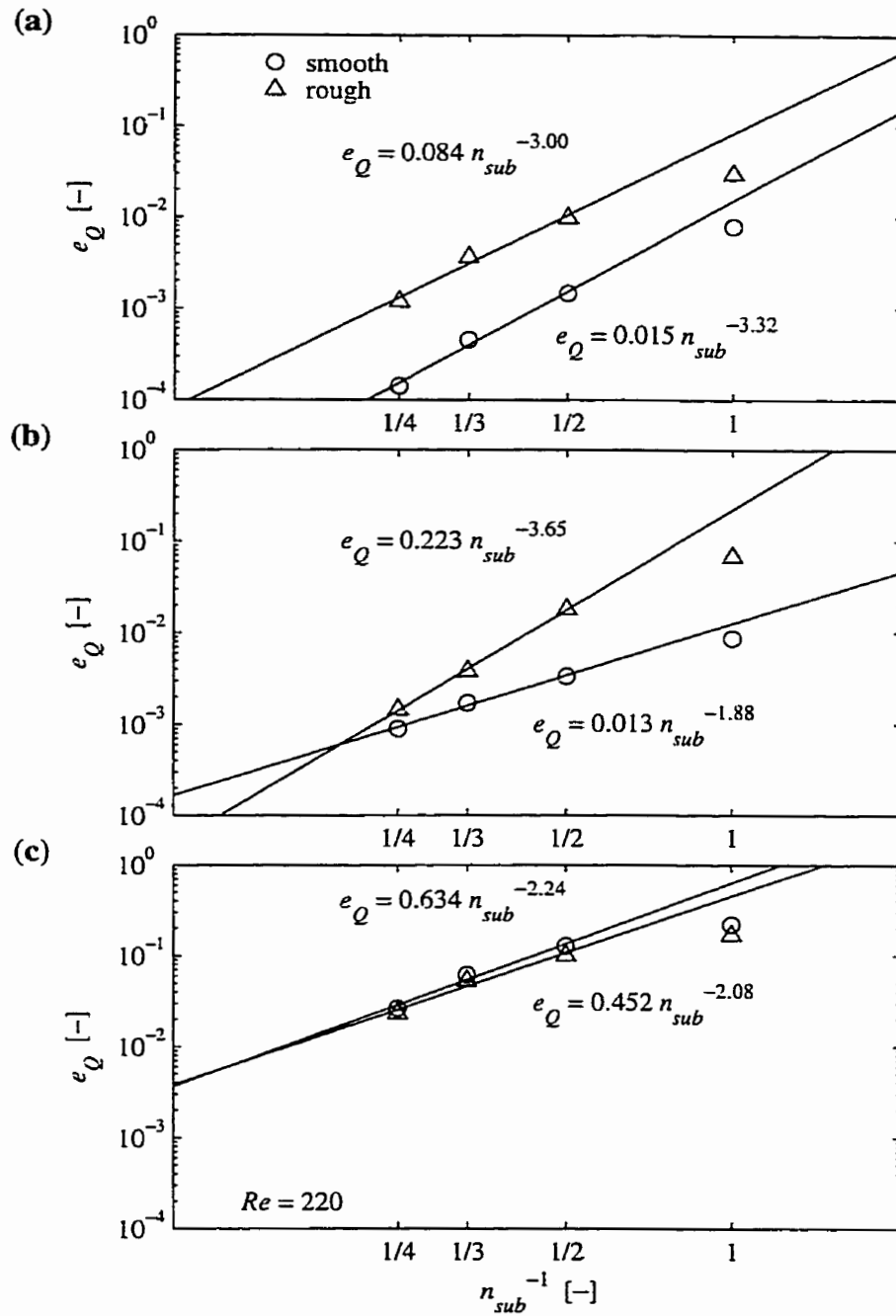


Figure 5.32. (a) LCL, (b) Stokes, and (c) Navier-Stokes synthetic fracture simulations: relative error e_Q versus the inverse number of subdivisions n_{sub}^{-1} applied to the base grids of 25×25 or $25 \times 25 \times 10$ CVs. The symbols represent smooth and rough fractures with $\sigma_m/b_m = 0.0625$ and 0.5 , respectively. The trend lines and equations display the regressed power relationship for each set of symbols.

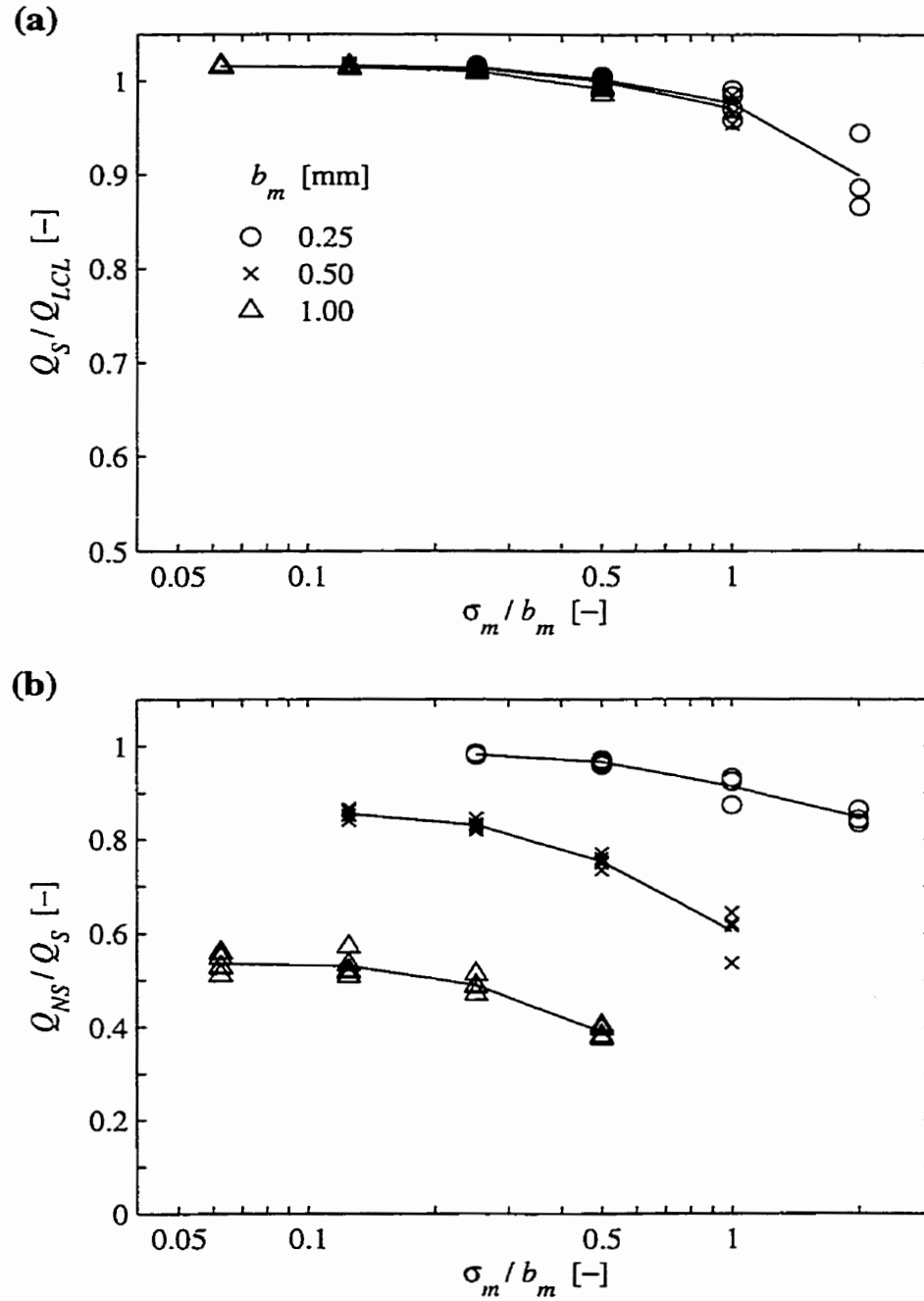
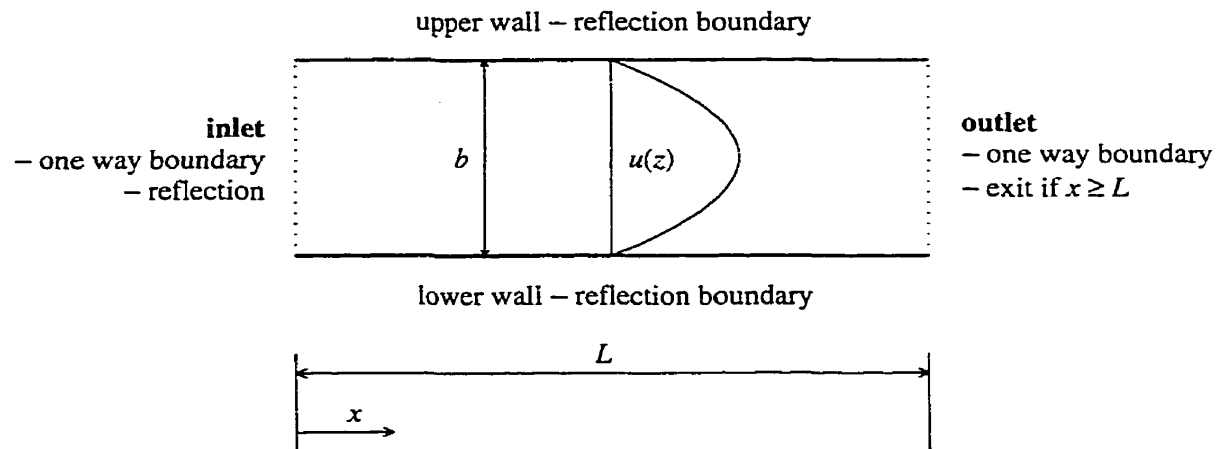


Figure 5.33. Stokes and Navier-Stokes synthetic fracture simulations: raw total flow ratio data Q_S/Q_{LCL} and Q_N/Q_S versus the relative roughness σ_m/b_m for fractures with normally distributed aperture, $\lambda_b = 2$ mm, and $\sigma_z = 1$ mm. The symbols represent three values of mechanical aperture b_m , and the lines represent the mean behaviour of each set of symbols. Each simulation used a hydraulic gradient $i = 1$.

(a)



(b)

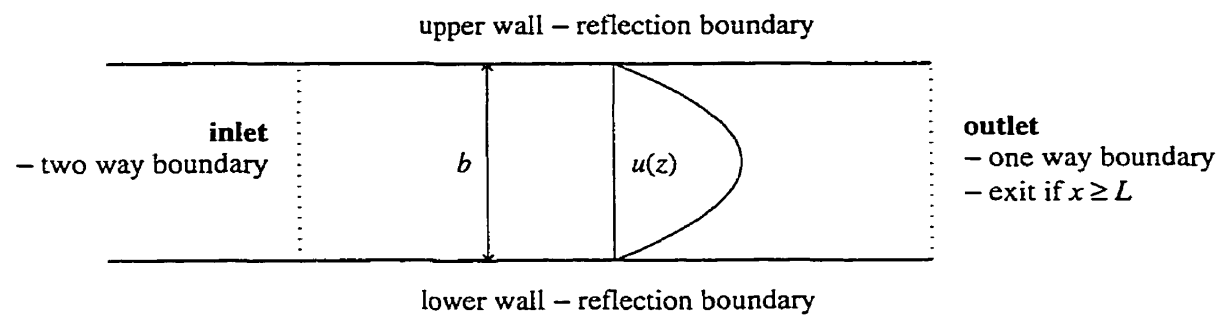


Figure 5.34. Schematic diagram of two-dimensional parallel plate domain and boundary conditions: (a) one-way inlet boundary, and (b) two-way inlet boundary.

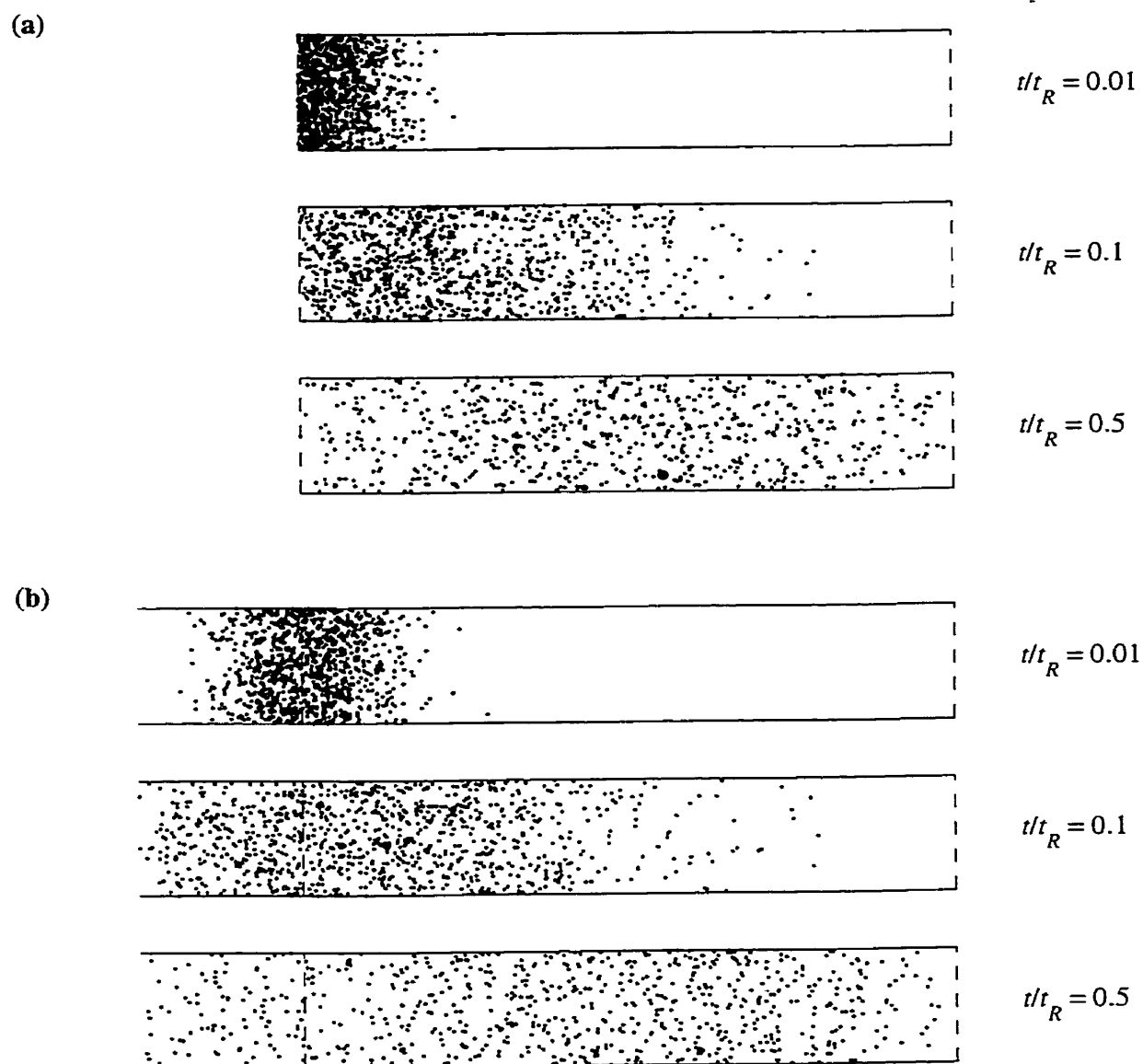


Figure 5.35. Simulated particle position at three values of normalized time (t/t_R) for parallel plate simulation T1 (see Table 5.4) with (a) the one-way inlet boundary, and (b) the two-way inlet boundary.

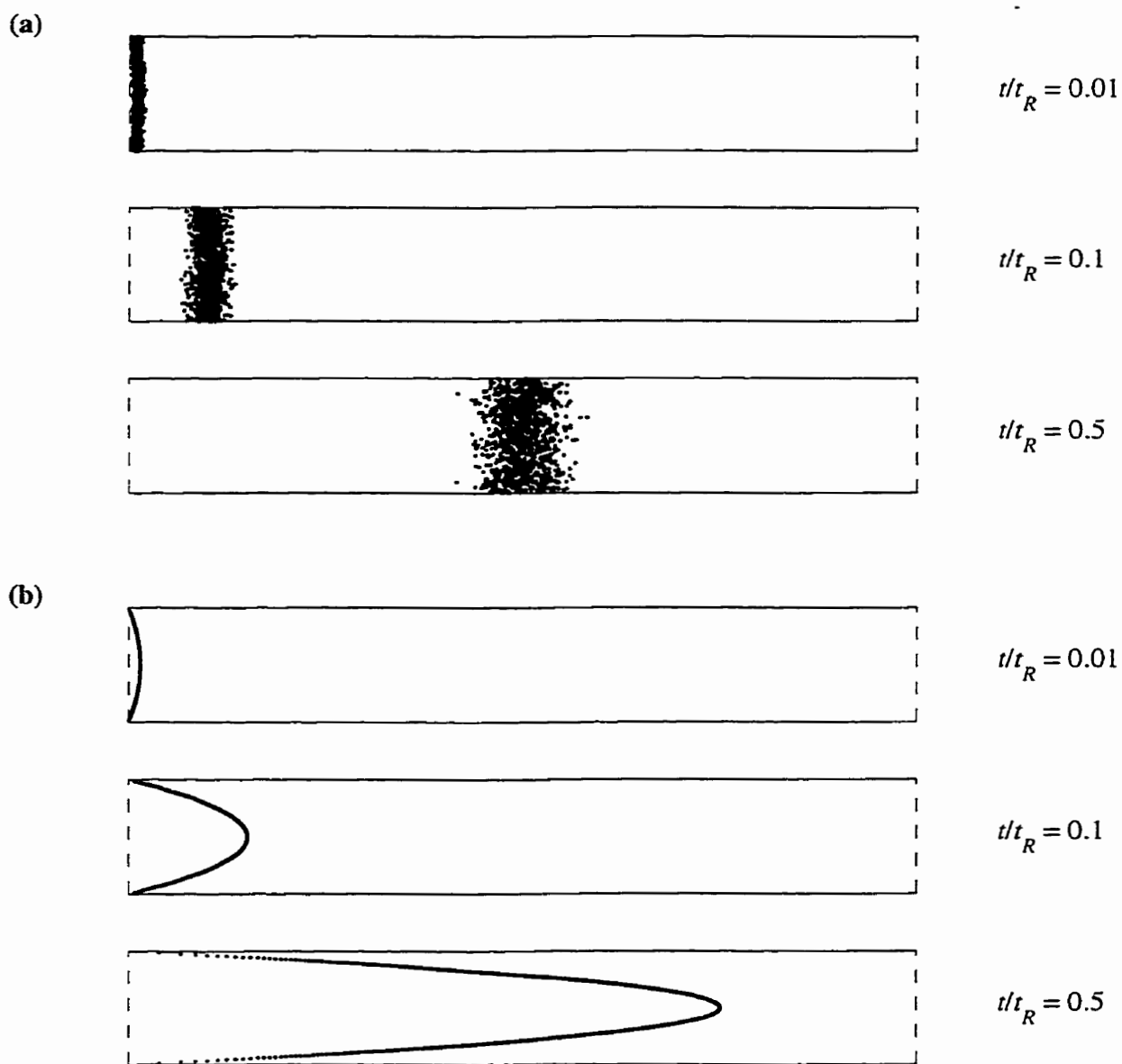


Figure 5.36. Simulated particle position at three values of normalized time (t/t_R) for parallel plate simulations (a) T4, and (b) T7. Both of these simulations use the one-way inlet boundary. Refer to Table 5.4 for simulation parameters.

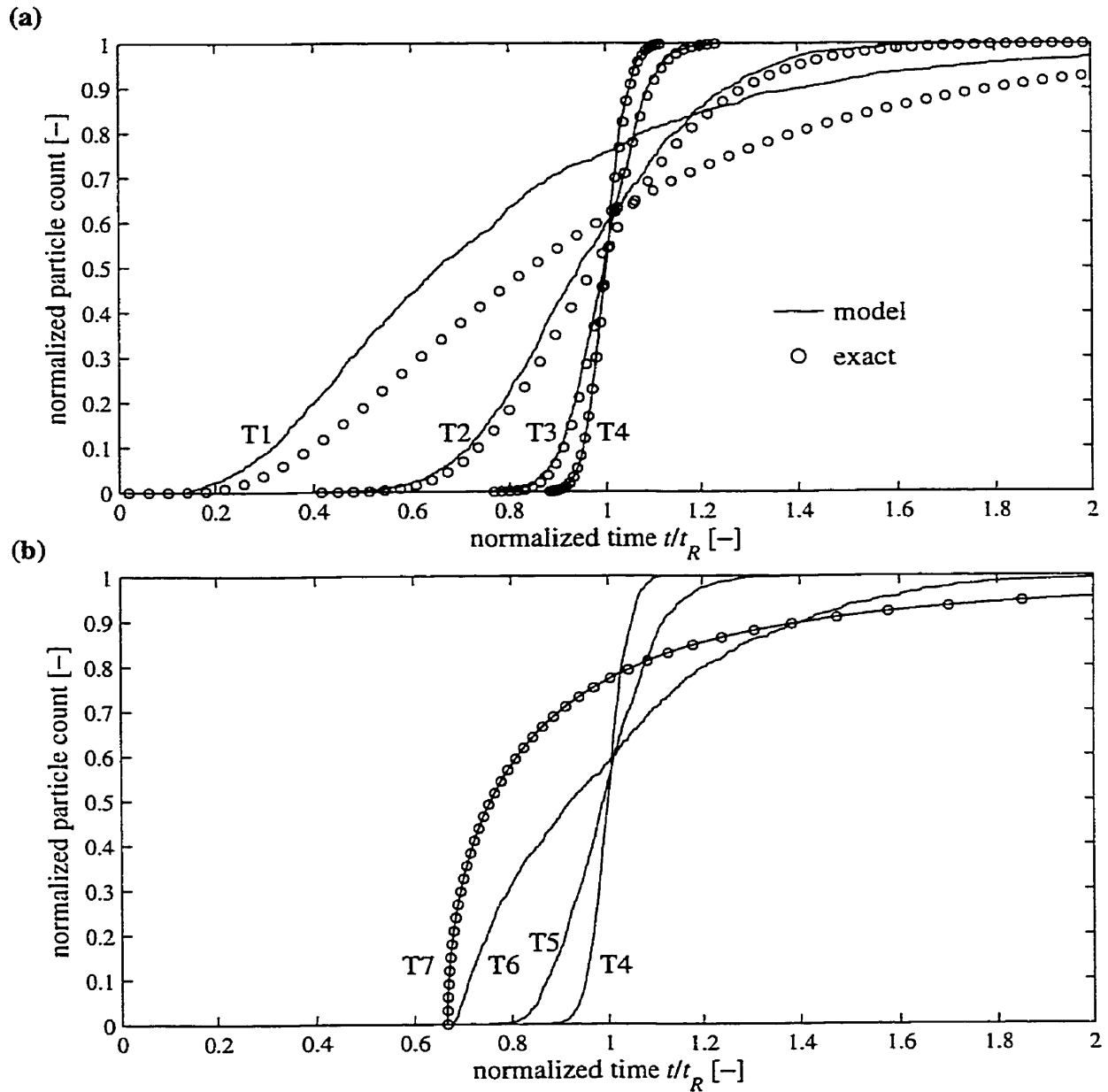


Figure 5.37. Normalized particle breakthrough curves using the one-way inlet boundary condition for parallel plate simulations: (a) T1 to T4, and (b) T4 to T7. Refer to Table 5.4 for simulation parameters.

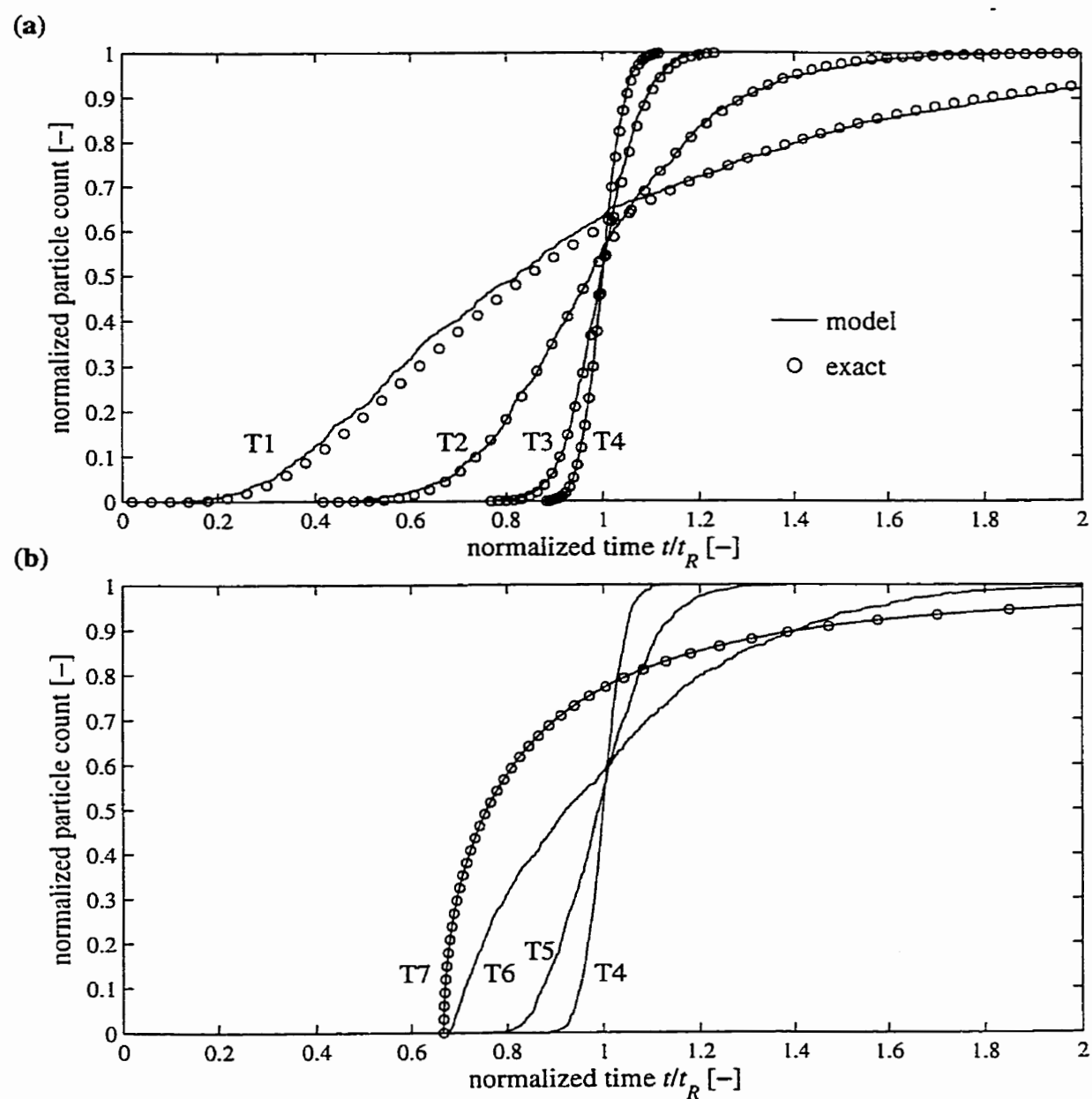


Figure 5.38. Normalized particle breakthrough curves using the two-way inlet boundary condition for parallel plate simulations: (a) T1 to T4, and (b) T4 to T7. Refer to Table 5.4 for simulation parameters.

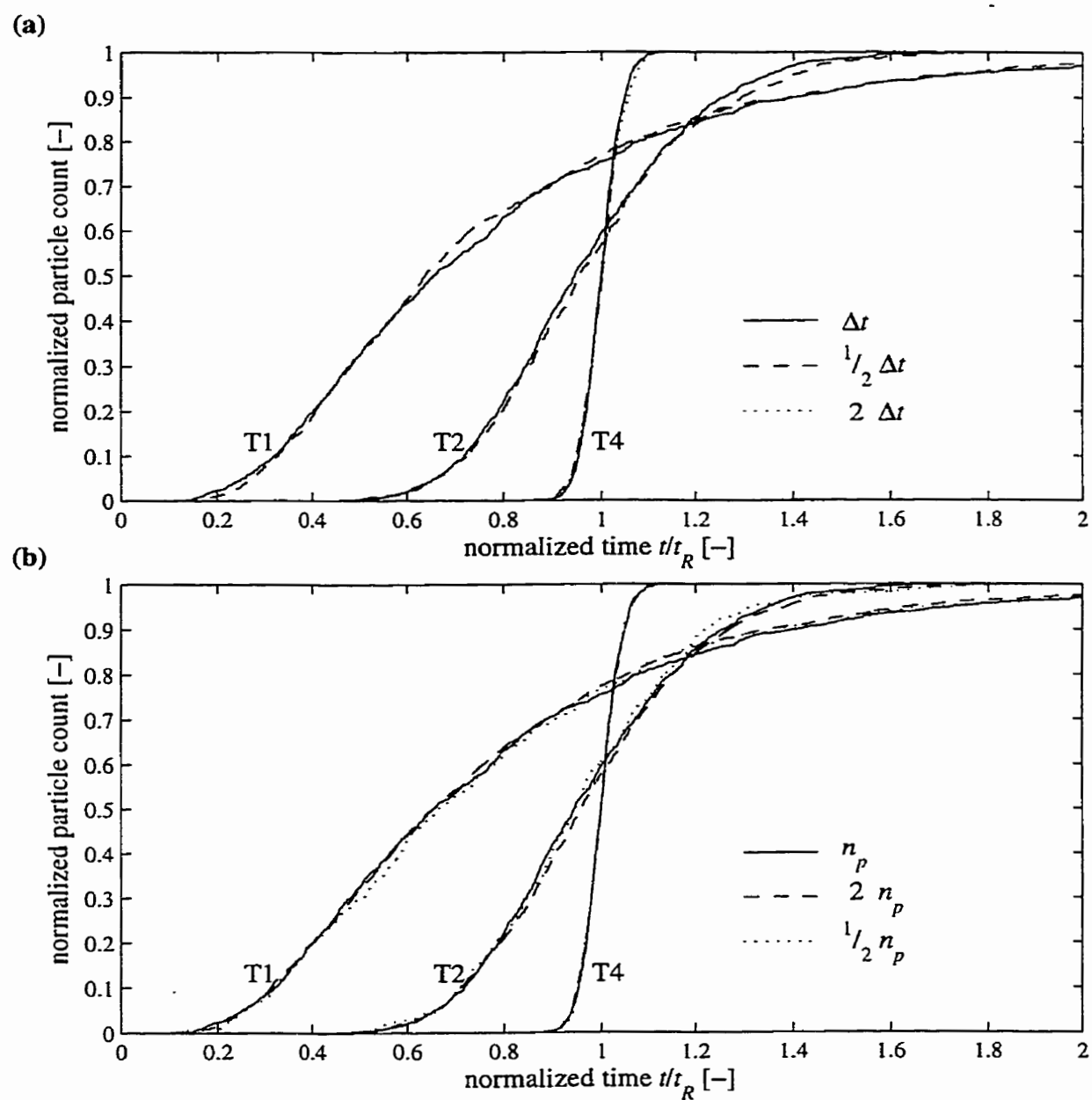


Figure 5.39. Normalized particle breakthrough curves using the one-way inlet boundary condition for parallel plate simulations T1, T2, and T4. (a) Results using the base time step Δt , $1/2 \Delta t$, and $2 \Delta t$. (b) Results using the base number of particles n_p , $1/2 n_p$, and $2 n_p$.

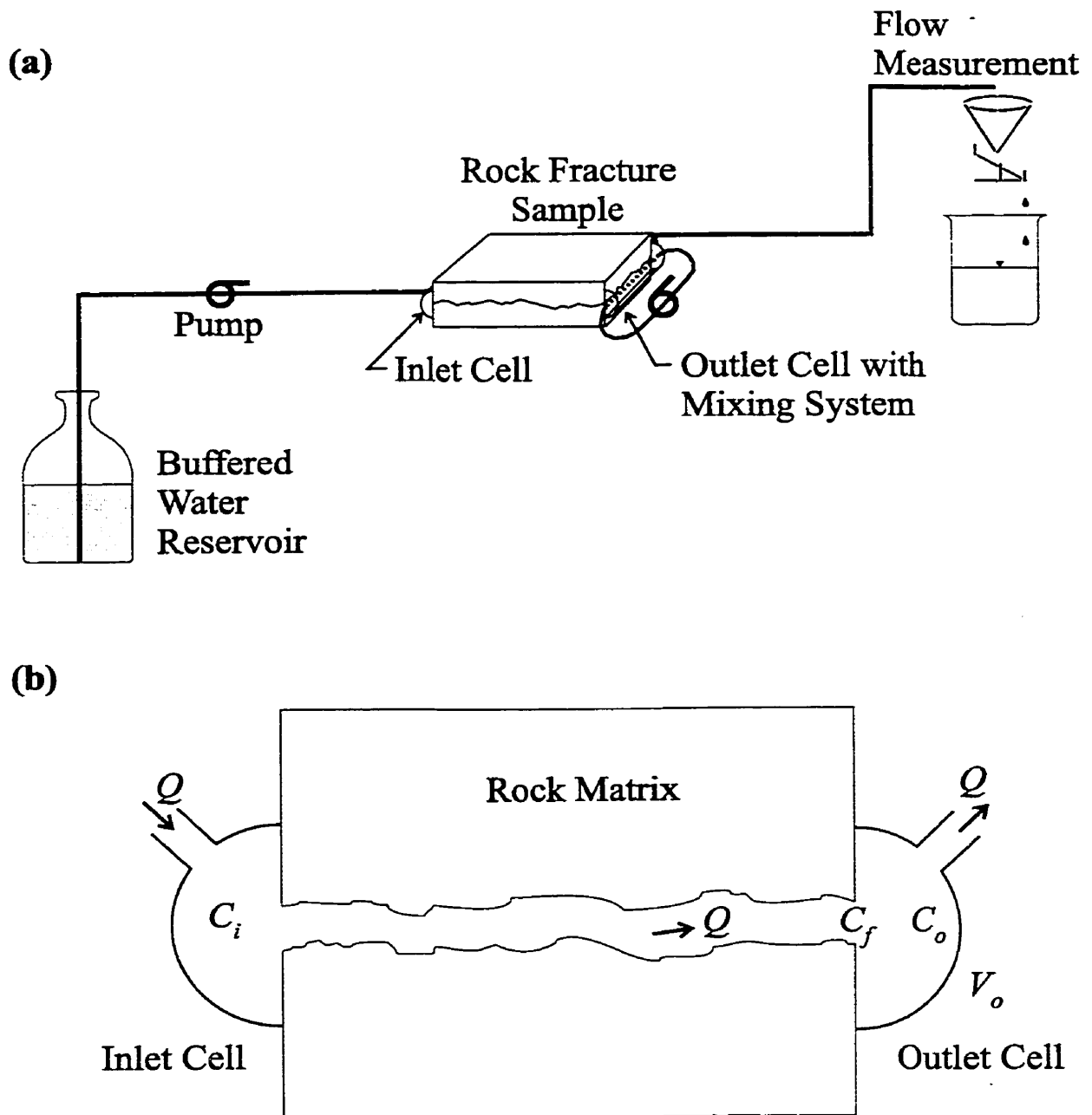


Figure 5.40. Schematic diagram of (a) laboratory apparatus used to perform hydraulic and tracer tests on fracture samples [Anderson, 2001], and (b) cross-section of fracture sample and inlet and outlet cells.

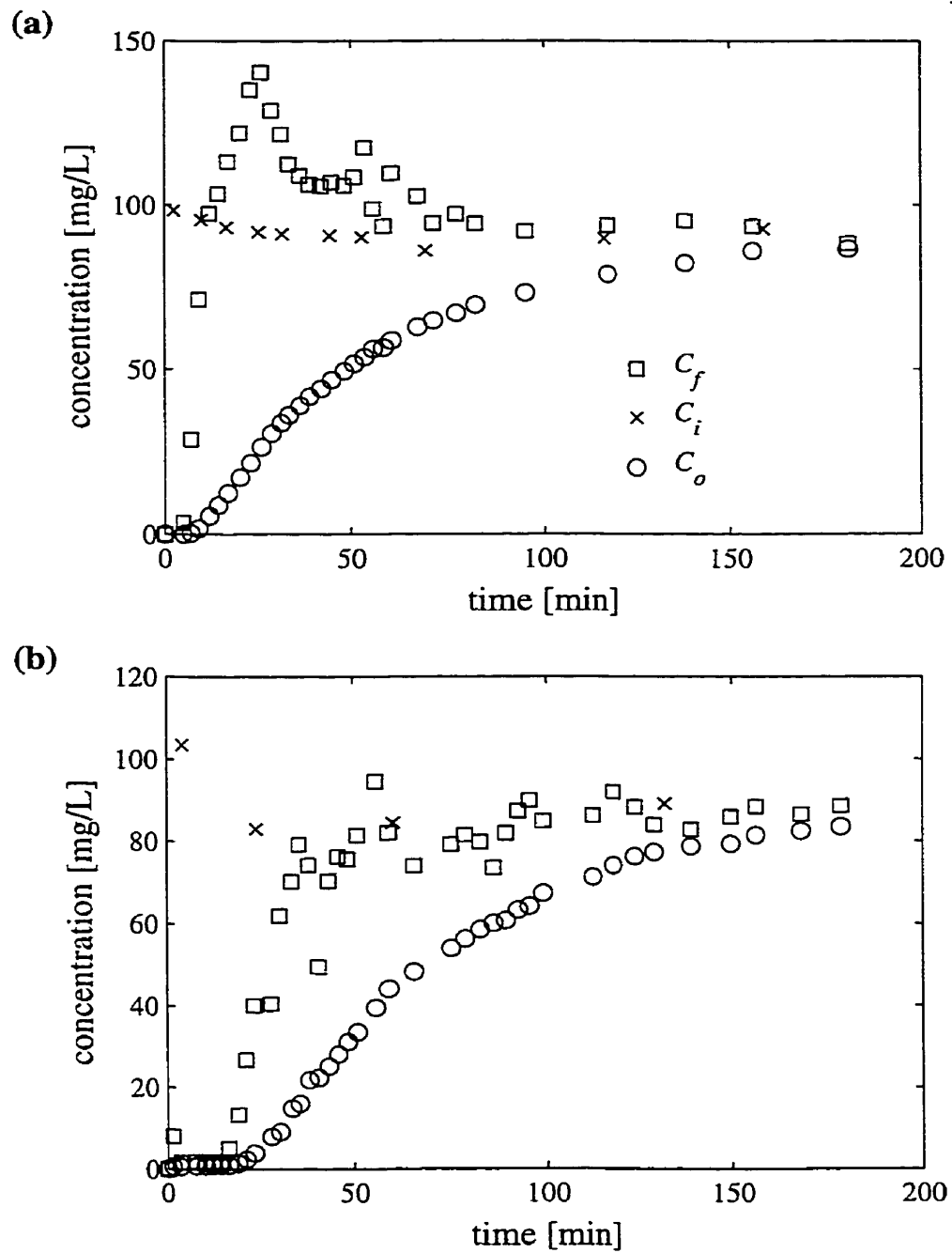


Figure 5.41. Observed laboratory tracer (bromide ion) concentrations at inlet cell C_i , outlet cell C_o , and fracture exit C_f over time for (a) Fracture I, and (b) Fracture II. The concentrations C_i and C_o were directly measured, and C_f was inferred using (5.3).

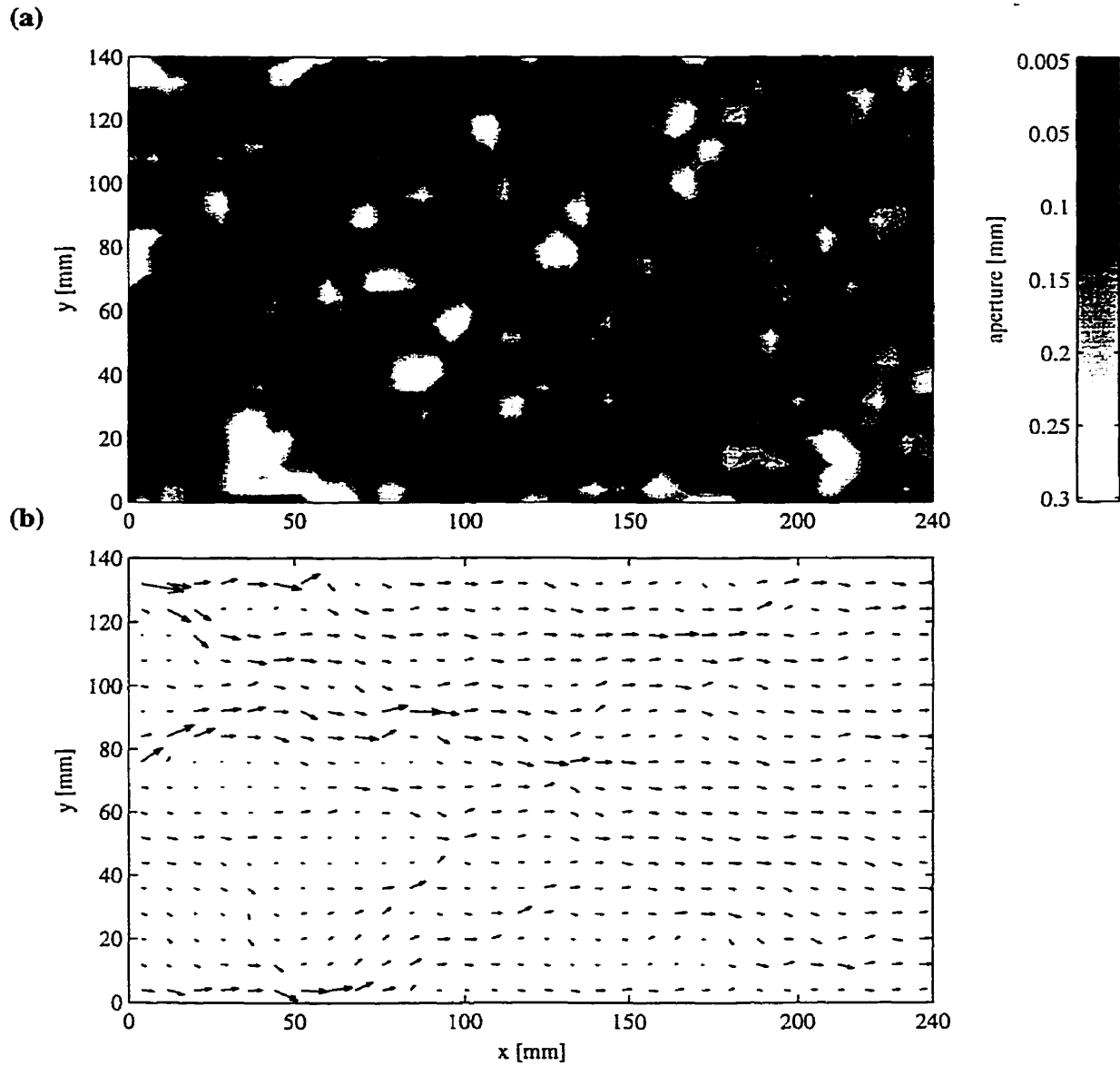


Figure 5.42. Fracture I flow simulation: (a) aperture field, and (b) simulated integrated flow field for b_m equal 0.130 mm. Statistics for the aperture field are listed in Table 5.5. The total flow through Fracture I is 0.5 mL/min and the maximum flow vector is 0.054 mL/min.

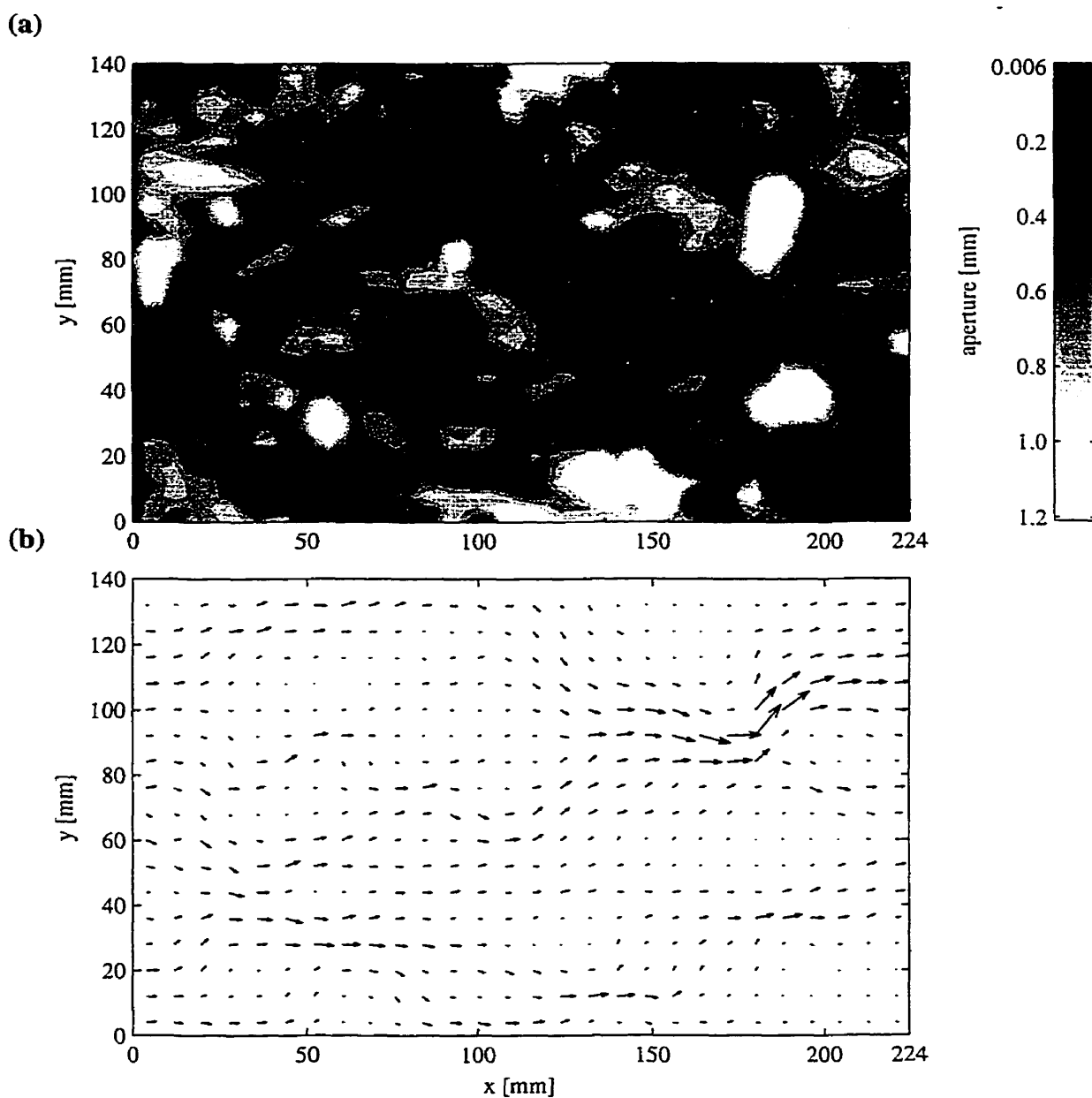


Figure 5.43. Fracture II flow simulation: (a) aperture field, and (b) simulated integrated flow field for b_m equal 0.585 mm. Statistics for the aperture field are listed in Table 5.5. The total flow through Fracture II is 1.3 mL/min and the maximum flow vector is 0.18 mL/min.

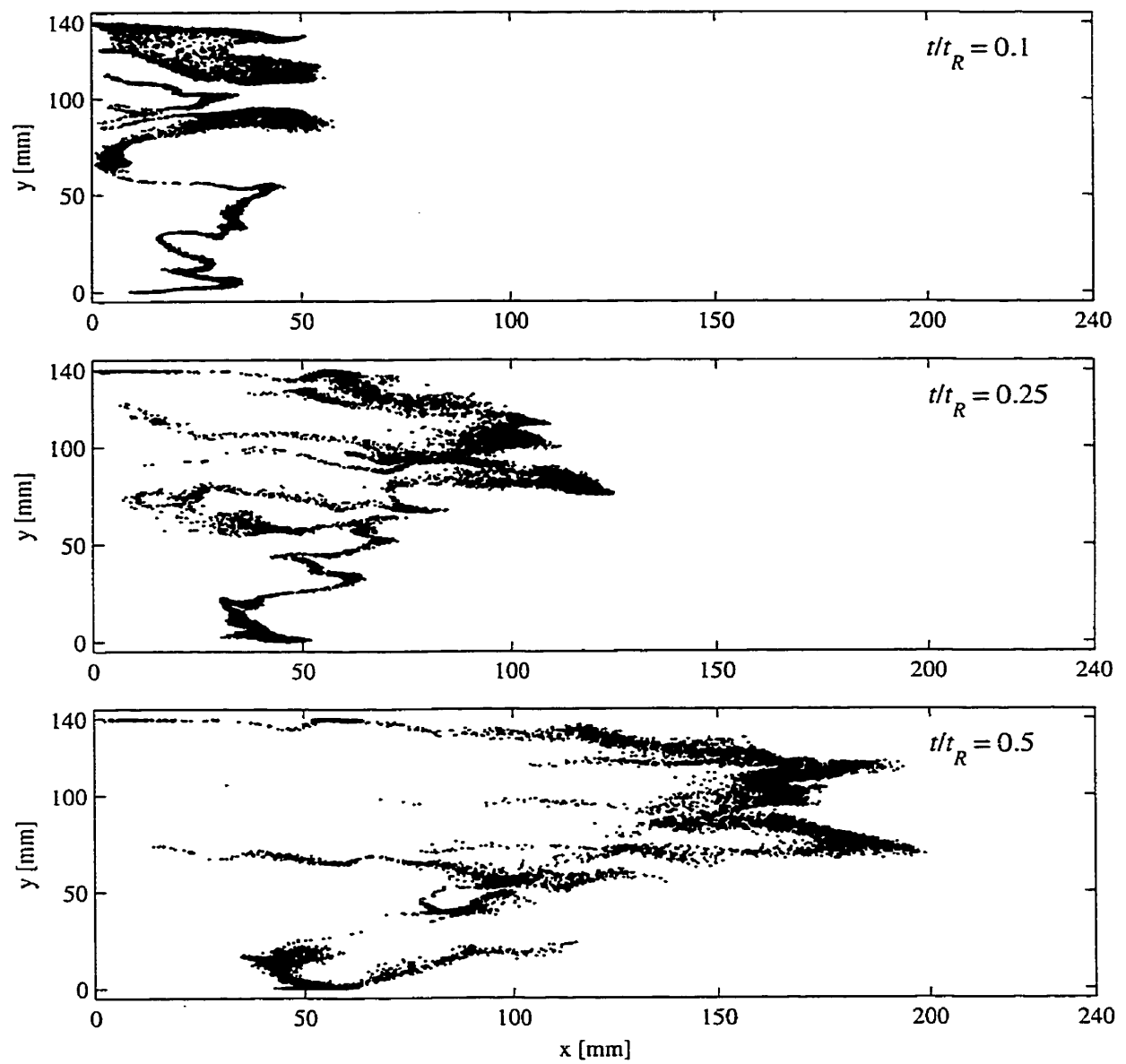


Figure 5.44. Fracture I transport simulation: x - y position of 10,000 particles at three values of normalized time t/t_R . Refer to Table 5.5 for simulation parameters.

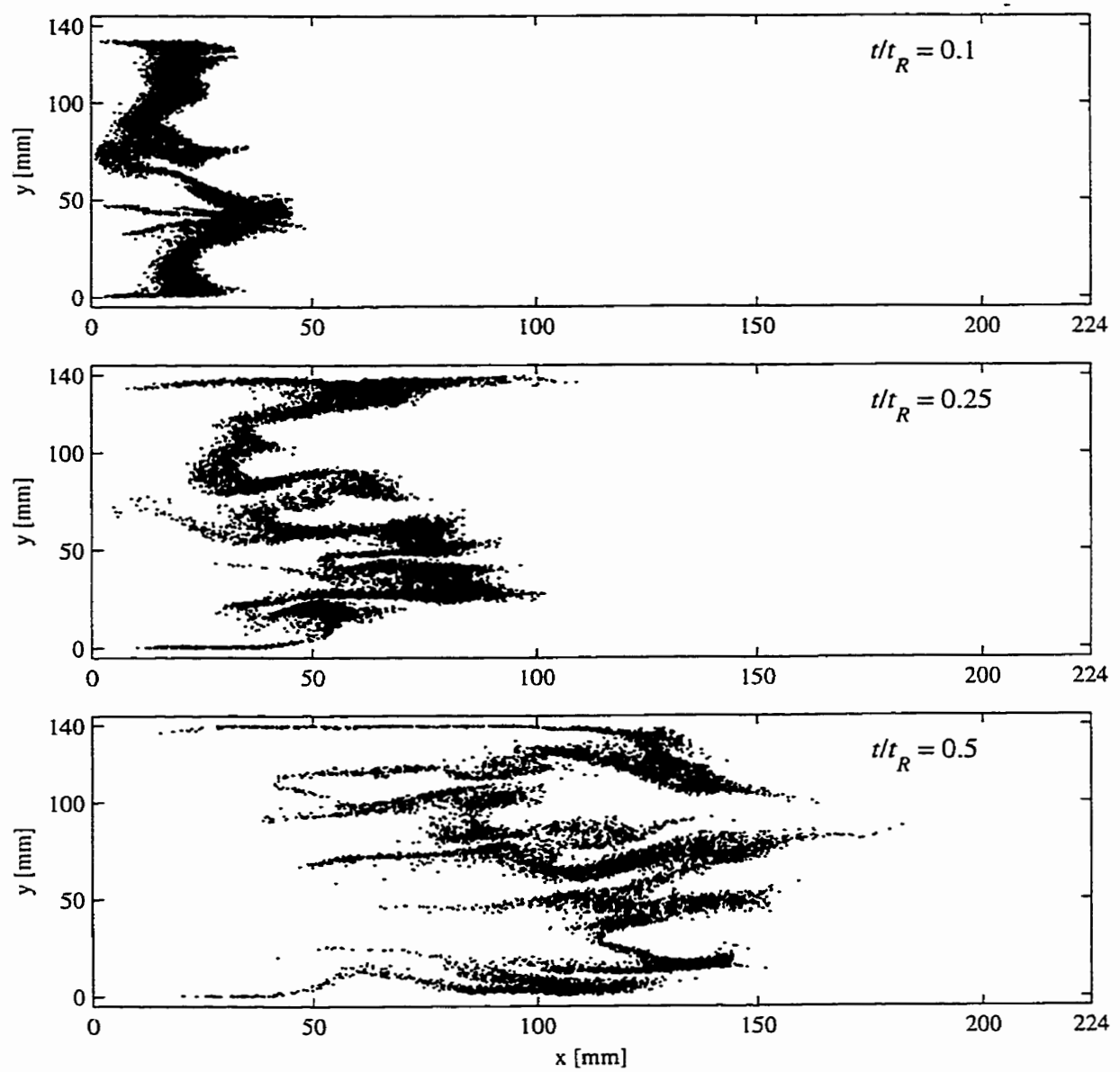


Figure 5.45. Fracture II transport simulation: x - y position of 10,000 particles at three values of normalized time t/t_R . Refer to Table 5.5 for simulation parameters.

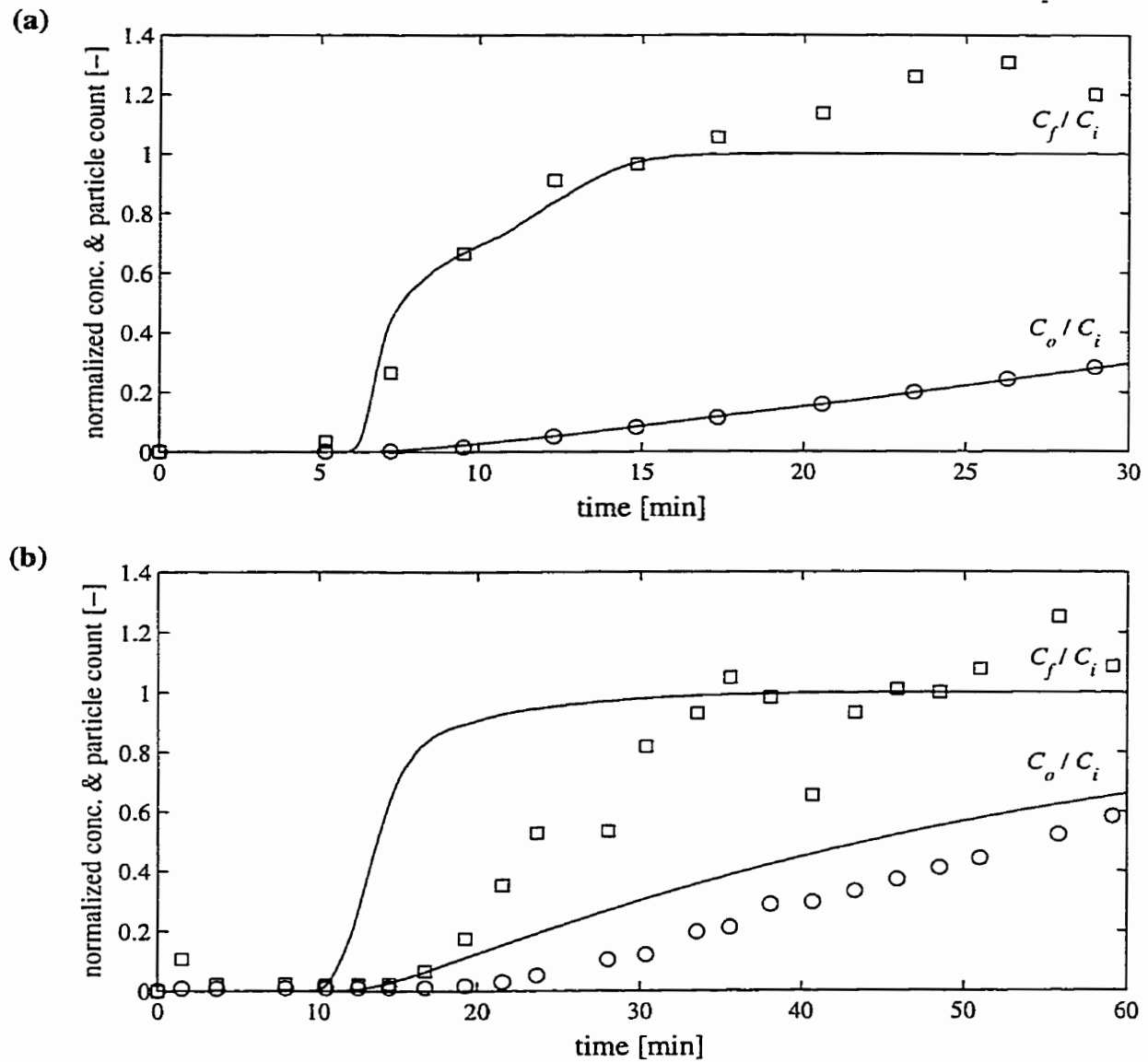


Figure 5.46. Normalized solute and particle breakthrough over time: (a) Fracture I, and (b) Fracture II. The measured concentration at the outlet cell C_o (circles) and the inferred concentration at the fracture exit C_f (squares) are normalized by inlet concentrations C_i of 107.3 and 75.6 mg/L for Fracture I and Fracture II, respectively. The solid lines for C_f/C_i are the normalized particle counts of breakthrough predicted by transport simulations. The solid lines for C_o/C_i are inferred from C_f/C_i using (5.3). Refer to Table 5.5 for simulation parameters.

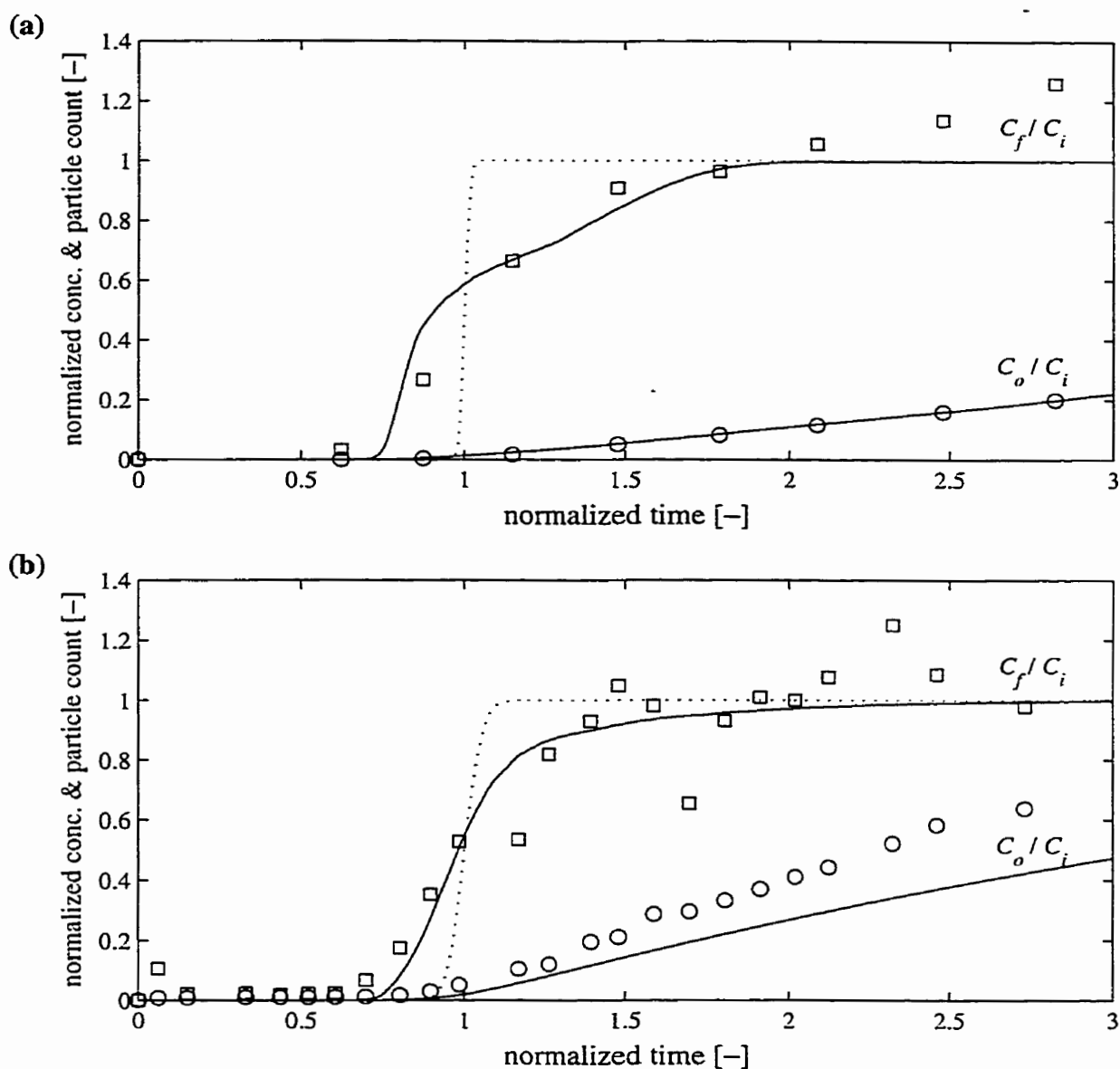


Figure 5.47. Normalized solute and particle breakthrough over normalized time: (a) Fracture I, and (b) Fracture II. Time for the laboratory data (symbols) is normalized by median arrival times of 8.3 and 24 min for Fracture I and II, respectively. Time for the simulated data (solid lines) is normalized by hydraulic residence times t_R of 8.3 and 14 min for Fracture I and II, respectively. particle. The dotted line is the exact solution of solute breakthrough for parallel plates with equivalent residence times and effective Péclet numbers as each fracture. Refer to Table 5.5 for simulation parameters.

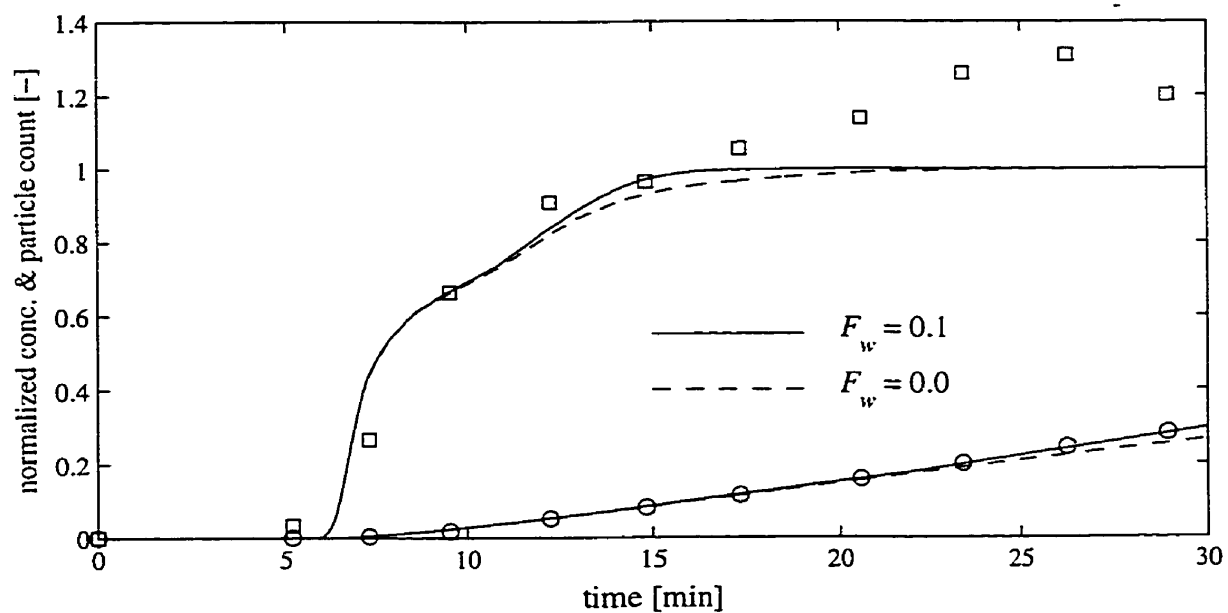


Figure 5.48. Normalized solute and particle breakthrough over time for Fracture I with two values of the minimum wall distance fraction ($F_w = 0.1$, and 0.0).

CHAPTER 6. Conclusions

The paramount conclusions of this thesis work are:

- ▶ Two numerical models that simulate three-dimension fluid flow and solute transport through a rough-walled fracture using the Navier-Stokes (NS) equations and the random walk particle method were successfully developed. The flow model employs the Finite Volume (FV) method to solve the NS equations and features a structured non-orthogonal colocated grid. The transport model uses the three-dimensional flow field from the flow model and the RWPM to transport massless marker particles through the FV grid. These models were verified by comparing simulations to exact and published results for flow and transport through parallel plates.
- ▶ A numerical model that simulates two-dimensional fluid flow through a rough-walled fracture using the local cubic law (LCL) approach was successfully developed. The model employs the FV method and features correction terms to account for non-orthogonal grid geometry due to fracture undulation. The model was verified by comparing LCL simulations to published results for flow through rough-walled fractures.
- ▶ The developed flow models were used to simulate fluid flow through various random rough-walled fractures to demonstrate differences in each approach and to determine criteria for the validity of the LCL approximation. These simulations clearly demonstrated that for larger values of relative roughness σ_m/b_m , mechanical or initial aperture b_m , and hydraulic gradient i that the inertial forces may significantly influence the internal flow field within a fracture and the bulk flow rate across the fracture. However, the influence of inertial forces on the bulk flow rate across the fractures was shown to be negligible when the following kinematic criteria were met:

$$Re < 1, \quad Re \langle b \rangle / \lambda_b < 0.1, \quad \text{and} \quad Re \sigma_b / \langle b \rangle < 1.$$

In addition, the bulk flow rates from three-dimensional simulations that met these criteria were within 10% of two-dimensional simulations using the LCL approach with geometric corrections. Therefore, for the range of random rough-walled fractures considered in this research, it may be concluded that the LCL is valid provided that the above kinematic criteria are satisfied.

- ▶ The three-dimensional flow and transport models were used to simulate hydraulic and tracer tests through laboratory samples of rough-walled rock fractures. The flow field for each simulation was calibrated by adjusting the mechanical aperture of the fracture void space until the total flow rate matched the observed value. The resulting flow fields, typical for rough walled fractures, displayed tortuous high-flow pathways along large aperture channels and low-flow zones in small aperture regions. The tracer transport simulations predicted particle distributions that exhibited channelling or fingering along the high-flow pathways, and particle entrapment in the low-flow zones. For one of the fractures the simulated breakthrough of particles was shown to be in very good agreement with the observed solute breakthrough curve. In fact, the simulation displayed a stair-step feature that matches the observed data. Therefore, it may be concluded that the models adequately describe fluid flow and contaminant transport through a single rough-walled fracture.

6.1 Research Contributions

The important research contributions of this thesis are:

- ▶ The only apparent solution of the three-dimensional NS equations for flow through realistic rough-walled fractures.
- ▶ The determination of kinematic criteria or constraints that delineate the influence of inertial forces on the bulk flow rate across rough-walled fractures.
- ▶ The direct validation of the two-dimensional LCL approximation with the geometric corrections presented in this thesis for conditions that satisfy the kinematic criteria.
- ▶ The flexible implementation of the RWPM to complex three-dimensional fracture flow fields.
- ▶ The successful prediction of tracer transport through a fully characterized laboratory fracture sample.

6.2 Future Work

Some examples of future extensions and/or applications of the developed models are:

- ▶ To perform additional flow simulations on a wider statistical range and a larger sample size of random rough-walled fractures.
- ▶ To develop more efficient FV grid generation and solution techniques (e.g., unstructured grids).
- ▶ To examine high Re laminar flow and transport processes with emphasis on improving convergence and accuracy of the numerical simulations.
- ▶ To compare the developed transport model to the two- and three-dimensional advection-dispersion equation.
- ▶ To include trapped immiscible fluids into the flow and transport models.

APPENDIX Recursive Equations of the Strongly Implicit Procedure

For three-dimensional systems the strongly implicit method (SIP) requires the definition of seven coefficient matrices which form the lower (L) and upper (U) triangular matrices of incomplete factorization. These SIP coefficients are represented with the symbol E (with the standard indices P, N, S, E, W, T , and B) and are defined as three-dimensional matrices by the following recursive loop:

$$\begin{aligned}
 & i = 1 \text{ to } n_i \\
 & \quad j = 1 \text{ to } n_j \\
 & \quad \quad k = 1 \text{ to } n_k \\
 & \quad \quad \quad E_{ijk}^W = -A_{ijk}^W \left(1 + \alpha_S (E_{i-1,jk}^N + E_{i-1,jk}^T) \right)^{-1} \\
 & \quad \quad \quad E_{ijk}^S = -A_{ijk}^S \left(1 + \alpha_S (E_{ij-1,k}^E + E_{ij-1,k}^T) \right)^{-1} \\
 & \quad \quad \quad E_{ijk}^B = -A_{ijk}^B \left(1 + \alpha_S (E_{ijk-1}^N + E_{ijk-1}^E) \right)^{-1} \\
 & \quad \quad \quad C_1 = \alpha_S (E_{ijk}^B E_{ijk-1}^N + E_{ijk}^W E_{i-1,jk}^N) \\
 & \quad \quad \quad C_2 = \alpha_S (E_{ijk}^B E_{ijk-1}^E + E_{ijk}^S E_{ij-1,k}^E) \\
 & \quad \quad \quad C_3 = \alpha_S (E_{ijk}^W E_{i-1,jk}^T + E_{ijk}^S E_{ij-1,k}^T) \\
 & \quad \quad \quad E_{ijk}^P = \left(A_{ijk}^P + C_1 + C_2 + C_3 - E_{ijk}^W E_{i-1,jk}^E - E_{ijk}^S E_{ij-1,k}^N - E_{ijk}^B E_{ijk-1}^T \right)^{-1} \\
 & \quad \quad \quad E_{ijk}^N = -E_{ijk}^P (A_{ijk}^N + C_1) \\
 & \quad \quad \quad E_{ijk}^E = -E_{ijk}^P (A_{ijk}^E + C_2) \\
 & \quad \quad \quad E_{ijk}^T = -E_{ijk}^P (A_{ijk}^T + C_3)
 \end{aligned} \tag{A.1}$$

where C_1 , C_2 and C_3 are temporary values, and α_S is the SIP parameter, which was set equal to 0.92. This step is required anytime the coefficients in (4.97) change. For the sequential solution of the momentum equations, (A.1) is required only once per outer iteration since the coefficients for the three velocity components are equivalent.

The correction step of the SIP begins by calculating the residual matrix using (4.99), then performs the following forward substitution loop:

$$\begin{aligned}
 & i = 1 \text{ to } n_i \\
 & \quad j = 1 \text{ to } n_j \\
 & \quad \quad k = 1 \text{ to } n_k \\
 & \quad \quad \quad R_{ijk} = E_{ijk}^P (R_{ijk} - E_{ijk}^W R_{i-1,jk} - E_{ijk}^S R_{ij-1,k} - E_{ijk}^B R_{ijk-1})
 \end{aligned} \tag{A.2}$$

and the following backward substitution loop:

$$\begin{aligned}
i &= n_i \text{ to } 1 \text{ by } -1 \\
j &= n_j \text{ to } 1 \text{ by } -1 \\
k &= n_k \text{ to } 1 \text{ by } -1 \\
R_{ijk} &= R_{ijk} - E_{ijk}^E R_{i+1jk} - E_{ijk}^N R_{ij+1k} - E_{ijk}^T R_{ijk+1} \\
\phi_{ijk} &= \phi_{ijk} + R_{ijk}
\end{aligned} \tag{A.3}$$

where R becomes the variable correction that is added to ϕ . This correction step becomes iterative by successively calculating (4.99), (A.2), and (A.3) over m iterations or until the absolute sum of the residuals is reduced to a specified fraction of its initial value.

REFERENCES

- Anderson, S. E., Dissolution of a residual NAPL in a variable aperture fracture, Ph.D. thesis in progress, Univ. of Waterloo, Waterloo, Ontario, 2001.
- Aitchison, J., and J. A. C. Brown, *The Lognormal Distribution*, Cambridge University Press, Cambridge, 1957.
- Aris, R., On dispersion of a solute in a fluid flow through a tube, *Proc. R. Soc. London A*, 235, 66-77, 1956.
- Bear, J., *Dynamics of Fluids in Porous Media*, Dover Publications, New York, 1972.
- Bird, R. B., W. E. Stewart, and E. N. Lightfoot, *Transport Phenomena*, John Wiley, New York, 1960.
- Brigerrsson, L., L. Moreno, I. Neretnieks, H. Widen, and T. Agren, A tracer migration experiment in a small fracture zone in granite, *Water Resour. Res.*, 29(12), 3867-3878, 1993.
- Brown, S. R., Fluid flow through rock joints: the effect of surface roughness, *J. Geophys. Res.*, 92(B2), 1337-1347, 1987.
- Brown, S. R., Simple mathematical model of a rough fracture, *J. Geophys. Res.*, 100(B4), 5941-5952, 1995.
- Brown, S., A. Caprihan, and R. Hardy, Experimental observation of fluid flow channels in a single fracture, *J. Geophys. Res.*, 103(B3), 5125-5132, 1998.
- Brown, S. R., R. L. Krans, and B.P. Bonner, Correlation between the surfaces of natural rock joints, *Geophys. Res. Lett.*, 13(13), 1430-1433, 1986.
- Brown, S. R., and C. H. Scholz, Broad bandwidth study of the topography of natural rock surfaces, *J. Geophys. Res.*, 90(12), 575-582, 1985.
- Brown, S. R., H. W. Stockman, and S. J. Reeves, Applicability of the Reynolds equation for modeling fluid flow between rough surfaces, *Geophys. Res. Lett.*, 22(18), 2537-2540, 1995.
- Cady, C. C., S. E. Silliman, and E. Shaffern, Variation in aperture estimate ratios from hydraulic and tracer tests in a single fracture, *Water Resour. Res.*, 29(9), 2975-2982, 1993.
- Coakley, K., K. Muralidhar, J. C. S. Long, and L. R. Myer, Equivalent permeability of statistically simulated single fractures, *Proc. of the Conf. on Geostatistical, Sensitivity, and Uncertainty Methods for Ground-Water Flow and Radionuclide Transport Modeling, San Francisco, California, Sept. 15-17, 1987*, edited by B. E. Buxton, pp. 441-469, Battelle Press, Columbus, Ohio, 1987.
- Cox, B. L., and J. S. Y. Wang, Single fracture aperture patterns: characterization by split-island fractal analysis, In *High Level Radioactive Waste Management Volume 2, Proc. Fourth Annual Int. Conf.*, Las Vegas, Nevada, 2053-2060, 1993.
- Durham, W. B., and B. P. Bonner, Self-propping and fluid flow in slightly offset joints at high effective pressures, *J. Geophys. Res.*, 99(B5), 9391-9399, 1994.

- Ferziger, J. H., and M. Peric, *Computational Methods for Fluid Dynamics 2nd Ed.*, Springer-Verlag, Berlin, 1999.
- Gale, J. E., Comparison of coupled fracture deformation and fluid flow models with direct measurements of fracture pore structure and stress-flow properties, in *Proc. 28th Symp. on Rock Mechanics, Tucson, AZ*, pp. 1213-1222, A. A. Balkema, Rotterdam, Netherlands, 1987.
- Gale, J., R. MacLeod, and R. LeMessurier, Site characterization and validation – Measurement of flowrate, solute velocities and aperture. Variation in natural fractures as a function of normal and shear stress, stage 3, *Stripa Project Report 90-11*, Swedish Nuclear Fuel and Waste Management Company Stockholm, 1990.
- Ge, S., A governing equation for fluid flow in rough fractures, *Water Resour. Res.*, 33(1), 53-61, 1997.
- Gentier, S., D. Billaux, and L. van Vliet, Laboratory testing of the voids of a fracture, *Int. J. Rock Mech. Rock Eng.*, 22, 149-157, 1989.
- Hakami, E., and N. Barton, Aperture measurement and flow experiments using transparent replicas of rock joints, in *Proc. of the Int. Symp. on Rock Joints*, edited by N. Barton and O. Stephansson, pp. 383-390, Balkema, Rotterdam, Netherlands, 1990.
- Hakami, E., and E. Larsson, Aperture measurement and flow experiments on a single natural fracture, *Int. J. Rock Mech. Min. Sci. & Geomech. Abstr.*, 33(4), 395-404, 1996.
- Hasegawa, E., and H. Izuchi, On steady flow through a channel consisting of a uneven wall and a plane wall, Part 1, Case of no relative motion in two walls, *Bull. Jap. Soc. Mech. Eng.* 26, 514-520, 1983.
- Hutchinson, B. R., and G. D. Raithby, A multigrid method based on the additive correction strategy, *Numerical Heat Transfer*, 9, 511-537, 1986.
- Iwai, K., Fundamental studies of the fluid flow through a single fracture, Ph.D. thesis, Univ. of California, Berkeley, 1982.
- James, S.C., and C.V. Chrysikopoulos, Transport of polydisperse colloid suspensions in a single fracture, *Water Resour. Res.*, 35(3), 707-718, 1999.
- James, S.C., and C.V. Chrysikopoulos, Transport of polydisperse colloids in a saturated fracture with spatially variable aperture, *Water Resour. Res.*, 36(6), 1457-1465, 2000.
- Keller, A. A., P. V. Roberts, and P. K. Kitanidis, Prediction of single phase transport parameters in a variable aperture fracture, *Geophys. Res. Let.*, 22(11), 1425-1428.
- Keller, A., High resolution, non-destructive measurement and characterization of fracture apertures, *Int. Jour. Rock Mech. Min. Sci.*, 35(8), 1037-1050, 1998.
- Kinzelback, W., and G. Uffink, The random walk method and extensions in groundwater modelling, In J. Bear and M.Y. Corapcioglu (eds.), *Transport Processes in Porous Media*, 761-787, 1991.
- Lomize, G. M., *Flow in Fractured Rocks* (in Russian), Gosenergoizdat, Moscow, 1951.

- Louis, C., A study of groundwater flow in jointed rock and its influence on the stability of rock masses, *Rock Mech. Res. Rep. 10*, Imp. Coll., London, 1969.
- Meakin, P., T. Rage, G. Wagner, J. Feder, and T. Jossang, Simulations of one- and two-phase flow in fractures, In *Fluid Flow and Transport in Rocks: Mechanisms and Effects*, B. Jamtveit and B. Yardley (eds.), 253-61, Chapman & Hall, 1996.
- Michell, A. G. M., *Lubrication: Its Principles and Practice*, Blackie & Son, London, 1950.
- Milne-Thomson, L. M., *Theoretical Hydrodynamics*, Macmillan, New York, 1968.
- Moreno, L., I. Neretnieks, and T. Eriksen, Analysis of some laboratory tracer runs in natural fissures, *Water Resour. Res.*, 21(7), 951-958, 1985.
- Moreno, L., Y. W. Tsang, C. F. Tsang, F. V. Hale, and I. Neretnieks, Flow and tracer transport in a single fracture: a stochastic model and its relation to some field observations, *Water Resour. Res.*, 24(12), 2033-2048, 1988.
- Mourezenko, V. V., J. -F. Thovert, and P. M. Adler, Permeability of a single fracture; validity of the Reynolds equation, *J. Phys. II France*, 5, 465-482, 1995.
- Murphy, J. R., and N. R. Thomson, Two-phase flow in a variable aperture fracture, *Water Resour. Res.*, 29(10), 3453-3476, 1993.
- NRC, *Rock Fractures and Fluid Flow: Contemporary Understanding and Applications*, National Academy Press, Washington, 1996.
- Neretnieks, I., T. Eriksen, and P. Tahtinen, Tracer movement in a single fissure in granitic rock: some experimental results and their interpretation, *Water Resour. Res.*, 18(4), 849-858, 1982.
- Neuzil, C. E., and J. V. Tracy, Flow through fractures, *Water Resour. Res.*, 17(1), 191-199, 1981.
- Nicholl, M.J., H. Rajaram, R.J. Glass, and R. Detwiler, Saturated flow in a single fracture: evaluation of the Reynolds equation in measured aperture fields, *Water Resour. Res.*, 35(11), 3361-3373, 1999.
- Novakowski, K. S., The analysis of tracer experiments conducted in divergent radial flow fields, *Water Resour. Res.*, 28(12), 3215-3225, 1992.
- Novakowski, K. S., and P. A. Lapcevic, Field measurement of radial solute transport in a fractured rock, *Water Resour. Res.*, 30(1), 37-44, 1994.
- Oron, A. P., and B. Berkowitz, Flow in rock fractures: the local cubic law assumption reexamined, *Water Resour. Res.*, 34(11), 2811-2825, 1998.
- Pantankar, S. V., *Numerical Heat Transfer and Fluid Flow*, Hemisphere, New York, 1980.
- Patir N., and H. S. Cheng, An average flow model for determining effects of three-dimensional roughness on partial hydrodynamic lubrication, *J. Lubrication Technology*, 100, 12-17, 1978.
- Piggott, A. R., and D. Elsworth, Laboratory assessment of the equivalent aperture of a rock fracture, *Geophys. Res. Lett.*, 20(13), 1387-1390, 1993.
- Poon, C. Y., R. S. Sayles, and T. A. Jones, Surface measurement and fractal characterization of naturally fractured rocks, *J. Phys. D: Appl. Phys.*, 25, 1269-1275, 1992.

- Power, W. L., and T. E. Tullis, Euclidean and fracture models for the description of rock-surface roughness, *J. Geophys. Res.*, 96(B1), 415-424, 1991.
- Pruess, K., and Y. W. Tsang, On two-phase relative permeability and capillary pressure of rough-walled fracture, *Water Resour. Res.*, 26(9), 1915-1926, 1990.
- Raven, K. G., and J. E. Gale, Water flow in a natural rock fracture as a function of stress and sample size, *Int. J. Rock Mech. Min. Sci. & Geomech. Abstr.*, 22(4), 251-261, 1985.
- Raven, K. G., K. S. Novakowski, and P. A. Lapcevic, Interpretation of field tracer tests of a single fracture using a transient solute storage model, *Water Resour. Res.*, 24(12), 2019-2032, 1988.
- Rasmussen, T.C., Laboratory characterization of fluid flow parameters in a porous rock containing a discrete fracture, *Geophys. Res. Lett.*, 22(11), 1401-1404, 1995.
- Reimus, P. W., and B. A. Robinson, Aperture characteristics, saturated fluid-flow, and tracer-transport calculations for a natural fracture, In *High Level Radioactive Waste Management Volume 2, Proc. Fourth Annual Int. Conf.*, Las Vegas, Nevada, 2009-2016, 1993.
- Renshaw, C. E., On the relationship between mechanical and hydraulic apertures in rough-walled fractures, *J. Geophys. Res.*, 100(B12), 24,629-24,636, 1995.
- Rhie, C. M., and W. L. Chow, A numerical study of the turbulent flow past an isolated aerofoil with trailing edge separation, *AIAA J.*, 21, 1525-1532, 1983.
- Romm, E. S., *Flow Characteristics of Fractured Rocks* (in Russian), Nedra, Moscow, 1966.
- Russell, L.D., H. Rajaram, and R.J. Glass, Solute transport in variable-aperture fractures: An investigation of the relative importance of Taylor dispersion and macrodispersion, *Water Resour. Res.*, 36(7), 1611-1625, 2000.
- Scheidegger, A. E., *The Physics of Flow Through Porous Media*, 3rd ed., University of Toronto Press, Toronto, 1974.
- Schrauf, T. W., and D. D. Evans, Laboratory studies of gas flow through a single natural fracture, *Water Resour. Res.*, 22(7), 1038-1050, 1986.
- Sharp, J. C., Fluid flow through fissured media, Ph.D. thesis, University of London, London, 1970.
- Sharp, J. C., and Y. N. T. Maini, Fundamental considerations on the hydraulic characteristics of joints in rock, In *Proceedings Symposium on Percolation Through Fissured Rock*, International Society for Rock Mechanics, Stuttgart, 1972.
- Silliman, S. E., An interpretation of the difference between aperture estimates derived from hydraulic and tracer tests in a single fracture, *Water Resour. Res.*, 25(10), 2275-2283, 1989.
- Snow, D. T., A parallel plate model of fracture permeable media, Ph.D. thesis, University of California, Berkeley, 1965.
- Snow, D. T., The frequency and apertures of fractures in rock, *Int. J. Rock Mech. Min. Sci.*, 7, 23-40, 1970.

- Thompson, M. E., and S. R. Brown, The effect of anisotropic surface roughness of flow and transport in fracture, *J. Geophys. Res.*, 96(B13), 21,923-21,932, 1991.
- Tompson, A. F. B., and L. W. Gelhar, Numerical simulation of solute transport in three-dimensional, randomly heterogeneous porous media, *Water Resour. Res.*, 26(10), 2541-2462, 1990.
- Tsang, Y. W., The effect of tortuosity on fluid flow through a single fracture, *Water Resour. Res.*, 20(9), 1209-1215, 1984.
- Tsang, Y. W., and C. F. Tsang, Channel model of flow through fracture media, *Water Resour. Res.*, 23(3), 467-479, 1987.
- Tsang, Y. W., C. F. Tsang, I. Neretnieks, and L. Moreno, Flow and tracer transport in fractured media: a variable aperture channel model and its properties, *Water Resour. Res.*, 24(12), 2049-2060, 1988.
- Tsang, Y. W., and C. F. Tsang, Flow channeling in a single fracture as a two-dimensional strongly heterogeneous permeable medium, *Water Resour. Res.*, 25(9), 2076-2080, 1989.
- Tsang, Y. W., Usage of "equivalent apertures" for rock fractures as derived from hydraulic and tracer tests, *Water Resour. Res.*, 28(5), 1451-1455, 1992.
- Tunnicliffe, B. S., Mass removal from a rough-walled fracture: experimental investigation using permanganate, Master's thesis, Univ. of Waterloo, Waterloo, Ontario, 1999.
- van Genuchten, M. Th., and W. J. Alves, Analytical solutions of the one-dimensional convective-dispersive solute transport equation, *U.S. Department of Agriculture, Technical Bulletin No. 1661*, 151 p.
- Walsh, J. B., The effect of pore pressure and confining pressure on fracture permeability, *Int. J. Rock Mech.*, 18, 429-435, 1981.
- Witherspoon, P. A., J. S. Y. Wang, K. Iwai, and J. E. Gale, Validity of cubic law for fluid flow in a deformable rock fracture, *Water Resour. Res.*, 16(6), 1016-1024, 1980.
- Yeo, I. W., M. H. De Freitas, and R. W. Zimmerman, Effect of shear displacement on the aperture and permeability of a rock fracture, *Int. J. Rock Mech. Min. Sci.*, 35(8), 1051-1070, 1998.
- Zheng, C., and G. D. Bennet, *Applied Contaminant Transport Modeling: Theory and Practice*, Van Nostrand Reinhold, New York, 1995.
- Zimmerman, R. W., and G. S. Bodvarsson, Hydraulic conductivity of rock fractures, *Transport in Porous Media*, 23, 1-30, 1996.
- Zimmerman, R. W., S. Kumar, and G. S. Bodvarsson, Lubrication theory analysis of the permeability of rough-walled fractures, *Int. J. Rock Mech. Min. Sci. & Geomech. Abstr.*, 28(4), 325-331, 1991.
- Zimmerman, R. W., and I. W. Yeo, Fluid flow in rock fractures: cubic law, lubrication equation and Stokes equation, *Proceedings of the International Symposium Dynamics of Fluids in Fractured Rocks, Concepts and Recent Advances*, Lawrence Berkeley National Laboratory, 13-16, 1999.